Bulk and Surface Electronic Structure of Rare Earth Metals

A thesis submitted in accordance with the requirements of the

University of Liverpool

for the degree of

Doctor in Philosophy

by

Robert I. R. Blyth

of the

Surface Science Research Centre

September 1991

Abstract

The basic properties of the rare earth metals, including single crystal growth, crystal and magnetic structures, and the relationship between electronic and magnetic structure, are reviewed. The problems encountered by the theoretical treatment of the partially occupied, but highly localised, lanthanide *4f* levels as bands are discussed, and bandstructure calculations presented for the hexagonal close-packed rare earths. These are compared with available experimental and theoretical data. It is suggested that the exchange-splitting of the lanthanide valence bands may well persist in the paramagnetic state, and that account should be taken of the localised *4f* moments in future calculations. The difficulties associated with the preparation of clean single crystal rare earth surfaces are described. The origin of the surface-order-dependent state seen in angle-resolved UV photoemission (ARUPS) spectra from rare earth (0001) surfaces is discussed. (7 × 1) reconstructions of the $(11\bar{2}0)$ surfaces of Ho, Er and Y are reported, with the resulting surface geometric and electronic structure being indistinguishable from those of the ideal (0001) structure. Momentum-resolved inverse photoemission measurements are presented for Y(0001), with results in good agreement with the calculated bandstructure. A comprehensive ARUPS study of the valence band of Ho(0001) is reported, and the results demonstrated to be entirely explicable in terms of emission from one-electron states. ARUPS data from Y(0001), Gd(0001) and Tb(0001) are presented, discussed in the light of the Ho results, and the conclusions of previous ARUPS studies of these surfaces revealed to be in error. Essentially similar ARUPS features are seen on all hcp rare earth (0001) surfaces so far studied and it is suggested that all other such surfaces will show the same features. The Ho(0001) *5p* levels are shown to have significant band character, suggesting that further refinements to the bandstructure calculations are required.

Acknowledgements

I would like to thank my supervisor Peter Andrews for giving me the opportunity to come to Liverpool, and for introducing me to alloys and electron spectroscopy, and Steve Barrett for recruiting me into the rare earth group.

The photoemission data in this work were collected with the assistance, on various SRS runs, of Steve Barrett, Sarnjeet Dhesi, Peter Gravil, Kay Newstead, Rossella Cosso, Neil Heritage, Tony Begley, Robin Jordan, Adam Patchett, Thanos Mitrelias and Nick Prince. The holmium photocurrent calculations were performed with the help of Sarnjeet Dhesi, using potentials calculated by Tony Begley.

I would also like to thank Walter Temmerman and Tony Begley for their patient assistance with the LMTO codes, John Murray and Ian Collins for technical assistance with the KRIPES spectrometer, and Tracy Turner for keeping 6.2 up and running under difficult conditions. The unseen talents of the SRS crews and the computer staff at Daresbury and Rutherford are also acknowledged.

David Fort *et al.* at the School of Metallurgy and Materials, University of Birmingham, U.K grew the high quality rare earth crystals used for this work, and their skills are much appreciated.

The Science and Engineering Research council is acknowledged for the provision of a research studentship, beamtime at the SRS and funding for the rare earth programme at Birmingham.

Contents

Publications

The work described in this thesis has been, or will be, published in the following papers:

Comments on the UV photoelectron spectrum of yttrium
S.D.Barrett, R.G.Jordan, A.M.Begley and R.I.R.Blyth
Z. Phys. B - Cond. Matter **76** 137 (1989)

(7 × 1) reconstruction of the $(11\bar{2}0)$ surfaces of Ho and Er
S.D.Barrett, R.I.R.Blyth, S.S.Dhesi, A.M.Begley and R.G.Jordan
Phys. Rev. **43B** 4573 (1991)

Observation of a (7 × 1) surface reconstruction on Y$(11\bar{2}0)$
S.D.Barrett, R.I.R.Blyth, S.S.Dhesi and K.Newstead
J. Phys.: Condens. Matter **3** 1953 (1991)

The unoccupied states of a rare earth metal: Y(0001)
R.I.R.Blyth, P.T.Andrews and S.D.Barrett
J. Phys.: Condens. Matter **3** 2827 (1991)

Surface structure of rare earth metals
R.I.R.Blyth, R.Cosso, S.S.Dhesi, K.Newstead, A.M.Begley and R.G.Jordan
Surf. Sci. **251/252** 722 (1991)

Determination of the Tb Γ_{4-} critical point energy from angle-resolved UV photoemission of Tb(0001)

R.I.R.Blyth, S.S.Dhesi, A.J.Patchett, T.Mitrelias, N.P.Prince and S.D.Barrett

J. Phys.: Condens. Matter **3** 6165 (1991)

Electronic structure of holmium

R.I.R.Blyth, S.D.Barrett, S.S.Dhesi, R.Cosso, N.Heritage, A.M.Begley and R.G.Jordan

Phys. Rev. **44B** (in press)

Band effects in the 5p levels of Ho(0001)

R.I.R.Blyth, A.J.Patchett, S.S.Dhesi, R.Cosso and S.D.Barrett

J. Phys.: Condens. Matter **3** (in press)

Surface electronic structure of rare earth metals

R.I.R.Blyth, S.S.Dhesi, P.A.Gravil, K.Newstead, R.J.Cole, A.J.Patchett, N.P.Prince and S.D.Barrett

J. Alloys and Compounds (in press)

Valence band electronic structure of Gd(0001) and Y(0001)

R.I.R.Blyth, S.S.Dhesi, K.Newstead, R.Cosso and S.D.Barrett

Z. Phys. B - Cond. Matter (submitted)

Self-consistent energy bands of the hcp rare earth metals

R.I.R.Blyth

Physica Scripta (submitted)

In addition, this work has been presented at the following conferences:

IOP Solid State Physics Conference, Warwick University, U.K. (1989)

Rare Earth and Actinide Meeting, Birmingham, U.K. (1990)

11th European Conference on Surface Science, Salamanca, Spain (1990)

9th Interdisciplinary Surface Science Conference, Southampton, U.K. (1991)

11th Annual Meeting of the Condensed Matter Division of the EPS, Exeter, U.K. (1991)

19th Rare Earth Research Conference, Lexington, U.S.A (1991)

12th European Conference on Surface Science, Stockholm, Sweden (1991)

CHAPTER 1

Introduction

The work described in this thesis, which began in 1988, opened the third century of rare earth research. In 1987 the two-hundredth anniversary of the discovery of the first rare earth mineral [1] had been celebrated by a souvenir publication [2] from the Rare Earth Information Center (RIC), Ames, Iowa, followed a year later by a commemorative volume of the *Handbook on the Physics and Chemistry of Rare Earths* [3]. In the first two centuries many of the unique properties of these metals were investigated, and some explained, but there is one problem that was evident from the start and still persists to this day: how many rare earths are there ? In the beginning, before the periodic table had been constructed, and the electronic structure which determined the periodicity understood, it was not at all obvious how many rare earths there were going to be. Present day scientists are well aware of the total composition of the periodic table, and the problem now is more subtle: how to convince the world that there are seventeen rare earths, *not* fifteen. The impatience of the rare earth *cognoscenti* with their colleagues is perhaps best summed up by the following quotation, from an article in the *Journal of the Less-common Metals* [1].

> 'At the outset of this paper I must, unfortunately, define the term "rare earths" since so many scientists still incorrectly use these two words to mean the "lanthanides" [i.e. the elements with atomic numbers Z = 57 (lanthanum) to Z = 71 (lutetium)]. The correct terminology as defined by the International Union of Pure and Applied Chemistry is that the *rare earths* comprise the elements scandium (Z =21), yttrium (Z=39) and the lanthanides, and this definition will be used in this paper.'
>
> K.A.Gschneidner Jr., RIC director, Ames, Iowa (1984) [4]

---

[1] Now, alas, renamed the *Journal of Alloys and Compounds*

The periodic table, slightly modified to emphasise the location of the seventeen rare earths, can be found at the back of this thesis.

The foregoing discussion might appear frivolous, but it isn't. If it is forgotten that Sc and (especially) Y are rare earths it can be easily overlooked that they have the same crystal structure and analogous outer electronic configurations to the heavy lanthanides. The configurations for Sc and Y are $(3d4s)^3$ and $(4d5s)^3$ respectively, while those of the heavy lanthanides are $4f^n\ (5d6s)^3$. As a result Sc and Y can be considered as the prototype rare earths, useful in determining if a lanthanide property is due to the presence of the $4f$s. The rare earths and their unique properties are more formally introduced in chapter 2, but for now it is worth emphasising that most, if not all, of these properties are a result of the underlying electronic structure. It should then be obvious that it would be highly desirable, from the point of view of first understanding and secondly exploiting their properties, to be able to calculate the electronic bandstructure of the rare earths from first principles. Given the relative ease with which this can nowadays be accomplished for other metals this may not seem a particularly arduous task, but as explained in chapter 3 this is far from the case. Of the seventeen rare earths only Sc and Y have well understood bandstructures, while those of the lanthanides are a subject of some controversy. This is fuelled not only by the inability of band calculations to cope with the partially occupied, but highly localised $4f$ levels, but also by the relative paucity of experimental data on the electronic structure of rare earths. There are numerous experimental techniques for determining the electronic structure of a solid, all of which require high-purity samples, and many of which additionally require high-quality single crystals. As described in chapter 2 their chemical similarity and high reactivity makes the preparation of suitable samples of the rare earths particularly difficult, and as a result the experimental study of rare earth electronic structure is still in its infancy. The experimental techniques can be loosely catagorised according to the kind of information they yield. Firstly, there are the Fermi surface techniques. As explained in chapter 2 the Fermi surfaces of the lanthanides play a major role in determining their magnetic structure, and for this reason rare earth Fermi surfaces have attracted much experimental interest. The majority of Fermi surface techniques are performed at liquid helium temperatures on specimens with long conduction electron mean free paths (mfps), usually assessed by means of the residual resistance ratio (RRR – the ratio of resistivities at 273 and ~ 0 K). Many materials can be refined to give single crystal samples with RRR values greater than 10^4, and here the choice of technique is wide. For rare earths, where RRR values of only a few hundred are considered exceptional, the only useful technique is the de Haas-van Alphen (dHvA) method [5]. This takes advantage of the quantisation of conduction electron energy levels in a magnetic field **B**. The allowed states in **k** space are a series of tubes about **B** with cross-sectional areas proportional to **B**. As **B** is increased these tubes expand, eventually passing through the Fermi surface, with the de-population of a tube at its most rapid as it passes through extremal cross-sections of the Fermi surface. Electron properties are thus periodic in 1/**B**, with frequency proportional to the extremal cross-sectional area of the Fermi surface. These oscillations are best observed in the conduction electron magnetisation – the de Haas- van Alphen effect. In general each extremal area perpendicular to **B** will give rise to a frequency, which will be resolvable only if the level spacing $h\omega_c$ (where h is Planck's constant and ω_c is e**B** divided by the cyclotron mass) is less than kT (dHvA measurements are usually performed at liquid helium temperatures). The various frequency components of the signal are separated by Fourier analysis, and are usually plotted as graphs of frequency against the angle between **B** and the crystal axes. If the crystal quality is poor then signals from different crystallites may interfere, and if the conduction electrons are unable to complete the larger real space orbits, due to scattering from crystal imperfections, then frequencies from the corresponding **k** space orbits will be missing. RRR values of ~ 100 are sufficient for most metals, but the high resistivity exhibited by rare earths at 273 K means that RRR values several times higher are needed. The raw dHvA data is not very informative on its own, and for its interpretation a model of the Fermi surface is required, such as those shown in chapter 3. For metals with strong magnetic anisotropy, such as the heavy lanthanides Tb - Tm, there is the problem of restraining the sample, *without introducing dislocations*, against the torque produced when the magnetisation is not parallel to **B**. Interpretation of any results is further complicated since the direction of **B** alters with changing H. There have been several dHvA studies of rare earths [6 - 14], but only one of a sample showing magnetic anisotropy : Tb [10].

Although there are other techniques, such as soft X-ray emission, the electron spectroscopies are the most informative and widely used to determine electronic structure away from the Fermi level (E_F). Other than Auger spectroscopy, which provides information on the local density of states (DOS) around a core hole, these can be conceptually divided into two sub-groups. The members of the first group are X-ray photoemission spectroscopy (XPS), bremsstrahlung isochromat spectroscopy (BIS), angle-integrated UV photoemission spectroscopy (UPS) and momentum-integrated inverse photoemission (IPE). These spectroscopies supply information on the occupied (XPS, UPS) and unoccupied (BIS, IPE) DOS, albeit modulated by electron-photon matrix elements, and the influence of the final state (UPS) or initial state (IPE) DOS. The common feature among them is their lack of momentum information. In XPS and BIS the photon momentum cannot be neglected and so the transition from initial to final state does not conserve electron momentum. In UPS and IPE the emitted / incident electrons are not sufficiently collimated, or the sample being used is not a single crystal. Polycrystalline samples are sufficient for these methods, and much early work on rare earths was performed using evaporated thin films (see the review by Netzer and Matthew [15]). The great disadvantage of electron spectroscopies is that due to the short mfp of electrons in solids they are surface sensitive. The experimentally determined mfps [16] for electrons in rare earths, as a function of their kinetic energy, are shown in fig. 1.1. Note that the mfp increases towards the high end of the energy scale, which means that XPS and BIS are much less surface sensitive than UPS or IPE. This surface sensitivity means that clean surfaces must be prepared, extremely difficult for the highly reactive rare earths, and maintained for the duration of the experiment, which entails use of ultra-high vacuum (UHV) technology. In addition to these experimental difficulties, the surface sensitivity alters the nature of the available information. For UPS and IPE especially, the spectra will contain features due to the

Fig. 1.1 Mean free paths of electrons in rare earths (after Gerken *et al.* [16])

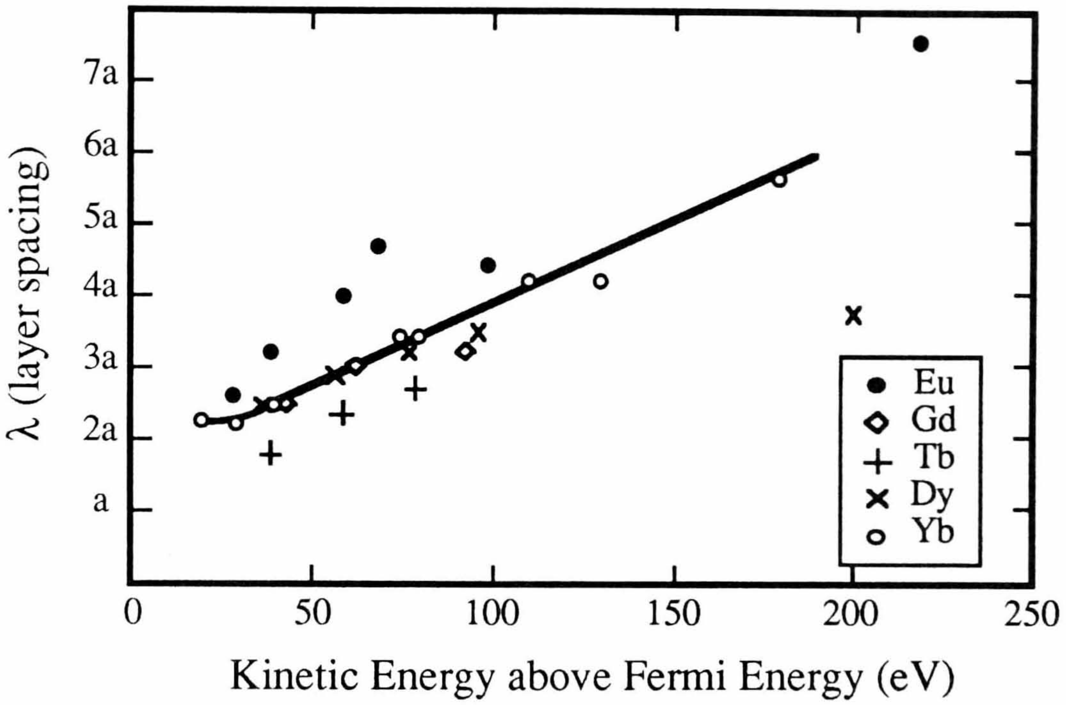

surface DOS, which may have a greatly altered lineshape compared to that of the bulk. Whether this is an advantage or a disadvantage depends on whether it is the bulk or surface DOS that is of interest.

The second sub-group is really an extension of the first. In UPS and IPE the photon momentum can be considered negligible. The transitions between initial and final states will thus proceed vertically in **k**-space, as shown schematically in figure 1.2. If a single crystal of known orientation is used, and the angular dispersion of the detected / incident electrons is small, then application of conservation laws can be used to map out the energy bands. These spectroscopies are known as angle-resolved UPS (ARUPS) [17] and momentum (**k**)-resolved IPE spectroscopy (KRIPES) [18]. The geometry for ARUPS is shown in figure 1.3 (that for KRIPES is the same, but with the direction of the arrows reversed), and descriptions of both an ARUPS and a KRIPES spectrometer can be found in chapter 4.

Fig. 1.2 Schematic diagram of the ARUPS and KRIPES processes

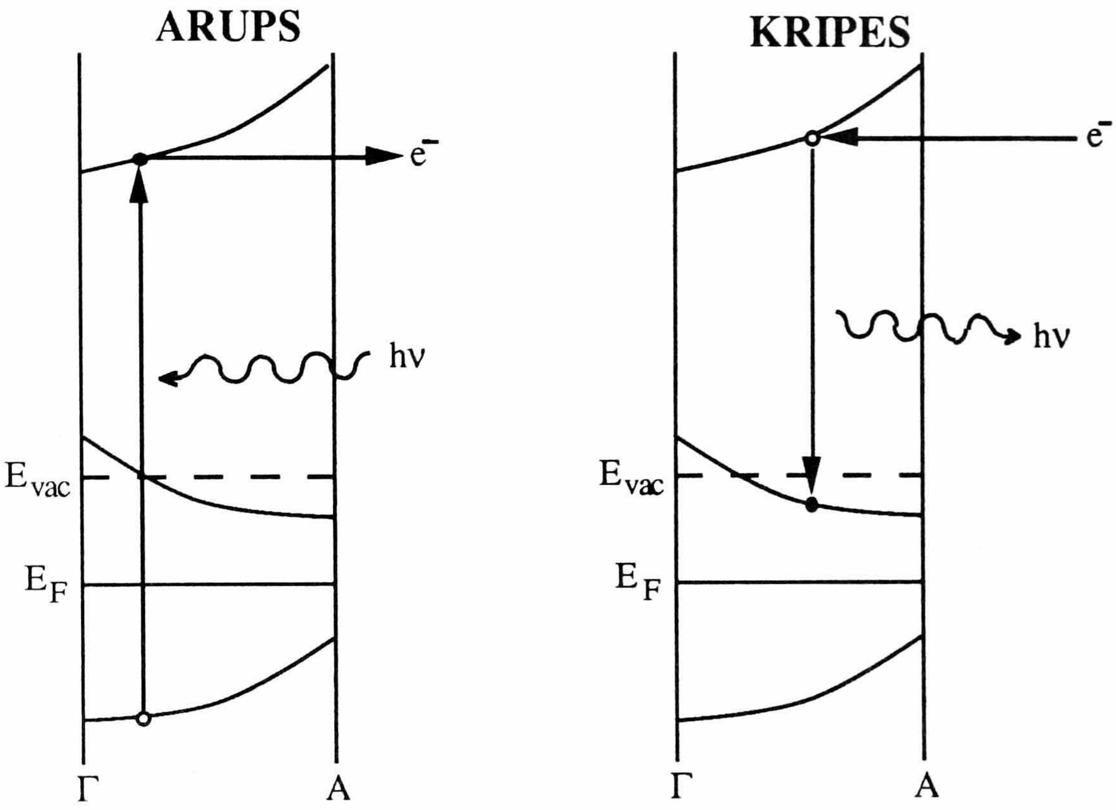

Fig. 1.3 ARUPS experimental geometry

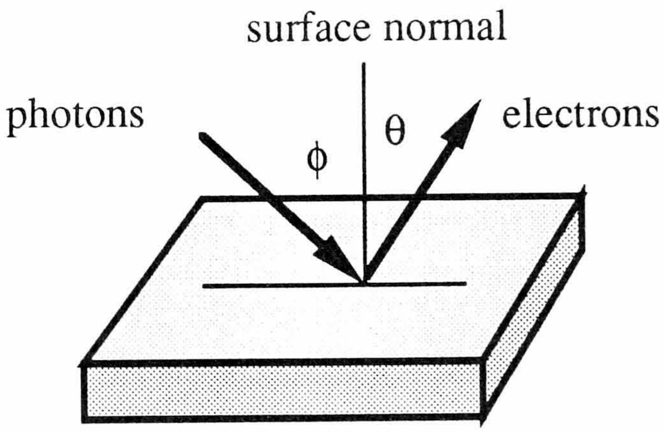

A peak in an ARUPS spectrum has a binding energy E (relative to E_F) determined by its kinetic energy E_{kin}, the photon energy $h\nu$ and the work function Φ, such that

$$E = h\nu - E_{kin} - \Phi \tag{1.1}$$

The component of electron momentum parallel to the surface, $\mathbf{k}_{||}$, is still a good quantum number at the surface. As a result $\mathbf{k}_{||}$ can be simply determined using the expression

$$\mathbf{k}_{||} = 1/\hbar \,.\, \sqrt{(2\, m_e\, E_{kin})}\, \sin\theta, \tag{1.2}$$

where m_e is the electron rest mass, $\hbar$ is Planck's constant divided by 2π, E_{kin} is the electron kinetic energy and θ is the emission angle relative to surface normal (see fig. 1.3). However, $\mathbf{k}_{\perp}$, the component normal to the surface, is no longer a good quantum number due to the absence of translational symmetry in this direction. As a result some form of empirical expression for the final state bands, such as the common free-electron approximation, is often used to determine $\mathbf{k}_{\perp}$ for the initial state. From the point of view of comparing *ab-initio* calculations to experimental data this is somewhat unsatisfactory, and increasing use is being made of photocurrent calculations, which explicitly calculate the final states, to bridge between experiment and theory (see chapter 3). However, for surface states, which by definition have $\mathbf{k}_{\perp} = 0$, both E and $\mathbf{k}$ can be determined and by taking a series of spectra with different emission angles their energy band dispersions can be directly mapped. In a similar manner these conservation laws can be applied to KRIPES spectra to yield the unoccupied bandstructure, with the same reservation regarding $\mathbf{k}_{\perp}$, and since KRIPES can be thought of as time reversed ARUPS [19] the photocurrent codes can also be used for KRIPES. In addition to the dispersions of surface states ARUPS can be used to measure other manifestations of surface electronic structure. The shift in the core level eigenvalues at the surface – the surface core level shift (SCLS) – can be measured in shallow core levels, varying the surface sensitivity to identify bulk and surface components either by changing the emission angle, or by tuning the photon energy. This latter method employs the variation of mfp with electron kinetic energy shown in fig. 1.1, and requires a tunable photon source such as a synchrotron. The practical requirements for ARUPS or KRIPES samples are even more stringent than for UPS and IPE in that clean, ordered *single crystal* surfaces must be prepared and maintained. As described in chapter 4, this requirement has effectively kept the number of such studies of rare earths down to a bare handful – the first two hundred years of rare earth research contain no KRIPES studies, and only only five using ARUPS [20 - 24].

This thesis contains an experimental and theoretical investigation of the electronic structure of the hexagonal and double c-axis hexagonal close packed (hcp and dhcp respectively) rare earths, although for completion that of the other rare earths is reviewed. The bulk energy bands have been calculated for all of the hcp and dhcp rare earths, while the experimental work (KRIPES and ARUPS) concentrates on the hcp metals. These form the largest rare earth sub-group, and offer the best opportunity to study systematics in electronic structure across the lanthanide series. While the primary motivation for this work was the bulk electronic structure problem, the use of KRIPES and ARUPS means that by default the surface electronic structure is also studied. As a result of this the surface geometric structure is of primary importance, and that of the $(11\bar{2}0)$ surfaces of the hcp rare earths in particular has proven to be of some interest.

CHAPTER 2

The Rare Earth Metals

"These elements perplex us in our researches, baffle us in our speculations and haunt us in our very dreams"

Sir William Crookes (1887)

"The family of rare earth metals has been termed a Pandora's box, but it has been pointed out that so far the list does not include either 'delirium' or 'pandemonium' "

William Alexander & Arthur Street (1989) [25]

First of all, they're not rare. Cerium is more abundant in the earth's crust than either lead or tin, and even the rarest of the rare earths – europium and lutetium – are more abundant than the platinum group elements. Further, the seventeen rare earth metals comprise about one in six of the total number of elements, one in five of the elements that are reasonably abundant in nature, and one in four of metals available in sufficient quantity for making useful alloys. And they're not earths either. The term 'common earth' was used in the late 18th century for the oxides of the more reactive metals such as Mg and Ca, which at the time were thought to be elemental. This terminology dates back to ancient Greece, where 'earth' was considered one of the four elements. Since yttria, yttrium oxide, was initially separated in very small quantities it became known as a 'rare earth'. In 1808 Sir Humphrey Davy showed that the earths were in fact compounds - metal oxides - but the name has stuck. Their family name is, like most family names, a historical accident, but it does contain a grain of truth. The rare earth metals in their pure metallic state are extraordinarily difficult to separate, and so the quantities of the

Figure 2.1

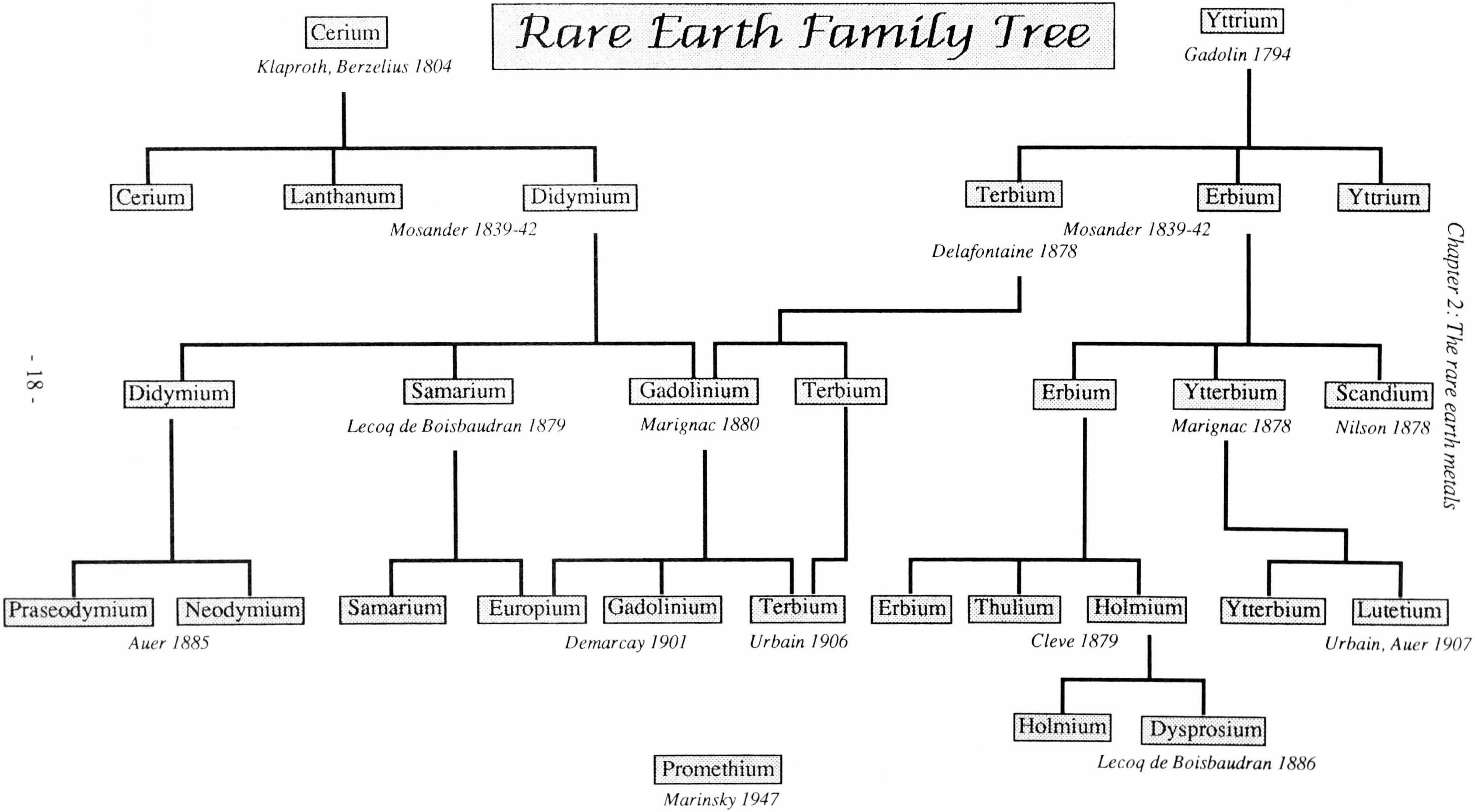

Rare Earth Family Tree

individual rare earths produced is much smaller than those of metals much less abundant. In addition they oxidise in air very rapidly, back to their 'earth' state. The paucity of surface studies of rare earth metals can thus be directly attributed to the properties implied by their name.

2.1 Discovery and nomenclature

In 1787 a lieutenant of the Royal Swedish Army on an excursion in the vicinity of a small town near Stockholm discovered a curious black stone [1]. The town, now a suburb of Stockholm, was called Ytterby, the lieutenant's name was Karl Axel Arrhenius and he named the black stone 'black stone'. History, showing a little more imagination, referred to it as ytterbite, and later gadolinite. This mineral was subsequently found to contain a new 'earth' – yttria. The story of the discovery and separation of the rare earth metals begins there, and ends in 1947 with the discovery of promethium in fission fragments. This story has recently been entertainingly told [26] and there seems little point in repeating it here. Instead fig. 2.1 shows a family tree for the rare earths, which gives some idea of the extreme difficulties experienced by the chemists of the 19th century in separating these very similar metals. By way of an individual introduction to the members of the rare earth family here is a brief description of how each acquired its name.

Scandium	Named after Scandinavia by a Swede in 1879, following a then current patriotic trend in the naming of new elements.
Yttrium	One of the four rare earths whose names are variations on 'Ytterby'
Lanthanum	From the Greek *lanthano* meaning 'I am hidden'. La remained

undetected in the 'earth' ceria for forty years after cerium metal was first isolated.

Cerium The discovery of the asteroid Ceres occurred at about the same time as the isolation of Ce metal. Ceres was the Greek god of fertility, which may or may not be irrelevant.

Praseodymium Pr was first separated from didymium, which had previously been thought to be an element. The name didymium stems from the greek word for 'twins' and a (probably apocryphal) story has it that Mosander (its discoverer) named it in honour of the twins to which his wife had just given birth. By coincidence didymium was later found to be a mixture of two elements, one of which had a green oxide and was named praseodidymium or 'green twin'. This is a rather awkward, and somewhat silly, name and over the years has evolved naturally into its current form.

Neodymium Neodymium was the other constituent of didymium, and like Pr suffered an intermediate name - neodidymium or 'new twin' - which was also rather silly.

Promethium Pm does not occur naturally, but was discovered in fission fragments of uranium in 1947. In view of this, its naming after Prometheus, who stole fire from the gods, seems entirely appropriate. Pm has been much less thoroughly investigated than the other rare earths as its isotopes are all radioactive.

Europium Possibly named as a counter to the nationalistic elements

	germanium (Germany) and gallium (Gaul = France).
Samarium	From the rare earth ore samarskite, named after its discoverer, a Russian mining officer called V.E. Samarsky.
Gadolinium	Another rare earth named after a person, Gd derives its name from that of Johan Gadolin, who in 1794 discovered the 'new earth' yttria in samples of ytterbite.
Terbium	Another Ytterby rare earth...
Dysprosium	A series of 32 precipitations with ammonia and 26 subsequent precipitations with oxalate, followed by separation of the fractions and spectroscopic studies, were required to first separate Dy from Ho. The name is derived from the Greek for 'difficult to obtain'.
Holmium	A variation on the patriotic theme, Ho derives its name from Holmia, the latin name for Stockholm. Officially it was named in honour of Per Cleve, Swedish chemist and biologist, who was born in Stockholm, but since the person proposing this honour was one O. Holmberg suspicions of a less noble motive cannot be discounted.
Erbium	...and another Ytterby rare earth...
Thulium	Named after the far-off northern mythical land Thule, perhaps in honour of the similar land, Scandinavia.

Ytterbium ...and the last Ytterby rare earth.

Lutetium The current name for this element is derived from the Latin name for Paris: 'Lutetia'. Discovered and named simultaneously (in 1907) by a Frenchman (who called it lutetium) and a German (who called it cassiopeium) it was for almost 50 years known by two names, with the respective nationalities continuing in their own use even after an international commission decided in favour of the French. It was not until they lost World War II that the name lutetium was accepted by the Germans.

2.2 Basic properties

The seventeen rare earths are generally considered to have extremely similar chemical properties, but this is not strictly the case. Most of the rare earths are trivalent in the metallic

Fig. 2.2 Metallic radii of the rare earths

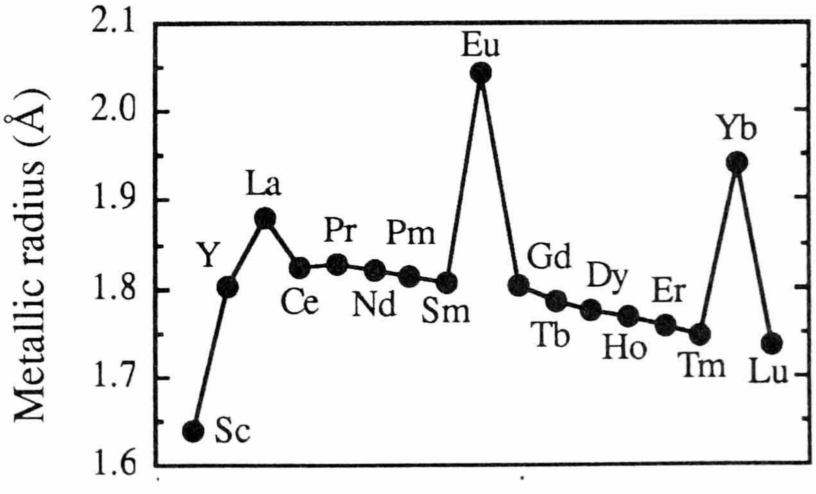

state, but two of them, Eu and Yb, are divalent, and form a range of divalent compounds, in addition to similar trivalent compounds to the other rare earths. Cerium has uncertain valency (see chapter 3) and as a result should really be considered separately. The remaining fourteen rare earths can be divided into two major sub-groups: (i) The heavy rare earths Gd - Lu , excepting Yb but with the addition of Sc and Y. The chemical properties of this group are indeed very similar, and these metals are almost always found together in mineral deposits. (ii) The light lanthanides La - Sm, excepting Ce and Eu. As with the first sub-group these are always found together, usually in deposits with Ce compounds. This division into two sub-groups is reflected in the two branches of the family tree (fig. 2.1). The physical properties of the rare earths generally show trends like that seen in fig. 2.2 for the metallic radii. There is usually a smooth variation along the trivalent series, with a 'glitch' for both Eu and Yb. For the particular case of metallic radii it is important to note the relatively low value of Sc. Scandium is classed with the other hcp rare earths, but it should be noted that this small value for the metallic radius sets Sc slightly apart from the rest. This suggests that, unlike Y which has very similar lattice parameters to the hcp lanthanides, there are some reservations in regarding Sc as an *f*-free prototype rare earth. Note also the gradual reduction in metallic radius along the series. This is known as the 'lanthanide contraction' and is a result of the electrostatic interaction between the nucleus and the steadily filling 4*f* shell.

Rare earths and their alloys and compounds exhibit a wide range of novel properties, including heavy Fermion behaviour, Kondo lattices, 'normal' superconductivity, high-temperature superconductivity, mixed valence and complex magnetic structures. Their uses include permanent magnets, catalysts, nuclear reactor control rods, lasers and metal-semiconductor contacts. They are used as getters in the steel industry, polishing powders in the glass industry and pyrophoric materials in the military. As additives or dopants they are used in searchlight arcs, fibre-optics, phosphors for television tubes and radiation dosimiters. There are few areas of solid state physics or chemistry where the rare earths do not have a role.

2.2.1 Crystal structures

The room temperature crystal structures adopted by the rare earths at atmospheric pressure are shown in fig. 2.3.

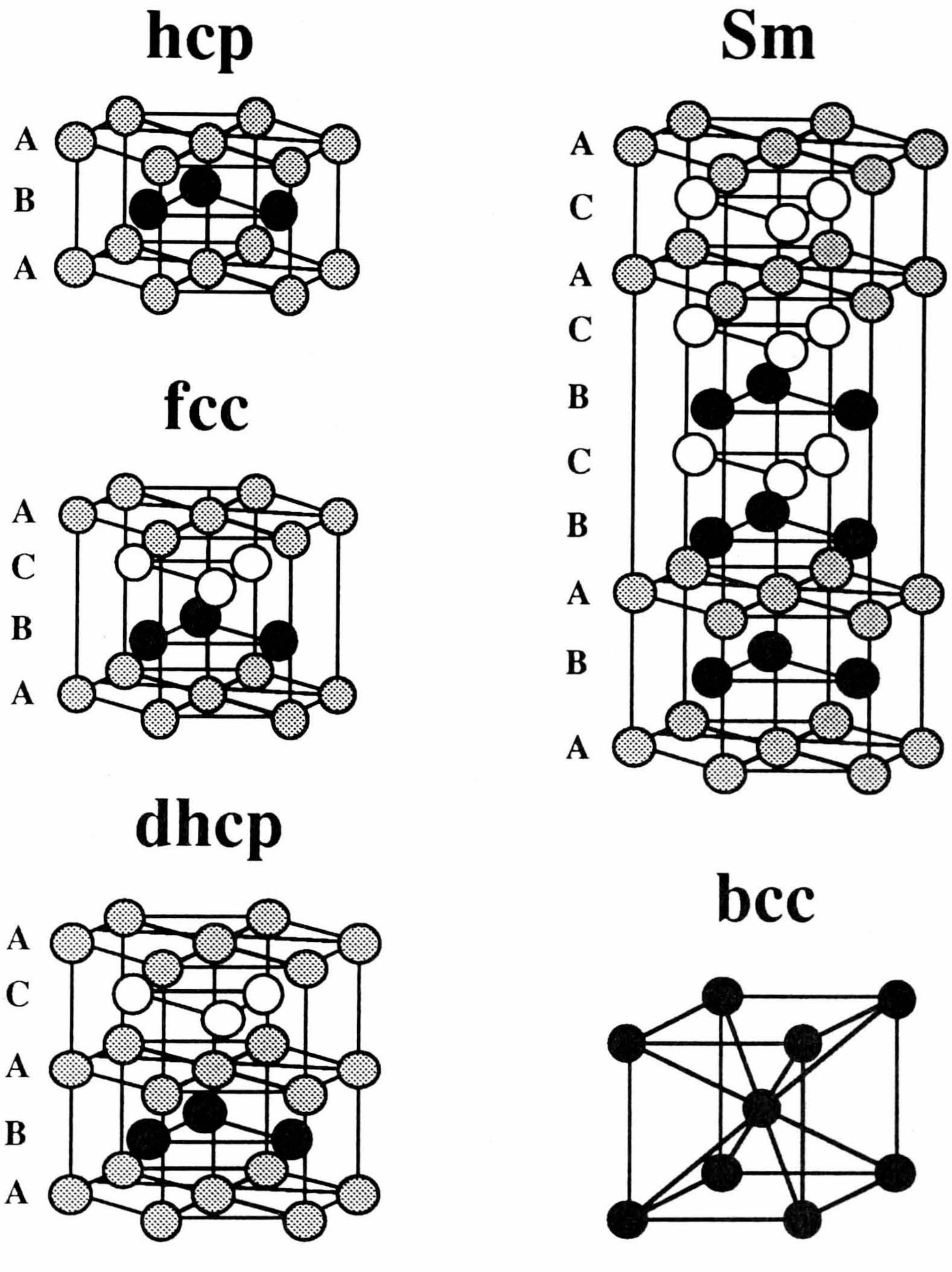

Fig. 2.3 Crystal structures of the rare earth metals

The sub-group (ii) metals adopt the dhcp structure at room temperature, while the sub-group (i) metals are hcp. The exception is Sm, which has a unique close-packed structure, as shown in fig. 2.3. La has either the dhcp or fcc structure at room temperature, being rather dependent on exactly how warm the room is, and in practice will have a large number of stacking faults irrespective of the nominal structure.

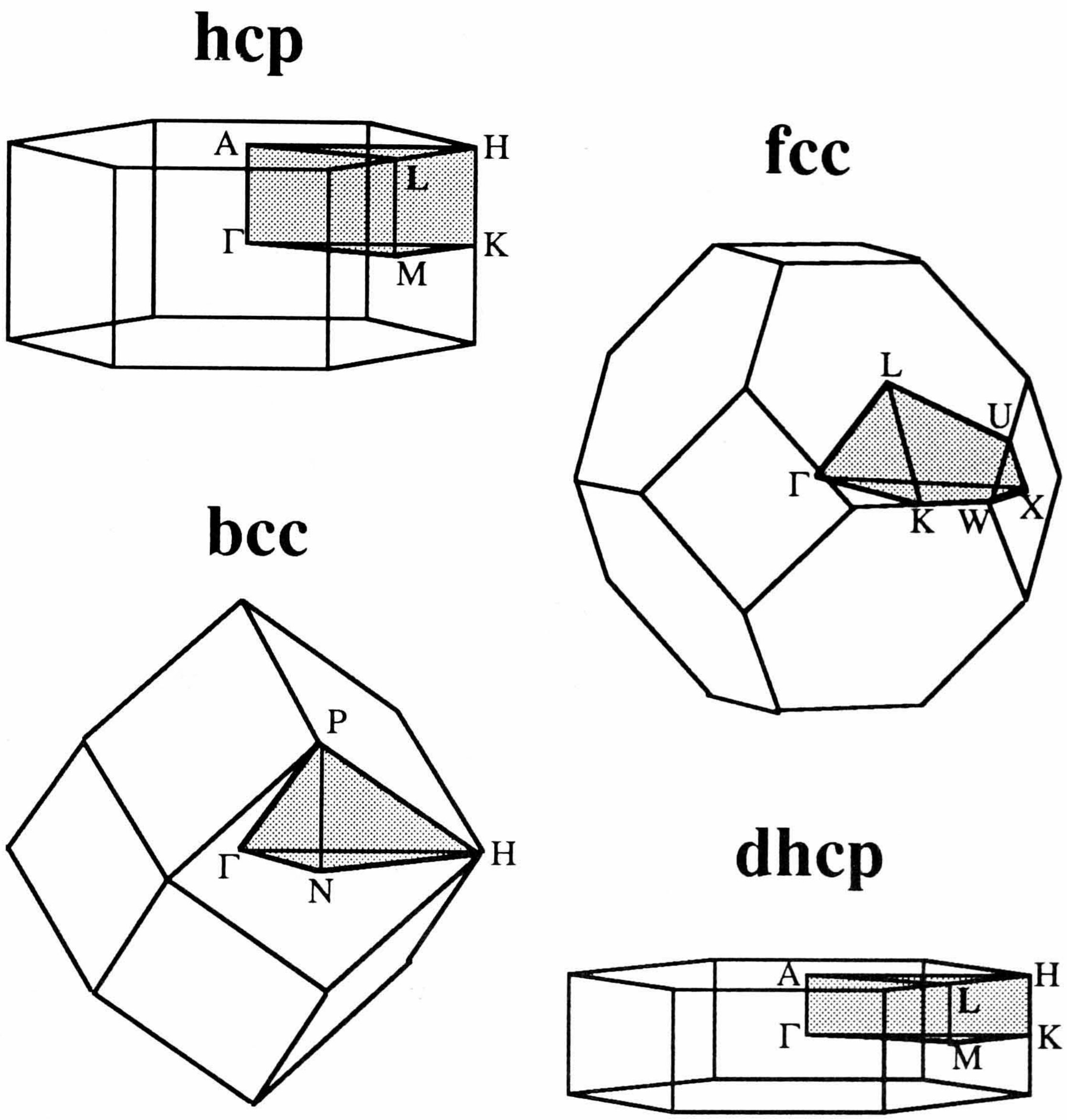

Fig. 2.4 Brillouin zones of some of the structures of fig. 2.3
The irreducible wedges have been shaded

As implied by their metallic radii (fig. 2.2) the divalent pair, Eu and Yb, are rather different, and at room temperature both are cubic, being bcc and fcc respectively. The Brillouin zones of these structures are shown in fig. 2.4, with that of the Sm structure being the same as that for hcp, with the larger *c*-axes reflected in a corresponding reduction of the ΓA dimension. The two-dimensional Brillouin zone of the (0001) surface of the hcp and dhcp structure is shown in fig. 2.5.

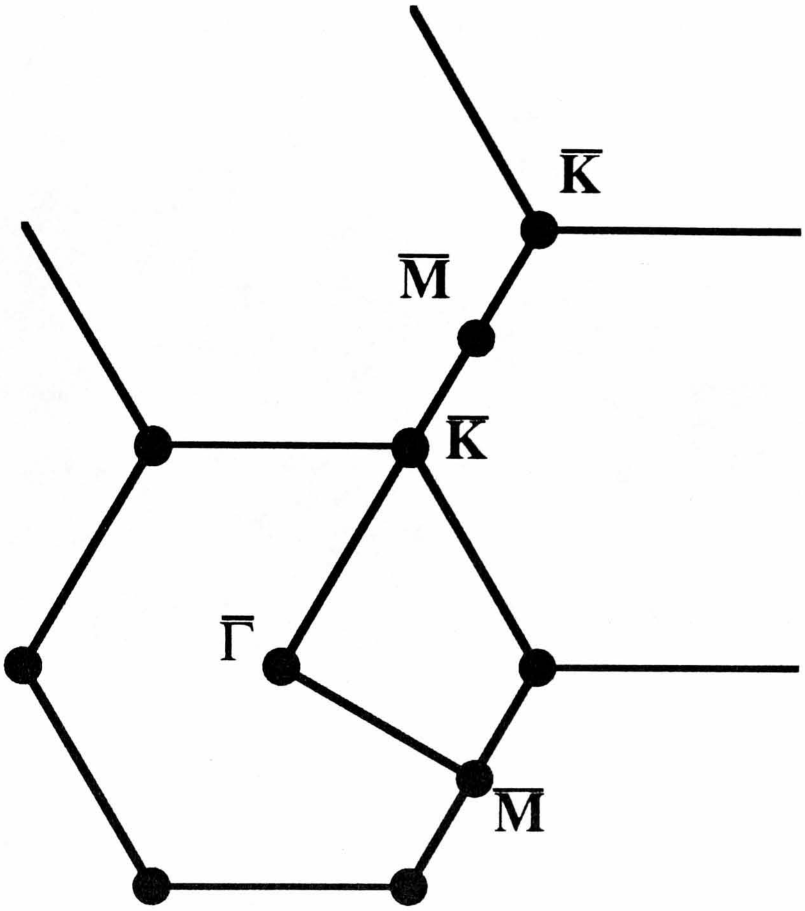

Fig. 2.5 Brillouin zone of the hcp (0001) surface

The existence of temperature dependent allotropes of all the rare earths (except Ce) are shown in fig. 2.6. Note again the divalent glitches, with the melting points of Eu and Yb being much lower than those of the trivalent rare earths. The high temperature phase of eleven of the fifteen close packed rare earths (including fcc Yb) is the bcc structure, with the exceptions being the heavy hcp lanthanides Ho, Er, Tm and Lu. However of these four at least two (Ho and Er) have an impurity-stabilised bcc phase. Below room temperature there is less uniformity in

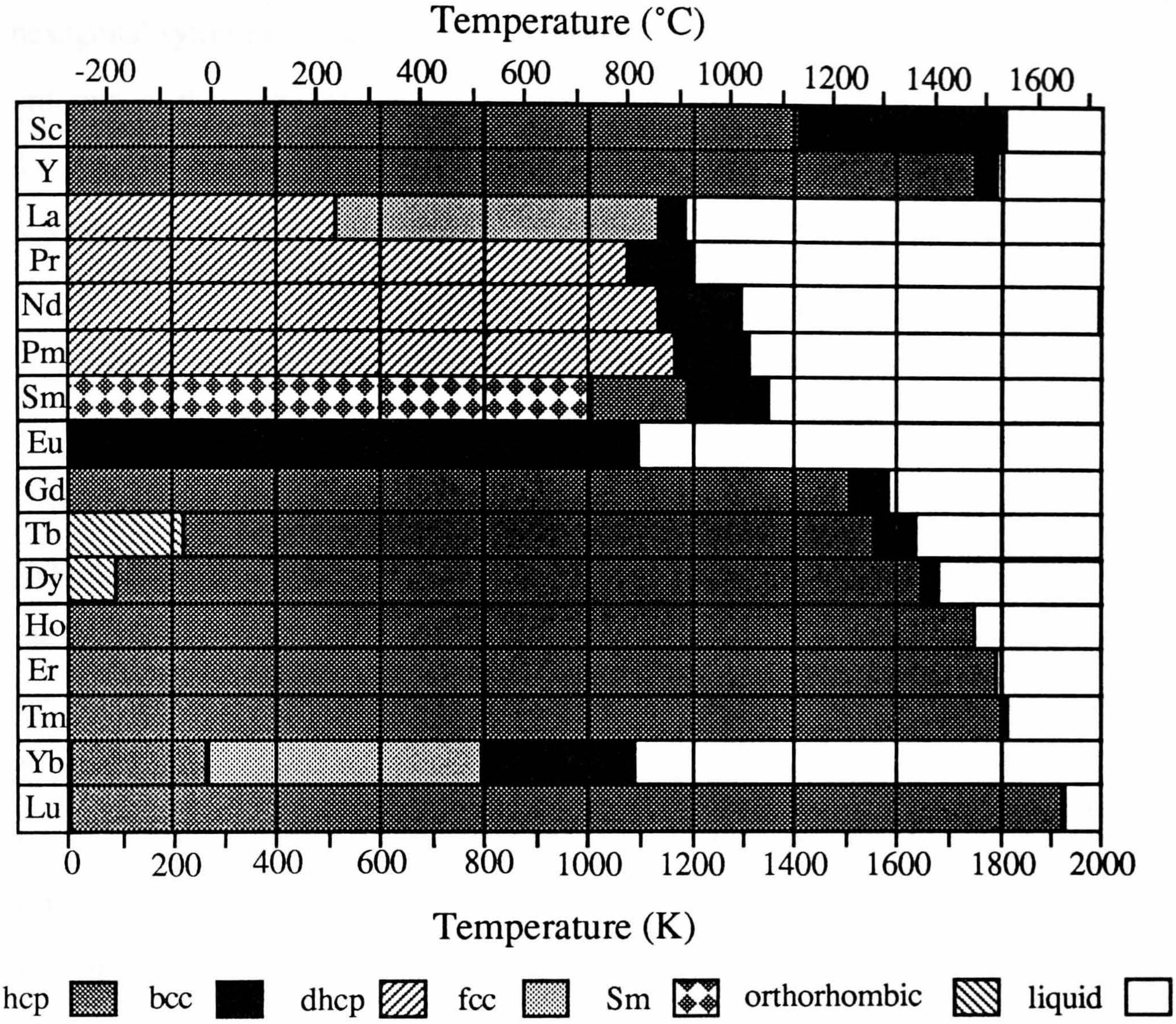

Fig. 2.6 Existence diagram of rare earth allotropes

allotrope occurrence and structure. The fcc - hcp phase transition of Yb at 270 K is important to note as it effectively prevents the use of dHvA measurements to determine the Fermi surface of fcc Yb (see chapter 3). The hcp - orthorhombic transition in Tb at 220 K is accompanied by a magnetic phase change (see section 2.2.2), whilst Dy undergoes a discontinuous change in lattice parameters to accompany its antiferromagnetic to ferromagnetic phase change at 86 K. No other rare earths have correlated magnetic and structural phase transitions.

Ignoring Eu and Yb, there is a systematic variation of the room temperature close packed crystal structures along the lanthanide series, with four different structures. The dhcp structure can be considered as a combination of fcc and hcp, with half the sites having hexagonal symmetry, and the other half cubic. This has important consequences for magnetic ordering, as these sites can order independently (see section 2.2.2). The Sm structure is also an fcc / hcp mix, but with two thirds of the sites hcp. Thus, along the lanthanide series the fcc : hcp ratio has the following sequence:

$$100 : 0 \text{ (fcc, La)} \rightarrow 50 : 50 \text{ (dhcp, La - Pm)} \rightarrow 33 : 67 \text{ (Sm)} \rightarrow 0 : 100 \text{ (hcp, Gd - Lu)}$$

Under the application of high pressure Gd and Tb adopt the Sm structure, Sm becomes dhcp and La, Pr and Nd become fcc. In other words the atmospheric pressure sequence of structures can be reversed by the application of high pressure. There has been much speculation regarding the origins of this sequence, and there appear to be two major schools of thought. Both of these schools employ systematic variations in electronic structure as the cause of the sequence, as might be expected, and the almost total absence of experimental data on the electronic structure of rare earths away from the Fermi surface has greatly hindered the discussion. Skriver [27] suggested that the sequence could be entirely explained by the variation in *d*-band occupancy across the series, supporting his argument with bandstructure calculations which showed a systematic lowering of the occupancy from La to Lu. He saw no need to invoke 4*f* hybridisation. There are two pieces of indirect experimental evidence to support this argument. Firstly, the observation of the pressure-induced hcp → Sm-type → dhcp → fcc sequence in yttrium [28], which suggests that this sequence does not require *f* electrons, since Y, of course, has none. Secondly the SCLSs measured for lanthanides [29] show a systematic increase along the series (see chapter 3), and a recent calculation [30] which correctly predicts the SCLS values shows the existence of a systematic reduction in *d*-band occupancy. Gschneidner Jr. [31] took a slightly different view, suggesting that the small *f*-*d* hybridisation also played a role, whilst not discounting the effect of *d*-band occupancy. He noted that Y and Lu have pressure induced phase transitions some 7 GPa higher than the corresponding transitions in the heavy lanthanides. The significance of this observation is that Y and Lu have no unpaired 4*f* electrons, while the heavy lanthanides do. As yet there is no definitive experimental evidence in favour of either of these viewpoints, and there is clearly a requirement for accurate, reliable bandstructure calculations supported by detailed ARUPS and / or KRIPES investigations.

Ce has been deliberately omitted from the preceding descriptions of crystal structure. Ce is a unique element. It is both an antiferromagnet and a superconductor, and is the only element to exhibit Kondo scattering (see section 2.2.2). These phenomena are a direct result of the partial delocalisation of its single 4*f* electron.

Fig. 2.7 Phase diagram of Ce (after Koskenmaki and Gschneidner [32])

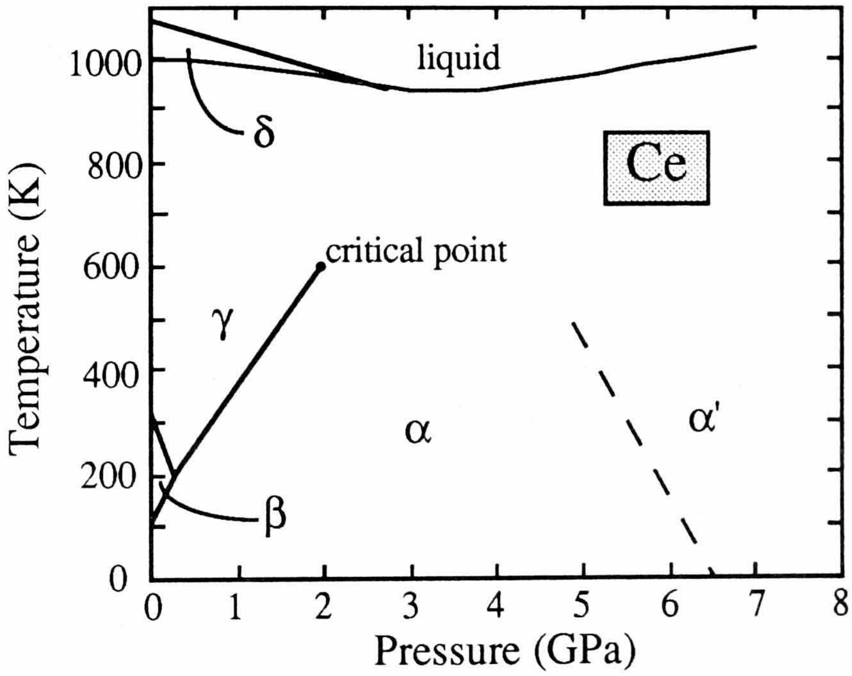

The pressure - temperature phase diagram of Ce (fig. 2.7) is also unique, as it is the only elemental phase diagram to contain a solid - solid critical point .

The five allotropes are as follows:

α : fcc, lattice parameter 4.8 Å
α' : C-centred orthorhombic, lattice parameters 3.05, 6.0 and 5.2 Å
β : dhcp, lattice parameters 3.7 and 11.9 Å
γ : fcc, lattice parameter 5.2 Å
δ : bcc, lattice parameter 4.11 Å

The α - γ phase transition has attracted much experimental and theoretical interest [kosk], much of it centred on the role of the single occupied 4*f* level (see chapter 3).

2.2.2 Magnetic structures

From Pr to Gd the magnetic moment of the *f*-shell increases as the electrons filling it obey Hund's rules, giving parallel spins. From Tb - Lu the magnetic moment decreases to zero as the spins gradually pair up. However, only Gd and Tb exhibit simple ferromagnetism, with a variety of complex magnetic structures found throughout the series. These structures have been the subject of detailed investigations by neutron scattering [33 - 35], and their form has been reasonably well established. As with crystal structure there are a number of temperature dependent phase transitions, with those of Tb and Dy accompanied by corresponding changes in the crystal structure. The existence diagram of the various magnetic phases is shown in fig. 2.8. The magnetic structures shown by the heavy lanthanides Gd - Lu are shown in fig. 2.9. A number of these structures are periodic in real space, often with a periodicity incommensurate with that of the crystal structure. The precise form of these structures for the individual phases is described elsewhere [33, 35]. The magnetic structures of Nd and Sm are interesting because the ordering occurs in the hexagonal and cubic sites of the crystal structures separately. In Nd as the temperature is lowered the moments on the hexagonal sites order at 19.2 K, giving the magnetic structure seen in fig. 2.10 (a), with the moments on layers B and C

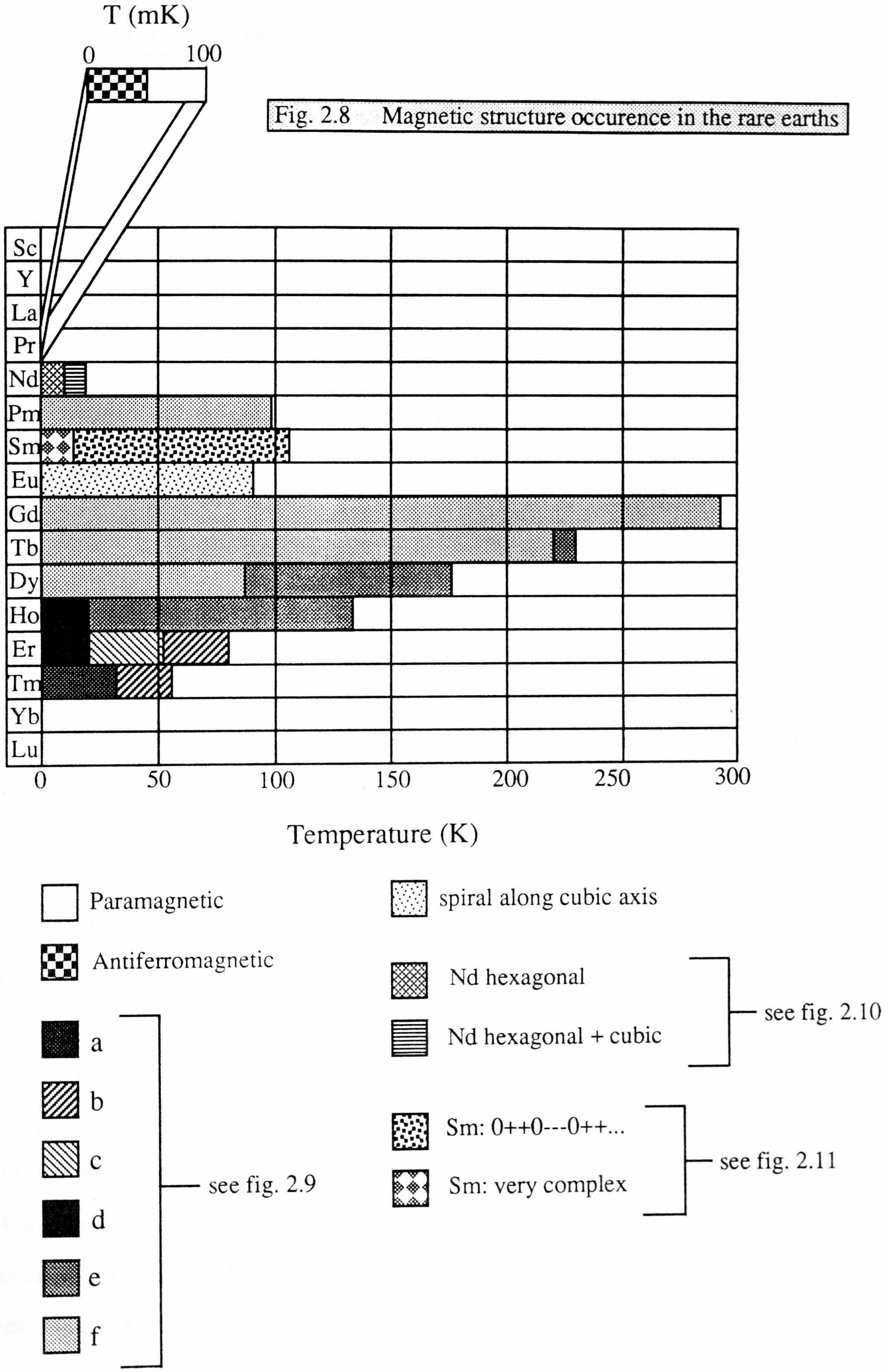

Fig. 2.8 Magnetic structure occurence in the rare earths

Fig. 2.9 Magnetic structures of the hcp lanthanides

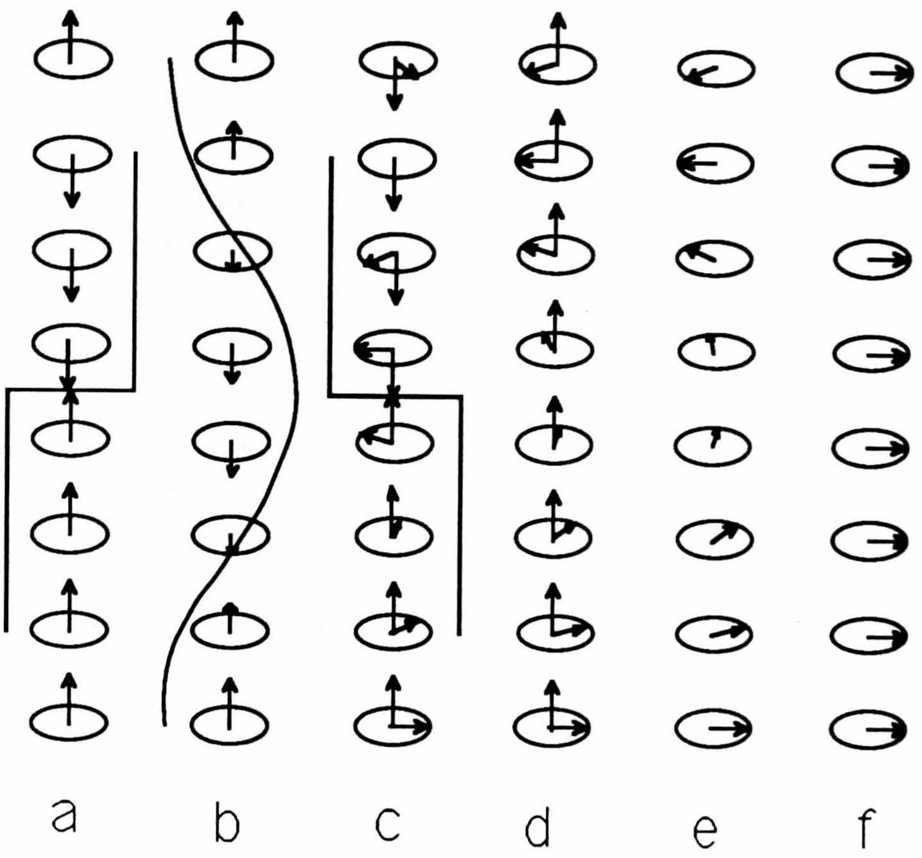

antiferromagnetically coupled. Below 7.8 K the moments on the cubic sites also order, giving the magnetic structure of fig. 2.10 (b). The structure of fig. 2.10 (a) is retained, but added to it is the antiferromagnetic coupling between alternate A layers. The behaviour of Sm is quite similar, although the complex crystal structure gives much more complex magnetic structures than those of Nd. With Sm as the temperature is lowered the hexagonal sites order at 106 K, giving the structure of fig. 2.11 (a), while the cubic sites order at 13.8 K, giving the magnetic structure of fig. 2.11 (b), which is superimposed on that of fig. 2.11 (a). The precise magnetic structure of Pm is unknown, as its radioactivity makes growth of single crystals virtually impossible. However, there is some evidence of the formation of ferromagnetic domains below 98 K [35]. Pr has a singlet ground state, with exchange smaller than the ordering threshold and would thus appear to be non-magnetic. However it has been established that due to a hyperfine 4*f*-nuclear spin interaction Pr orders antiferromagnetically below 50 mK [36]. β-Ce orders antiferromagnetically at 13 K, with the other phases being non-magnetic.

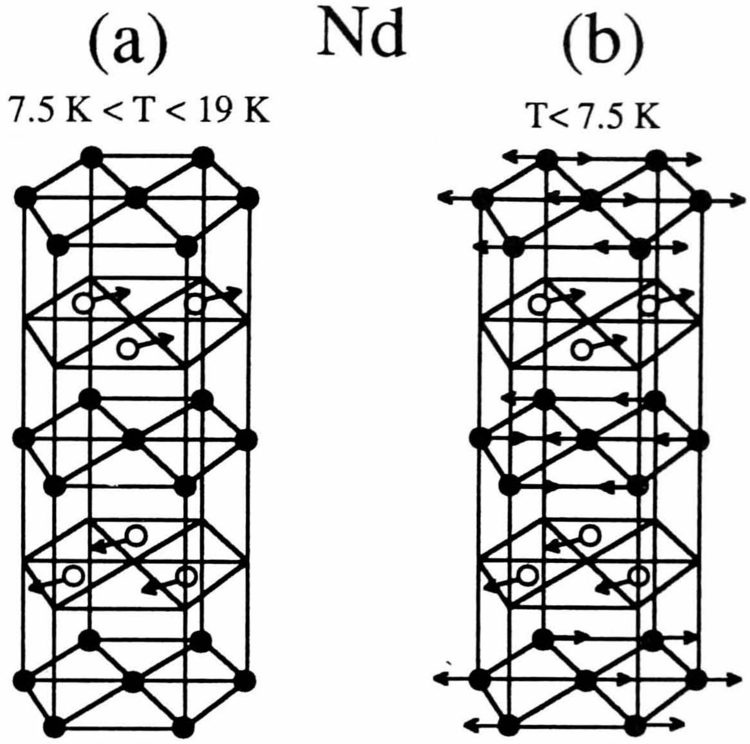

Fig. 2.10 Magnetic structures of Nd (after Koehler [33])

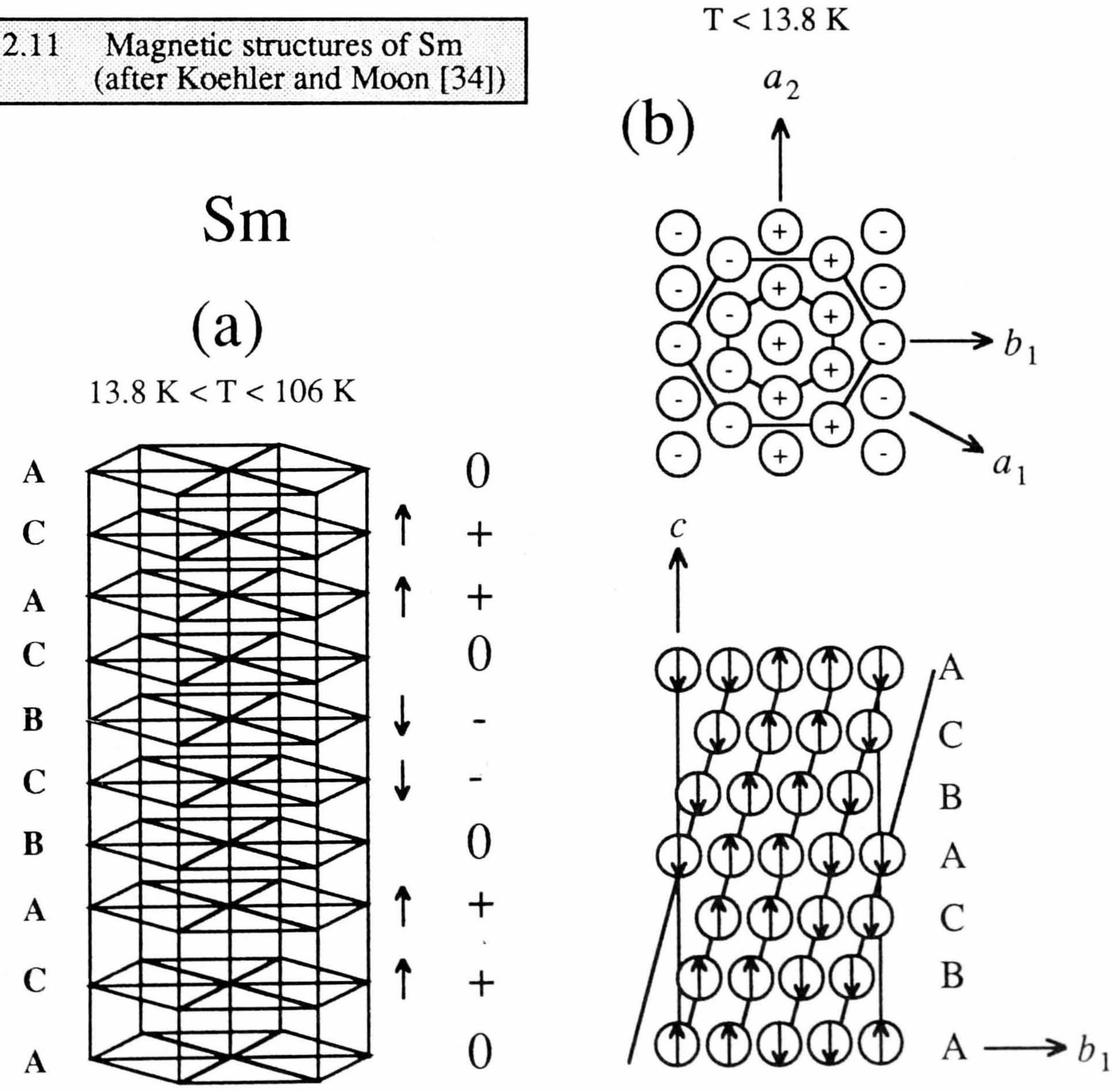

Fig. 2.11 Magnetic structures of Sm (after Koehler and Moon [34])

The unique combination of partial occupancy and high spatial localisation that the lanthanide 4*f* levels exhibit means that the lanthanides provide probably the best examples of localised-moment magnetic systems. There is essentially no overlap between *f*-wavefunctions on neighbouring sites, and so the ordering must proceed via some form of *indirect* exchange mechanism. It was not until the late 1950s that a model for a mechanism by which such an interaction could occur was formulated. This model proposes that there is a spin-density cloud set up around each site by the direct exchange interaction between the *f* levels and the valence electrons. The direction of the *f* spin at a particular site is determined by the net polarisation of the valence electrons at that site, which is in turn induced by all the other spins within the radius of the spin cloud. The details for this model were worked out principally by Kasuya [37] and Yosida [38], based on the earlier mechanism for the long range interaction of nuclear spins proposed by Ruderman and Kittel [39]. The model is thus named the RKKY interaction. The most important feature of the RKKY interaction is its extreme range, a superb example of which was reported recently by Erwin *et al.* [40]. They showed that in a Dy-Y superlattice (see fig. 2.12) the phase, and even the chirality, of the helical ordering in the Dy layers was preserved across layers of Y typically 10 - 40 atomic planes thick. At the time the RKKY interaction was being formulated the bandstructure of the lanthanides was thought to consist of the localised *f* levels with a predominantly free-electron like valence band. This proved to be an adequate description for many purposes, but failed to explain the incommensurate ordering. For a helical structure the components of the spins at the *i*th site are given by

$$J_{ix} = A\cos(\mathbf{q}\cdot\mathbf{R}_i + \Phi) \quad \text{and} \quad J_{iy} = A\sin(\mathbf{q}\cdot\mathbf{R}_i + \Phi) \tag{2.1}$$

where A is an amplitude factor, **q** is the wave vector determining the helical structure, **R** is the position vector of the site, and Φ is an arbitrary phase angle. Setting $\mathbf{q} = 0$ gives the ferromagnetic structure. The value of **q** for a particular structure is determined by the maximum in the generalised susceptibility function $\chi(\mathbf{q})$, which can be thought of as the response of the valence electrons to an external magnetic field. For a ferromagnet the maximum in χ (**q**) will occur for **q** = 0, while for a helical structure the maximum will occur for **q** ≠ 0. The form of χ(**q**) depends on the shape of the Fermi surface. If the Fermi surface contains two sheets which can be brought into point-by-point contact by translation through a vector **Q** these sheets are described as 'nesting'. It can be shown [41] that χ (**q**) will then have a singularity at **q** = **Q**. In practice perfect nesting never occurs, but if there exist large nearly-parallel sheets of Fermi surface, with average separation **Q**, then imperfect nesting will occur, and instead of a singularity in χ (**q**) there will be a maximum at **q** = **Q**. In this case the magnetic structure will be helical with characteristic wave vector **Q**. Since the Fermi surface geometry is unlikely to be simply related to the crystal structure, it is to be expected that the magnetic periodicity should be incommensurate with the real space lattice. If this analysis is correct then the Fermi surfaces of rare earths should show nesting features, with the exception of that of Gd. The experimental and theoretical search for these Fermi surface features is described in chapter 3.

The unusual magnetic properties of the rare earths are not limited to bulk magnetism. Weller *et al.* [42, 43] found that the Curie point of the (0001) surface of an epitaxial Gd film was somewhat higher than the bulk value of 293 K. The surface Curie temperature depended on the film thickness, with values of 315 K and 307 K quoted for films of thickness 14 and 50nm respectively. They proposed that the spins of the surface layer were not coupled ferromagnetically to the underlying bulk spins, with an ordered surface magnetic structure existing on top of a disordered bulk in the temperature range between the bulk and surface Curie temperatures. This is a magnetic analogy to the reconstructions seen on many metal and semiconductor surfaces, where the surface structure is not a simple termination of that of the bulk – in effect it is a magnetic reconstruction.

The RKKY interaction between different ions competes with the Kondo coupling present on individual ions. In alloys with dilute magnetic impurities the interaction between the localised impurity moments is often very weak, and these exhibit Kondo scattering. In the dhcp and hcp lanthanides the RKKY interaction is strong enough to overcome this local scattering to give magnetic order. In β- and γ-Ce however , the RKKY interaction is just weak enough for the Kondo effect to dominate, and as a result Ce is the only element to show Kondo scattering. Nowhere else in the periodic table is found the combination of a local moment with the weak indirect magnetic interaction required for this phenomenon. At low temperature β-Ce orders antiferromagnetically. α- and α'-Ce are superconducting, as are La, Sc, Y and Lu. These latter elements share with α- and α'- Ce a lack of either Kondo scattering or magnetism.

2.3 Single crystal growth

Single crystal samples are essential for any momentum-resolved investigation of electronic structure. The relative scarcity of such studies of the rare earths can be attributed directly to the difficulties associated with the growth of crystals of sufficient purity for ARUPS and KRIPES, or of sufficient crystalline quality for dHvA experiments. The work done at Ames laboratory (Iowa State University, Ames, Iowa, USA) and the School of Metallurgy and Materials (University of Birmingham, UK) made possible both the detailed dHvA studies [5] which provoked such interest in rare earth electronic structure twenty years ago (see chapter 3), and the recent renaissance in that interest provided by ARUPS and KRIPES data. All the ARUPS and KRIPES data reported from rare earth single crystals has been obtained from samples grown at either Ames or Birmingham. Rare Earth crystal growth has been reviewed by Beaudry and Gschneidner Jr. [44] (of Ames) and more recently by Fort [45, 46] and Abell [47] (of Birmingham). There are essentially three stages to the production of a single crystal: (i) separation of the raw material, (ii) purification and (iii) growth. For the rare earths their chemical similarity largely prevents their separation by chemical means, and use has to be made of the considerable variations in their physical properties. This is now performed on an industrial scale, and as a result individual rare earths are available commercially from a number of sources, notably the Rare Earth Products division of Johnson Matthey, and the Materials Preparation Center of Iowa State University (the commercial division of Ames laboratory).

2.3.1 Purification

The purification of raw material may go through a number of stages before the material can be considered to be of research grade:

(i) Vacuum melting - the metal is melted in a vacuum furnace to remove volatile impurities such as fluorides and hydrogen. For rare earths with low vapour pressure at their melting points this method works well. For other rare earths, metal loss makes this method difficult, even under an argon atmosphere.

(ii) Distillation / sublimation - many of the rare earths can be distilled or sublimed to separate the rare earth from the less volatile impurities, such as Ta or W. In addition, the rare earths with higher vapour pressure can be purified with respect to lighter impurities such as C, N or O.

(iii) Zone refining - a molten zone is repeatedly moved along the length of a solid rod in one direction. Impurities that are more soluble in the molten metal will tend to move in the same direction as the zone. Impurities that are less soluble in the liquid metal will be deposited in the solid and cannot be removed to below the equilibrium concentration by this method. Zone refining can produce significant purification with respect to transition metal impurities but is less successful for interstitial impurities such as N and O, which tend to move in the opposite direction.

(iv) Solid state electrotransport (SSE) - A large DC current (up to ~300 A) is passed through a solid rod of the material for hundreds, even thousands, of hours. Impurities migrate under the influence of the electric field to one end of the rod, with the speed of purification determined by the magnitude of the applied electric field. This is performed under UHV conditions, to prevent atmospheric impurities from entering the solid, and so the heat produced by the large currents is dissipated by radiation from the surface. Thus the applied field is limited by the particular combination of vapour pressure, melting point and diameter of the rod. The final degree of purification is determined by the balance between electrotransport and re-diffusion of the impurities. This technique is particularly effective for rare earths with high vapour pressure, producing material of higher quality than any other method. It also has the advantage that crystal growth is promoted during purification (see section 2.3.2)

2.3.2 Crystal growth

A number of different techniques have been developed or adapted for the growth of rare earth single crystals:

(i) Recrystallisation - an arc-melted sample is annealed at ~100 K below its melting point for ~24 hours to induce grain growth of the polycrystalline material. This has been used to grow large crystals (> 5 cm^3) of Sc [48], Y [49] and the heavy rare earths [44, 50, 51]. The structural quality of crystals grown by this method is normally better than for melt growth.

(ii) Vapour deposition, or sublimation - rare earth vapour condenses on to a cooled substrate held close to the material. For rare earths with relatively high vapour pressures (Sm, Eu, Tm and Yb [52]) this has produced crystals a few mm long, although of poor structural quality. It has also been used to grow a Gd crystal ~ 1 cm^3 [53].

(iii) Bridgman - a Ta crucible containing the melt is slowly lowered through the furnace to induce nucleation at the bottom tip of the crucible, with subsequent crystal growth. This method is most suited to rare earths with low melting points as at high temperatures contamination from the crucible material, forming new nucleation sites, can be a problem. A 1 cm^3 crystal of Yb has been grown using this method [44].

(iv) Czochralski - a seed crystal is introduced into the melt and slowly drawn upwards, acting as a nucleation point for growth. This has the same problems with crucible material as the Bridgman method, but these can be overcome by levitating the melt [54]. This method has been used to grow crystals of Eu [55] Y and Gd.

(v) Zone melting, or float zoning - a molten zone is moved along the length of solid rod of the metal by localised electron beam or RF induction heating. This is particularly suited to rare earths which do not undergo high temperature structural phase transitions, and can produce very large crystals. Crystals of Er and Lu ~10 cm^3 [56] have been grown with this method.

(vi) SSE - it has been observed that during purification by SSE (see section 2.2.1) grain size can increase dramatically [46, 57, 58], due to crystalline defects migrating under the influence of the electric field. SSE is often used to finish off growth started by one of the other methods, and this combination has produced the highest quality rare earth crystals grown to date (see table 2.1).

In addition to these methods for bulk single crystals, increasing use is being made of epitaxial techniques to grow crystalline thin films. For many years surface studies of rare earths have been performed on evaporated thin polycrystalline films, but there have recently been a number of reports of studies using thin single crystals grown *in-situ* on transition metal substrates. As yet only a few rare earths have been grown by this method. Gd(0001) was grown on W(110) at 450 - 500 °C [42, 43] by Weller *et al.*for their study of the magnetic reconstruction described in section 2.2.2. They reported a sharp hexagonal LEED pattern, but did not determine the stacking sequence, and thus it is not certain that this truly represented an hcp (0001) surface. The growth mode was determined to be of the Stranski-Krastonov type (formation of a single epitaxial monolayer followed by 3D island growth). This was later confirmed by Kolaczkiewicz and Bauer [59], who also found the same growth mode for Tb on W(110). In contrast Frank-van der Merwe growth (layer by layer) was found for Yb [60, 61] and Sm [62, 60], both on Mo(110), by Stenborg and Bauer. Martensson *et al.* [63] showed that for the Yb/Mo(110) system this growth mode persisted to at least four monolayers. In addition there have been several studies of adsorption of low coverages of rare earths on various substrates. These will undoubtedly contribute to a further understanding of rare earth epitaxial growth, but are rather outside the scope of this work. Although much work remains to be done to determine the ideal growth conditions for the various rare earth - substrate combinations, and to determine stacking sequences, epitaxy appears to be a potentially fruitful method of producing clean, ordered rare earth surfaces. It neatly bypasses the difficult cleaning

Element	Highest RRR	Largest high quality crystal (cm^3)
Sc	520	0.4
Y	> 1000	2.0
La	260	n/s
Ce	–	–
Pr	400	2.0
Nd	120	1.5
Pm	–	–
Sm	–	–
Eu	–	–
Gd	800	1.7
Tb	> 1000	> 5.0
Dy	125	1.0
Ho	90	2.0
Er	60	n/s
Tm	–	–
Yb	–	–
Lu	150	1.0

Table 2.1 Highest quality and largest rare earth crystals grown by SSE

procedures required for bulk crystals (see chapter 4), and for Yb in particular, where the fcc - hcp phase transition has so far prevented the growth of sufficiently large bulk crystals, epitaxial growth may well be the only option.

A final crystal growth technique has allowed the fabrication of an entirely new class of materials. Highly sophisticated molecular beam epitaxy (MBE) technology, developed largely for use in the semiconductor industry, has reached the level where it is possible to alternate deposition of one material with that of another in a tightly controlled manner. Pioneering work by Flynn and co-workers [40] has led to the use of this technology to grow rare earth superlattices. These consist of alternating layers, each several atomic planes thick, of two different rare earths, grown on a suitable substrate material. An example, $[Dy_xY_y]_n$, is shown in fig. 2.12 for two different substrate configurations. The sapphire / Nb / Y configuration may seem excessively complex, but it does avoid the necessity of cleaning a bulk rare earth crystal, and is of course relatively easy to prepare as it uses the same technology as the superlattice growth. However it is limited to the growth of c-axis superlattices. To grow a- or b-axis superlattices requires the use of a rare earth single crystal substrate, as to date suitable transition metal substrates for $(10\bar{1}0)$ or $(11\bar{2}0)$ layers have not been found. The novel properties of these superlattices have recently been reviewed by Majkrzak *et al.* [65].

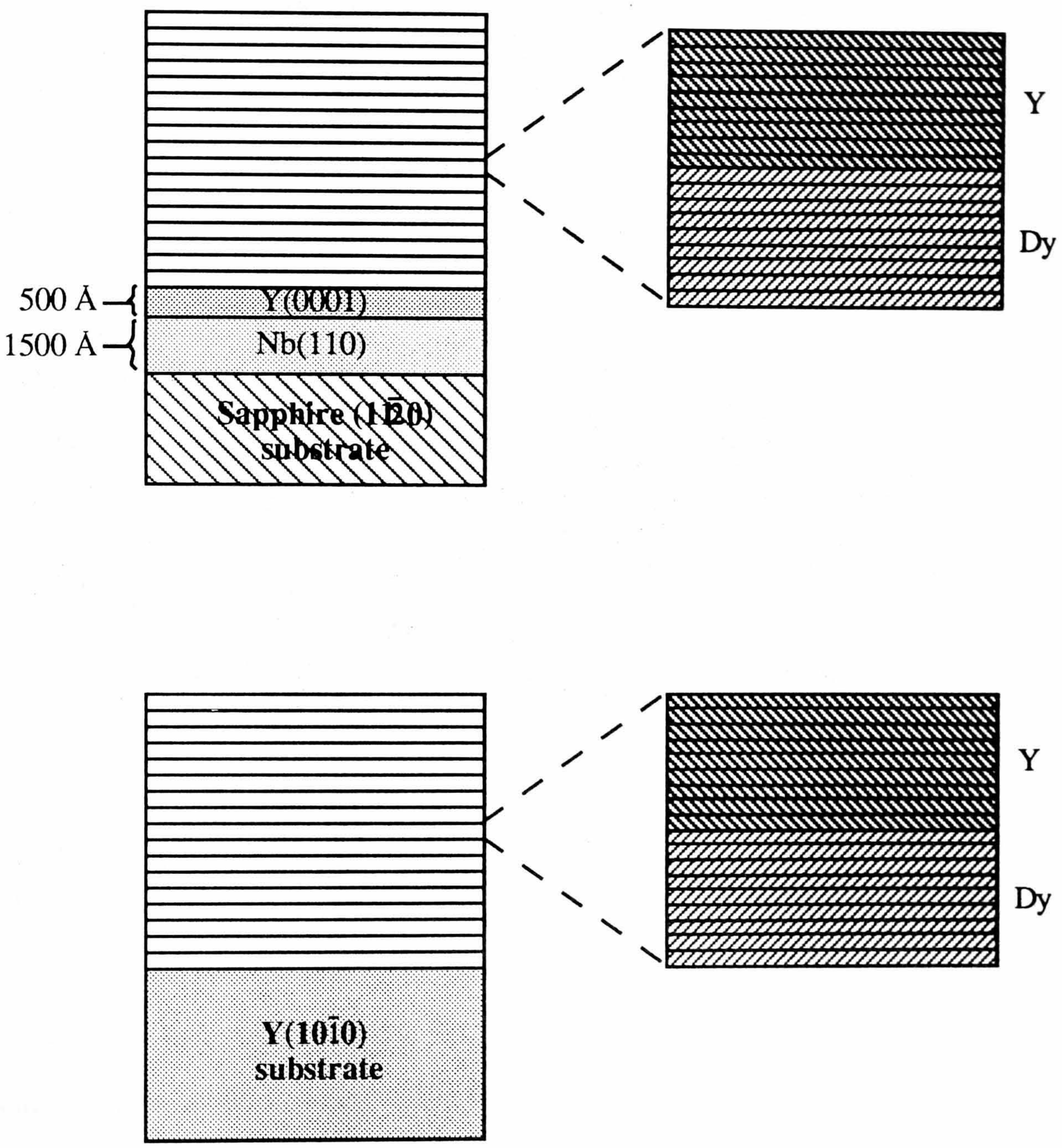

Fig. 2.12 Two geometries for MBE growth of rare earth superlattices

CHAPTER 3

Bandstructure calculations

3.1 Bulk bands

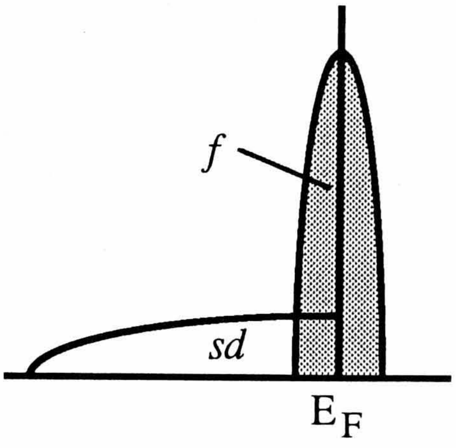

Figure 3.1 An intuitive picture of the location of bands in a lanthanide metal.

Intuitively the density of states of a lanthanide metal looks something like that shown in fig. 3.1. Since the 4*f* band is partially filled the Fermi level (E_F) must lie inside it, and from their position in the periodic table we might expect a predominantly free-electron-like form for the *sd* bands. In fact this picture is almost entirely incorrect. Our intuitive model ignores correlation effects, which is exactly the problem in calculating energy bands using any form of one-electron potential. Correlation effects become important when the correlation energy becomes greater than the bandwidth. The correlation energy U is the energy required to remove an electron from an atom and place it on the neighbouring site.

This may be simply defined [66] as

$$\underset{(1)}{U = E\,(f^{n+1})} - \underset{(2)}{E\,(f^{n})} + \underset{(3)}{E\,(f^{n-1})} - \underset{(4)}{E\,(f^{n})} \tag{3.1}$$

where n is the ground state *f*-shell occupancy. Since the one-electron terms (2) and (4) in eq. 3.1 cancel, it follows that U may be thought of as the energy difference between adding one electron to the *f* shell and taking one away. This is of course a rather crude description of two common experimental techniques - photoemission and inverse photoemission - and so we are able to access U directly. Fig. 3.2 shows the results of Lang, Baer and Cox [67] for polycrystalline samples of the entire lanthanide series (except Pm). U is the energy separation between the highest occupied and lowest unoccupied states, which are the labelled peaks in fig. 3.2. Thus for lanthanide 4*f*s U is of the order of several eV, while their width is considerably less then 1 eV [67]. Note also that fig. 3.2 shows *atomic* multiplets - the solid bars are the *free atom* fractional parentages assuming a Hund's rule $4f^n$ ground state. So it appears that we cannot calculate the energy of the 4*f*s correctly by treating them as Bloch states since correlation effects are ignored (compare figs. 3.1 and 3.2), but that treating them as localised core levels may not be such a bad approximation.

Early attempts to model the electronic and magnetic properties of the lanthanides assumed that the 4*f*s were fully localised core levels, and that the valence band was essentially free electron like, i.e., a modified version of our intuitive model of fig. 3.1. This proved to be a very successful description and many of our basic ideas about *f-f* and *d-f* interactions in rare earth metals, including the RKKY model, stem from this period. However there were some experimental results which could not be explained using a free-electron model: the electronic contribution to the specific heat of Gd, for example, required a density of states at E_F an order of magnitude greater than that given by the free-electron model. It was not until 1964, when Dimmock and Freeman [68] published the first bandstructure calculation for a lanthanide

Fig. 3.2 XPS and BIS spectra for all the lanthanides except Pm (after Lang *et al.* [67])

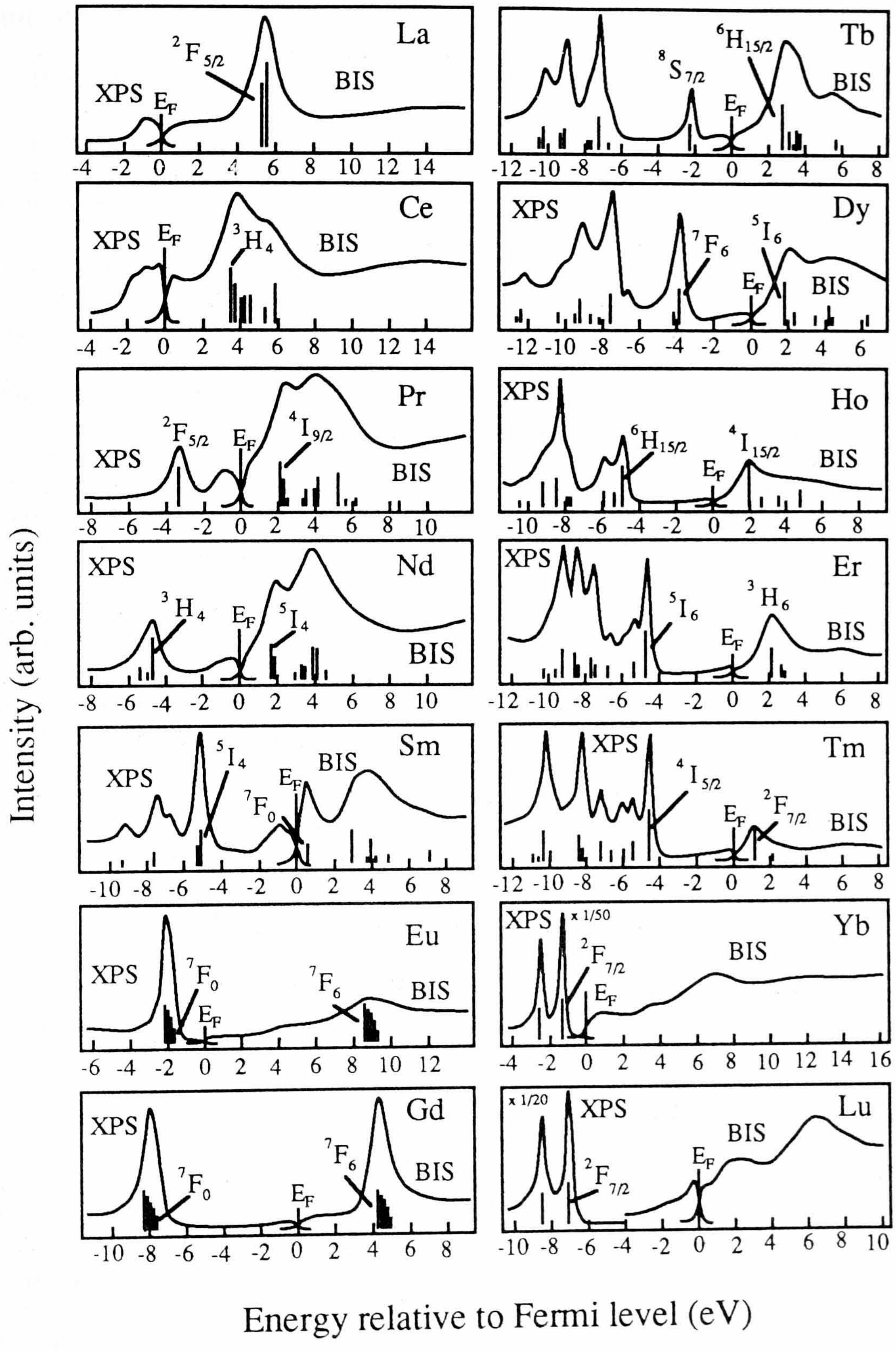

- Gd - that it was realised that the valence bands of rare earths were not free-electron like, but showed true transition metal character. This prompted a large amount of work on their electronic structure, particularly their Fermi surfaces. The first dHvA experiments on rare earths followed a few years later, after developments in crystal growth techniques. The theoretical and experimental results from this era have been extensively reviewed elsewhere [41]. Advances in computer technology which led to the widespread use of self-consistent calculations largely post-dated this great burst of theoretical interest in rare earth bands, and so for many of the lanthanides the most sophisticated bandstructures available are the relativistic augmented-plane-wave (RAPW) calculations dating from the late 1960s. These calculations, which by no means cover all the lanthanides, were not self-consistent and so only the broadest trends across the series could be investigated. With high resolution ARUPS data from rare earths now becoming available such trends may now be accessible experimentally, and with that in mind, together with a need for filling in the gaps left over from the 1960s, bandstructure calculations for all the hexagonal (i.e., hcp and dhcp) rare earths were performed.

3.1.1 Details of bandstructure calculations

Self-consistent bandstructure calculations, within the local density approximation (LDA), were performed on the Convex C-220 at the Science and Engineering Research Council (SERC) Daresbury Laboratory, United Kingdom. The linear muffin-tin orbital (LMTO) method [69, 70] with the atomic sphere approximation (ASA) was used. The LMTO method is one of the three main methods currently in use in bandstructure calculations for metals and alloys, the others being the linear APW (LAPW) and Korringer-Kohn-Rostoker (KKR) methods. Both these latter methods are slightly more accurate but require considerably greater computer time. The ASA replaces the Wigner-Seitz polyhedra of the solid by overlapping Wigner-Seitz spheres, an approximation particularly suited to close-packed elemental solids. This forces the potential to be isotropic so the deviation from ideal c / a ratio, of order 3% for the rare earths, will tend to introduce inaccuracies. However comparison of the results for Sc and Y with those from LAPW calculations [BSD], in which the potential is allowed to be of arbitrary shape, suggests that the results are not significantly affected. The experimentally observed lattice parameters were used, with the number of **k**-points sampled in the irreducible wedge of the Brillouin zone being 225 (hcp) or 135 (dhcp). The von Barth-Hedin form [71] for the local exchange and correlation was employed and calculations performed for a scalar relativistic Hamiltonian :

$$\mathcal{H} = -\nabla^2 + V - c^{-2}\,[\,\underset{\substack{\uparrow\\ \text{Mass-velocity}}}{(E-V)^2} + \underset{\substack{\uparrow\\ \text{Darwin}}}{V'\,\partial/\partial r}\,] + \underset{\substack{\uparrow\\ \text{Spin-orbit}}}{\xi\ s.l} \tag{3.2}$$

with spin-orbit coupling introduced variationally [72]. For the lanthanides the $4f$ levels were treated as part of the core, with their occupancy fixed at that observed in the solid, giving an outer electronic configuration of $(5d6s)^3$, the core eigenvalues being determined by an atomic scheme. Spin-polarisation was not included since at room temperature, where most ARUPS experiments are performed, all the rare earths except Gd are paramagnetic. The bandstructures and densities of states for all the hcp and dhcp rare earths were calculated. In addition, and by way of illustrating the problems the LDA encounters with localised states, the bands and densities of states for Ho were calculated with the $4f$s treated as bands. These results are shown in fig. 3.3. Note that the position of the f bands is that predicted from our intuitive model (fig. 3.1) i.e., E_F occurs part way through the (spin-orbit split) f band. The f bands show significant hybridisation with the *sd* bands, despite being very flat and thus very localised. The density of states at E_F for this calculation is 296 Ryd.$^{-1}$, compared to the value of 23.36 Ryd.$^{-1}$ for Ho with $4f$ core levels. Such a high value would virtually imply heavy Fermion behaviour were this to be a 'physical' result, and is entirely due to the absence of correlation effects in the calculations. Very similar results were obtained by Wu *et al.* [73] by treating the Tb $4f$s as bands.

Fig. 3.3 LMTO bandstructure of Ho, treating the 4*f* levels as band states

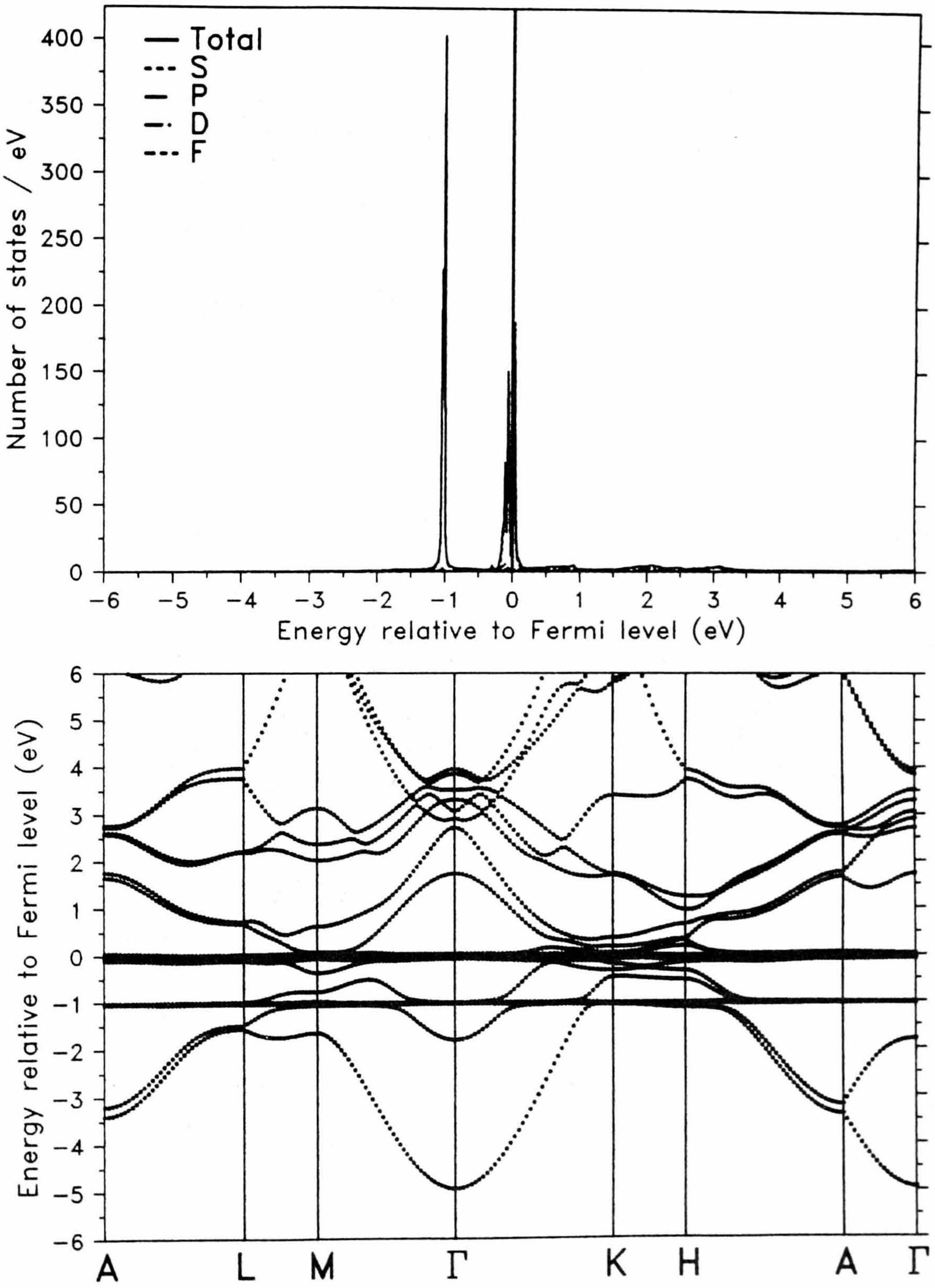

In the following sections the LMTO results are compared with available experimental data, and the more important of the earlier calculations, and a brief overview given of calculations for the cubic rare earths Ce, Eu and Yb.

3.1.2 Sc and Y

The uncertainties governing the treatment of partially occupied *f* shells do not of course apply to Sc or Y since they have no *f* electrons. The history of their bandstructure calculations has thus proceeded on entirely different lines as they are in every respect ordinary transition metals. Recently self-consistent KKR [74] and LAPW [75] calculations have appeared in the literature and the LMTO calculations reported here (fig. 3.4) complete the set of the three common methods. The form of the bandstructures for these two metals is entirely uncontroversial – critical points for Y determined by ARUPS [23] and KRIPES (see chapter 6) have been in good agreement with the calculations – and these LMTO results are essentially identical to the KKR and LAPW results. For that reason, however, they are not without interest. As mentioned in chapter 1, the outer electron configurations of Sc [$(3d4s)^3$] and Y [$(4d5s)^3$] are analogous to that adopted by most of the solid lanthanides [$(5d6s)^3$], and as a result their bandstructures are a useful benchmark. To serve as a guide when discussing critical point energies for the hcp rare earths in general, the Y bands along the ΓA direction, with critical point labels added (adapted from the LAPW calculation of Blaha *et al.* [75]) are shown in fig. 3.5.

Fig. 3.4 (a) LMTO bandstructure of Sc

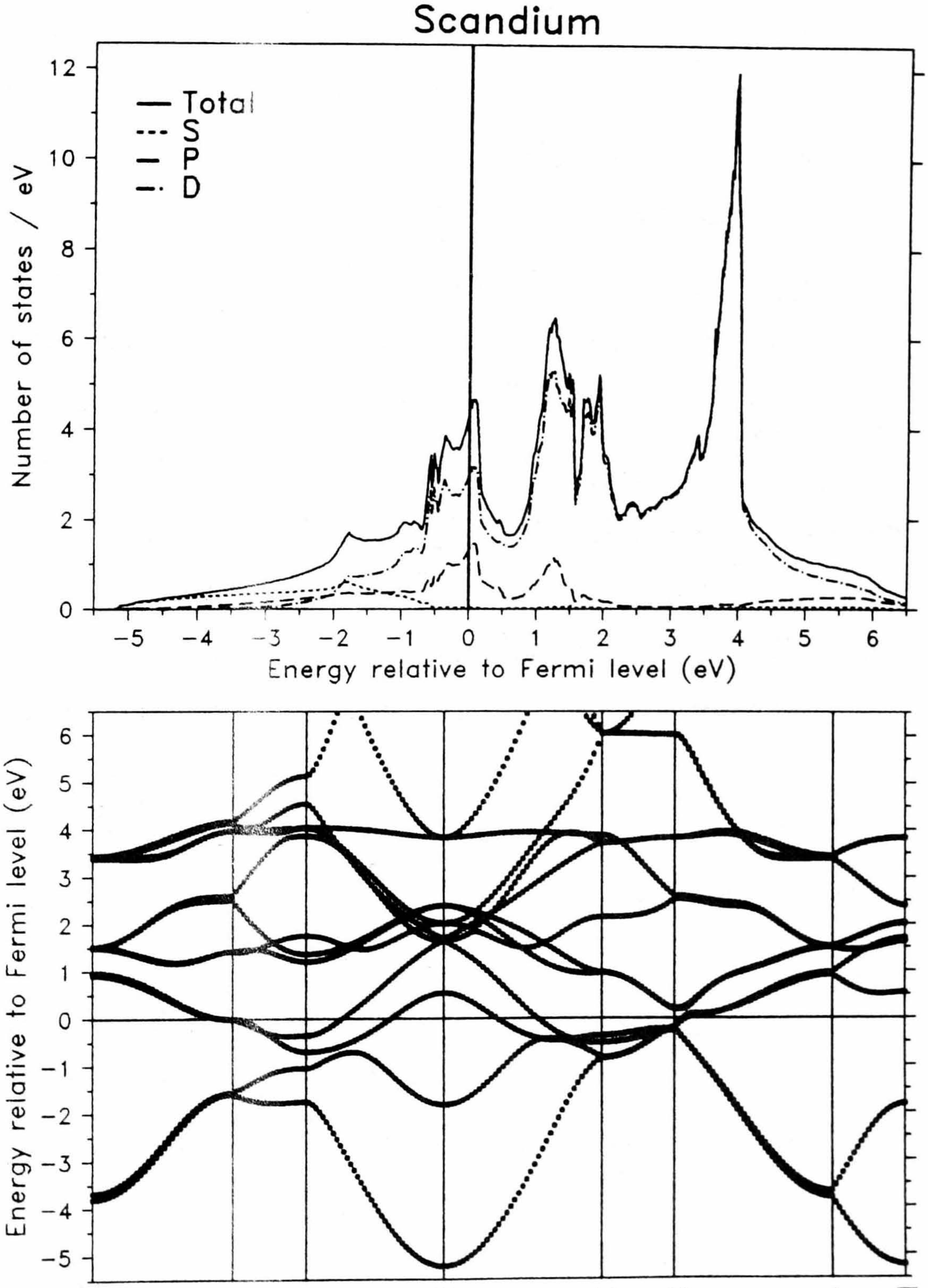

Fig. 3.4 (b) LMTO bandstructure of Y

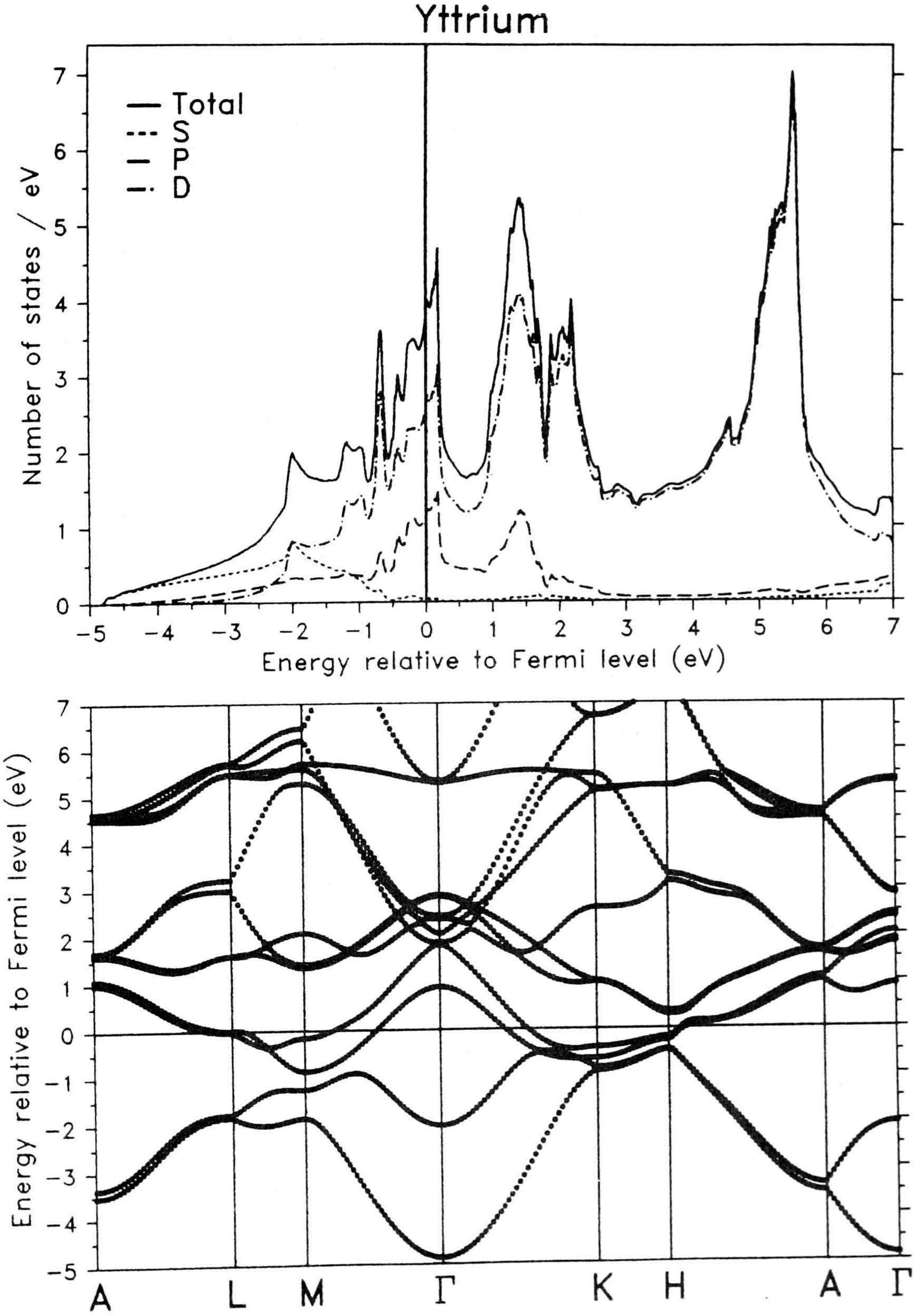

Fig. 3.5 LAPW bands of Y along ΓA (after Blaha *et al.* [75])

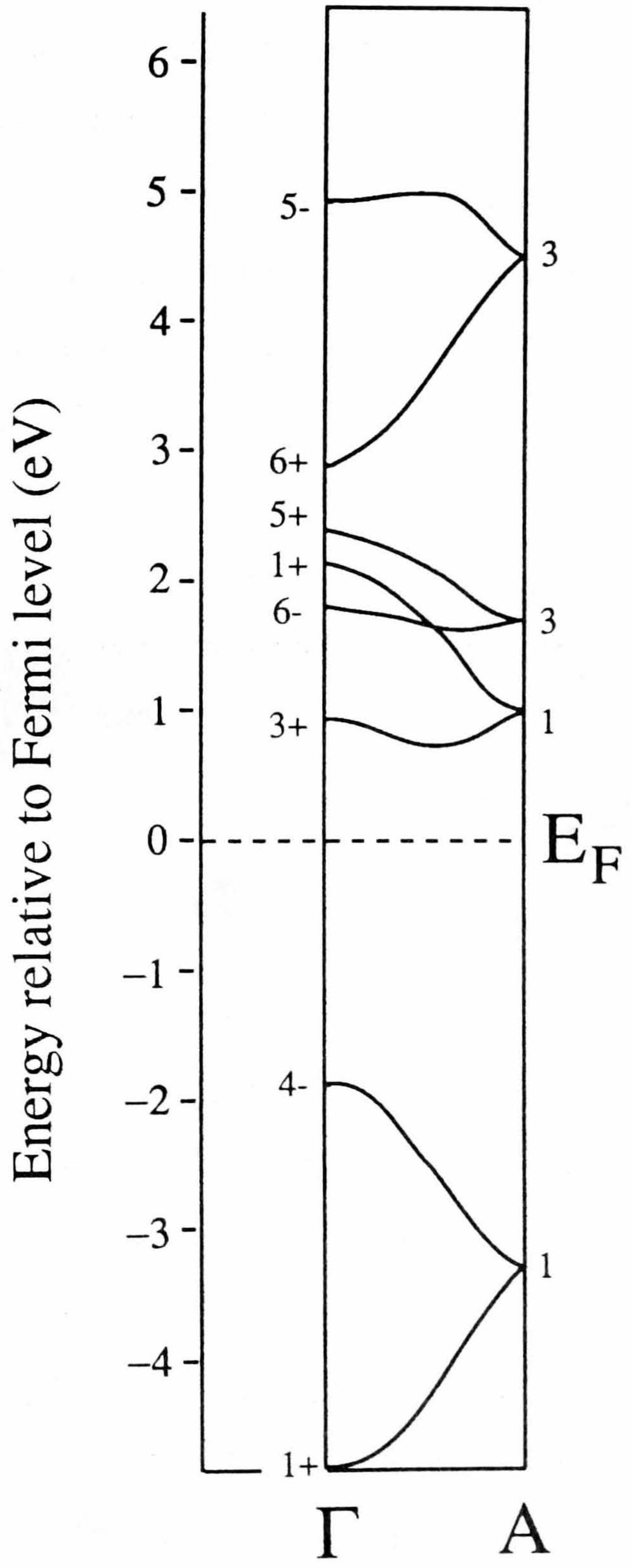

3.1.3 The hcp lanthanides: Gd, Tb, Dy, Ho, Er, Tm and Lu

Much of the early work on the electronic structure of rare earths centred on the form of their Fermi surfaces. In general the shape of the Fermi surface of an hcp rare earth, including of course Sc and Y, is that shown in fig. 3.6 for Tb [76]. There is a central column of holes, with a complex multiply connected electron surface around the Brillouin zone boundary. The broad head and feet of the hole column consists of radial fingers connected by a thinner webbing structure, and it is this webbing feature which attracted much of the theoretical and experimental attention, particularly with respect to Gd. The RAPW Fermi surfaces [77] of Gd and Er (representative of the other hcp lanthanides) are shown in fig. 3.7.

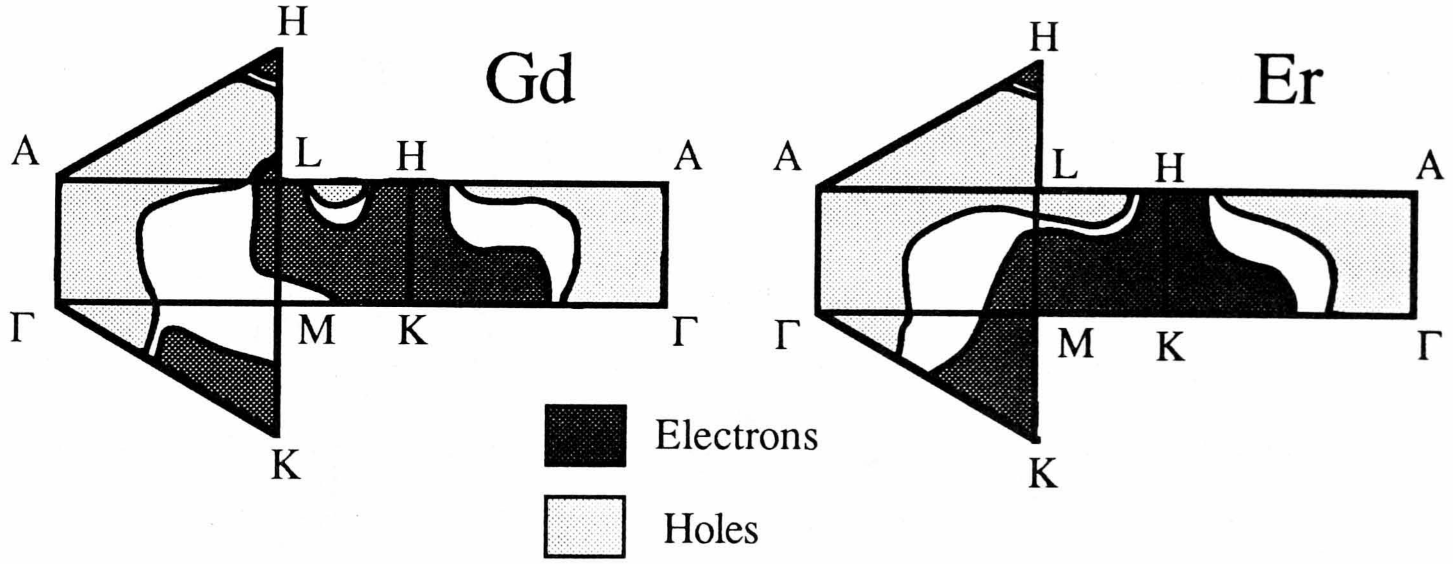

Figure 3.7 Intersections of the Fermi surfaces of Gd and Er with the irreducible wedge of the Brillouin zone (after Keeton & Loucks [77])

These surfaces are very similar, but the two main differences are the arm at M on Gd, not present on Er, and the webbing feature on Er which is not present on Gd. Tb [76] is intermediate between the Gd and Er surfaces as it has both the webbing features and the M arm. The webbing feature, shown in close-up in fig. 3.8, was first noted for Y [78] and it was thought that it might be a suitable nesting feature to explain the incommensurate spiral ordering

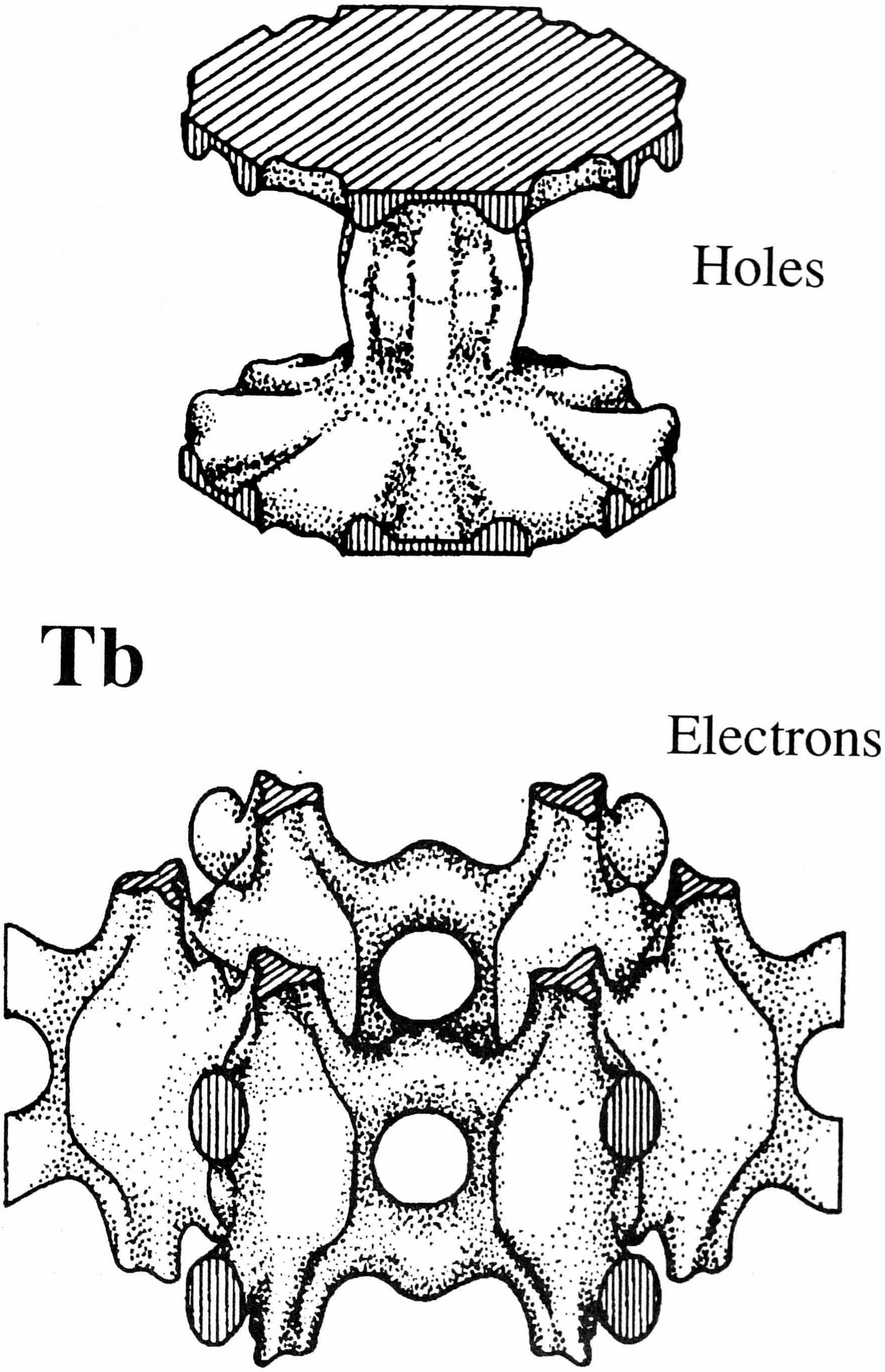

Figure 3.6 Fermi surface of Tb (after Jackson [76])

found in the magnetic rare earths (see chapter 2).

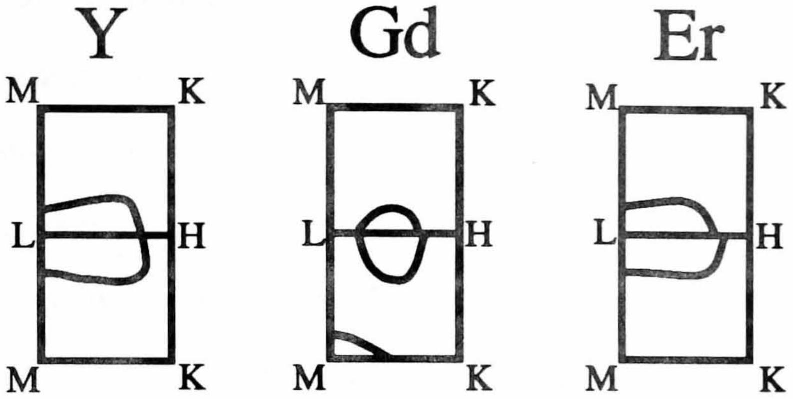

Figure. 3.8 The webbing feature of the Fermi surfaces of Y and Er, and its absence in Gd (after Keeton & Loucks [77])

Gd orders ferromagnetically and so does not show the webbing feature. Keeton and Loucks [77] also showed that the presence or absence of the M arm on Dy was dependent on the potential used, and that non-relativistic calculations for the lanthanides always produced a Gd type Fermi surface. This suggests that accurate bandstructure calculations for the lanthanides need to be both relativistic and self-consistent. Subsequent dHvA measurements on Gd [9, 11], Y [13], Tb [10] and Lu [8, 14] largely confirmed these theoretical results, including the presence of the webbing feature on Y and its absence on Gd, but as the quality of the single crystal sample of Tb was rather poor the results from this metal are somewhat sketchy.

Since the late 1960s there have been relatively few published calculations. A self-consistent relativistic LMTO calculation for Tb was published by Wu *et al.* [73], but the rest of the recent self-consistent calculations [79, 80, 81] have been for Gd. Since the 4*f* shell of Gd is exactly half full all its *f* electrons have parallel spins. Thus, included as bands in a spin-polarised calculation, they are exchange split around E_F, avoiding the piling up at E_F which would otherwise be the case. Gd is thus the only lanthanide for which 4*f* *bands* produce anything close to a sensible result. There remains considerable doubt about the validity of treating these highly localised states as Bloch states, but treating them as core levels produces large discrepancies in the calculated magnetic moment [79]. One of the more unusual results thrown up by these calculations is that the Gd $5p$ core levels appear to play a crucial role in determining the lattice constant. Temmerman and Sterne found [81] that treating the $5p$ levels as bands reduced the calculated lattice parameter by 7% compared to treating them as core states, both results ~3 % from the experimental value, i.e., from the point of view of comparison with experiment both appear equally correct. That this is a surprising result is perhaps best indicated by the fact that the Temmerman and Sterne labelled it with a *double* exclamation mark, the only such occurrence in a refereed journal that this author has ever encountered.

The bandstructures of the hcp lanthanides are shown in fig. 3.9. Note that they are all very similar both to each other, and to those of Sc and Y (fig. 3.4). A comparison of these results with the most important previous calculations and with available ARUPS data is shown in table 3.1. The ARUPS data from this work will be discussed in full in chapter 6. The LMTO results give deeper binding energies than those from the RAPW calculations, presumably because the RAPW did not include spin-orbit coupling. As an example of the difference between relativistic and non-relativistic calculations for the lanthanides, the non-relativistic bands and densities of states for Ho were calculated, and these are shown in fig. 3.10. Compared to the scalar relativistic calculation of fig. 3.9 (d) there are several notable differences: (i) The bandwidth is reduced, with the Γ_{4-} point occurring at 4.5 eV. (ii) Several band crossings become allowed, notably around the K point. (iii) The Fermi surface is altered by the bands around the M point, removing the webbing feature to produce a Gd type surface. (iv) The density of states now has a squared off appearance. (v) Some degeneracy is introduced, e.g. the unoccupied bands along ΓA. The fully relativistic LMTO calculation for Tb [Wu] gives a lower value for the Γ_{1+} energy and a higher value for that of the Γ_{4-} point compared to the scalar relativistic result of fig. 3.9 (d) , but the differences are only of order 0.1 eV. This suggests that the scalar relativistic calculations produce reliable results for these high Z metals. In general the ARUPS results give lower values for the critical point energies than the calculations, with the best agreement found for Y and spin-polarised Gd, with

Fig. 3.9 (a) LMTO bandstructure of Gd

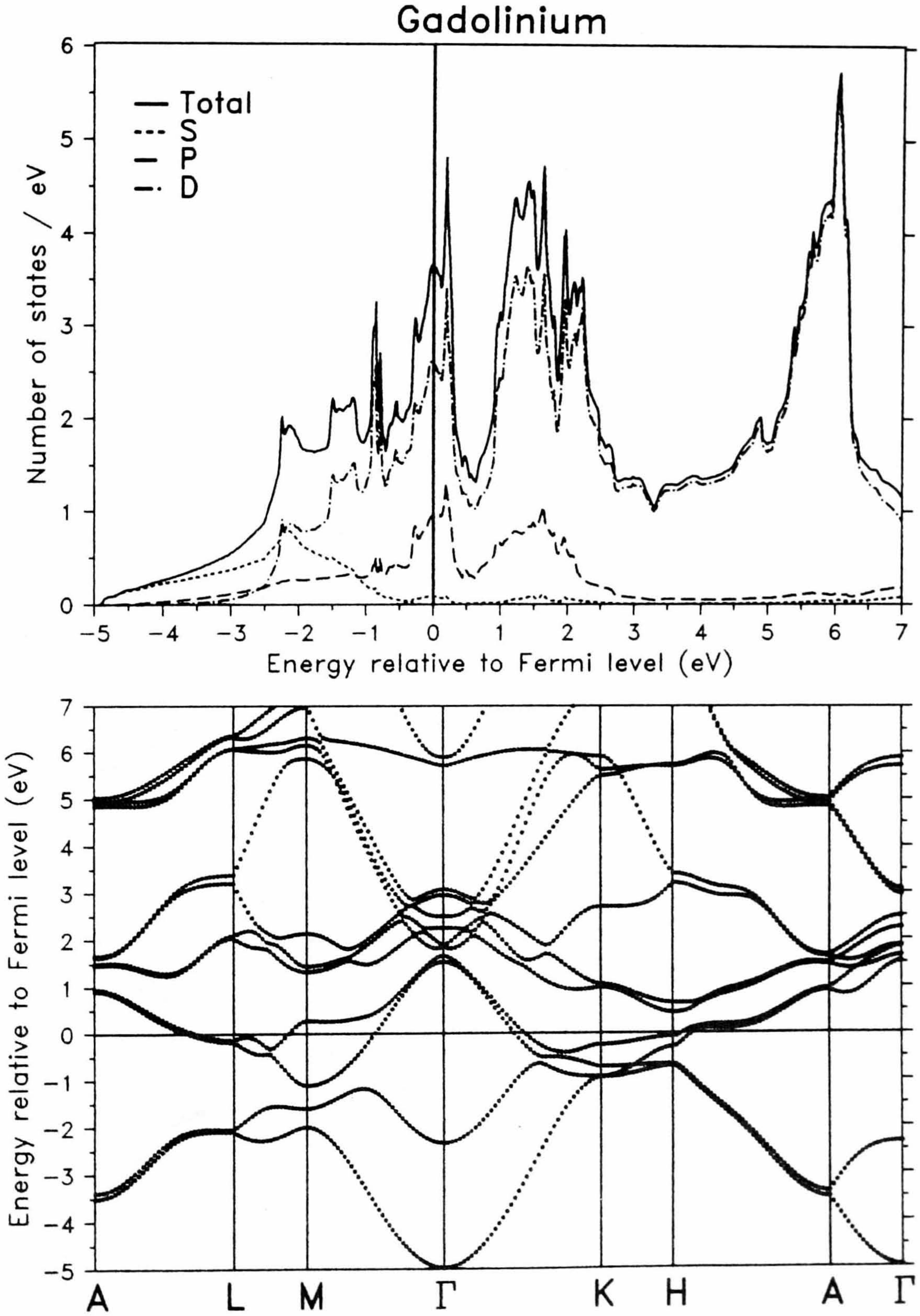

Fig. 3.9 (b) LMTO bandstructure of Tb

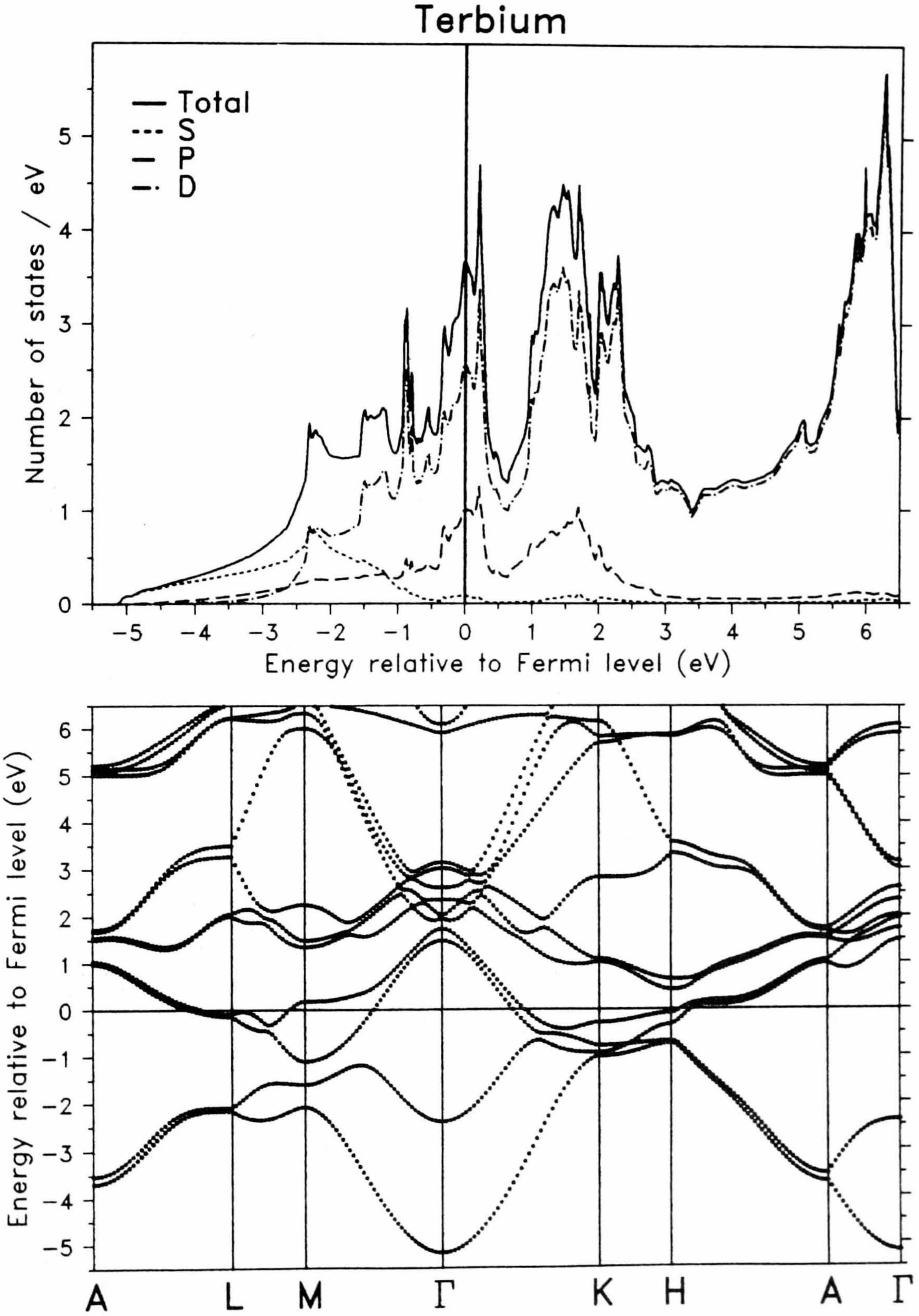

Fig. 3.9 (c) LMTO bandstructure of Dy

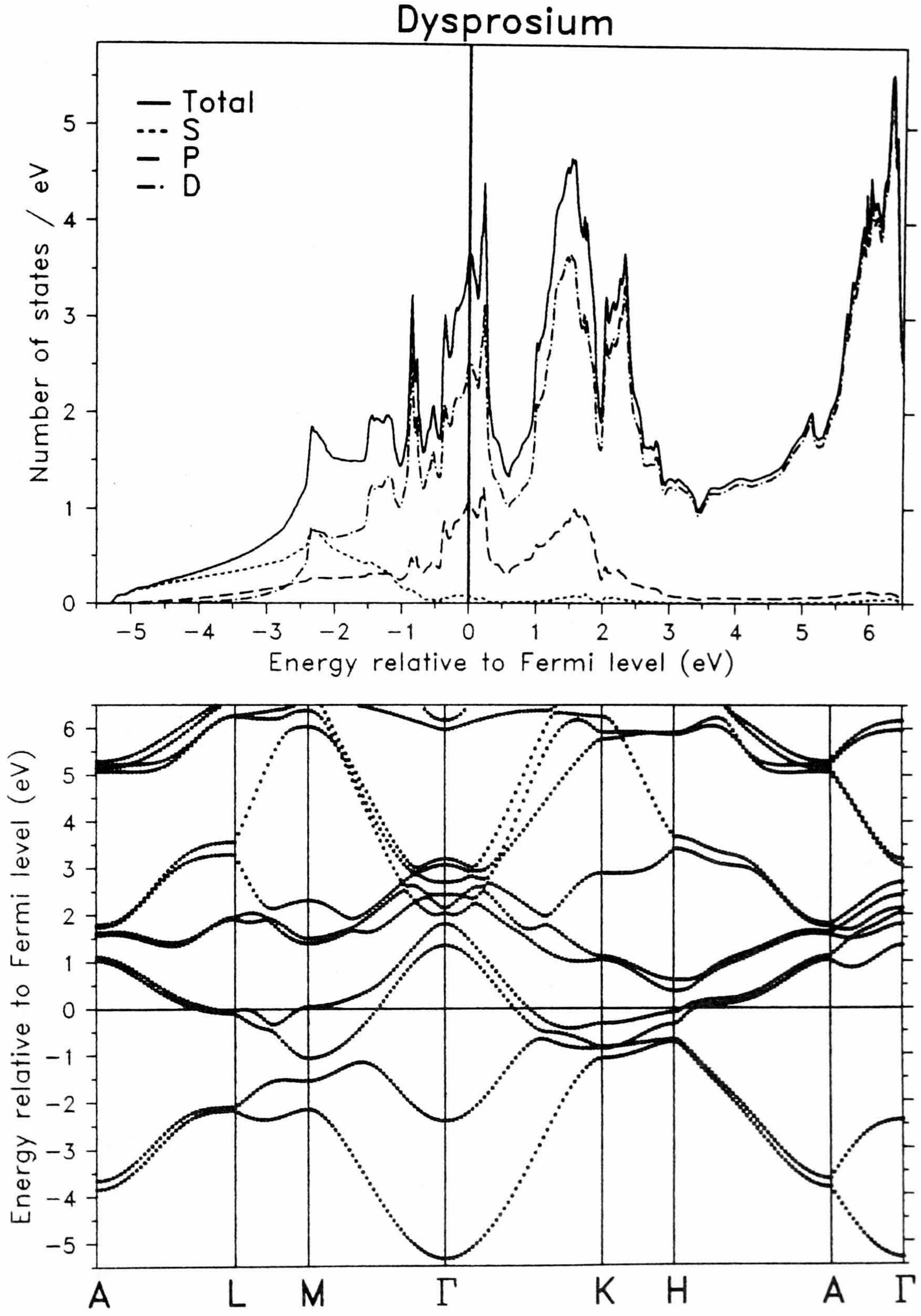

Fig. 3.9 (d) LMTO bandstructure of Ho

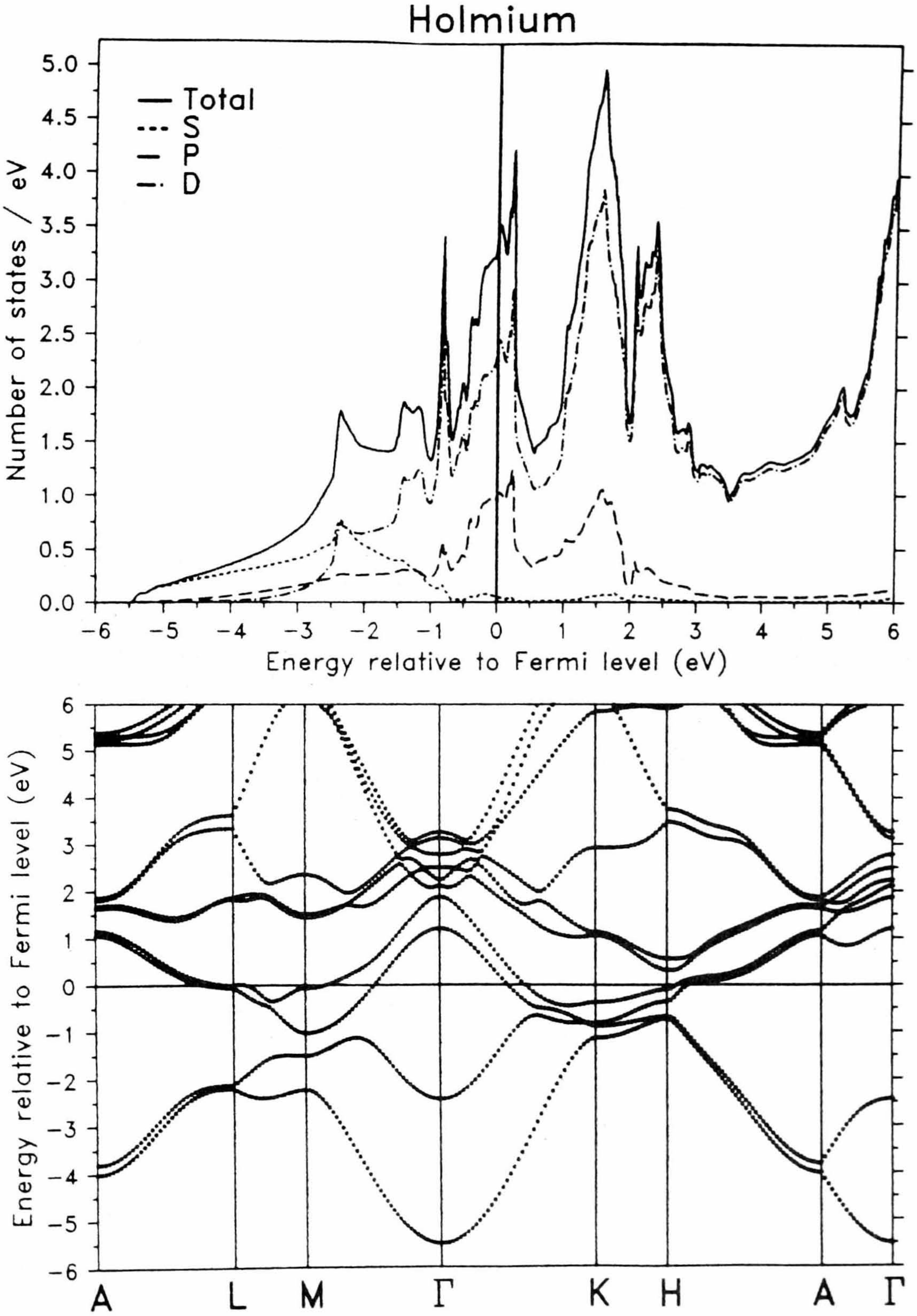

Fig. 3.9 (e) LMTO bandstructure of Er

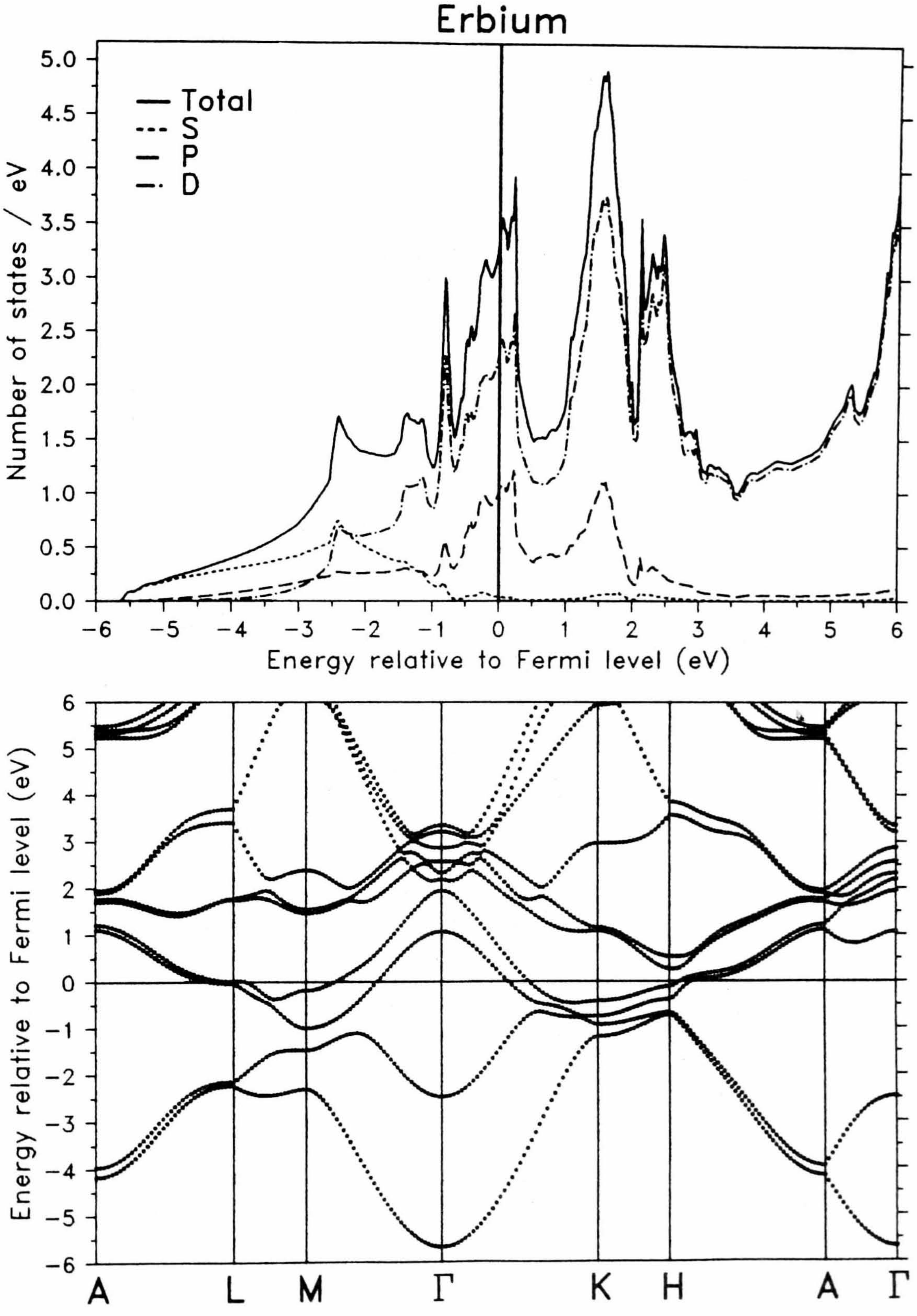

Fig. 3.9 (f) LMTO bandstructure of Tm

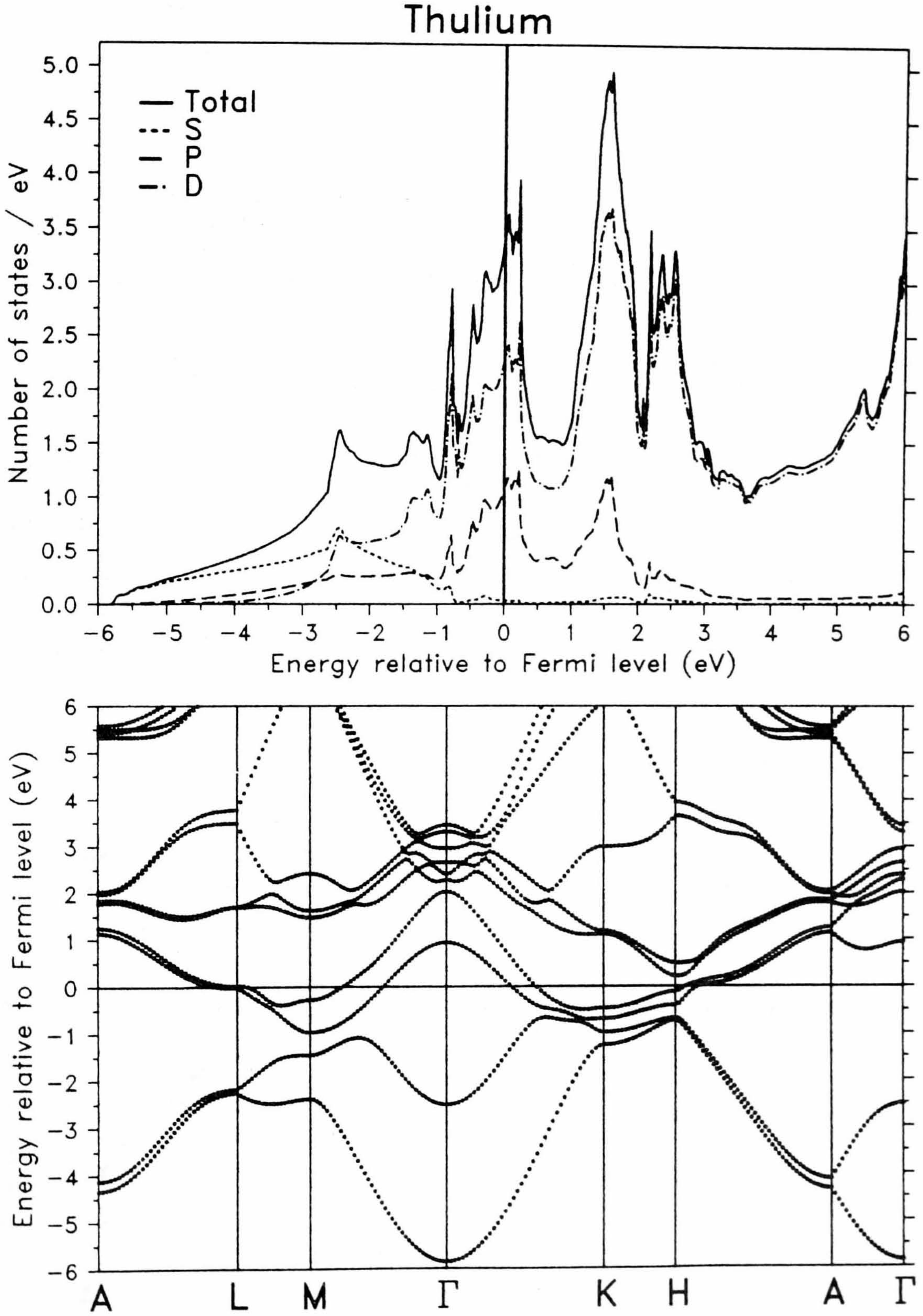

Fig. 3.9 (g) LMTO bandstructure of Lu

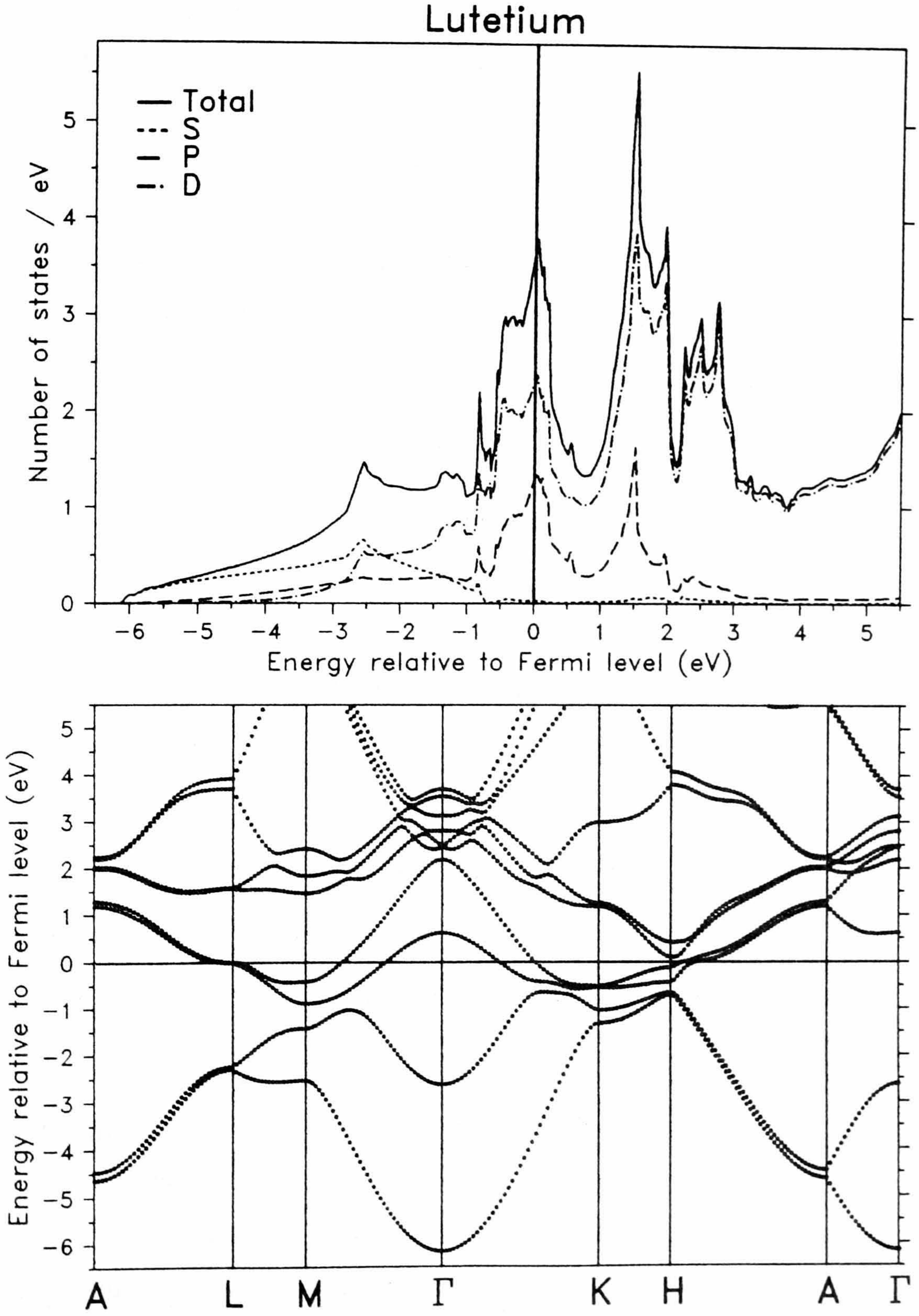

Table 3.1 Theoretical and experimental critical point energies of the hcp rare earths

	Calculated				Experimental		
Element	Γ_{4-}	Γ_{1+}	Method	Ref.	Γ_{4-}	Γ_{1+}	Ref.
Sc	1.62	4.97	LAPW	[75]			
	1.85	5.16	KKR	[74]			
	1.83	5.23	LMTO	this work			
Y	1·9	4·9	LAPW	[75]	1.7		[23]
	1.84	4.80	KKR	[74]			
	2.05	4.86	LMTO	this work			
Gd	1·7	3·5	APW	[68]	1.4	2.8	[20]
		4·7	RAPW	[77]			
	1·6	4·7	ASW	[79]			
	2·4	5·3					
	1·5	4·4	SPRASW	[80]			
	2·45	5·3					
	1·7	4·3	LMTO	[81]			
	2·5	5·1					
	2.33	4.96	LMTO	this work			
Tb	1·9	4·7	RAPW	[82]	3.6	6.9	[73]
	2·0	4·8	RAPW	[68]	1.5		this work
	2·3	5·3	RLMTO	[73]			
	2.39	5.17	LMTO	this work			
Dy		5·1	RAPW	[77]			
	2·40	5·33	LMTO	this work			
Ho	2·43	5·50	LMTO	this work	1.7		this work
Er		5·4	RAPW	[77]			
	2·46	5·68	LMTO	this work			
Tm	2·51	5·85	LMTO	this work			
Lu	2.2	5·9	RAPW	[83]			
	2·61	6·16	LMTO	this work			

Fig. 3.10 Non-relativistic LMTO bandstructure of Ho

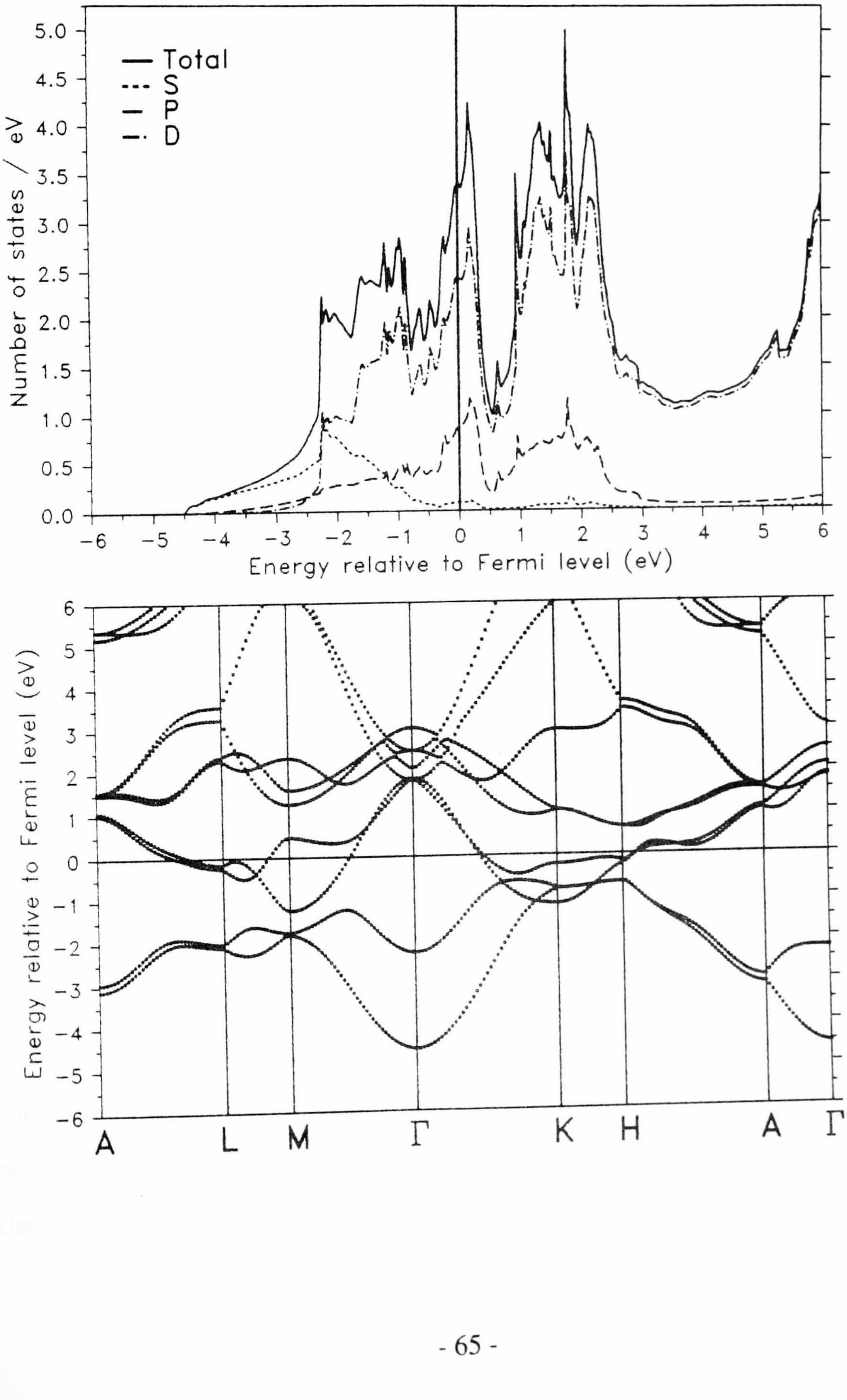

discrepancies of only ~0.3 eV. The high binding energies for the Tb critical points determined from the ARUPS data of Wu *et al.* [73] are almost certainly a result of sample contamination – this will be discussed in full in chapter 6. The discrepancies for Ho and Tb, with the calculations giving values for the Γ_{4-} critical point energy more than 0.8 eV too high, are rather too large to dismiss lightly. A possible explanation is that the exchange splitting is persisting well into the paramagnetic region of the magnetic phase diagram. This would result in values for the spin-down Γ_{4-} point energy much closer to E_F – compare the non-spin-polarised LMTO results for Gd with the spin-polarised values – and would result in much better agreement between experiment and theory. If this is in fact the case then the discrepancy should reduce along the series, as the magnetic moment decreases. Fig. 3.11 suggests that this is in fact the case, but additional ARUPS experiments are clearly required further along the series.

Figure 3.11: Theoretical and experimental Γ_{4-} values

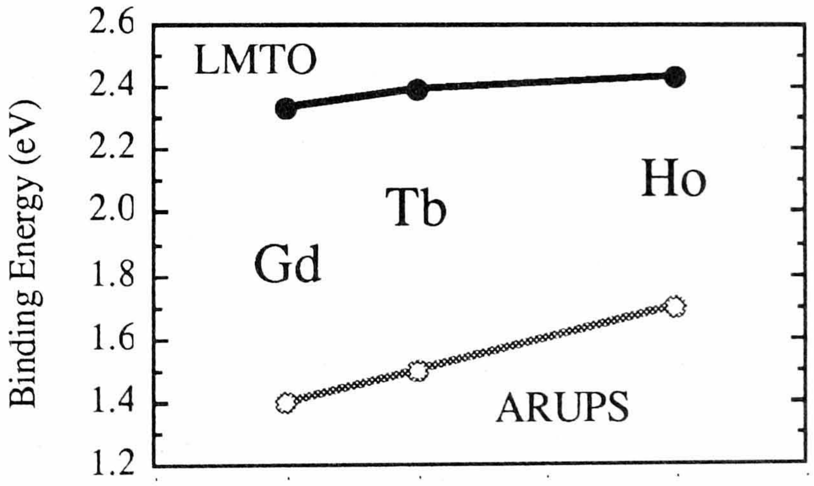

3.1.4 The dhcp lanthanides: La, Pr, Nd and Pm

There have been very few calculations for the dhcp rare earths. Calculations for La, Pr and Nd using the RAPW method were reported by Fleming *et al.* [84], but only the bands for La were shown, with the bands of Nd and Pr reported to be "very similar". Fermi surfaces were also calculated for La [84] and Nd [85], again with the intention of understanding magnetic ordering, in this case that of Nd. Because of its complexity it is very difficult to visualise the Fermi surface of a dhcp metal, but its intersection with the Brillouin zone boundaries is illustrated for La in fig. 3.12.

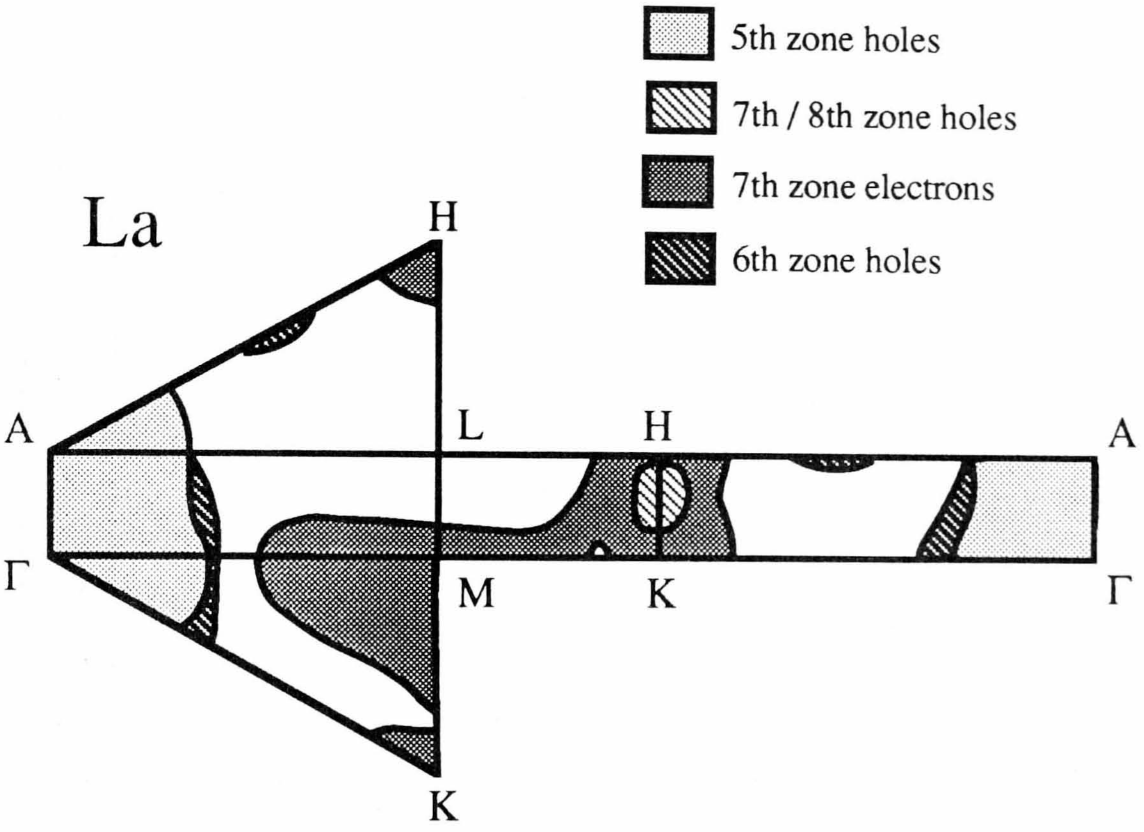

Figure 3.12 Intersections of the La Fermi surface with faces of the irreducible wedge of the Brillouin zone (after Fleming *et al*. [84])

There is no feature directly analogous to the hcp webbing feature, but Fleming *et al.* suggested that the seventh zone hole surface, which forms a flat region parallel to the KMHL plane, formed a nesting structure, giving the incommensurate magnetic ordering seen in Nd (fig. 2.10). The only dhcp rare earth for which dHvA measurements have been performed is Pr. Irvine *et al.* interpreted their results [12], for an essentially paramagnetic Pr sample, in terms of the Nd calculation of Fleming *et al.* [85] and found them to be consistent.

A self-consistent LMTO calculation for La which included the (unoccupied) *f* levels was reported by Glotzel [86]. He found that there was a significant contribution of *f* partial waves below E_F through hybridisation, but given the tendency of the LDA to overestimate bonding of localised states [27] it is unclear whether this is a realistic result. The LMTO bands

Fig. 3.13 (a) LMTO bandstructure of La

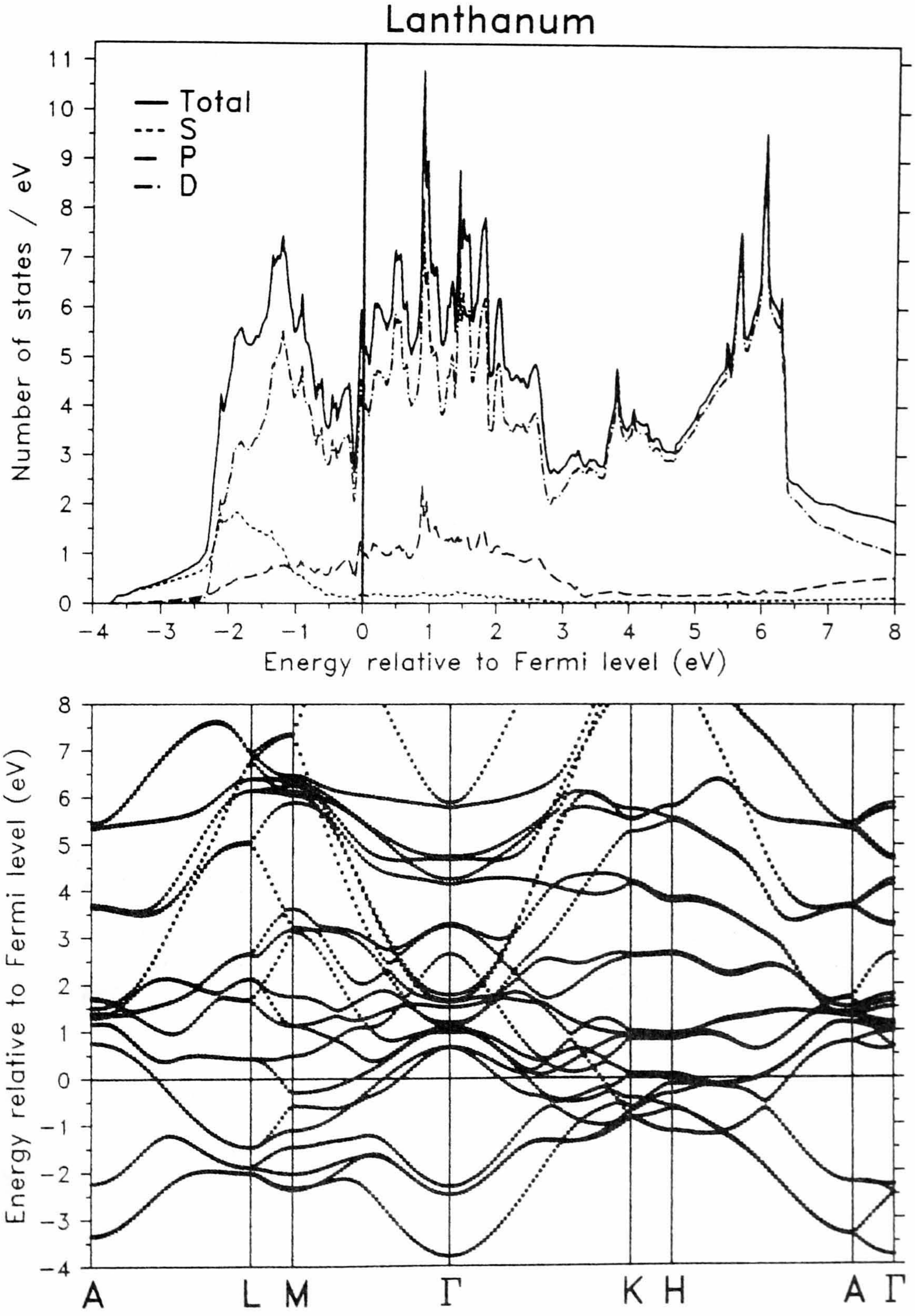

Fig. 3.13 (b) LMTO bandstructure of Pr

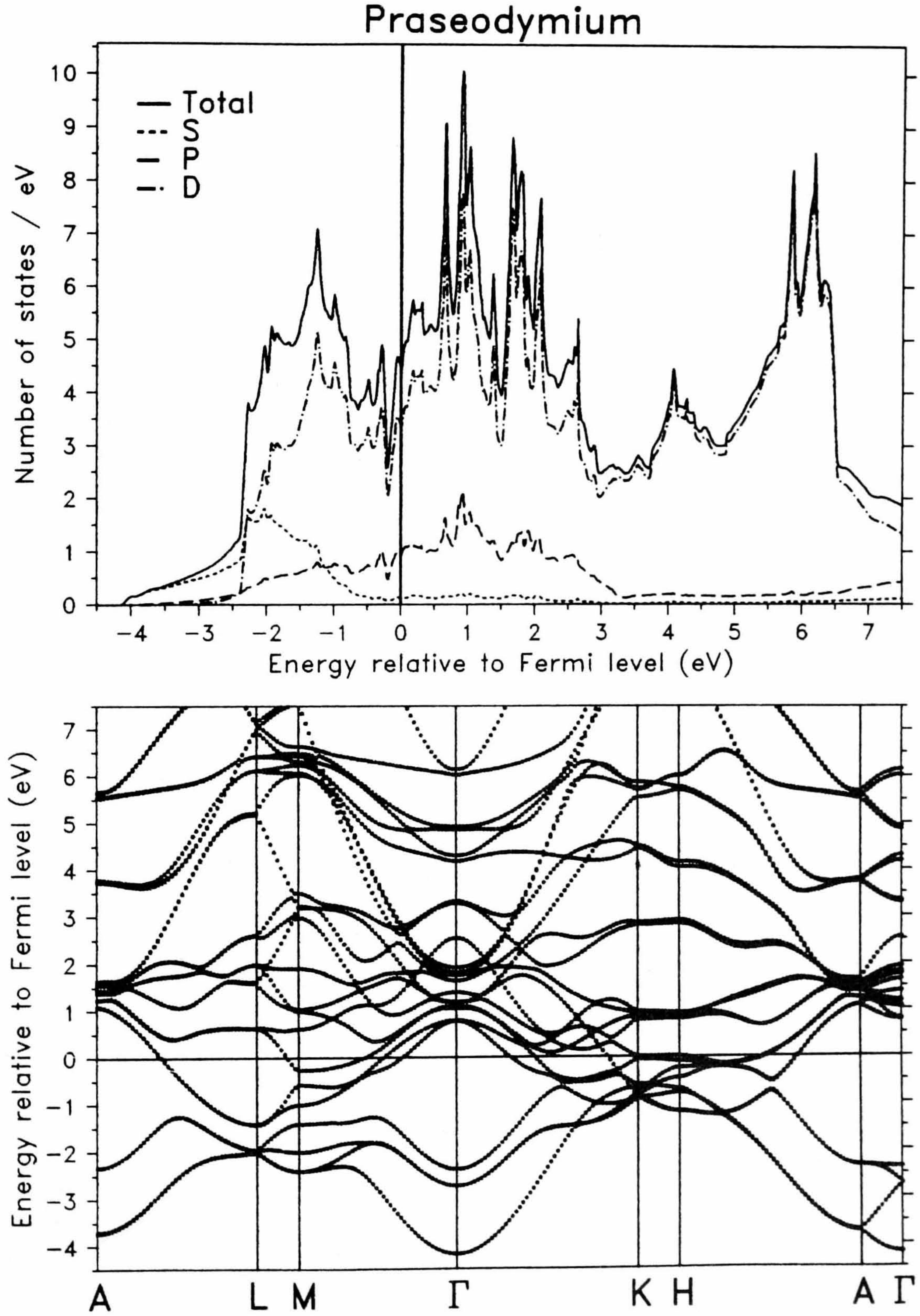

Fig. 3.13 (c) LMTO bandstructure of Nd

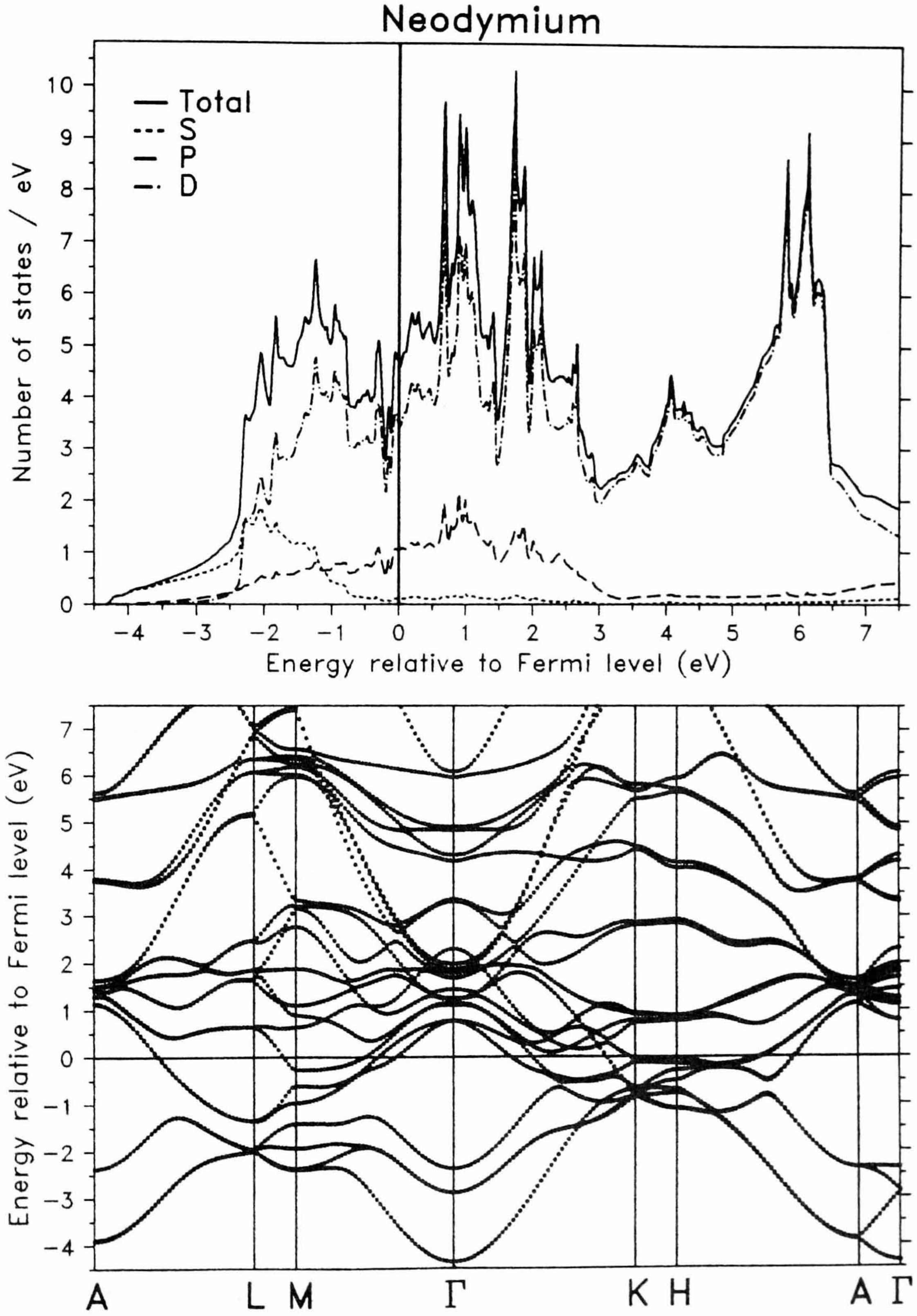

Fig. 3.13 (d) LMTO bandstructure of Pm

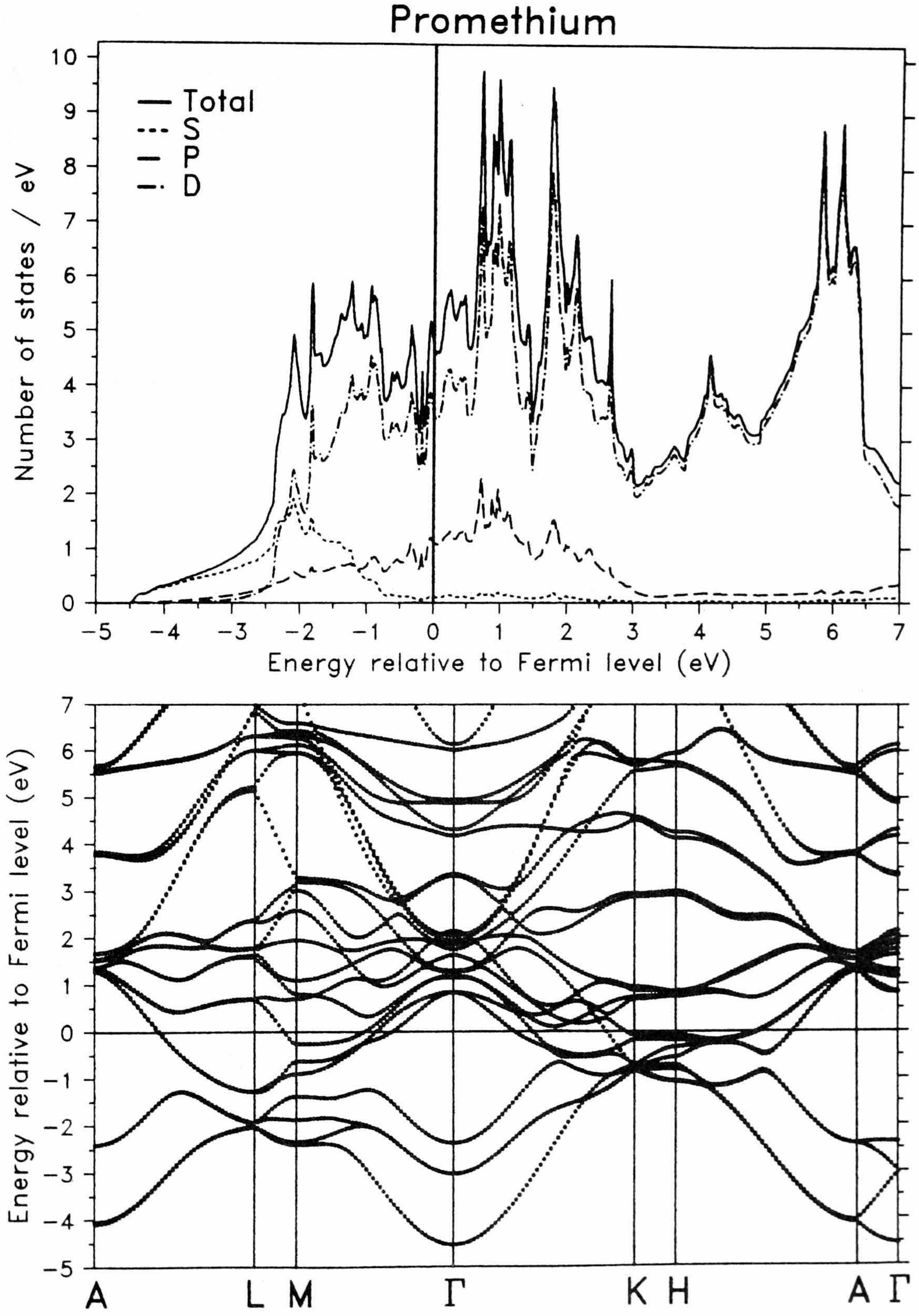

for all the dhcp rare earths are shown in fig. 3.13. Aside from the fact that the number of bands is doubled (the dhcp structure has four atoms per unit cell) the bands are of the same form as the hcp rare earths shown in fig. 3.9. The magnetic moments of all the dhcp rare earths are rather smaller than those of Tb and Ho, so the paramagnetic bands of fig. 3.13 would be expected to show reasonable agreement with ARUPS data. Dhesi *et al.* have performed a detailed ARUPS study of Pr(0001), with preliminary results [87] indicating good agreement with the bands of fig. 3.13 (b).

3.1.5 Eu and Yb

The bandstructures of divalent Eu and Yb differ greatly from those of the hexagonal rare earths.

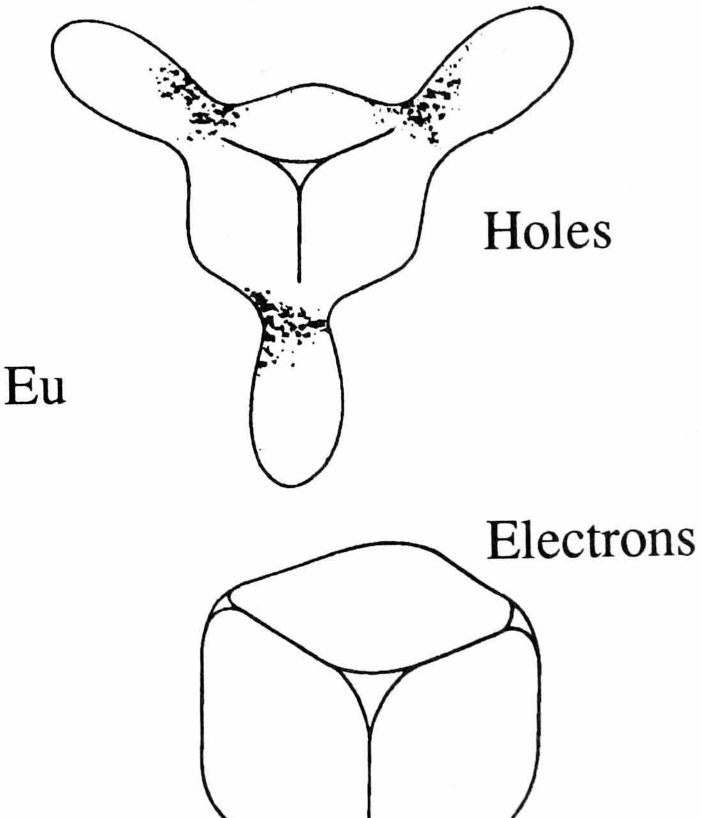

Fig. 3.14 Fermi surface of Eu (after Anderson and Loucks [89])

The bands of Eu (bcc) were calculated during the 1960s by Freeman and Dimmock [88] (APW) and Anderson and Loucks [89] (RAPW). Interest in the Fermi surface did not reach the levels of the hcp rare earths, but it has been calculated. The RAPW Fermi surface of Eu is shown in fig. 3.14. In both papers the authors noted the similarity between the bands of Eu and those of the bcc transition metals, with non-zero *d*-band occupancy due to *s*-*d* hybridisation. The RAPW bands of Eu [89] are shown in fig. 3.15.

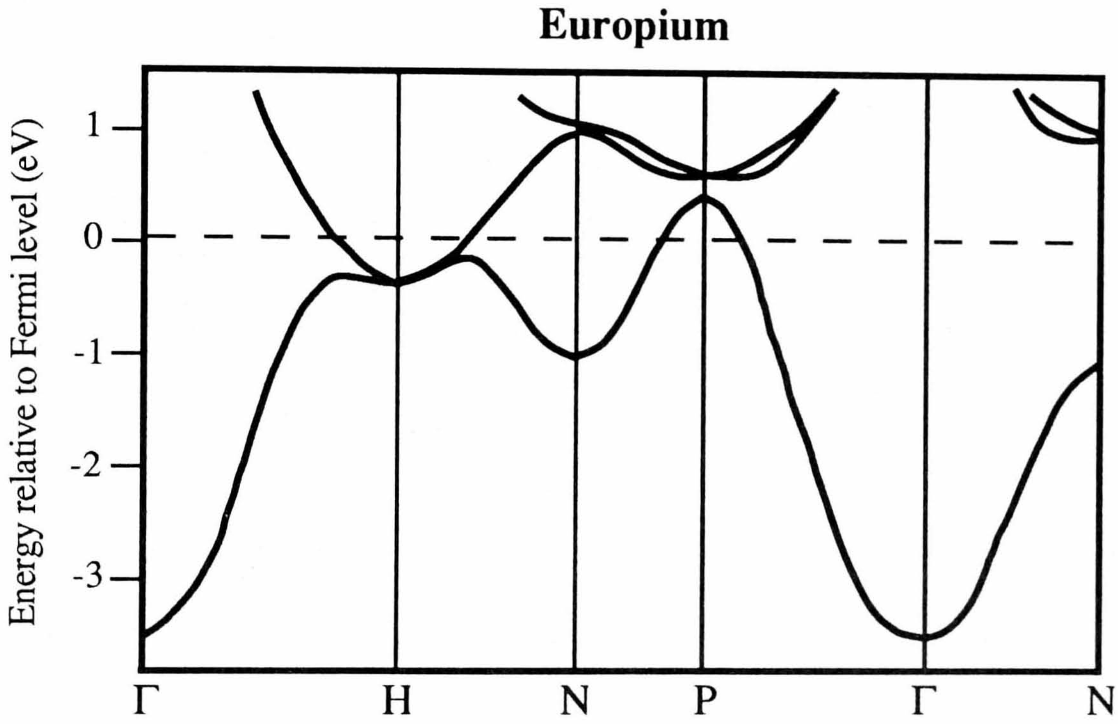

Fig. 3.15 Energy bands of bcc Eu (after Anderson and Loucks [89])

For comparison the LMTO bands of Ta and W [90] are shown in fig. 3.16. The shape of *d*-bands in transition metals is largely determined by the crystal symmetry and so the bands of Eu, W and Ta are extremely similar, with E_F migrating upwards in energy as the *d*-band occupancy increases. There exists little experimental confirmation of the Eu results, but the separation of the sides of the hole cube of the Fermi surface, forming a nesting feature, is consistent with the known magnetic periodicity. There have been no ARUPS or dHvA studies of Eu, and in XPS the valence band is obscured by 4*f* emission (see fig. 3.2).

Fig. 3.16 LMTO bandstructures of Ta and W

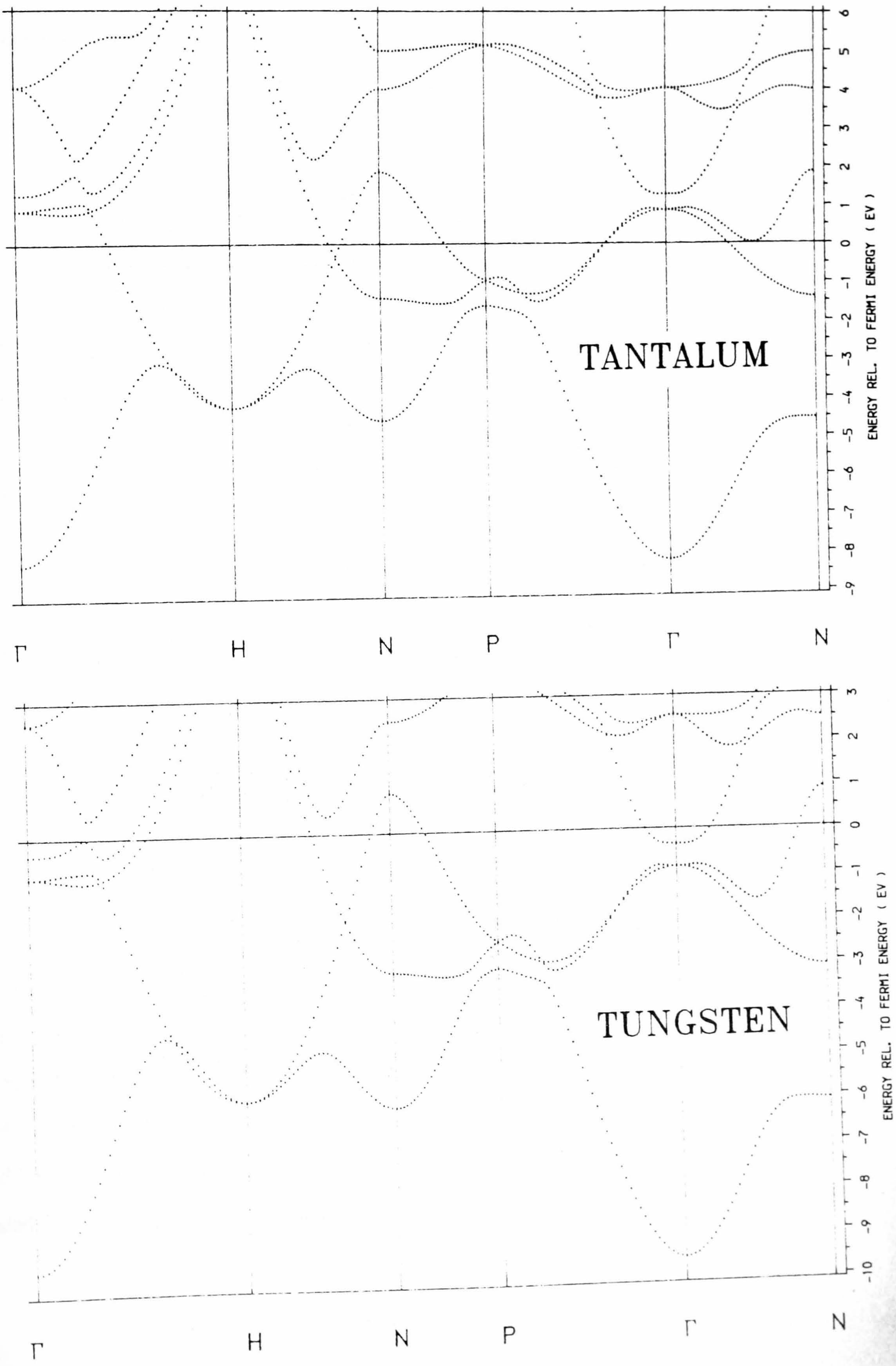

There exists some confusion over the bands of fcc Yb. The results of a non self-consistent RAPW calculation [91] are shown in fig. 3.17.

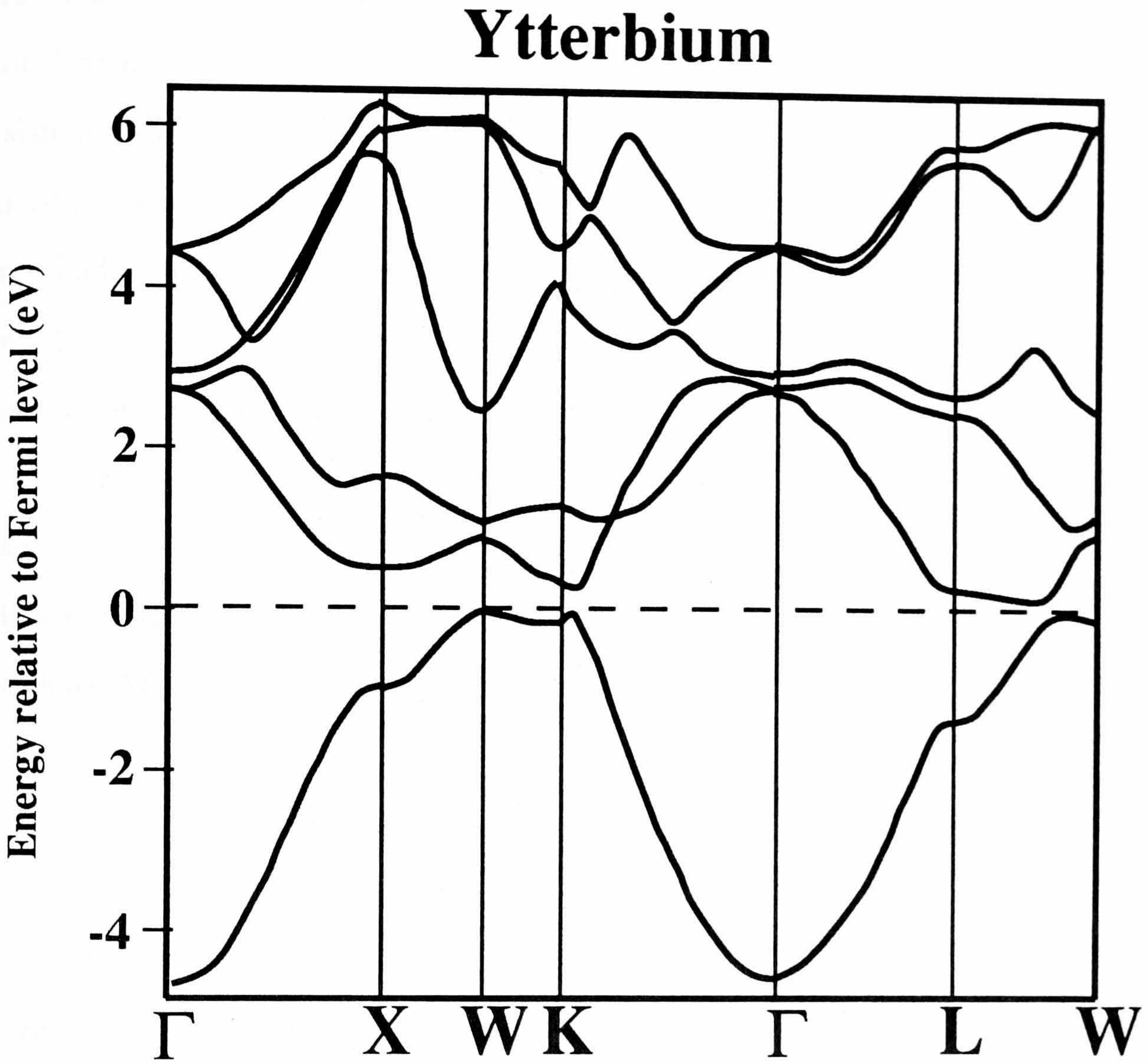

Figure 3.17 Energy bands of Yb (after Johansson and Mackintosh [91])

Instead of the observed semimetallic character of fcc Yb, a small gap at E_F is found. The atomic 4*f* levels (not shown) were calculated to be 0.2 and 0.3 Ryd. below E_F and thus would have had little effect on bands close to E_F. However a small change in potential could easily alter the band structure sufficiently to produce overlapping bands. A self-consistent calculation would be expected to overcome this problem but the only such calculation for fcc Yb [92] included the 4*f*s as band states. These appeared, hybridised with the *sd* bands, less than 0.05

Ryd. below E_F, close enough to influence directly the bands at E_F. This produces semimetallic character, with one small pocket of holes and another of electrons, but given that the LDA will overestimate the 4*f* hybridisation this may be a fortuitous coincidence rather than a physical result. Tanuma *et al.* [6] performed dHvA measurements on Yb and found two orbits, consistent with two small, closed pieces of Fermi surface. However it was subsequently realised [7] that Yb transforms to an hcp structure at low temperatures, so that these results correspond to the hcp Fermi surface rather than that of fcc Yb. Jepson and Anderson [93] found that the dHvA results were consistent with their RAPW calculation for hcp Yb, which suggests that the RAPW calculation for fcc Yb may be more reliable than was at first thought.

The fcc to hcp phase transition, at 270 K, is sufficient to induce stress in bulk single crystals of fcc Yb at room temperature which is relieved during annealing by a reduction in grain size [94]. This has meant that it has so far proved impossible to grow Yb crystals large enough for ARUPS measurements which might settle the argument.

3.1.6 Ce

The electronic structure of cerium is unique. The single 4*f* electron cannot readily be described as either a band or a core level, as it is partially de-localised. In that sense Ce has more in common with the actinides, whose 5*f* wavefunctions are considerably less localised than the lanthanides' 4*f*s. For example, heavy Fermion behaviour, attributed to de-localised *f* levels piling up at E_F at low temperatures, is found in both actinide and cerium compounds but is almost unknown among compounds of the other lanthanides. The α - γ phase transition in Ce is thought to be the result of an increased localisation of the 4*f* level [95, 96]. The LAPW band calculations of Pickett *et al.* [97] showed an effective valency of 3.6 for α-Ce and 3.15 for γ-Ce, due to the increased localisation of the *f* level. The bands for α- and γ-Ce are shown in fig. 3.18, illustrating the reduced 4*f* bandwidth in γ-Ce.

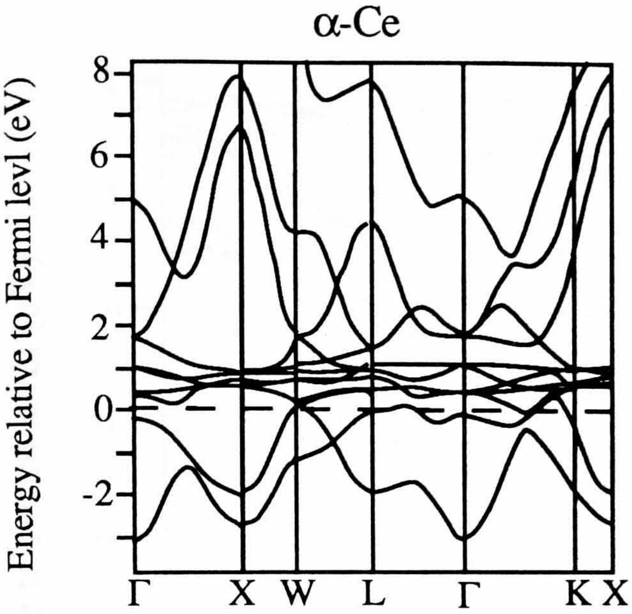

Fig. 3.18 Energy bands of α- and γ-Ce (after Pickett *et al.* [97])

ARUPS studies of γ-Ce(001) [21, 22] showed dispersions in good agreement with the LAPW bands, whilst also showing two apparently localised (non-dispersing) 4*f* derived peaks. These were located at binding energies of 0.2 and 2.0 eV, the occurrence of two peaks being attributed to differently screened final states. It thus appears that unlike the other lanthanides the 4*f* levels cannot be treated as core-like, but as they are still very localised there will be correlation effects which the calculations do not include.

3.2 Surface Electronic Structure

In stark contrast to the vast amount of work on the bulk bands of rare earth metals there has been only one published calculation for a rare earth surface, and that for the simplest surface – (0001) – of the least interesting of the series: Sc. As part of a general investigation of transition metal surfaces Feibelman and Hamann [98] calculated the bands of an 11 layer slab. Their results are shown in fig. 3.19, with the heavy lines indicating bands localised to the surface layers. The large number of 'bulk' bands in the slab calculation is a result of the number of chemically distinct atomic sites within the slab.

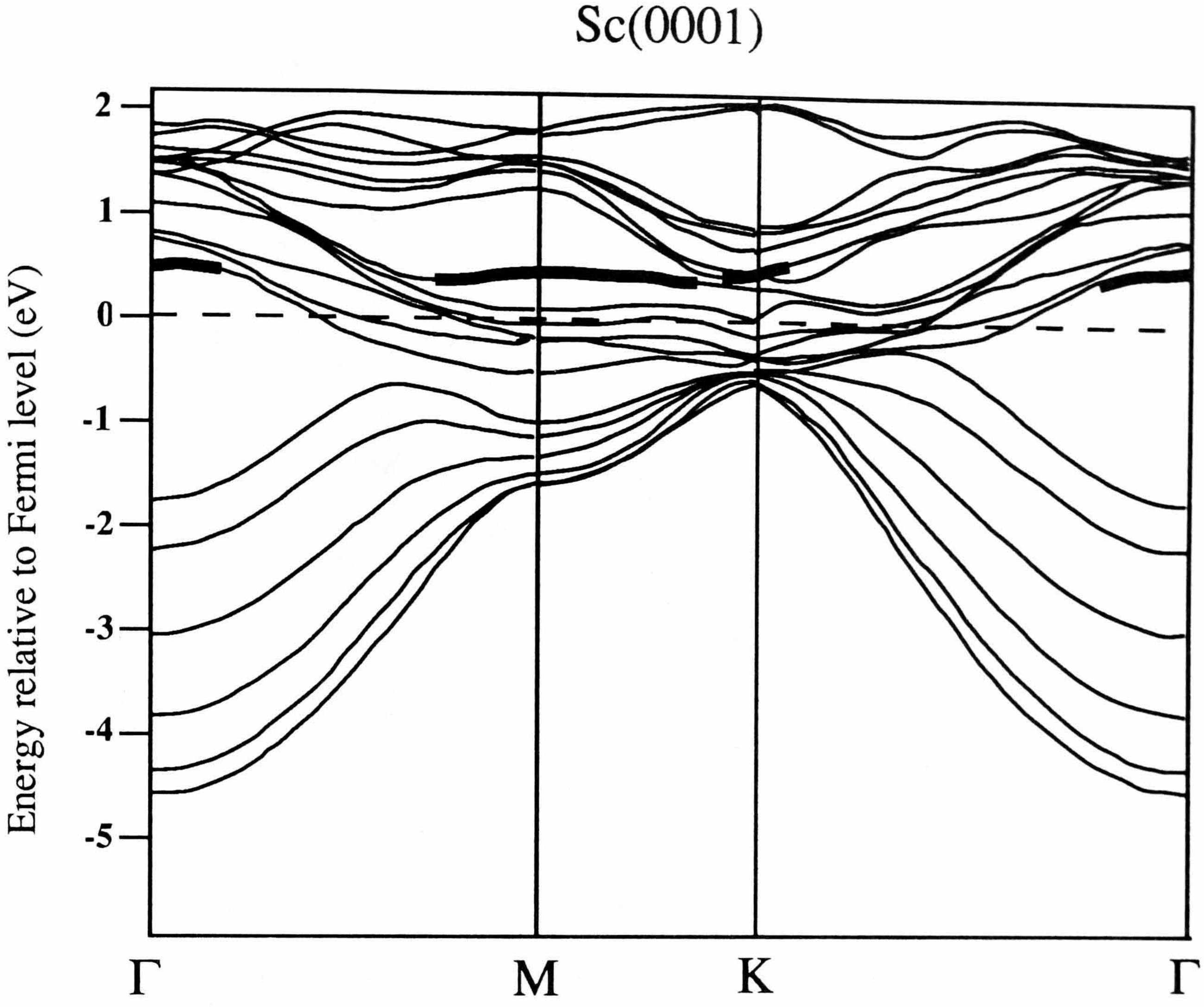

Figure 3.19 Energy bands of the Sc(0001) surface (after Feibelman & Hamann [98])

The surface states are located just above E_F, resulting in a low value of work function (2.1 eV) compared to the value for Ti(0001) (3.9 eV), where the surface states are partially occupied, which was determined from the same work. The SCLS was also determined, and found to be 0.48 eV to higher binding energy. The results of this calculation remain largely untested, although an XPS study of the 3*p* levels of polycrystalline Sc [99] indicated an SCLS of 0.5 ± 0.1 eV. There have been no measurements of the work function of clean Sc, either as polycrystalline films or single crystals and there have not been any ARUPS or KRIPES measurements. The small atomic radius of Sc means that it is probably invalid to extrapolate these results to the surfaces of the other hcp rare earths, and also that the ARUPS and KRIPES results from Y(0001) cannot be regarded as tests of the calculation.

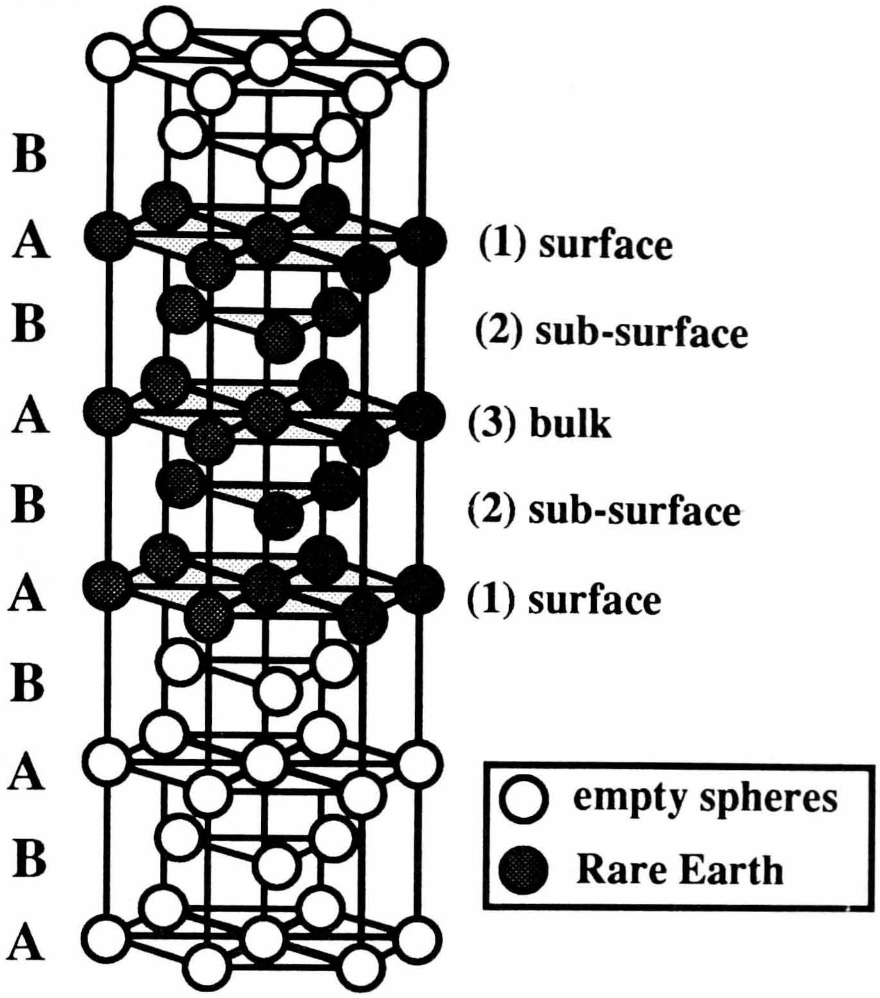

Fig. 3.20 Unit cell for supercell slab calculations

The surface core-level shifts for the (0001) surfaces of Y [100] and the hcp and dhcp lanthanides [30] have been calculated by Begley and co-workers. Their method of calculation is interesting as it employed a novel unit-cell geometry in a standard bulk bandstructure code to calculate a surface property. They used the self-consistent LMTO method exactly as described in section 3.1.1, with a unit cell as shown in fig. 3.20. The site-projected density of states for layer 3, i.e. the 'bulk' site, was found to be very similar to those of the LMTO calculations of figs. 3.9. The surface core-level shift was taken to be the difference between the eigenvalues of the core-levels of layers 3 ('bulk') and 1 ('surface'). For Y(0001) the SCLS was found to be 0.6 eV to higher binding energy. In view of the somewhat crude nature of the surface model this is in good agreement with the value of 0.8 (± 0.1) eV determined by Barrett *et al.* [101] from ARUPS measurements of the Y(0001) 4*p* levels. The calculated SCLSs for the lanthanides are shown in fig. 3.21, together with the experimental values of Gerken *et al.* [29].

Fig. 3.21 SCLS for the lanthanides (after Begley *et al.* [30])

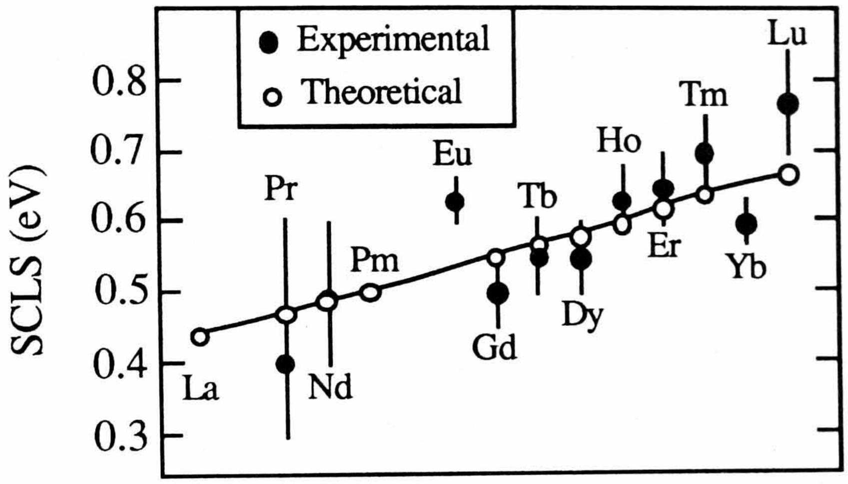

These experimental results are from the 4*f* levels of polycrystalline samples and thus represent an average over the three principle faces, but the agreement is rather encouraging. As yet there have been no SCLS measurements from single crystal lanthanides. Begley *et al.* also found that the core-level shift for layer 2 ('subsurface') was both smaller than the SCLS and in the opposite direction i.e., to lower binding energy. This was found to be accentuated by poor convergence but has been seen experimentally for Ir(100) [102] so it is possible that this may be a real effect, and not just an artifact of the calculations. The calculated value for the shift between the first two Y layers was 0.74 eV, which is in much better agreement with the experimentally determined shift of 0.8 eV than the "true" SCLS. It may well be that the experimental result, limited to the near surface region by the short electron mfp, in fact represents the relative shift of the first two layers.

3.3 Photocurrent calculations

Direct comparison of features seen in ARUPS spectra with bulk bandstructure calculations presents several difficulties. (i) ARUPS probes only the first few atomic layers of the solid and thus the spectra will contain surface related features in addition to features arising from bulk bands. This can be at least partially overcome by the use of surface electronic structure calculations such as that shown for Sc(0001) in fig. 3.19. However such slab calculations do not reproduce the bulk bands correctly, which requires comparison of different experimental features with different calculations. (ii) It is often necessary to use some form of empirical expression for the dispersion of the final states in order to map the initial state bands, which is most unsatisfactory as it effectively negates the first principles basis of the calculations. (iii) It is assumed that the results from ARUPS, an excited state spectroscopy, can be described in terms of the (single particle, ground state) calculations. In practice there will be many-body effects such as energy shifts and broadening of the ARUPS features, and more dramatic deviations such as the appearance of satellites. (iv) The finite lifetimes of the initial and final states, and dynamic effects such as diffraction, may cause broadenings of the energy and momentum of the ARUPS features. This may mask any dispersion and give rise to spectra dominated by regions of **k**-space with high DOS. In view of all these pitfalls what is surprising is how often direct comparison has been successful, rather than the few occasions in which it has failed. Many of these problems can be circumvented by the use of photocurrent calculations to simulate ARUPS spectra. For this work photocurrent calculations for Ho(0001) were performed using the NEWPOOL code [103]; the results can be found in chapter 6. This code uses the time-reversed multiple scattering LEED formalism of Pendry [104], and is essentially the earlier PEOVER1 code [105] modified to allow more than one atom per unit cell (essential for use with hcp surfaces). The surface model used by NEWPOOL is shown in fig. 3.22. The potentials used in the code need to be supplied from elsewhere, and those used in this work were obtained from an LMTO supercell calculation performed by Dr. A.M. Begley of Florida

Atlantic University[2]. The potential from layers 1, 2 and 3 of the slab, representing surface,

Fig. 3.22 Surface model used for NEWPOOL calculations

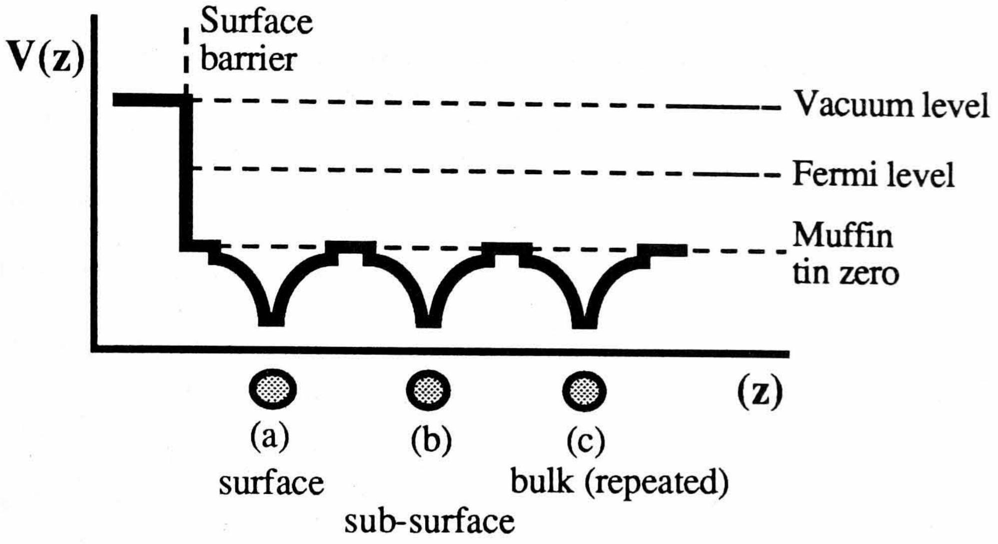

subsurface and bulk respectively, were placed on layers a, b and c of the NEWPOOL geometry. This provides a much improved model of the surface potential than the use of bulk potentials combined with the rather crude surface barrier seen in fig. 3.22, and there is some cause for confidence that this provides a reasonable model of the surface electronic structure. The slab calculation has been used to calculate the Ho(0001) SCLS, showing good agreement with experiment (see fig. 3.21), while the combination of NEWPOOL and LMTO slab potentials has been successfully used to model the 4*p* photoemission lineshape of Y(0001) peak [106], which has significant contributions from both the bulk and surface 4*p* levels (see chapter 7). NEWPOOL calculates the final states explicitly, and also includes realistic initial and final state lifetimes, but does not represent a full solution of all the previously listed problems. Its main drawback, especially for calculating photoemission from heavy elements such as Ho, is that it does not include relativistic effects. A fully relativistic theory of photoemission has recently been developed [107], and codes developed from it are at present undergoing trials. A notable success with these new codes has been reported by Collins *et al.*

---

[2] Now at SUNY, Stony Brook.

[108] who calculated KRIPES spectra from W(001) and W(110), obtaining excellent agreement with experiment (KRIPES can be considered as time reversed ARUPS, permitting the use of the same code for both spectroscopies). NEWPOOL also fails to take into account many body effects. These can be introduced into photocurrent codes by the inclusion of the "self-energy", which represents a generalised correction to the one electron eigenvalues. Such effects are very difficult to calculate from first principles, but various models have been used to calculate the self-energy [109]. Jordan [110] used a modified version of the NEWPOOL code, including the self-energy calculated by Treglia *et al.*[111], to model the photoemission from Ni(110), a system in which many body effects are significant. The self-energy depends on the structure of the valence and conduction band DOS, and for holmium, given the uncertainty concerning the location of the 4*f* levels, it is difficult to see how a meaningful self-energy could be calculated. However, if due regard is taken of the limitations mentioned above, the calculations still represent a considerable improvement over empirical comparisons.

CHAPTER 4

Experimental details

As mentioned in chapter 1 photoemission and inverse photoemission spectroscopies can be conceptually divided according to whether the electron momentum is conserved. In ARUPS and KRIPES the photon energies are in the UV range, photon momentum can be regarded as negligible and so band mapping is possible. In XPS and BIS the photon energies are in the X-ray range, photon momentum is no longer negligible, and the resulting loss of momentum conservation means that only density of states information can be obtained about the valence or conduction bands. This conceptual division is mirrored by, and at least partly stems from, the two different types of monochromatic photon sources available in the early days of electron spectroscopy i.e., the gas discharge lamp and the conventional X-ray source. For the discharge lamp limited tunability could be obtained by using different gases, giving a realistic upper limit of 40.8 eV (He II radiation). Similarly limited X-ray tunability could be obtained by the use of different anode materials: a typical twin anode source has Mg and Al anodes, giving radiation at hν = 1254 and 1487 eV respectively. Such X-ray sources produce characteristic X-rays, having a broad linewidth (~ 1 eV) and satellite features, but this can be improved, albeit with considerable reduction in flux, by the use of a crystal monochromator. The resolution thus obtainable is limited by the intrinsic width of the diffraction peak and is typically a few tenths of an eV. The use of synchrotron radiation sources bridges the gap between UV and X-ray sources as they produce radiation all the way from infra-red to hard X-rays. Combined with a suitable monochromator this provides a high intensity, tunable source of polarised photons, with both linear and circular polarisations available. This has given rise to "soft" XPS, i.e. the photoemission study of shallow core levels with binding energies typically less than 100 eV, using grating monochromators giving photon energies below about 200 eV. The resulting low kinetic energies of the photoemitted electrons means that the surface sensitivity is considerably enhanced compared to conventional XPS, and this is accompanied by a much better photon energy resolution than is available from a crystal monochromator. These advantages make this spectroscopy ideal for looking at interface electronic structure via core level shifts [112], and also for measuring intrinsic surface core level shifts on clean surfaces [113]. For ARUPS there are additional advantages. Tunability of the photon source allows three different modes of operation: (1) Energy distribution curve (EDC), i.e., holding the photon energy constant and scanning electron energies. (2) Constant initial state (CIS), i.e., scanning photon energy and electron energy together such that the difference between the photon energy and the detected electron energy remains constant. This is used to measure the photon energy dependence of non-dispersing features, or to determine the final state DOS, although in practice it is difficult to separate the two contributions. (3) Constant final state (CFS) i.e., holding the kinetic energy of the detected electron constant and scanning photon energy. This removes effects due to changing final state DOS but, like CIS mode, is very slow due to the need for mechanical scanning, and EDC remains the most commonly used mode. As a result of these advantages much ARUPS work is now performed at synchrotrons, but the limited availability of these expensive machines means that there is still a large body of work being done with discharge lamps. The ARUPS studies for this work were all performed using synchrotron radiation, as have been all the other ARUPS studies of hcp rare earths, whereas Rosina *et al.* [22] used a discharge lamp for their study of Ce(001).

4.1 ARUPS spectrometer

The ARUPS studies for this work were performed using the spectrometer on beamline 6.2 of the Synchrotron Radiation Source (SRS) at SERC Daresbury Laboratory, U.K. The design of synchrotron radiation sources has recently been reviewed by Wille [114] and the interested reader is referred there for further details. The Daresbury SRS is a storage ring operated at a beam energy of 2 GeV. Synchrotrons optimised for UV and soft X-rays (VUV rings) have beam energies of around 600 MeV, but the SRS has to service the whole of the UK

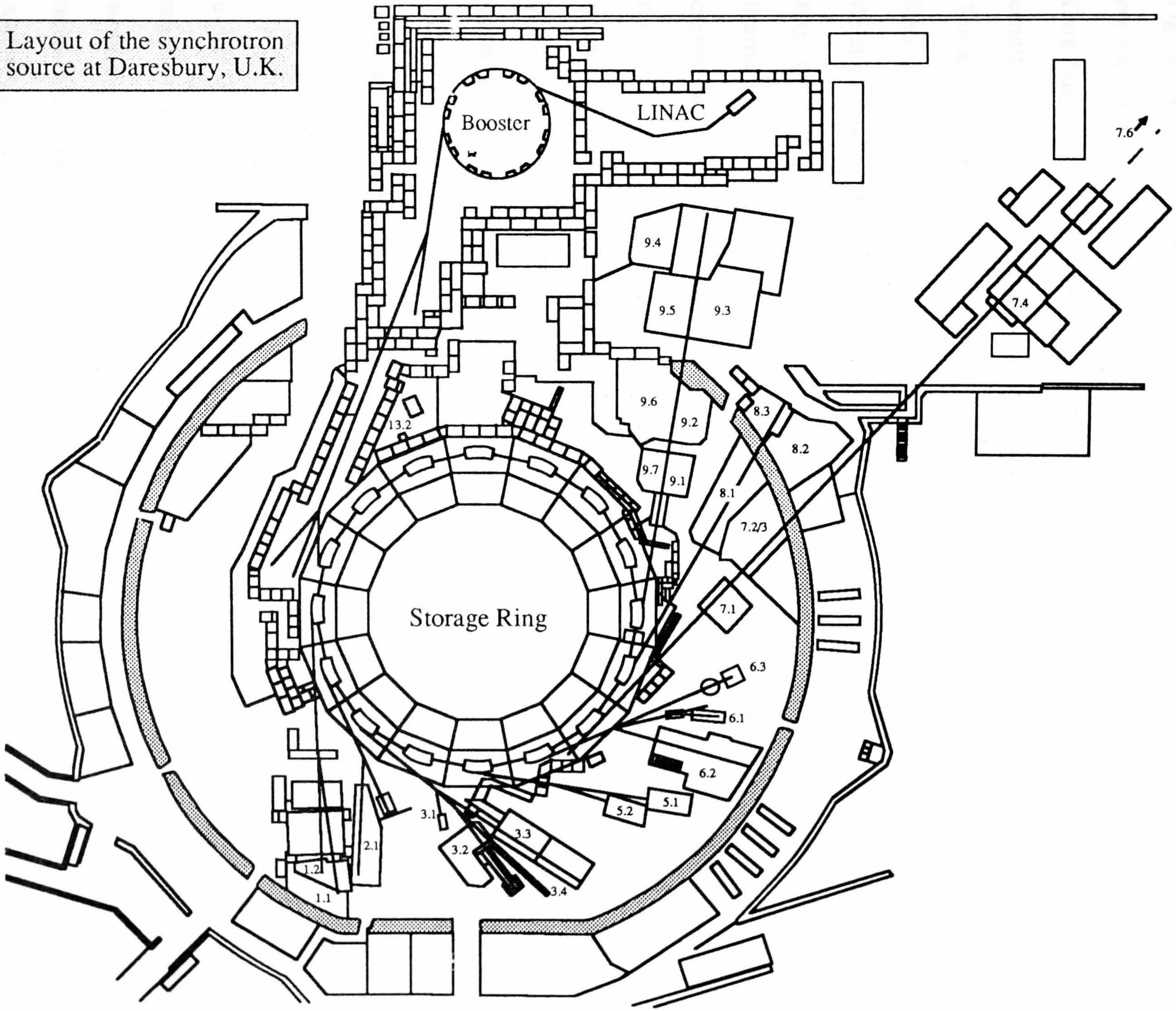

Fig. 4.1 Layout of the synchrotron radiation source at Daresbury, U.K.

synchrotron radiation user community, which includes a substantial number of hard X-ray users. The requirement for beam energies of 2 GeV is met by using a two-stage synchrotron. Fig. 4.1 shows the layout of the SRS and its accompanying beamlines. The near-circular corridor surrounding the storage ring is the tunnel which housed the first synchrotron built at Daresbury - NINA, a collider with a few parasitic beamlines. Components of NINA were cannibalised to build the SRS when the nuclear and particle physicists had moved elsewhere. The accelerator system consists of a modified commercial linear accelerator (LINAC) which feeds into a booster synchrotron operating at 600 MeV. "Bunches" of electrons are injected into the storage ring at 600 MeV until a beam current approaching 300 mA is achieved. The storage ring energy is then ramped to 2 GeV and the stored beam steered to direct radiation down the beamlines. This process (called a refill) is repeated approximately every 24 hours, as the beam current (and hence flux intensity) slowly decays due to interaction with residual gases in the ring vacuum pipes. The production of hard X-rays effectively bakes the storage ring and as a result the vacuum is much better than that in a dedicated VUV ring. This gives much longer beam lifetimes, hence the need for only a daily refill cf. the ~ hourly refills at a VUV ring, partially compensating for the poorer flux in the UV region. In 1987 / 88 the SRS was fitted with a "high brightness lattice " (HBL) which constricts the diameter of the stored electron beam, giving roughly an order of magnitude increase in the output photon brilliance.

The ARUPS system at the SRS is situated on port VUV 6. Port 6 has three beamlines (see fig. 4.2) all of which are used for surface science / electron spectroscopy. The beamline usage is dictated by the type of monochromator. Beamline 6.1 has a grazing incidence monochromator (GIM) giving UV and soft X-rays (20 - 200 eV), 6.2 has a toroidal grating monochromator (TGM) giving UV photons (12 - 120 eV) and 6.3 has a double crystal monochromator giving hard X-rays (1.7 - 10.3 keV). Thus 6.1 is used for soft XPS, 5.2 for ARUPS and 6.3 for SEXAFS. The design of monochromators for synchrotron radiation is discussed elsewhere [115], with the TGM being the most commonly used for ARUPS.

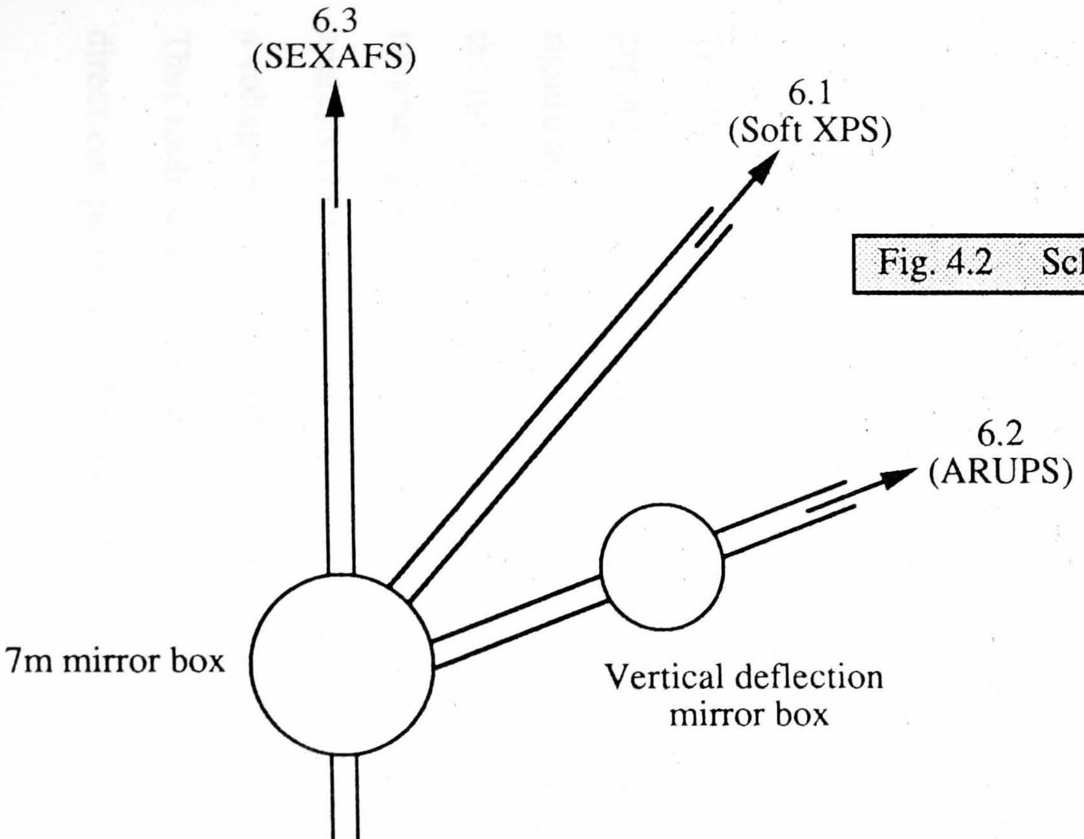

Fig. 4.2 Schematic diagram of line VUV 6 at the SRS, Daresbury Laboratory

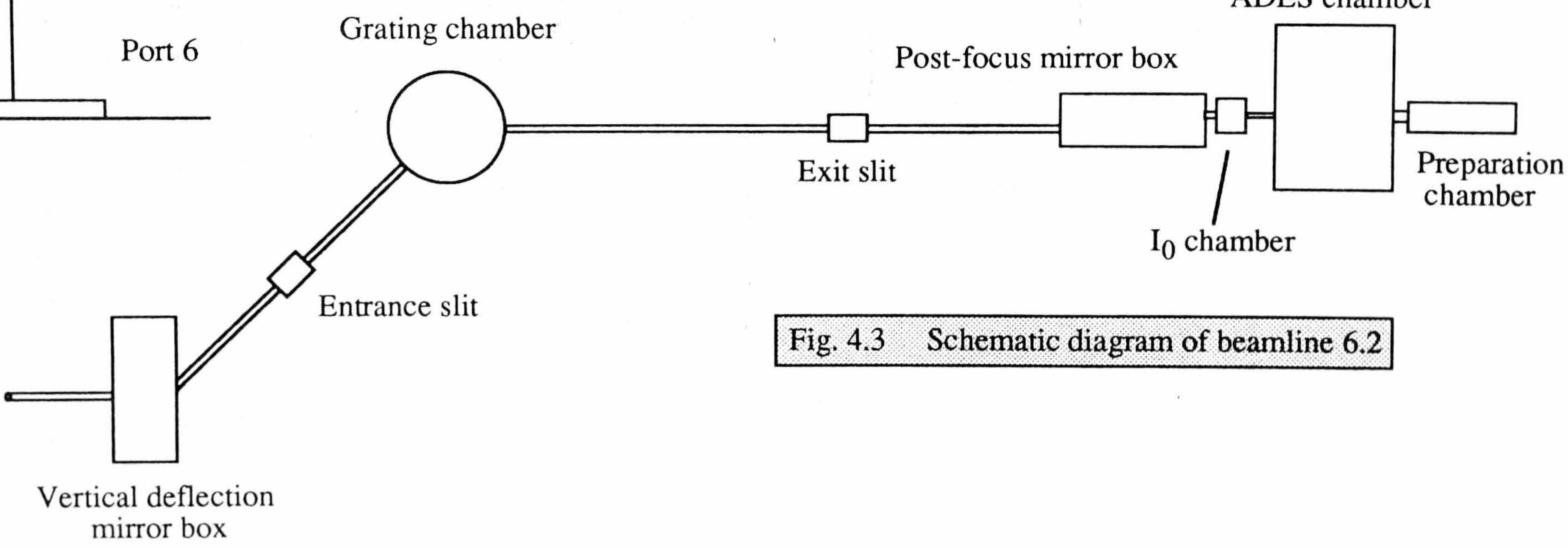

Fig. 4.3 Schematic diagram of beamline 6.2

The TGM on 6.2 consists of a grating and entrance and exit slits. The layout is shown in fig. 4.3. The grating and analysis chambers are mounted on a gantry about 2.5m above ground level, hence the need for vertical deflection of the beam. The photon energy resolution is determined by the exit slit width and this is manually adjustable, if required giving resolution below 0.1 eV (with a corresponding reduction in flux). The grating chamber contains two manually interchangeable toroidal gratings. The different ruling widths of the two gratings (710 and 1800 mm^{-1}) give different usable photon energy ranges, as shown in fig. 4.4.

Fig. 4.4 Flux output from the TGM as a function of photon energy

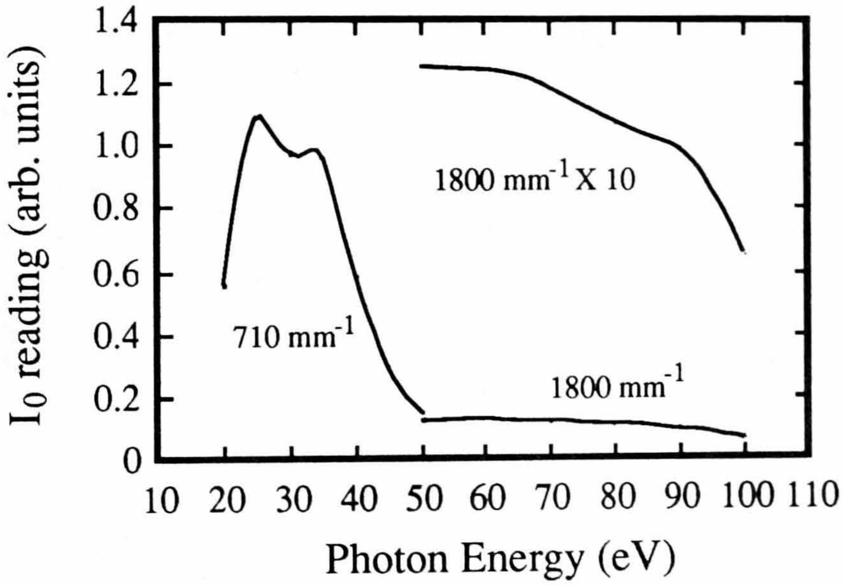

The 1800 mm^{-1} grating allows shallow core levels to be accessed, whereas the 710 mm^{-1} grating is largely used for valence band work. Below 20 eV the second order content becomes significant, and care has to be taken to avoid superimposing second order core level peaks onto the first order valence band. The flux level (I_0) is monitored by passing the beam through a tungsten grid mounted in a small chamber located between the post-focus mirror and the analysis chamber (see fig. 4.5). The drain current from this grid is converted to a count rate via a voltage to frequency converter and is recorded with the count rate from the electron analyser. Thus each data point in an ARUPS spectrum can be normalised to the incident flux, enabling direct comparison of the intensities of features in spectra recorded using different photon energies.

The post-focus mirror focuses the beam from the TGM exit slit onto the sample. This was installed during the SRS HBL installation and contributed greatly to the increased count rates when compared to pre-HBL data acquisition. These improvements made possible the detailed off normal measurements presented in chapter 6.

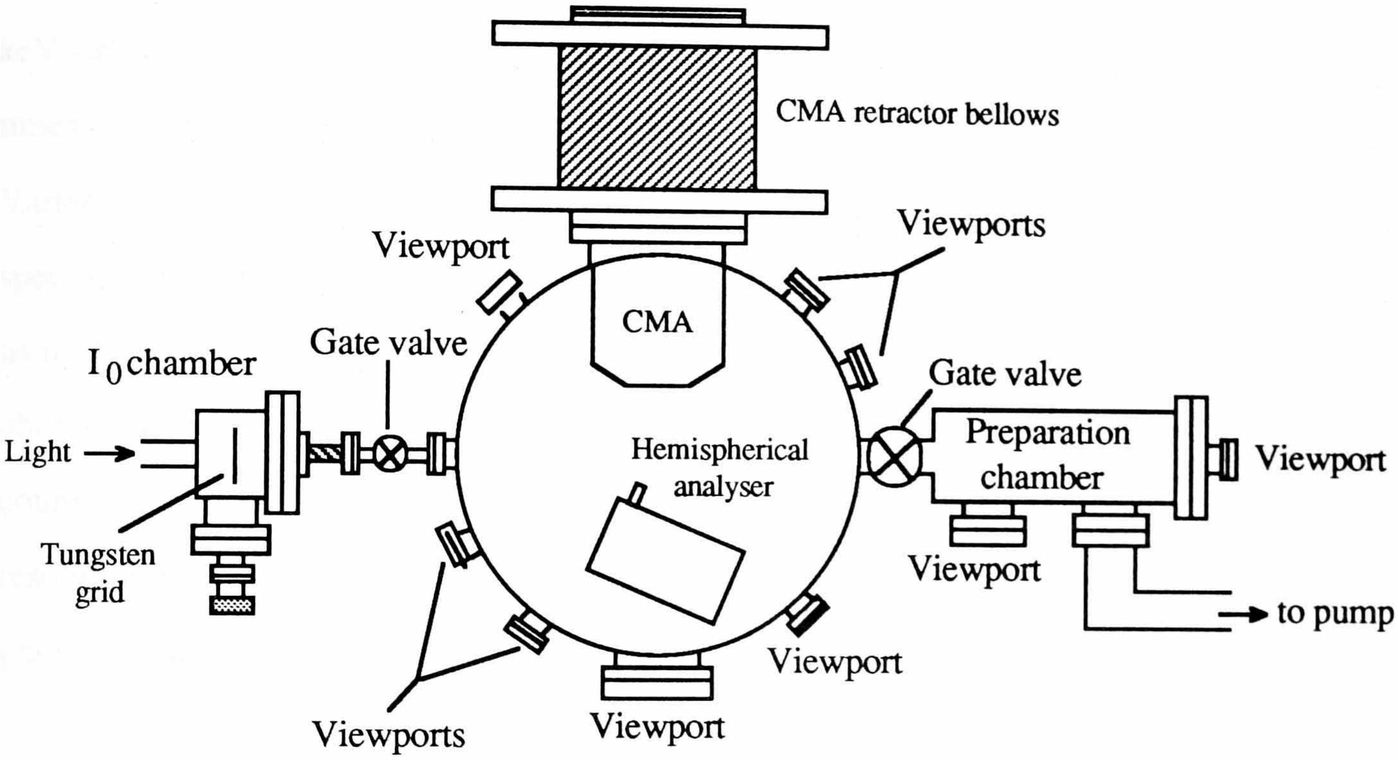

Fig. 4.5 Layout of the VG ADES 400 spectrometer on beamline 6.2

The spectrometer on beamline 6.2 is a commercial (Vacuum Generators) ADES 400, slightly modified for beamline use. The chamber layout at the ARUPS level is shown in fig. 4.5. The hemispherical analyser is of 50 mm radius and is mounted on a twin axis goniometer giving rotation both in and out of the plane of fig. 4.5. The analyser entrance aperture was fitted with a collimator of diameter 0.5 mm, giving an angular acceptance of 3°. The preparation chamber was not used in this work, other than to provide extra pumping capacity as it has its own turbomolecular pump. The (Pb glass) viewport at the rear of the preparation chamber looks directly down the beamline and is used for chamber alignment. The main chamber is pumped by turbomolecular and titanium sublimation pumps, and the pressure during ARUPS measurements was of the order of 10^{-10} mbar. The cylindrical mirror analyser (CMA) is shared between beamlines 6.1 and 6.2 and is used both for Auger spectroscopy (it has its own integral electron gun) and (angle-integrated) photoemission. It is mounted on a retractor and during ARUPS measurements is fully withdrawn as it otherwise interferes with rotation of the hemispherical analyser. On the upper level of the main chamber are mounted LEED optics and an ion gun. The ion gun is a cold cathode VG gun, capable of delivering 4 keV Ar^+ with drain currents approaching 100 μA. The LEED optics have been changed several times during the duration of this work and have been variously 3 and 4 grid VG optics and Varian 4 grid. The LEED optics can also be used as a retarding field analyser (RFA) for Auger spectroscopy, although the signal to noise ratio is considerably worse than that obtainable using the CMA. The overall resolution for ARUPS is determined by a combination of the photon energy resolution and the analyser pass energy. In both cases resolution is traded for count rate and so for valence band spectroscopy using the 710 mm^{-1} grating the overall resolution was typically set to 0.15 eV, and for core level spectroscopy using the 1800 mm^{-1} grating it was set to 0.25 eV.

4.2 KRIPES spectrometer

The experimental requirements for a KRIPES spectrometer are somewhat different from ARUPS, but are clearly related. For KRIPES a monoenergetic electron gun is required, together with some form of photon monochromatisation and detection. The various solutions to these two independent problems pursued by various workers have recently been reviewed by Johnson and Hulbert [116] and so will only be briefly described here. Firstly, the design of the electron gun is crucial to both the energy and momentum resolution. An ideal gun would provide a high current at low energies, in a well-focussed narrow beam. The high current is needed to give a photon yield large enough to detect, remembering that the difference in cross section between the ARUPS and KRIPES processes is some five orders of magnitude, with

KRIPES very much the poor relation in this respect. This effectively prevents the use of HREELS-type electron gun / monochromator combinations, which would give energy resolutions comparable to that routinely attainable in ARUPS, as they produce beam currents in the nA range. In addition KRIPES requires low electron energies, and this combined with high beam current produces space-charge effects which cause the beam to diverge. This would lose momentum resolution and the need to avoid this places an upper limit on the usable beam current, which is typically of order 2 μA at ~ 20 eV. The energy resolution of the electron gun is largely determined by the thermal spread of electrons emitted from the gun filament. The two materials most used for this filament are LaB_6 and BaO, operating at ~1800 °C and ~ 880 °C respectively, giving thermal spreads of ~ 0.25 eV and ~ 0.15 eV. The obvious advantage of BaO as a filament material is somewhat offset by its rapid degradation on exposure to air, making it unsuitable for spectrometers which are often opened to atmosphere. The electron gun in the spectrometer used in this work was custom built for KRIPES and has a LaB_6 filament. The design of this gun is discussed in detail elsewhere [117, 118].

There have been three different solutions to the problem of photon monochromatisation. The first type is based on a Geiger-Muller detector, and was first used for KRIPES by Dose and co-workers [119]. This uses the combined transmission range of a CaF_2 window and the photoionisation properties of iodine to produce a narrow bandpass photon detector, capable of detecting only photons with energy below the cut-off point of the window but with enough energy to ionise the gas. Various combinations of window and gas are possible, with the standard CaF_2 / I_2 combination giving a band pass of ~ 0.8 eV, centred at hν = 9.7 eV. The second type is based on the chromatic aberration of a LiF lens [120]. This uses the strong wavelength dependence, in the UV region, of the focal properties of an alkali halide lens. Detection at different wavelengths (and hence photon energies) is achieved by moving an exit aperture along the focal axis, or by using several detectors at different positions along the axis. Typically, photon energy tunability over a range of a few eV can be achieved using a particular lens, with the photon energy resolution determined by the size of the exit aperture. Both these types of detector (bandpass and lens) are essentially isochromat detectors i.e., a particular photon energy is selected and the electron energy is scanned. This is analogous to EDC mode in ARUPS. The third type of detector, which uses a diffraction grating, allows the use of isochromat mode but also permits the use of fluorescence mode. In this mode the electron energy is held constant and multi-channel detection is used to detect the signal as a function of photon energy. This is analogous to CFS mode in ARUPS, except that as this is *inverse* photoemission it is CIS mode. In contrast to CFS ARUPS, CIS KRIPES is faster than isochromat mode as all photon energies are scanned simultaneously. There is no mechanical scanning required, but some form of multi-channel detection is necessary and so not all grating KRIPES spectrometers can take advantage of it. For example, the KRIPES spectrometer at Liverpool is of the grating type but has only single channel detection, thus only isochromat mode is possible. The first grating spectrometer [121] used a grazing incidence toroidal diffraction grating giving a wide photon energy range (10 - 100 eV), but a low count rate due to the small solid angle of detected radiation. Subsequent designs have used normal incidence spherical gratings giving a detected upper limit of ~ 40 eV, but a much improved count rate. The layout of the KRIPES level of the Liverpool spectrometer is shown in fig. 4.6.

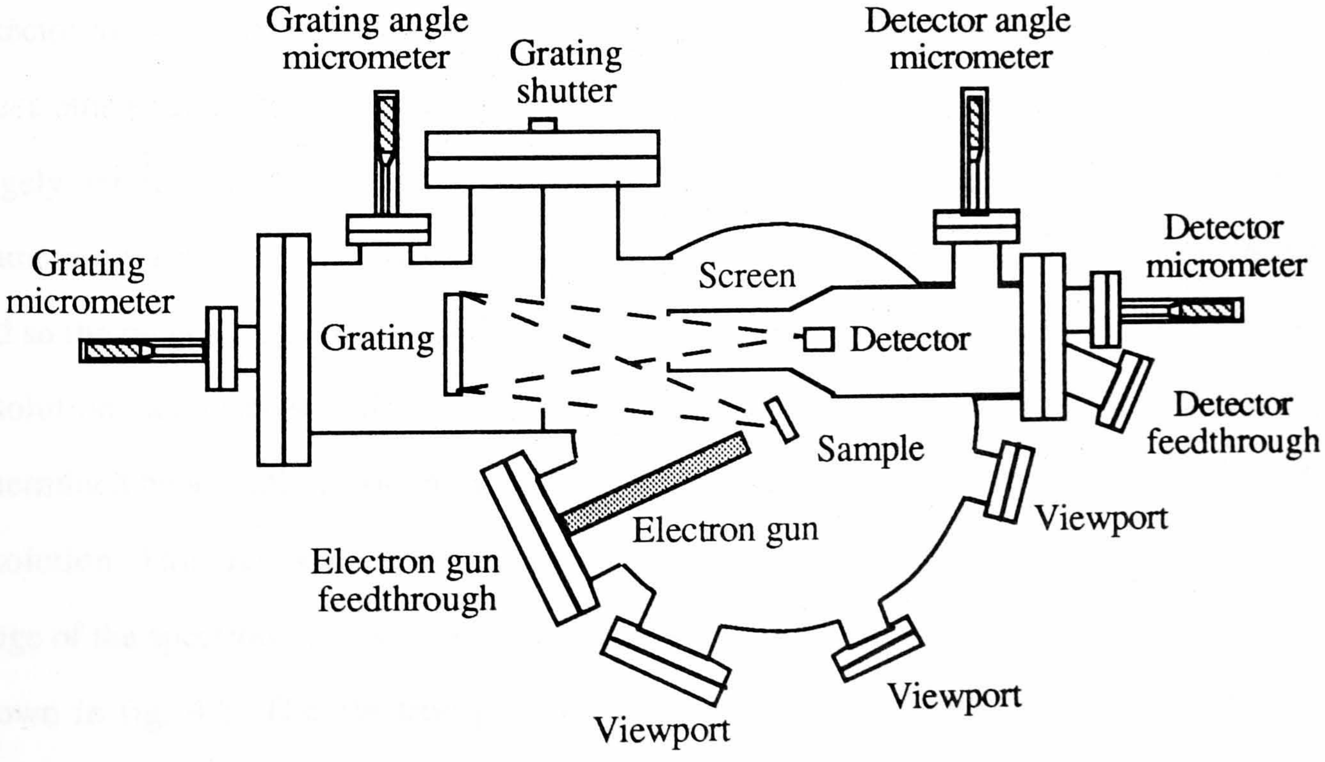

Fig. 4.6 Layout of the Liverpool KRIPES spectrometer

The spherical grating is platinum coated and ruled at 3600 mm^{-1}. The calculated reflectivity of the grating, analogous to the flux intensity curves of fig. 4.4, is shown in fig. 4.7.

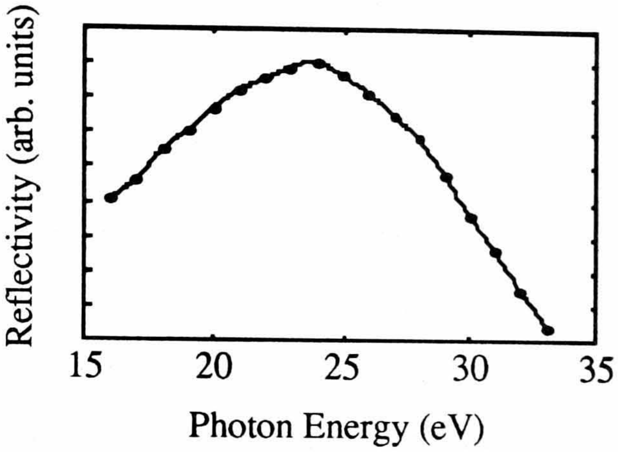

Fig. 4.7 Reflectivity of the KRIPES grating

The sample, grating and detector are arranged in a Rowland circle geometry such that light of a particular wavelength is focussed onto the detector, a single channel electron multiplier (channeltron). Different detected photon energies are obtained by moving the grating and detector to form different Rowland circle configurations. A full discussion of the optics of this spectrometer may be found elsewhere [117, 118]. The energy resolution of the detector is largely determined by the size of the aperture in front of the channeltron, which is fixed at a diameter of 1 mm. As the photon energy is increased the dispersion of the grating decreases and so the range of photon energies admitted by the aperture increases. Thus the photon energy resolution becomes steadily worse as hν is increased. The overall energy resolution is determined by a combination of the energy spread of the electron beam and the photon energy resolution. This has been determined by Collins *et al.* [108] over the useful photon energy range of the spectrometer by measuring the width of the gold Fermi edge step. Their results are shown in fig. 4.8. The electron gun is in a fixed position, and as a result the sum of the electron incidence angle θ and the photon emission angle ϕ is fixed at 40°. This means that it is impossible to vary θ and ϕ independently, which tends to greatly complicate the interpretation

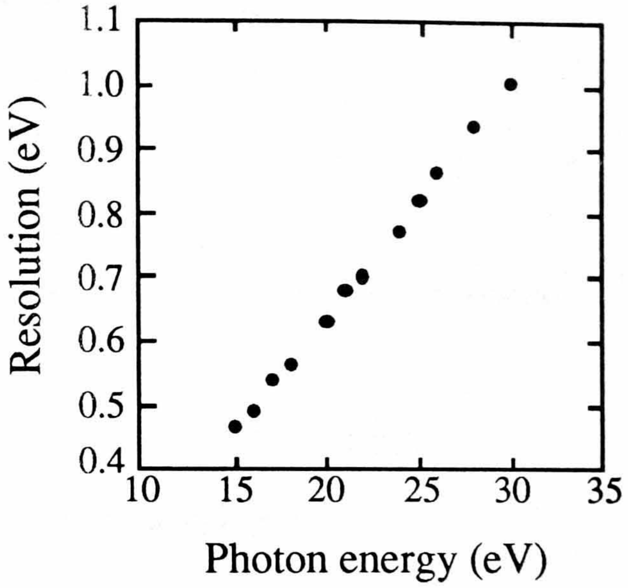

Fig. 4.8 Resolution as a function of photon energy for the IPE spectrometer (after Collins *et al.* [108])

of off-normal incidence spectra. In a similar manner to flux normalisation on the ARUPS system, the electron beam current is recorded with the photon flux at each electron energy, in order that the spectra can be normalised to the incident charge.

The upper level of the spectrometer is used for sample cleaning and characterisation. An ion gun is available for Ar^+ sputtering, giving a maximum beam energy of 2 keV with a drain current of ~ 20 μA. A three grid front view Varian LEED system is fitted, which was originally used as an RFA for Auger spectroscopy to monitor sample cleanliness. This function is now performed by XPS, as recently a twin anode (Mg / Al) X-ray source and externally mounted 50mm radius hemispherical analyser (both from Vacuum Science Workshops) have been fitted. The chamber is pumped by diffusion and titanium sublimation pumps, and base pressures in the low 10^{-11} mbar range are routinely attainable.

To date the Liverpool spectrometer has largely been used to study clean surfaces, particularly those of metals [122]. Early work [117] concentrated on tungsten surfaces as it was suggested by Pendry [19] in his paper on the theory of KRIPES that tungsten was the most suitable material for initial investigation. Subsequently normal incidence spectra of

W(001) and W(110) [108] have been used to test the relativistic photocurrent scheme (see chapter 3), and the dispersion of the surface state believed to drive the W(001) reconstruction [123] has been mapped [124]. Later work [118] concerned the related metal Ta (001), as the surface states seen in ARUPS of W(001) [123] are mostly unoccupied on Ta(001), and Na(110) [125] in an attempt to explain its anomalous ARUPS spectra [126]. This was not a particularly successful exercise except that it demonstrated that meaningful KRIPES results can be obtained even from materials like Na, a nearly free electron metal which meets none of the Pendry criteria for a good inverse photoemitter. Recently the high lying states of Ni(110) have been studied [127], as well as disordered Ni-Fe (110) alloys [127], with a view towards understanding the electronic structure underlying the Invar effect. Polycrystalline AuCr [118] has also been investigated, again with interest primarily in magnetism, in this case the minority spin states of the Cr impurity. The one study of an adsorbate-substrate system was of Pd(110) - CO [128], where the CO - derived state was much weaker than in earlier KRIPES work [129] which used a bandpass detector (hν = 9.7 eV), due to relatively low initial state density when using 15 eV photons (the lowest energy for which reasonable count rates can be obtained for this spectrometer). Law and co-workers have used the Liverpool spectrometer to study a number of layer materials - graphite [130], VSe_2 [131, 132], $HfTiSe_2$ [133] and $FeTaS_2$ [134], mainly using off-normal incidence spectra to map the essentially two-dimensional bandstructures of these materials, although the graphite interlayer state was observed and mapped using normal incidence data [130].

4.3 Sample cleaning

The reason that ARUPS studies of rare earths are so few is quite simple. Cleaning single crystals is extremely difficult and time consuming, and in some cases, notably hcp $(10\bar{1}0)$, the reproducible production of clean surfaces has so far proven impossible. Allied to the difficulties associated with growing single crystals of sufficient purity it is not difficult to see why, for example, ARUPS studies of Ni(110) [135] far outnumber the combined total of all rare earth ARUPS studies, including those of this work. Superficially the cleaning procedures used for rare earths to date have all been very similar as each employed noble gas ion bombardment and annealing, but there are several factors to be taken into account when comparing cleaning procedures. Principally these are the origin and purity of the crystal, the *ex-situ* cleaning process i.e., electropolishing and / or mechanical polishing, the ion beam energy and the annealing temperature.

Sc(0001) was one of the first rare earth single crystals to be cleaned. Tougaard and Ignatiev [136] did not report the origin or purity of their crystal and did not describe their *ex-situ* procedures. Initial cleaning in UHV was performed by Kr^+ bombardment (beam energy 1 keV, current density 20 μA cm^{-2}) while maintaining the sample at 600 - 900 °C. After 15 hours C, S and Cl contaminants were removed and the O level was below 5% of a monolayer. Final cleaning consisted of a room temperature Kr^+ bombardment and a subsequent anneal to 500 °C. For Gd(0001) Himpsel and Reihl [20] used a Gd sample from Ames Laboratory, electropolished in a mixture of 90 % methanol and 10 % perchloric acid. This process produces a passivating chloride layer that prevents the surface from oxidation during exposure to atmosphere. This of course requires the removal of Cl during *in-situ* cleaning, which may well be a problem equal to that of removing surface oxide. Himpsel and Reihl used cycles of Ar^+ bombardment and annealing to 600 °C. Annealing at 700 °C produced a surface roughened by sublimation. Rosina *et al.* [22] also used an electropolished Ames sample for their work on Ce(001). Ion bombardment (Ar^+, 500 eV, 8μA) and annealing (500 °C) initially produced reconstructed surfaces which showed hydrogen induced features in ARUPS spectra. Only after "many" cycles was a (1 × 1) surface showing negligible hydrogen features obtained. A short abstract of a paper presented at a meeting [137] describes the attempts of Sokolov *et al.* to clean Dy(0001), Tb(0001) and Tb($10\bar{1}0$). They used Ar^+ bombardment and annealing, and reported "acceptable" (1 × 1) LEED patterns from Dy(0001) following annealing at 350 - 400 °C, but disordered surfaces if annealing was performed below 300 °C or above 500 °C. "Excellent" (1 X 1) patterns were obtained from Tb(0001) after annealing at 600 °C, but they were unable to obtain reproducible, clean, ordered surfaces of Tb($10\bar{1}0$). This report was not followed up by a detailed publication, but recently the same group reported an ARUPS study of Tb(0001) [73] in which the cleaning procedure was described in some detail. The sample was again an electropolished Ames crystal. *In-situ* cleaning used cycles of Ar+ bombardment (400eV, 2 -3 µA, 20 mins.) and annealing (650 °C, 10 mins.). 50 hours of cleaning were required to remove the Cl and reduce O and C contamination to acceptable levels (< 5%). However major difficulties were experienced with Fe impurities, with some 10 -15 % of a monolayer of Fe present on their "clean" surface. Given the quoted Fe concentration of their crystal (59 ppm) it seems unlikely that such a level of Fe could be due to intrinsic impurity levels, and this implies that contamination occurred at some time during sample preparation.

The cleaning procedure used for this work was that originally developed by Barrett and co-workers at Birmingham University, U.K., and first reported with their ARUPS results for Y(0001) [23]. The samples used were spark machined from high quality boules supplied by Dr. D. Fort of the School of Metallurgy and Materials at Birmingham, and were grown using SSE (Y, Gd, Tb) or zone refining (Ho, Er, Pr). The Y samples were machined from the same boule used by Barrett *et al.* for their ARUPS and LEED studies of Y(0001) [23, 101] and Y($11\bar{2}0$) [24]. The Gd(0001) sample was the same one used by Jordan [138] for a preliminary ARUPS study. The samples were not electropolished, but were mechanically polished using a number of grades of diamond paste down to a particle size of 0.25 µm. The absence of a passivating chloride layer leaves the polished surfaces extremely vulnerable to corrosive oxidation and so the samples were stored under rough vacuum. Tantalum spring clips were used to mount the samples on the manipulator sample holder, enabling fast transfer from rough vacuum storage to the UHV chamber, with the samples in atmosphere for only one or two minutes. Significant oxidation still occurred during transfer however, and this oxide layer had to be removed by Ar^+ bombardment. The beam energy and current used (2 - 4 keV, up to 100 µA) are thus somewhat higher than have been used for electropolished samples. Ar^+ bombardment (30 mins.) is followed by annealing to 600 - 650 °C for 30 mins. This temperature range is consistent with those used by other workers for Tb(0001) [73, 137] and

Gd(0001) [20], as was the observation that anneal temperatures outside this range produced disordered surfaces. Typically 20 - 30 cleaning cycles were required to obtain clean ordered surfaces, if performed consecutively (i.e., 24 hour operation). For the KRIPES study of Y(0001) (see chapter 6), sample cleaning was not performed on a 24 hour basis, and a maximum Ar^+ energy of only 2 keV was available. As a result 45 cleaning cycles were required. With the time needed to allow for cooling to room temperature after an anneal adding to the overall duration of a cycle, it is often of the order of several days after bakeout before the sample is ready for serious data acquisition. Reproducibly clean, ordered surfaces of Y(0001), Y(11$\bar{2}$0), Pr(0001), Gd(0001), Ho(0001), Ho(11$\bar{2}$0), Er(11$\bar{2}$0) and Tb(0001) were produced using this cleaning method during the course of this work, but, as explained in chapter 5, considerably less success was encountered with Ho(10$\bar{1}$0). Barrett *et al.* [23, 24] found that surface order and cleanliness were best monitored using ARUPS. Fig. 4.9 shows ARUPS spectra from Y(0001) surfaces. Spectrum (a) is from a clean ordered surface. The feature at 9.6 eV binding energy is indicative of hexagonal order - the intensity of this surface-order-dependent state (SODS), whose origin is discussed in chapter 5, has been correlated with LEED pattern quality and is attenuated by both light Ar+ bombardment and surface contamination [23, 24]. Spectra (b) and (c) are from dirty surfaces. Spectrum (c) has O , C and H contamination, and shows considerable weight around 6 eV binding energy. Note the much smaller SODS compared to spectrum (a), and the smeared out lineshape of the valence band emission, with a broad, triangular feature at E_F. This DOS-like lineshape (see fig. 3.4 (b)) near E_F is strongly suggestive of surface disorder as it implies loss of momentum resolution. Spectrum (b) is from a sample which had been in a vacuum chamber that was accidentally back-filled with H_2 to a pressure of 10^{-3} mbar for a few seconds. This spectrum shows a dominant hydride peak, an almost totally quenched SODS and a distorted valence band lineshape. Given the increased surface sensitivity of ARUPS compared to AES, and the known effects of contamination, particularly hydrogen (invisible to AES), on ARUPS spectra of rare earths, cleanliness of the samples used in this work was monitored, where possible, by ARUPS. XPS was used on the KRIPES spectrometer, so the absence of hydrogen

Fig. 4.9 Normal emission ARUPS spectra of Y, hν = 40 eV
(a) clean Y(0001)
(b) with hydrogen contamination
(c) with oxygen and carbon contamination

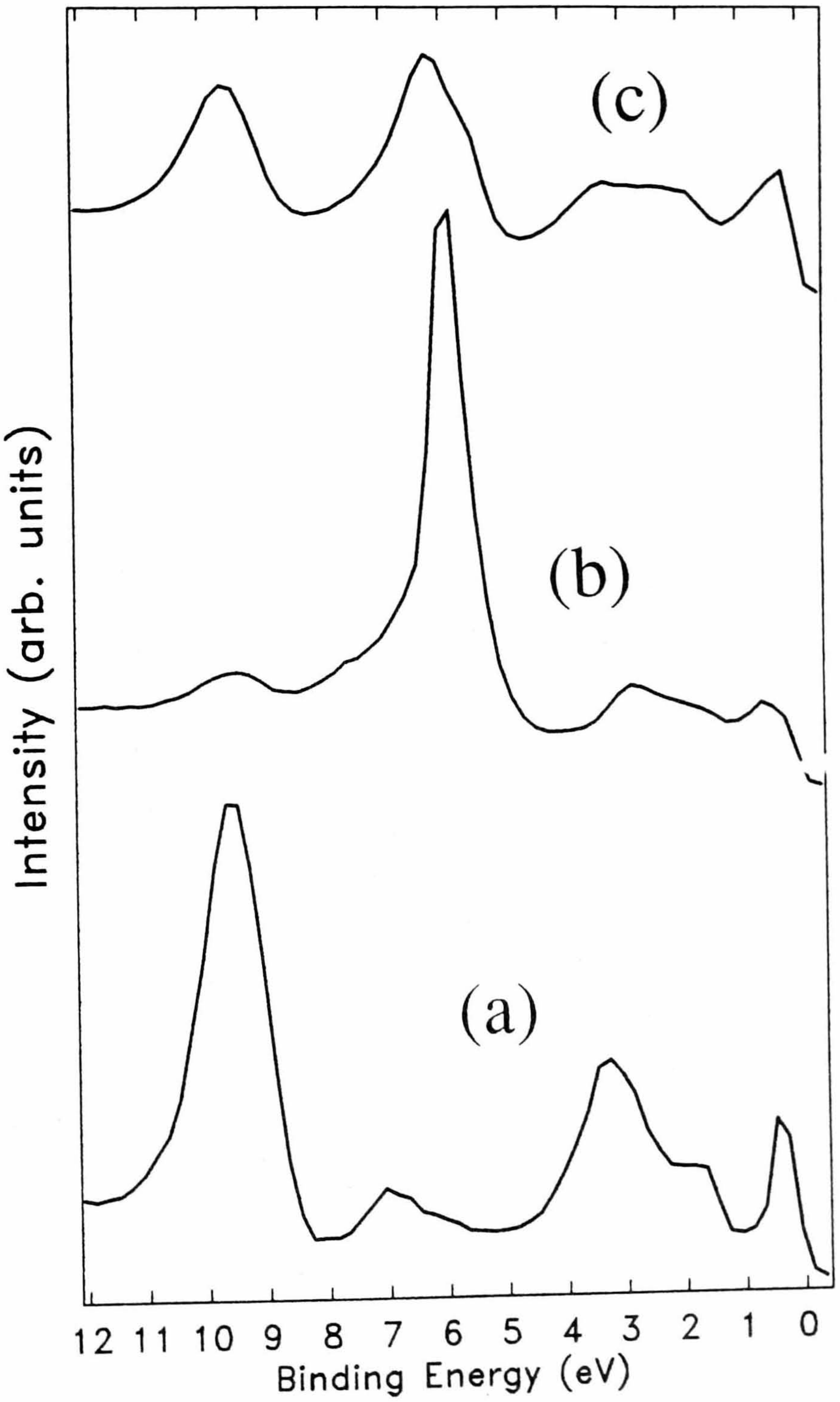

contamination could not be determined.

CHAPTER 5

Surface Structure

In addition to any intrinsic interest the determination of surface geometric structure is a pre-requisite to any investigation of electronic structure by means of ARUPS or KRIPES. Geometric and electronic structure are interdependent, which means that the features seen in the spectra are likely to depend very closely on the actual surface structure. It might be expected that the structure adopted by a surface would be that obtained by simply terminating the bulk crystal at a particular plane. The surface structures of the three principal faces of the hcp lattice as produced by this process are shown in fig. 5.1.

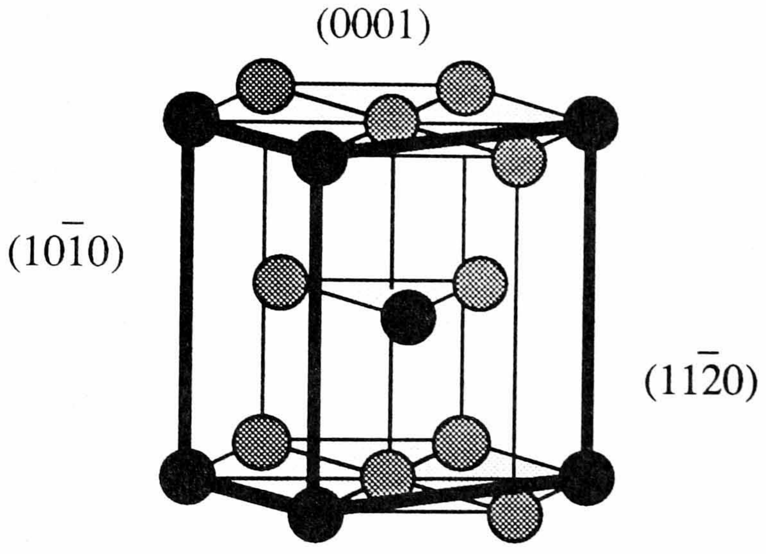

Fig. 5.1 Principal planes of the hcp structure

In many cases, at least for metal surfaces, the surface structure is essentially a bulk termination, but this is often accompanied by a small relaxation or contraction of the layer spacings close to the surface. From the point of view of calculating surface electronic structure it is useful to know the extent of these deviations from the ideal bulk layer spacings, particularly for calculating photocurrents. In some cases the surface structure is completely different from a simple bulk termination and these surfaces are referred to as 'reconstructed'. For this work qualitative surface structure was performed using LEED and ARUPS (since electronic and geometric structure are related it follows that qualitative comparisons of geometric structure of two surfaces can be made by comparing their ARUPS spectra).

5.1 hcp and dhcp (0001) surfaces

There have been several reports of the observation of LEED patterns from (0001) surfaces of hcp rare earths [23, 24, 73, 136, 137, 139, 140]. In each case the reported patterns were six-fold symmetric, indicating an ideal bulk termination. LEED patterns from the (0001) surfaces of Y (hcp) and Pr (dhcp) are shown in fig. 5.2.

Fig. 5.3 R-Factors for different Sc(0001) structures (after Tougaard and Ignatiev [136])

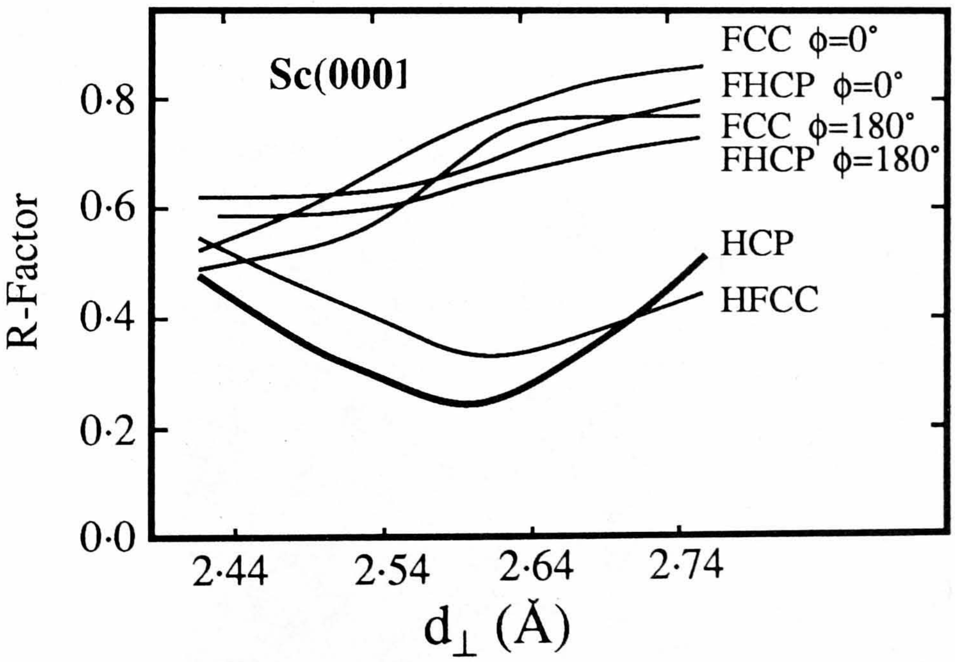

The only quantitative confirmation that the (0001) surfaces are indeed bulk terminated comes from the LEED I-V study of Sc(0001) performed by Tougaard and Ignatiev [136], one of the earliest studies of the surface of a rare earth single crystal. They tested their experimental

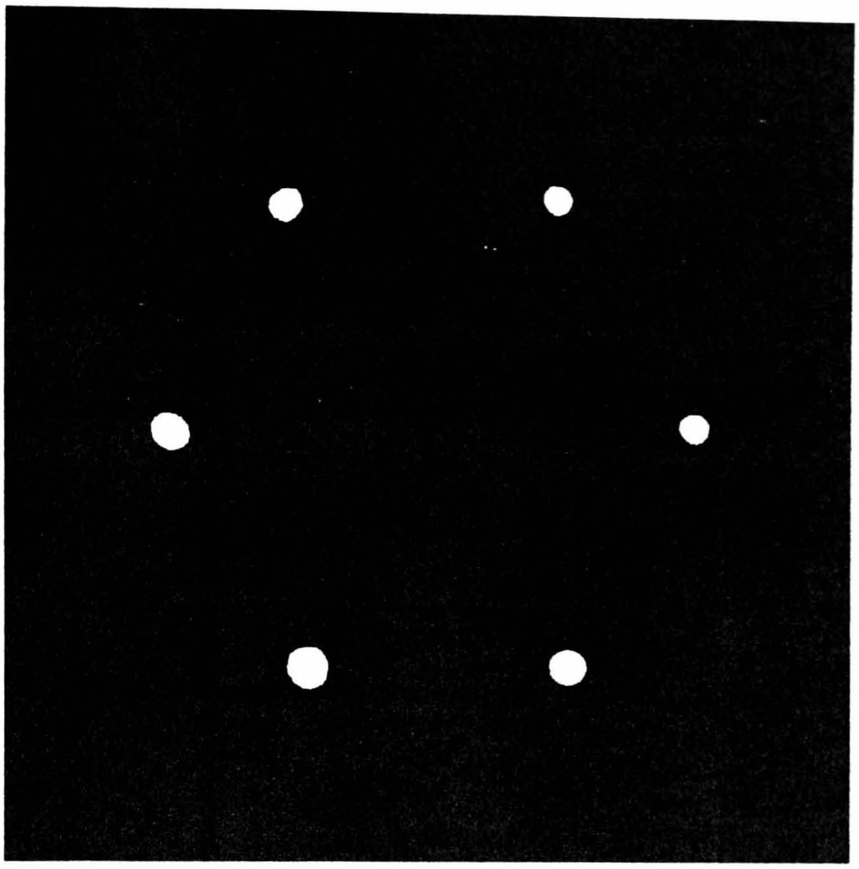

Fig. 5.2 LEED patterns from Y(0001) [above] and Pr(0001) [below], beam energies 50 and 82 eV

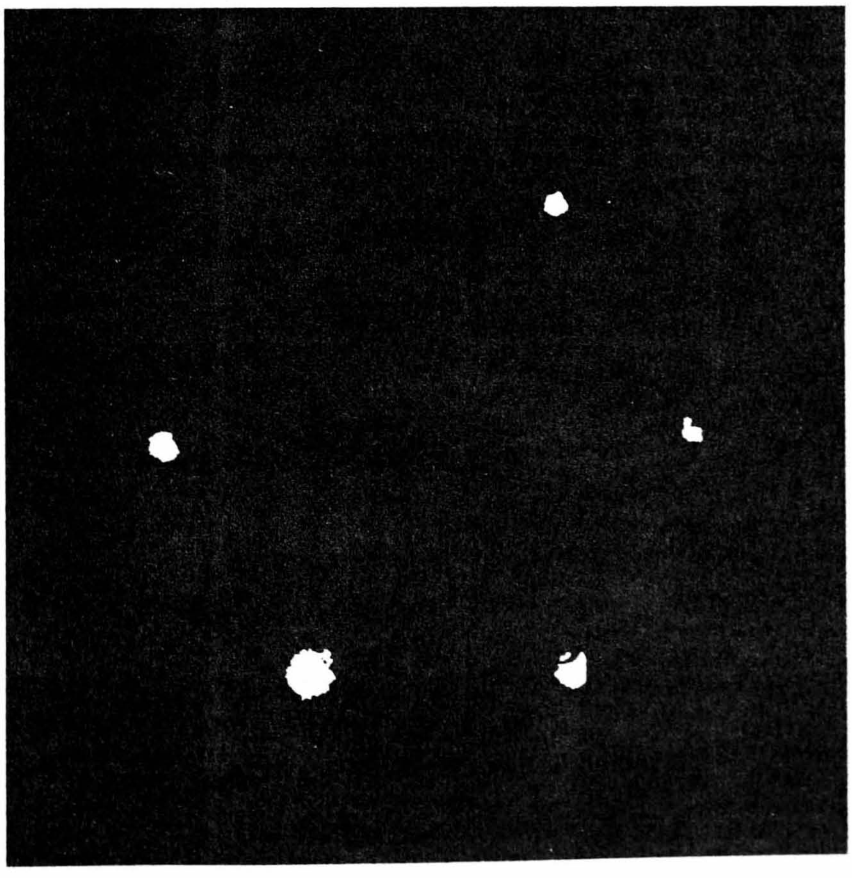

results against calculations for model close-packed structures, each of which would give a six-fold LEED pattern. The model structures were : (i) hcp, (ii) hcp termination on fcc bulk ("hfcc"), (iii) fcc termination on hcp bulk ("fhcp") and (iv) fcc. The Zanazzi-Jona R-factor [141] as a function of layer spacing for these comparisons are shown in fig. 5.3. The best agreement is found for the hcp structure with a layer spacing of 0.259 nm, a 2% contraction compared to the bulk value, with an R-factor of 0.2, which indicates a very probable structural model [141]. As the properties of Sc, notably its small atomic radius, are subtly different from the other hcp rare earths it is far from clear whether within the rare earths this result is a general one, or unique to Sc. As yet their have been no further *quantitative* surface structure determinations for any of the rare earths.

5.1.1 The surface-order-dependent state

The first ARUPS study of Y(0001) [23] showed that the majority of peaks observed on that surface could not be explained in terms of emission from one-electron bands of the bulk bandstructure. Fig. 5.4 shows the Y(0001) normal emission ARUPS spectra of Barrett and Jordan for a range of photon energies. The origins of the valence band peaks, labelled *a* - *c* in fig. 5.4, are discussed in chapter 6. Of particular interest with reference to surface structure is the peak at 9.6 eV binding energy - the SODS. As shown in chapter 4 the SODS is associated with clean, ordered hexagonal surfaces. This peak is by no means unique to the Y(0001) surface, and has been observed on all the clean hcp / dhcp rare earth (0001) surfaces studied by ARUPS. Spectra taken using a photon energy of 40 eV where, as fig. 5.4 suggests, the SODS has maximum intensity, are shown in fig. 5.5. The Pr(0001) spectrum was taken by Dhesi *et al.* during a detailed ARUPS study of this surface. The results from this study are at present being analysed and will be reported elsewhere – a preliminary report was presented at the 12th european conference on surface science in Stockholm, September 1991 and has been submitted for publication [87]. Note that the binding energy of the SODS on (dhcp) Pr(0001)

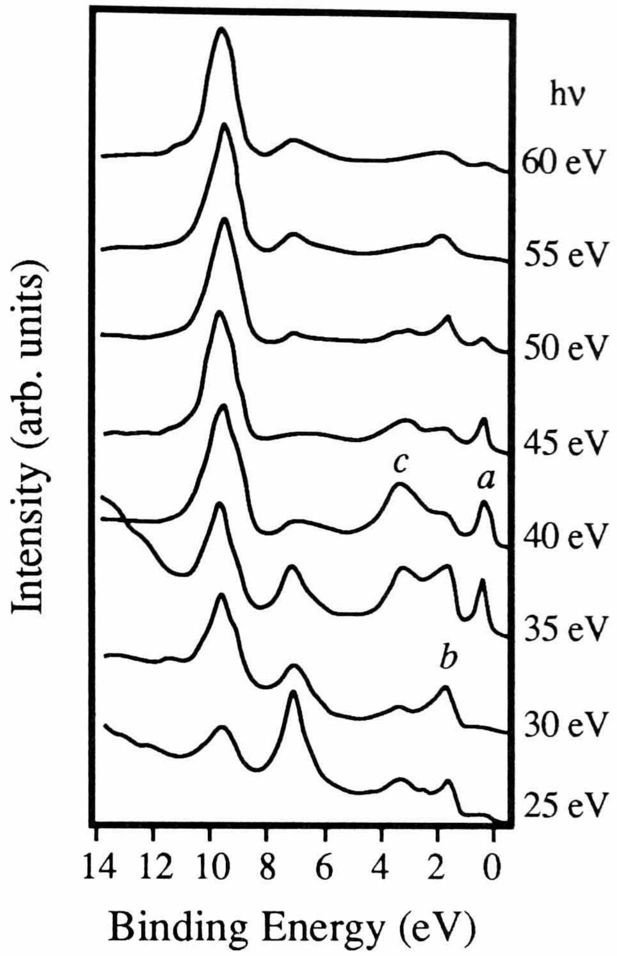

Fig. 5.4 Normal emission ARUPS spectra from Y(0001) (after Barrett and Jordan [23])

is somewhat less than on the hcp (0001) surfaces. Although the existence of the SODS was first discussed by Barrett and Jordan [23] it seems very likely that it was first observed by Himpsel and Reihl [20] on Gd(0001). In their paper [20] they describe monitoring the surface order by the intensity of the surface 4*f* emission, with the surface core-level shift "somewhat greater" than the value of 0.48 eV found by Kammerer *et al.* [142] for polycrystalline Gd. Since the bulk Gd 4*f* emission occurs at a binding energy of 8.3 eV [142] it follows that they observed a feature at a binding energy "somewhat greater" than ~ 8.5 eV, the intensity of which was extremely sensitive to surface order. They did not show binding energies greater than 3 eV, but fig. 5.6 shows that in the valence band region at least their spectra are entirely consistent with those of this work, and by implication it seems likely that their spectra also showed a SODS.

Fig. 5.5 Normal emission ARUPS spectra from the (0001) surfaces of Y, Pr, Gd and Ho hν = 40 eV, incident angle 30°, p-polarised radiation

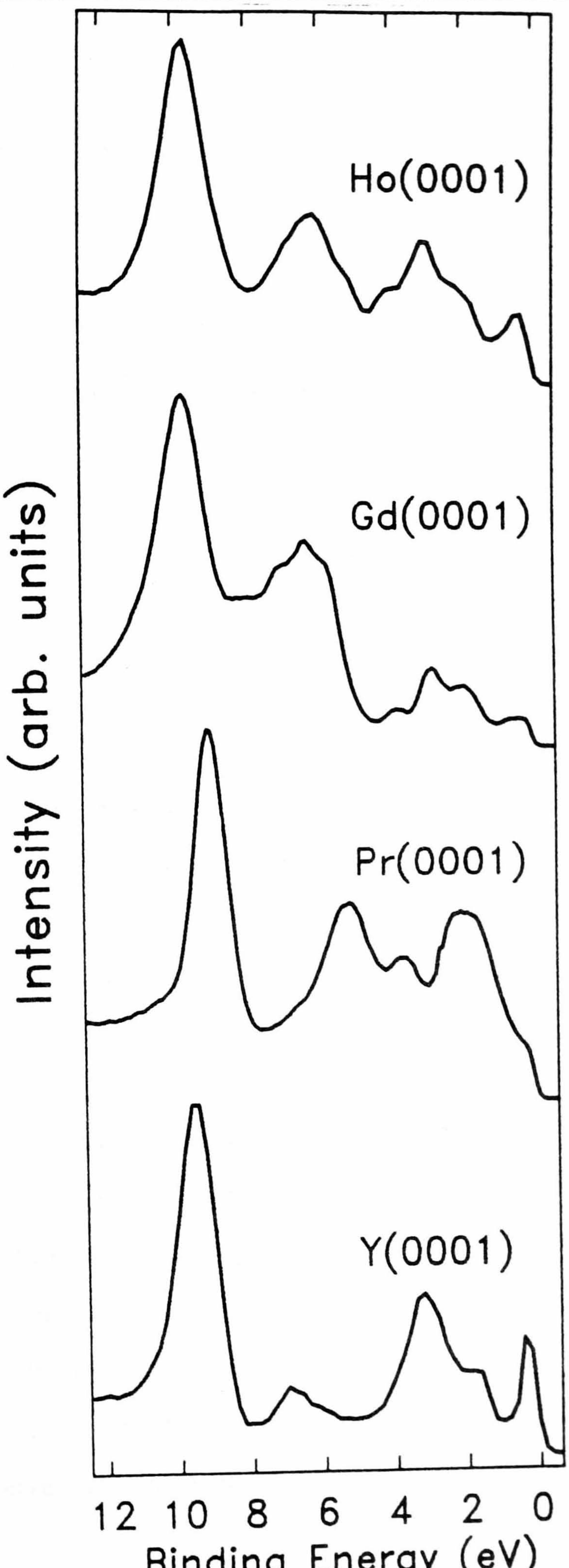

Fig. 5.6 Normal emission ARUPS spectra from Gd(0001)
(a) this work
(b) Himpsel and Reihl [20]

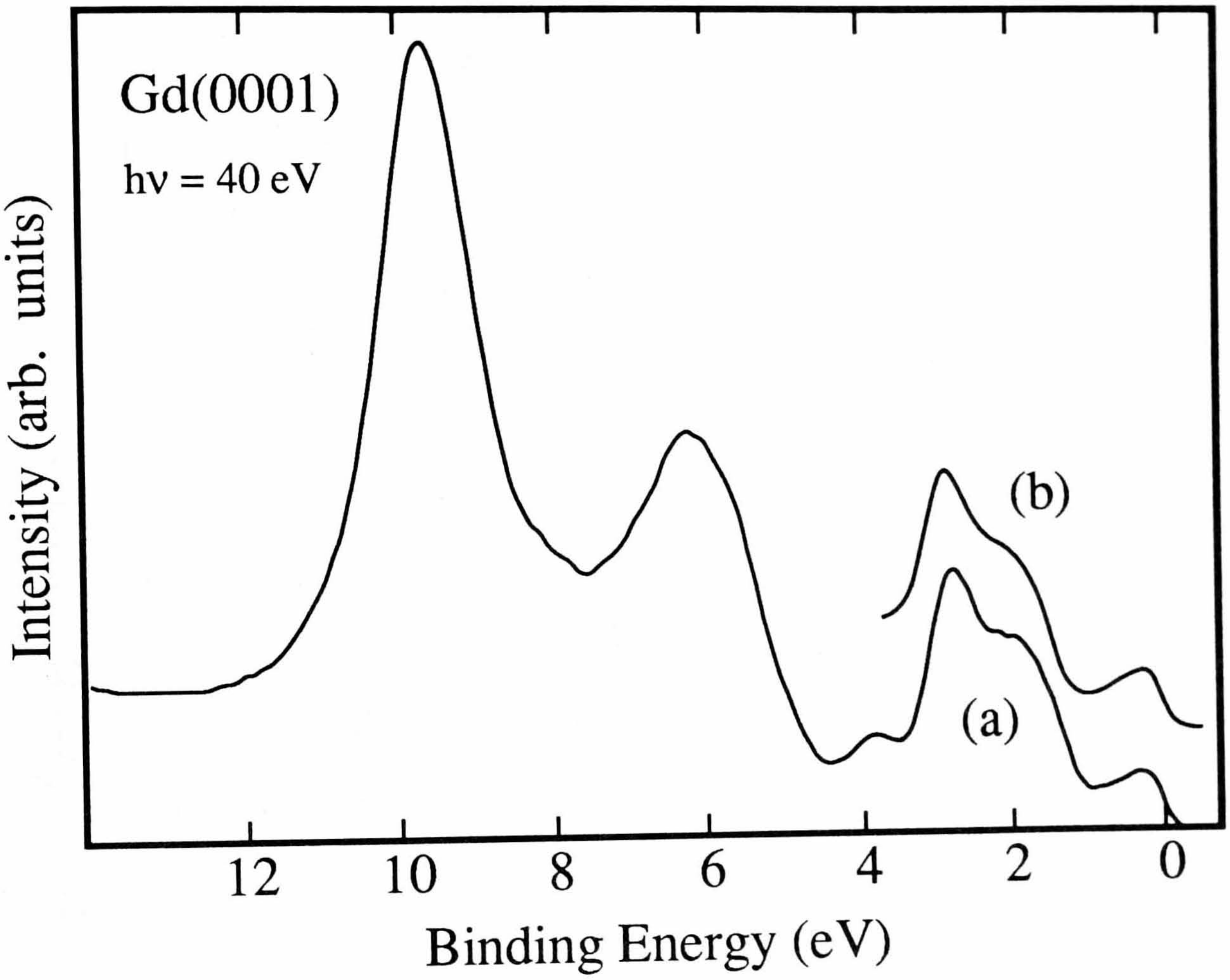

Fig. 5.7 shows ARUPS spectra from Gd(0001) taken at a photon energy of 90 eV, where the 4*f* photoionisation cross-section is much higher than at 40 eV [143]. This shows the SODS as a shoulder on the 4*f* peak, a shoulder which is enhanced at off-normal emission where the surface sensitivity is greater. It is fairly straightforward to imagine how this could be misinterpreted as a surface shifted 4*f* level. However this does not detract from the validity of the ARUPS data of Himpsel and Reihl since their misinterpretation led them to correctly view the intensity of the SODS as an indicator of surface order.

The properties of the SODS have been found to be the same for all the surfaces on which it has been observed. The only real question mark concerns its photon energy

Fig. 5.7 Normal and off-normal emission ARUPS spectra from Gd(0001)
$h\nu = 90$ eV, incident angle 30°, p-polarised radiation

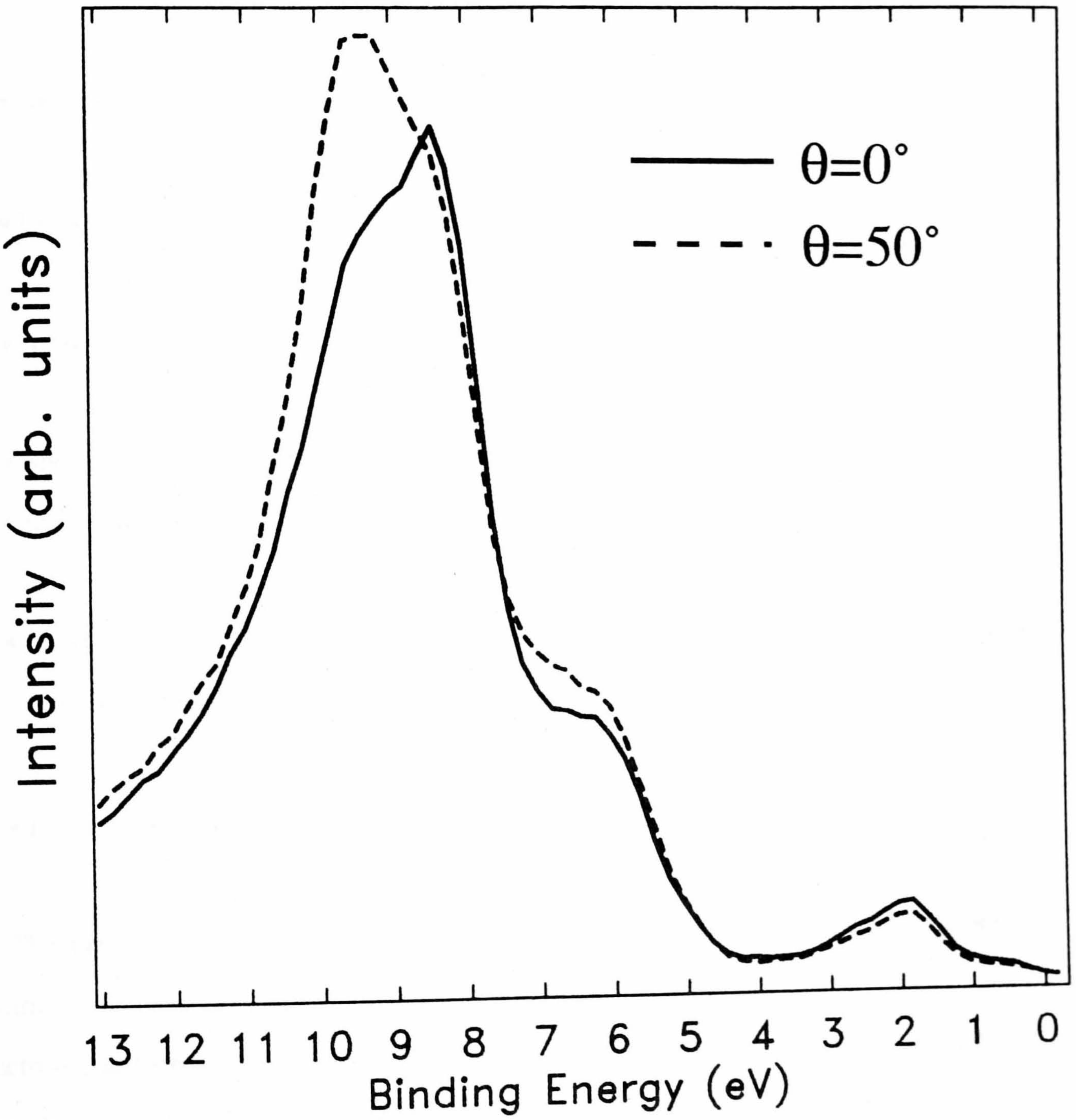

dependence, as the $N_{2,3}VV$ (Y) or $O_{2,3}VV$ (Lanthanides) Auger peaks cross the SODS binding energy region for photon energies around 35 eV. The other properties of the SODS are as follows :

- Binding energy is 9.6 eV, except on Pr(0001) where it is 9.1 eV.
- Narrow width (less than 1 eV FWHM).
- Does not disperse with either photon energy or emission angle.
- Attenuated by Ar^+ bombardment or surface contamination.
- Shows maximum intensity at ~ hν = 40 eV, which is very close to the same intensity maximum shown by the 4*p* (Y) or 5*p* (Lanthanides) photoemission peaks.
- Is associated with peak *c* in fig. 5.4. They always occur together and show the same intensity maximum.
- Is not associated with any other photoemission peaks at binding energies > 4 eV.

The origin of the SODS is not at present understood but there are a number of possibilities which can be ruled out. Its presence on Y(0001) clearly precludes the involvement of *f* electrons, and since it has essentially the same binding energy on all surfaces it does not appear to be a satellite of the 4*p* or 5*p* levels, whose binding energies cover the range 20 - 30 eV. The high reactivity of the rare earths means that surface contamination must always be considered as a possible source of unexpected photoemission peaks, even if the levels of C and O are as indicated by XPS / AES i.e. < 5 at. %. The main contaminants of the bulk material are

C and O, and the main residual gases in the UHV chambers are CO, CO_2, H_2 and H_2O. Dosing experiments for all these gases on polycrystalline rare earths have been performed and none of them have shown any features remotely resembling the SODS. The results of Netzer *et al.* [144] for Er are shown in fig. 5.8.

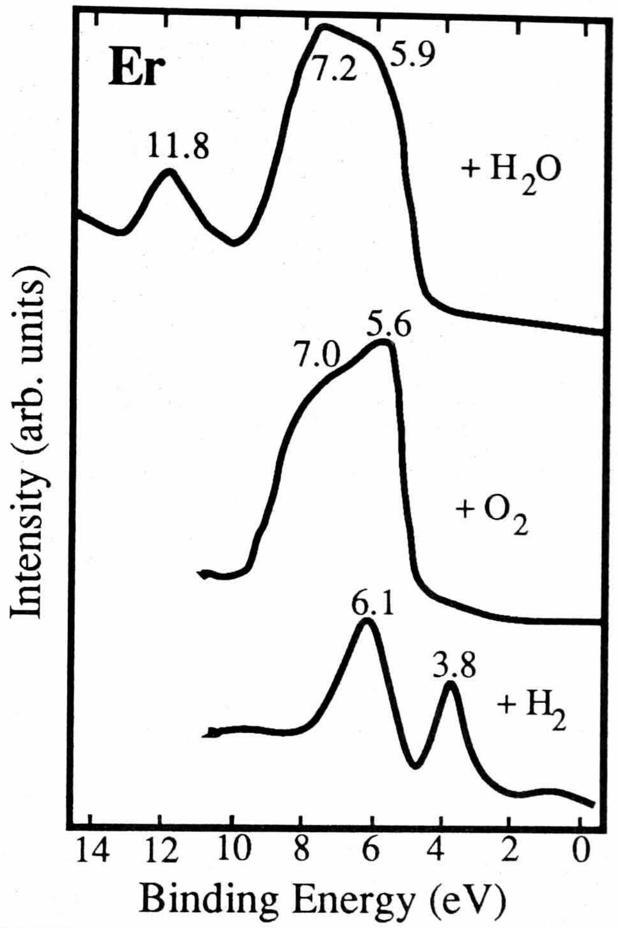

Fig. 5.8 UPS spectra of Er with various adsorbates (after Netzer *et al.* [144])

Note that most of the spectral weight is in the binding energy range 5 - 7 eV, i.e. exactly where the contamination related peaks on the single crystal surfaces occur (see chapter 4). The exception is for water dosage, where an OH (N.B. not an H_2O) orbital occurs at 11.4 eV. Netzer *et al.* [145] also showed that the binding energies of the adsorbate features were largely independent of dosage level. The results all indicate dissociative adsorption [145], which is not a surprising result given the known high reactivity of rare earths, and suggest that the reproducible presence of the SODS is most unlikely to be due to a molecular adsorbate. Further, the narrow SODS width would tend to suggest an ordered overlayer if it were due to an adsorbate orbital, which would be visible in the LEED pattern and all surfaces showing an intense SODS have exhibited excellent (1 × 1) LEED patterns. The affinity of rare earths for hydrogen is well documented [146] and another possibility is that the SODS could be associated with interstitial H atoms in the hcp lattice i.e., the formation of bulk hydrides in the subsurface layers. Rare earth hydrides have been the subject of a comprehensive experimental and theoretical study by Weaver, Peterman and co-workers [146 - 155] and no features resembling the SODS have been observed. Their photoemission results for YH_2 are shown in fig. 5.9.

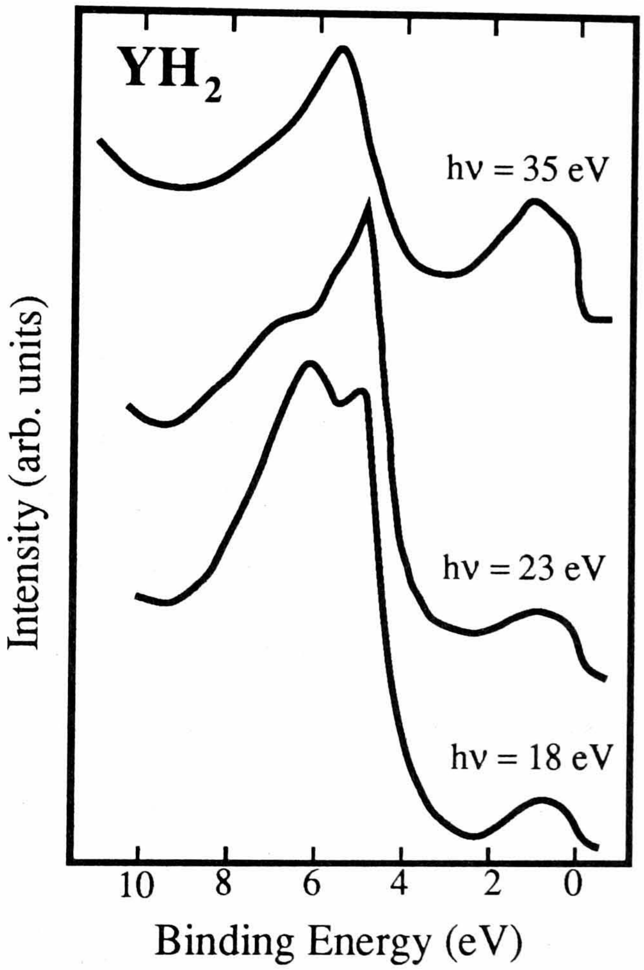

Fig. 5.9 UPS spectra of YH_2 (after Weaver *et al.* [153]

Note in particular that as the photon energy is increased towards 40 eV, the spectra begin to closely resemble fig. 4.9 (b). Baptist *et al.* [156] attempted to explain the SODS in terms of hydrogen contamination as they observed a SODS on a supposedly polycrystalline surface.

They thus argued that the SODS could not be a feature of an ordered (0001) surface, and must be due to hydrogen contamination, although they presented no data which supported this. That their argument was fundamentally flawed is indicated by their observation of a hexagonal LEED pattern from their "polycrystalline" sample. Since the SODS is associated with hexagonal order it follows that a SODS might be expected on such a surface. Fig. 4.9 (b) shows that the SODS is in fact quenched by hydrogen contamination, and given the similarity already noted between this spectrum and those from YH_2 provides further evidence that the SODS is not a hydride feature. One final contaminant possibility is Ar since this is used in the cleaning process. Ar^+ bombardment attenuates the SODS and gives an extra peak at ~ 6 ev binding energy, but ordered rare earth - Ar structures produced on annealing might produce peaks at higher energies. However this explanation suffers from the same problem as the ordered molecular adsorbate i.e. no extra LEED spots, and additionally there is no Ar visible in XPS or AES of clean, ordered (0001) surfaces. It is difficult to see how a level of Ar contamination invisible to AES / XPS (< 1 at.%) could be responsible for a peak as intense as the SODS.

Barrett and Jordan [23] suggested that the SODS might be due to a many body effect, involving the presence of an unoccupied surface state. Their reasoning was that since their were no one-electron states at that binding energy it must be a many body effect, since it was a surface feature therefore a surface state must be involved and since they did not identify any occupied surface states the surface state must be unoccupied. In fact, as will be shown in chapter 6, peak *c*, which always occurs with the SODS, is probably a (one-electron) surface state. The coincidence of the maximum in hν dependence shown by the *4p* / *5p* levels, the SODS and peak *c* suggests that it is at least plausible that the SODS may be due to the autoionisation decay of a *4p* core hole (or *5p* in the Lanthanides), giving rise to a satellite of peak *c*, but as yet no mechanism by which this could occur has been proposed. The SODS remains an enigma.

5.2 hcp $(11\bar{2}0)$ surfaces

In contrast to the case for hcp rare earth (0001) surfaces there has been only study of a $(11\bar{2}0)$ surface prior to this work – a qualitative LEED and ARUPS study of Y$(11\bar{2}0)$ [24]. The cleaning procedure used was as described in chapter 4, but the resulting surface structure was found to be temperature dependent. After a 'natural' cool from annealing LEED showed the rectangular pattern with missing spots characteristic of the $(11\bar{2}0)$-(1×1) structure (fig. 5.10). However if the sample was cooled slowly to room temperature LEED showed a twelve-fold pattern (fig. 5.11), which the authors interpreted as being the superposition of two hexagonal patterns, one rotated by $\pi/2$ with respect to the other. It thus appeared that the reconstructed surface comprised domains having internal hexagonal structure in two possible orientations with respect to the underlying (ideal) crystal structure. This implies that the collapse of the open $(11\bar{2}0)$ structure was equally probable along either of the two orthogonal directions [0001] and $[10\bar{1}0]$. No substrate spots were seen, indicating that the structure was homogeneous over the full sampling depth of the LEED beam. The ARUPS spectra from this surface were found to be very similar to those from Y(0001) [23] and the authors concluded that the $(11\bar{2}0)$ surface had reconstructed into close packed domains with a structure very similar to that of a (0001) surface. They also found that a reversible phase transition between the two structures (i.e. ideal and reconstructed) occurred at 610 K, which was monitored using the SODS intensity as an order parameter (fig. 5.12). Y$(11\bar{2}0)$ surfaces have also been used as substrates for the growth of rare earth superlattices (see chapter 2). In one such study [157] the authors reported that the substrate underwent a temperature dependent reconstruction to a close packed structure. No further details regarding the clean structure were given but the authors noted that epitaxial growth of thick Y films on the Y$(11\bar{2}0)$ substrate gave Bragg X-ray diffraction patterns as good as the substrate alone, although RHEED still showed reconstructed surfaces. This implies that the buried surface reverts to the ideal structure and only the surface remains reconstructed. Unfortunately as X-ray diffraction is a bulk technique and LEED is very

Fig. 5.10 LEED pattern from the ideal Y(11$\bar{2}$0) surface, beam energy 50 eV (from Barrett *et al.* [24])

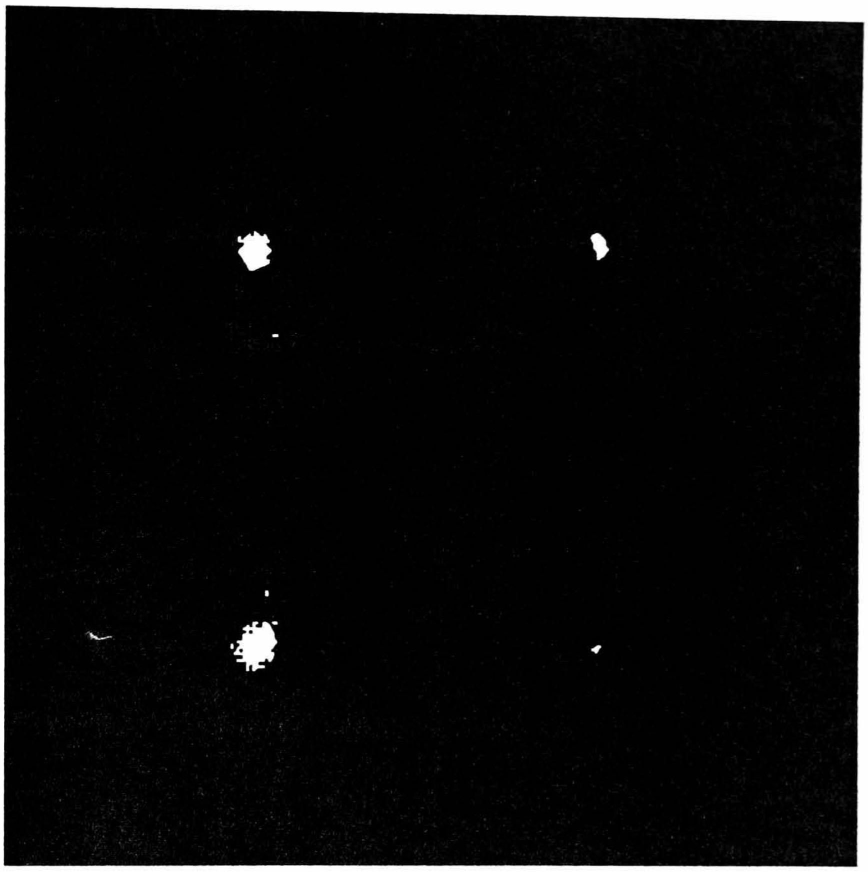

Fig. 5.11 LEED pattern from the reconstructed Y(11$\bar{2}$0) surface, beam energy 50 eV (from Barrett *et al.* [24])

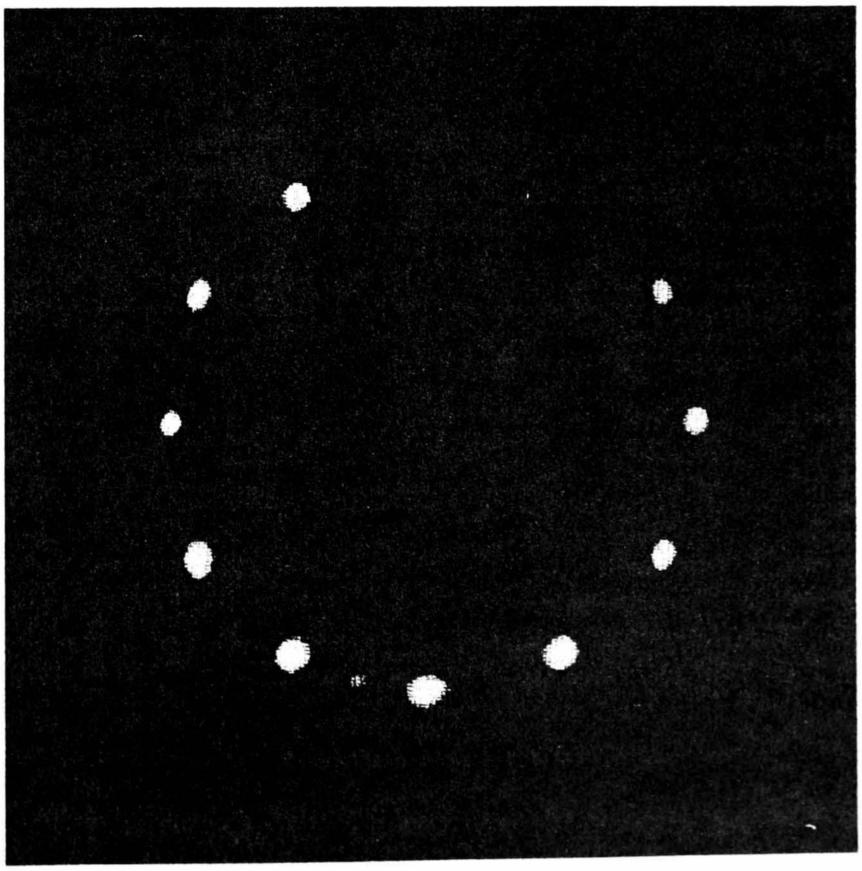

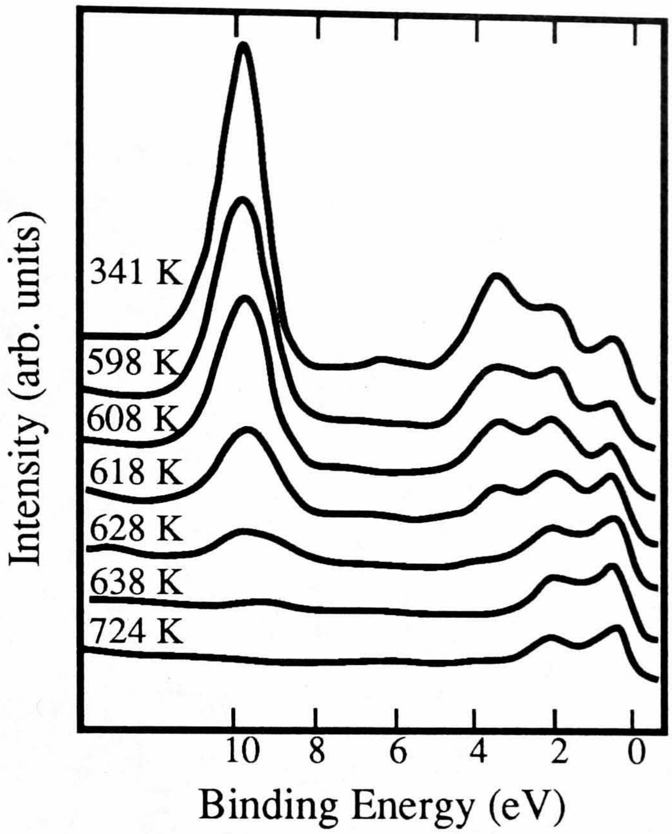

Fig. 5.12 ARUPS spectra from Y(11$\bar{2}$0) as a function of temperature (after Barrett *et al.* [24])

surface sensitive the extent of the reconstructed layer cannot be determined. In order to determine whether this type of reconstruction is characteristic of all hcp rare earth (11$\bar{2}$0) surfaces similar studies were performed for the (11$\bar{2}$0) surfaces of Ho and Er, which have lattice parameters close to those of Y.

5.2.1 Ho(11$\bar{2}$0) and Er(11$\bar{2}$0)

Cleaning procedures for Ho(11$\bar{2}$0) and Er(11$\bar{2}$0) were as described in chapter 4 i.e., the same as Barrett *et al.* [24] used for Y(11$\bar{2}$0). The LEED patterns obtained at room temperature from Ho and Er immediately after a cleaning cycle are shown in figure 5.13. The patterns, clearly six-fold symmetric, are very similar to those those obtained from (0001) surfaces. As for the Y(11$\bar{2}$0) reconstruction there are no visible diffraction spots that could be attributed to the substrate. Thus, as is the case for Y, the six-fold symmetry of the reconstruction must extend over many atomic layers; a LEED beam energy of 50 eV

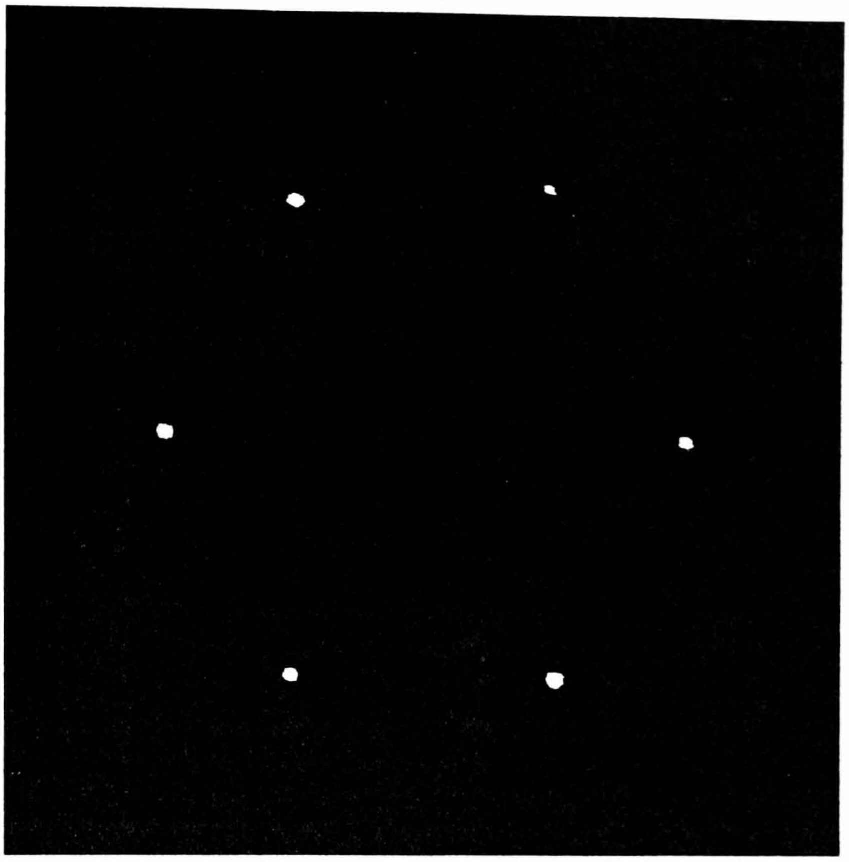

Fig. 5.13 LEED patterns from the $(11\bar{2}0)$-(7 × 1) surfaces of Ho [above] and Er [below], beam energy 50 eV

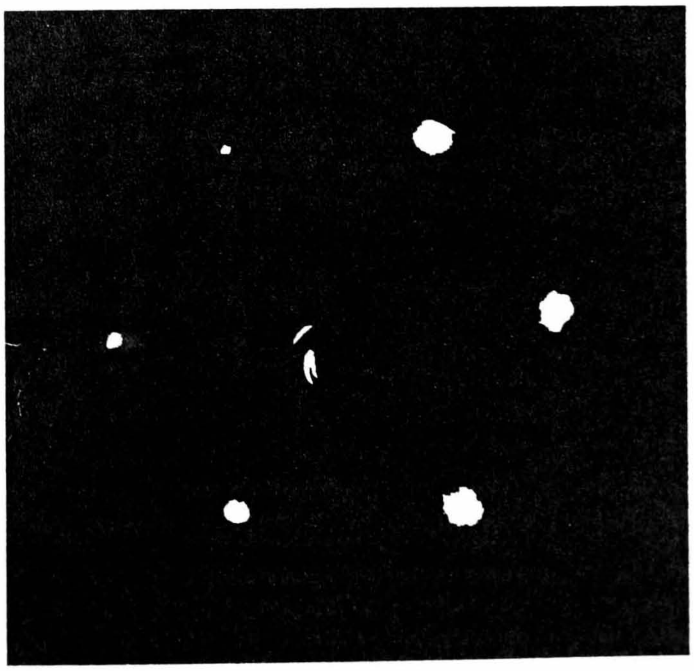

(mfp ~ 0.7 nm) and a layer separation ~ 0.35 nm require a reconstruction depth of at least five layers in order that substrate spots are not observed. A visual comparison between the Ho($11\bar{2}0$) diffraction pattern and that of Ho(0001) at the same beam energy indicated that the lattice parameter of the reconstructed surface was within a few percent of that of the (0001) surface.

The LEED patterns from Ho and Er do not show any sign of a second set of hexagonal spots, suggesting that the collapse of the unit cell occurs exclusively along the [0001] direction for both samples. Figure 5.14 shows the orientation of the reconstructed surface lattice with respect to that of the ideal ($11\bar{2}0$) surface. It can be seen that the magnitude of the lattice vectors of the two structures match in the [$10\bar{1}0$] direction of the ideal lattice, and have the ratio c/a in the [0001] direction. For Y, Ho and Er the c/a ratio is 1.570 ± 0.001, which is very close to the integer ratio $11/7$ (= 1.571). Thus, for the reconstruction of the Ho and Er surfaces, 11 unit cells of the surface lattice match almost exactly to 7 unit cells of the ideal ($11\bar{2}0$) structure beneath, giving the Wood notation ($11\bar{2}0$)-(7 × 1) for the reconstruction. For the other domain orientation seen on Y($11\bar{2}0$) [24] the lattices are incommensurate and no such notation can be applied to the Y reconstruction. It is presumably the incommensurate nature of this orientation that prohibits the surfaces of Ho and Er from exhibiting such a two-domain reconstruction. Relating the surface structure to the underlying ideal structure has some meaning if the two are in close proximity, as is the case for all the surface reconstructions observed on cubic metals [158]. However, for the reconstructions described here, the large increase (~60%) in atomic area density from the bulk to the surface means that it is likely that the reconstruction is accommodated over many atomic layers. Thus, the commensurate relationship between the surface lattice parameters and those of the bulk lattice, giving rise to the (7 × 1) notation, may be only coincidental.A further substantial difference between the reconstructions reported here and that of Y concerns their time dependence. The ideal Y($11\bar{2}0$) structure could be obtained by a natural cool, while the reconstruction required a slow cool. By contrast, the reconstructions of Ho and Er appear to be spontaneous; the observed structure is independent of the rate at

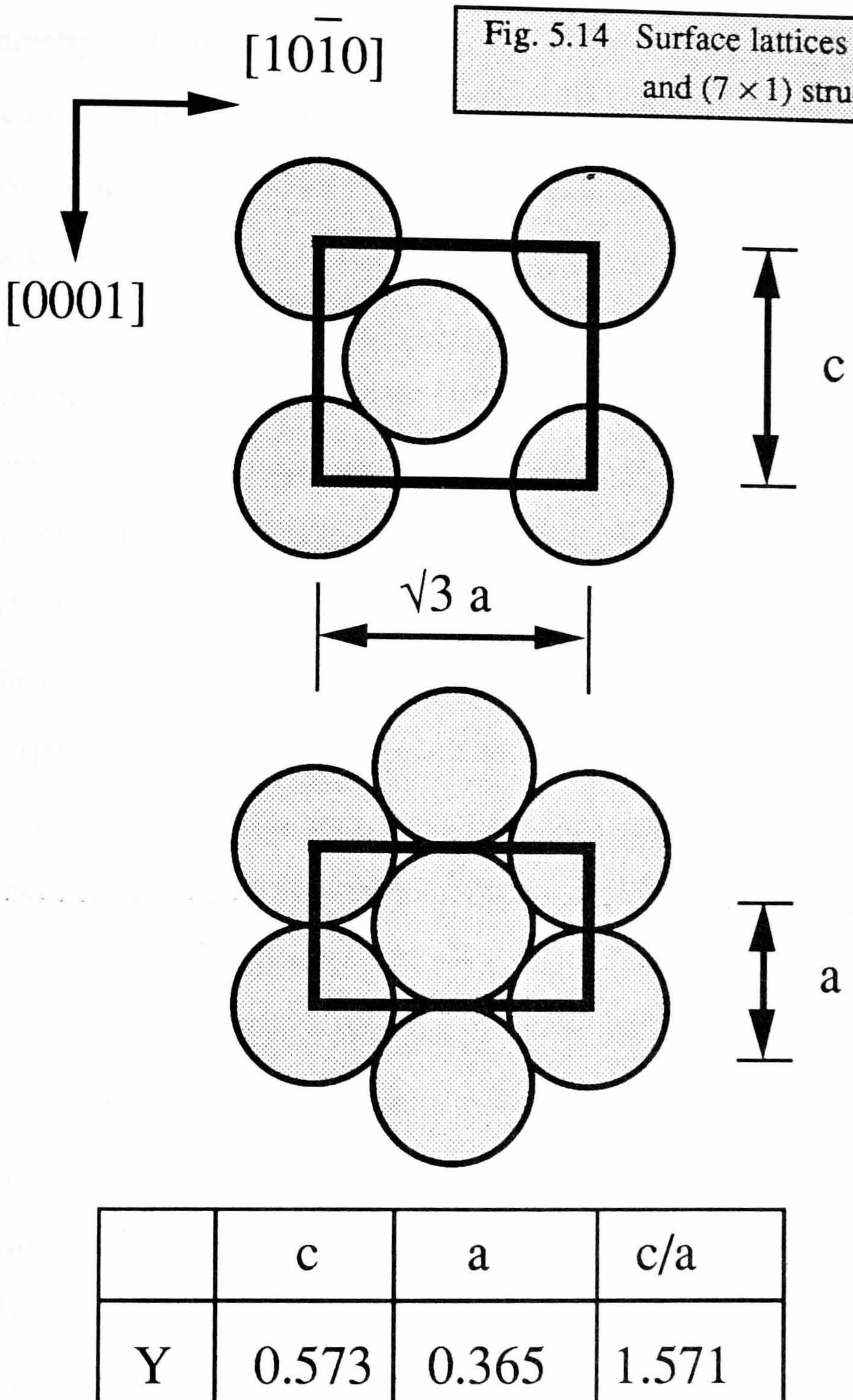

Fig. 5.14 Surface lattices of the $(11\bar{2}0)$-(1×1) and (7×1) structures

	c	a	c/a
Y	0.573	0.365	1.571
Ho	0.562	0.358	1.570
Er	0.559	0.356	1.569

which the samples are cooled. It was therefore not possible to obtain the ideal $(11\bar{2}0)$ structure for either Ho or Er, which from the point of view of learning about bulk electronic structure is somewhat inconvenient.

As LEED indicated that the $(11\bar{2}0)$-(7×1) surface has a structure of the same symmetry and similar lattice constant as a (0001) surface it is to be expected that the ARUPS spectra from these two surfaces are likely to have features in common. In fact the normal emission spectra from Ho$(11\bar{2}0)$-(7×1) and Ho(0001) are virtually indistinguishable, as can be seen from figure 5.15. The spectra from Ho$(11\bar{2}0)$ showed essentially no change (except for phonon broadening of the peaks) as the samples were heated from room temperature up to ~ 1100 K (the maximum attainable temperature of the resistive heating stage). This is in marked contrast to the temperature-dependence of the spectra from Er$(11\bar{2}0)$ shown in figure 5.16. The most obvious change with temperature is the disapperance of the SODS, which for the Y$(11\bar{2}0)$ reconstruction was indicative of the surface reverting to its ideal structure. However, in the case of Er, the disappearance of the SODS could also be interpreted as a roughening or 'amorphising' of the surface, as this too would reduce the degree of hexagonal order. These two alternative explanations cannot be distinguished using LEED because of the elevated temperature of the reconstruction transition. For both Ho and Er, unlike the situation for Y, the LEED pattern of the ideal $(11\bar{2}0)$ surface could not be observed as the diffraction pattern from the reconstructed surfaces persisted up to the point at which the pattern was rendered invisible due to the glow from the samples (at $T \sim 800$ K). The ARUPS spectra from Er$(11\bar{2}0)$ at high temperature ($T > 1000$ K) have most of their intensity weighted close to E_F (apart from the multiplet 4*f* peaks spread over the binding energy range 5-11 eV) but this observation is insufficient to distinguish between an ideal $(11\bar{2}0)$ and an amorphous (or polycrystalline) surface. Spectra from the ideal Y$(11\bar{2}0)$ surface have their most intense features within ~ 2 eV of E_F (see fig. 5.12), and given the similarity between the bandstructures of the hcp rare earths (see chapter 3) it follows that the same would almost certainly apply to the ideal $(11\bar{2}0)$ structures of Ho and Er.

Fig. 5.15 Normal emission ARUPS spectra from the three principle faces of Ho
hv = 40 eV, incident angle 30°, p-polarised radiation

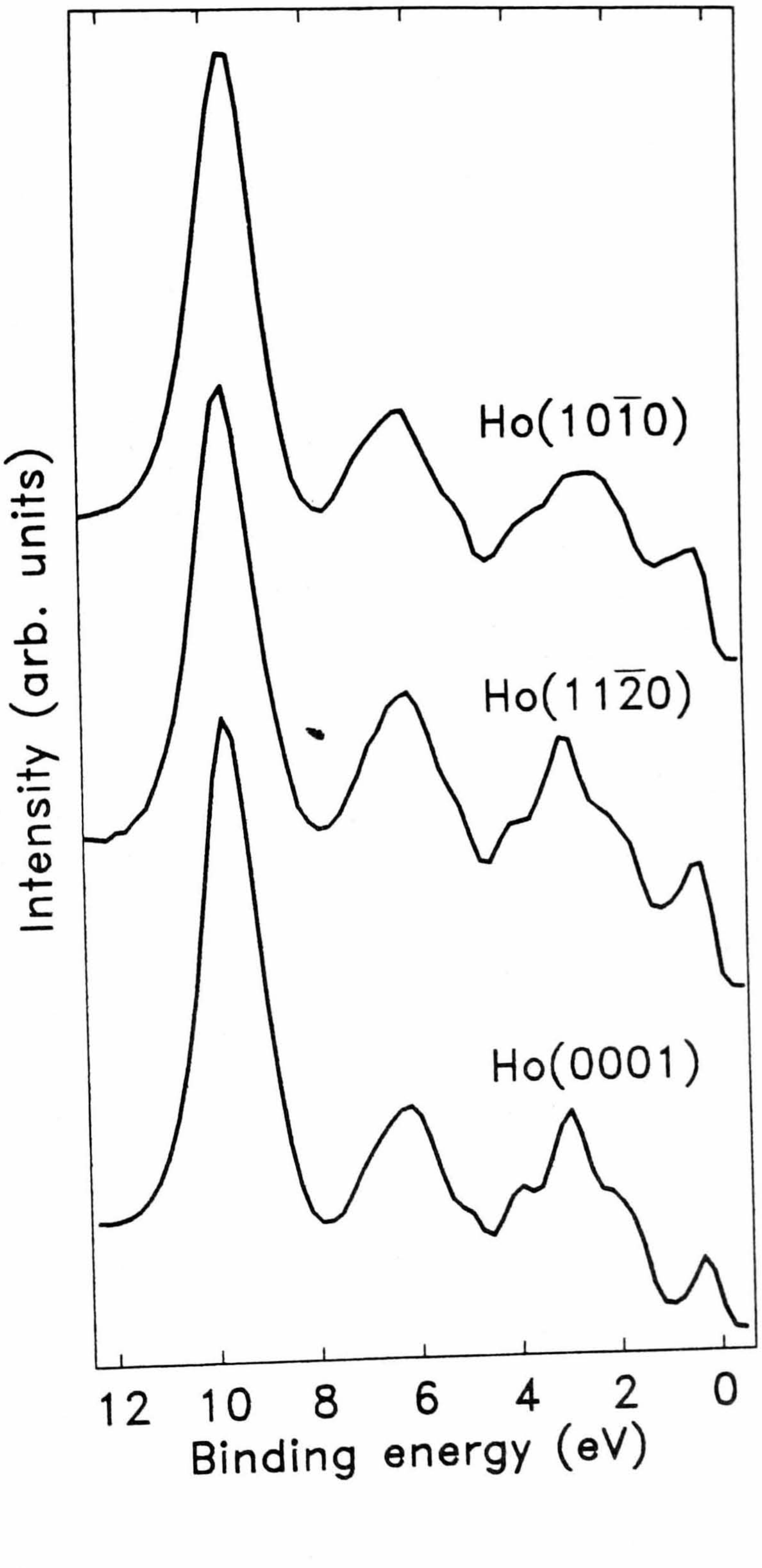

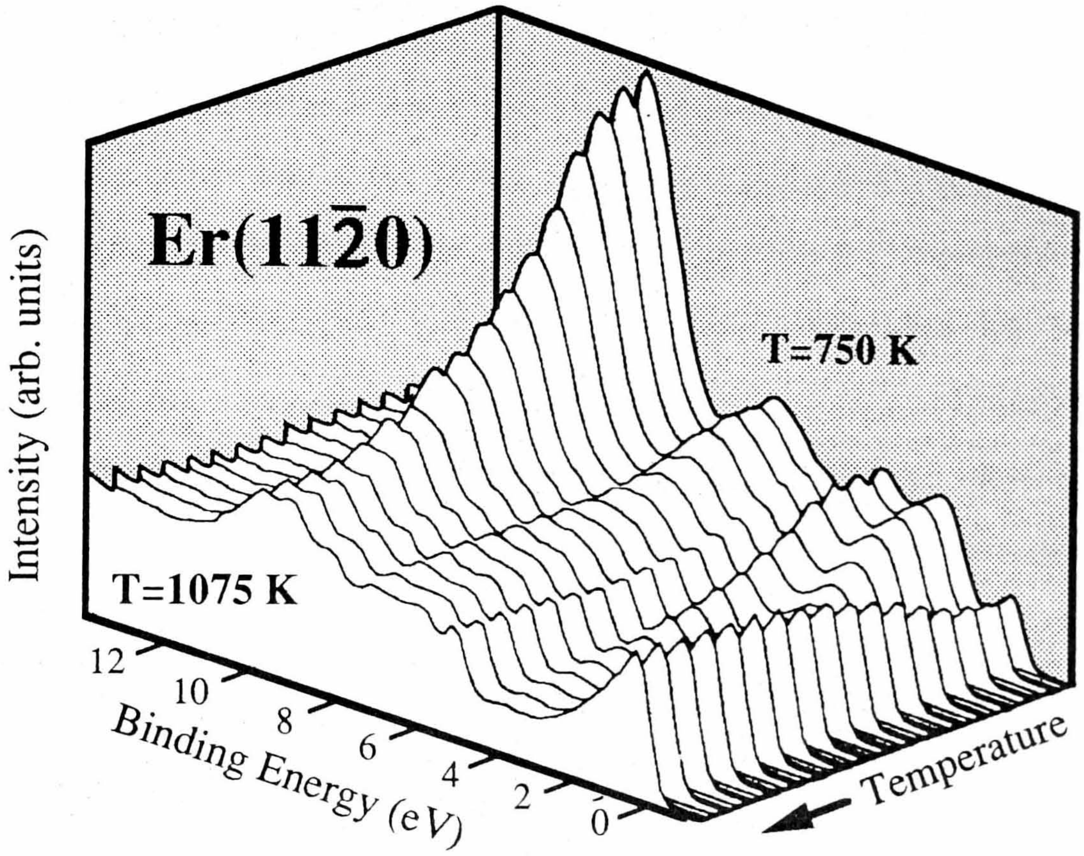

Fig. 5.16 ARUPS spectra from Er(11$\bar{2}$0) as a function of temperature

However the (occupied) densities of states of Ho and Er [see fig. 3.9 (d) and (e)] also have most of their weight within 2 eV of E_F.

As the binding energy of the 4*f* electrons in Er cover the range 5-11 eV (see fig. 3.2), some of the corresponding peaks overlap the SODS (at 9.6 eV) and so the intensity of the photoemission at that energy will not be a reliable indicator of the state of the surface reconstruction. (This was not a problem for Y (fig. 5.12) which showed a flat background in the region of 10 eV binding energy at temperatures above the reconstruction temperature). For Er, a more representative quantity to use is the integrated photoemission intensity between suitable energy limits either side of the SODS. The *integrated* intensity of the 4*f* electron emission can be assumed to be independent of the surface structure and so will give rise to a contribution to this quantity that will vary only slightly with temperature due to phonon broadening. Analysing the Y data of fig. 5.12 in a similar way allows direct comparison of the temperature dependence of the Y and Er reconstructions, as shown in figure 5.17. The reconstruction temperature T_R, defined as the temperature at which the integrated intensity has fallen by one half of its total change, is found to be 875 ± 25 K for Er (c.f. $T_R = 610 \pm 10$ K for Y). The larger uncertainty in the reconstruction temperature for Er is due to the increasing phonon broadening of the 4*f* peaks with temperature. The latter results in a decreasing contribution to the measured integrated intensity, which is evident in the Er curves of fig. 5.17 as a non-zero gradient at high temperatures. Apart from the effects of the 4*f* emission in Er, the qualitative shape of the curves, including the dip for increasing (but not decreasing) temperature at $T \sim T_R$ - 100K, is the same for both elements. Its presence in the Er data indicates that the surface is undergoing a transition similar to that of Y, i.e., a reconstruction rather than surface roughening.

As already shown in figure 5.15, the normal emission spectra from Ho(11$\bar{2}$0)-(7 × 1) and Ho(0001) are virtually indistinguishable at a photon energy of 40 eV. A more critical test of the similarity between the structure of these two surfaces involves comparison of the valence band (0-5 eV binding energy) spectra taken over a range of emission angles in order to probe

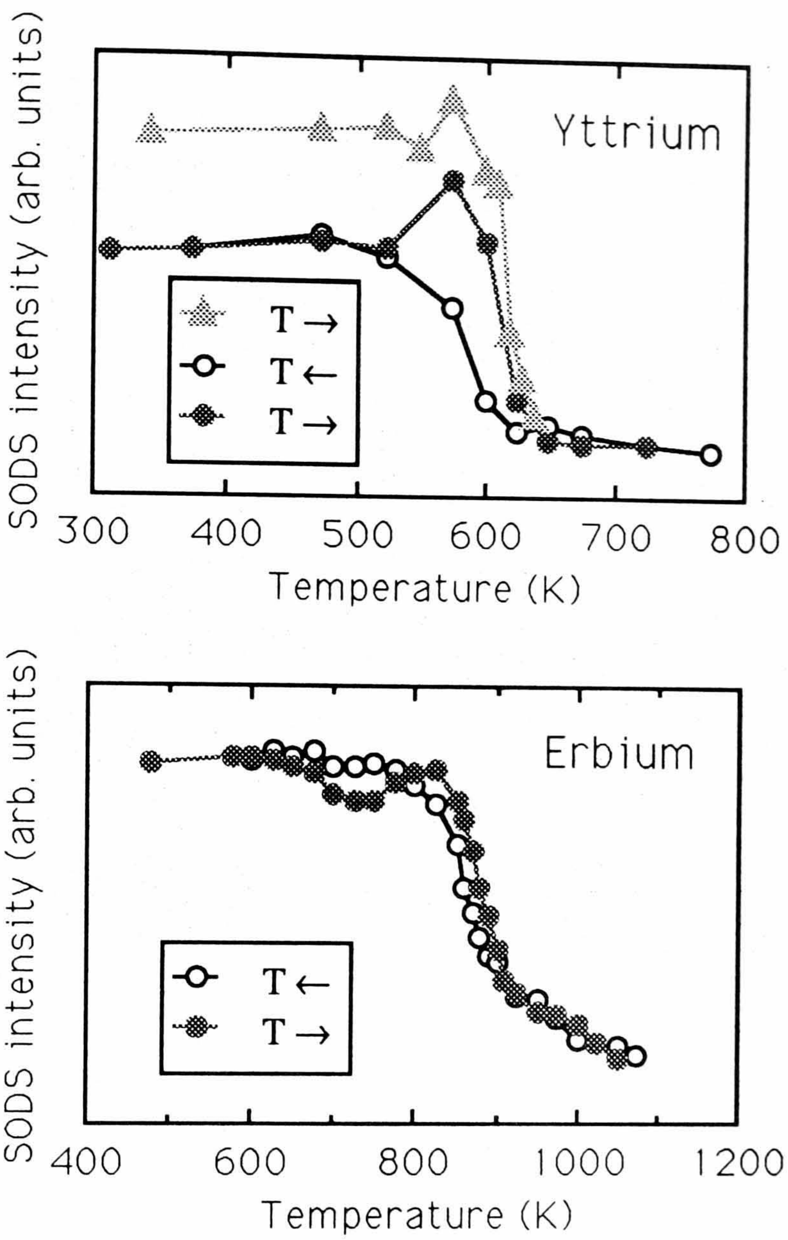

Fig. 5.17 Comparison of the integrated SODS intensity as a function of temperature for Er(11$\bar{2}$0)-(7 × 1) and the earlier Y(11 $\bar{2}$0) reconstruction [24]

various regions of the surface Brillouin zone. These spectra are shown in fig. 5.18. A detailed analysis of the Ho(0001) spectra can be found in chapter 6, but it can be seen that at very least the electronic structure, and by implication the geometric structure, of these two surfaces is extremely similar. A more rigorous comparison will have to wait until quantitative LEED studies of the (11$\bar{2}$0)-(7 × 1) and (0001) structures are performed, but at present the available evidence suggests that these two structures are identical.

Fig. 5.18 Off-normal emission ARUPS spectra from Ho(0001) and Ho(11$\bar{2}$0)-(7 × 1) hν = 40 eV, incident angle 55°

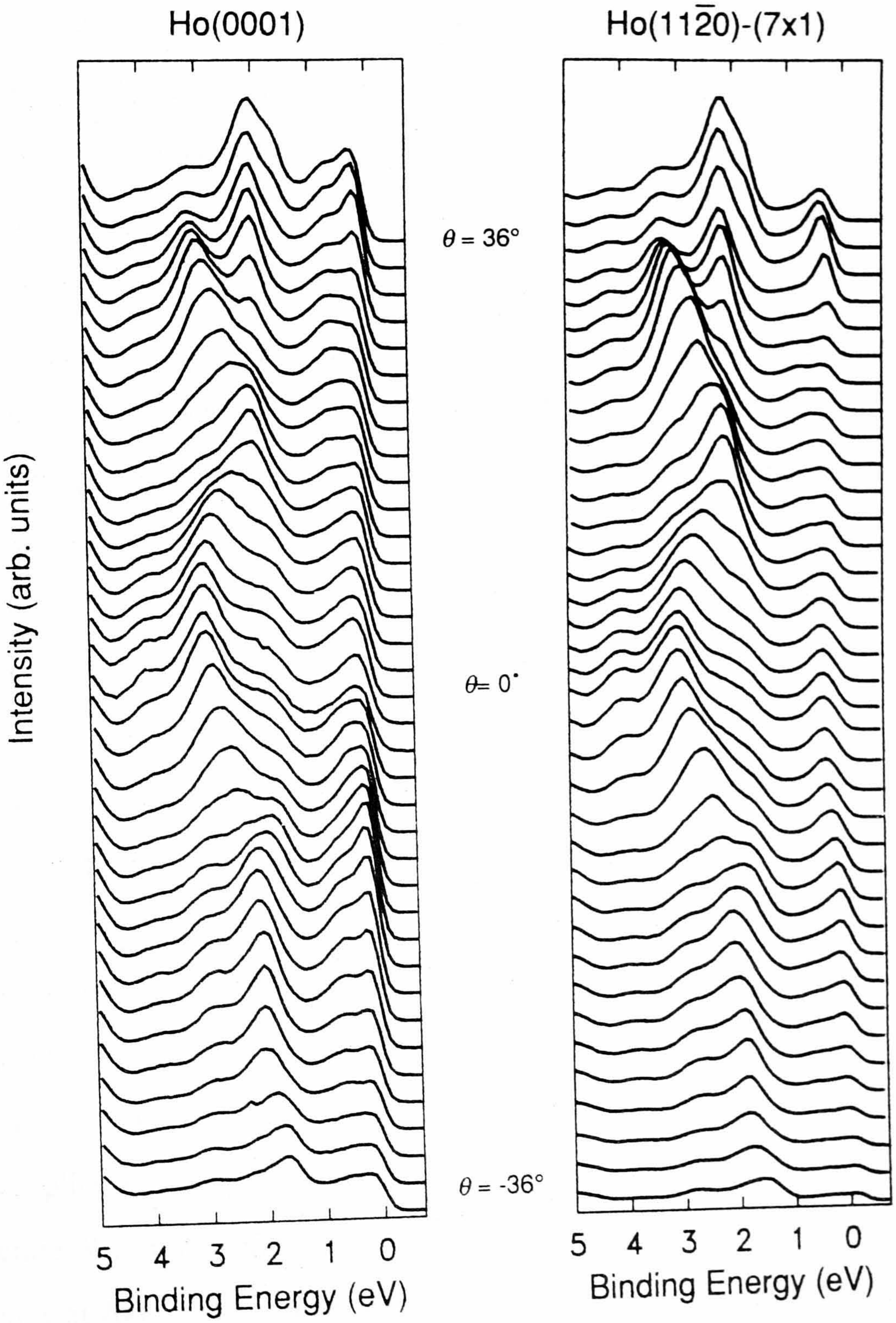

5.2.2 Y(11$\bar{2}$0)

In the light of the differences between the surface reconstruction of Y(11$\bar{2}$0) [24] and those of Ho(11$\bar{2}$0) and Er(11$\bar{2}$0), the study of Y(11$\bar{2}$0) was repeated. In order to determine whether the two-domain structure is a characteristic of the Y(11$\bar{2}$0) reconstruction or is dependent on the sample preparation, a new sample was cut from the same high-quality single crystal boule as the original sample. The experimental equipment and *in situ* cleaning procedure used were as described in chapter 4. Any difference in behaviour between the two Y samples can be ascribed to the different extent of surface defects – slight misalignment of either surface with respect to the crystallographic axes (producing terraces of steps), surface roughness, or levels of surface contamination.

The LEED pattern from the new Y(11$\bar{2}$0) sample was found to be six-fold symmetric (figure 5.19), in contrast to the 12-fold symmetric pattern observed previously. In common with the results for Ho(11$\bar{2}$0) and Er(11$\bar{2}$0) the orientation of the LEED pattern indicated that the (11$\bar{2}$0) surface unit cell had collapsed uniaxially along the [0001] direction to form the close-packed (7 × 1) structure.

The photoemission spectra were identical to those of the 12-fold reconstruction [24], which is not surprising as at normal emission the two six-fold domains should give identical spectra. Fig. 5.20 shows the integrated SODS area against temperature curve for the present study of Y(11$\bar{2}$0); part of the corresponding data for the previous study of Y(11$\bar{2}$0) [24], and for Er(11$\bar{2}$0) are shown for comparison. The transition occurs in the region of ~ 600-800 K, with the mid-point at 700 ± 25 K (*c.f.* 610 ± 10 K in the previous study). The higher transition temperature implies a higher stability for the (7 × 1) reconstruction compared to the two-domain structure. When the latter was destroyed by heating there was no sign of the (7 × 1) phase remaining at 700 K. This implies that the deconstruction of incommensurate phase at ~ 610 K induced the premature deconstruction of the (7 × 1) phase at a temperature ~ 100 K below its nominal transition temperature. Due to the large change of surface atom density

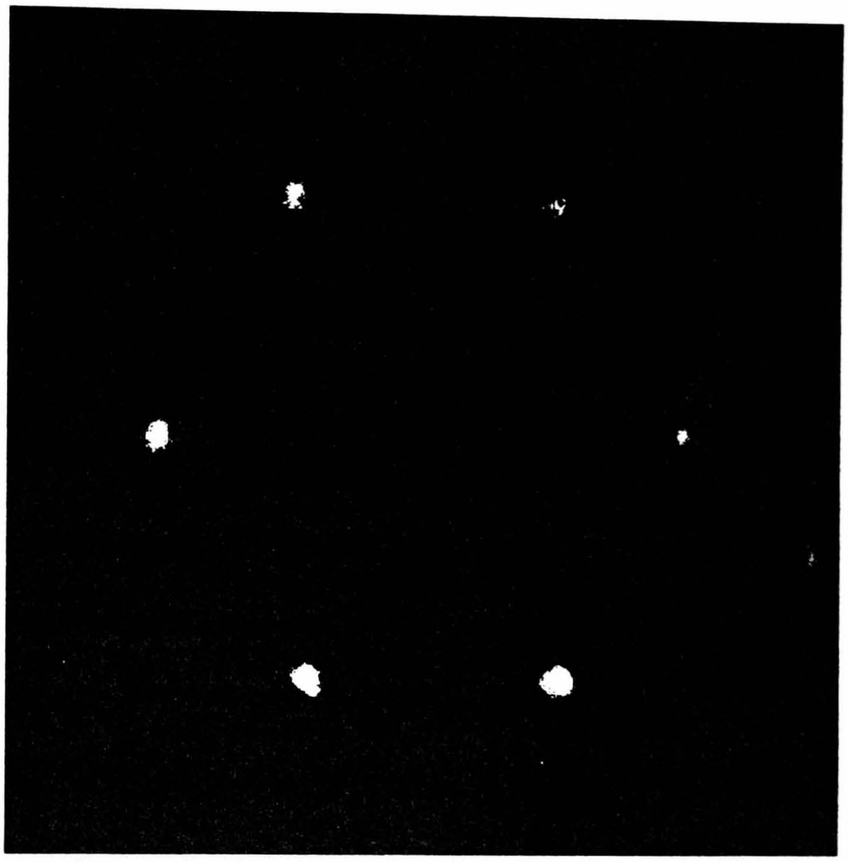

Fig. 5.19 LEED pattern from Y(11$\bar{2}$0)-(7 × 1), beam energy 50 eV

accompanying the rearrangement from the reconstructed to the ideal surface structures, it is perhaps not surprising that the two domains could not revert to the ideal structure independently.

Fig. 5.20 Integrated SODS curves for Y and Er

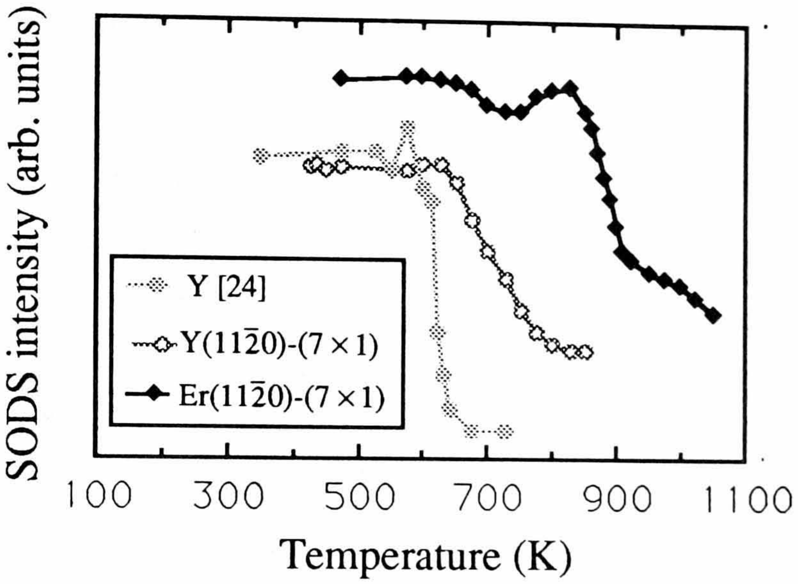

The shape of the curve of SODS intensity versus temperature for the present study of Y(11$\bar{2}$0) is qualitatively closer to that displayed by Er(11$\bar{2}$0) than in the previous study of Y [24]. This may indicate that at high temperatures the surface does not have the ideal bulk termination structure (in contrast to the earlier results [24]), as the spectra from ideal (11$\bar{2}$0) surfaces look very similar to those from disordered surfaces. As was found for the Ho and Er reconstructions the ideal (11$\bar{2}$0) structure was not obtained after a natural cool, the (7 × 1) reconstruction occurring spontaneously after a natural cool from annealing.

In summary, the surface reconstruction of Y(11$\bar{2}$0) conforms to the behaviour found for the (11$\bar{2}$0) surfaces of the other rare earth metals Ho and Er. This suggests that the earlier study of the Y reconstruction was influenced by the presence of surface defects, the most likely of which were terraces of steps formed due to the surface not being exactly perpendicular to the [11$\bar{2}$0] direction; Laue x-ray diffraction indicated that the surfaces of both Y samples were within 1° of (11$\bar{2}$0). If the terraces are oriented in a particular direction, they may act as nucleation regions for the incommensurate reconstruction; as the reconstruction to a close-packed structure requires a ~ 60% increase in atom density at the surface, it seems likely that steps must influence the formation of the reconstructed domains. Conversely, it is possible to interpret the results of these studies of $(11\bar{2}0)$ surface reconstructions as indicating that surface defects (on the Y sample of this work, Ho and Er) *inhibit* the formation of an incommensurate domain. This is thought to be less likely as this interpretation would require that all of these samples have defects with the required surface structure. An alternative explanation to steps assumes that the level of contamination influences the formation of domains. As the surfaces of bulk single crystal samples of rare earth metals always have a residual contamination level of a few atomic percent (usually C and O), this is a possibility that cannot be ruled out.

5.3 Other surfaces

Other than the studies already mentioned there have been only four surface structure determinations for any rare earth surface. Two of these were qualitative LEED analyses of the Ce(001) surface (21, 22), both performed as sample preparation for ARUPS measurements. Both papers reported (1 × 1) structures, i.e., bulk terminations, although neither showed any LEED patterns. There has been one report – an abstract of a paper presented at a conference [137] - of an attempted LEED study of Tb$(10\bar{1}0)$. The authors reported that this surface was particularly difficult to clean, and stable LEED patterns could not be obtained. However (7 × 1) and (8 × 1) patterns were at times observed, but whether this indicates the kind of reconstructions seen on hcp $(11\bar{2}0)$ surfaces, or merely superlattice spots due to contamination is unclear. This abstract was not followed by a full paper, suggesting that the contamination problems were never overcome. For this work attempts were made to clean the $(10\bar{1}0)$ of Ho, particularly to compare the ARUPS results with those from the other two principal faces of Ho. This proved much more difficult than was found for either the (0001) or $(11\bar{2}0)$ surfaces, or indeed of any of the other rare earths studied. The ideal $(10\bar{1}0)$ structure (fig. 5.1) is very open, providing large hollow sites which are particularly inviting to contamination. Hexagonal LEED patterns were observed however, although they were rather poor and deteriorated rapidly with time. A normal emission ARUPS spectrum is shown in fig. 5.15. The spectrum shows a SODS - to be expected given the hexagonal LEED pattern - but the valence band lineshape is rather different from, though clearly related to, those from the (0001) and $(11\bar{2}0)$-(7 × 1) surfaces. It is possible that the $(10\bar{1}0)$ surface was also attempting to reconstruct to a (0001) structure, but was being inhibited by adsorbed contaminants. It was not possible to perform detailed off-normal measurements to compare with those of fig. 5.18 as the sample contaminated too quickly. These results were obtained on one particular 'run', and as yet have not been reproduced as it has proven impossible to re-clean this sample. These results must therefore be regarded as extremely provisional. However the intriguing possibility remains that all three principal faces of hcp rare earths form the same surface structure.

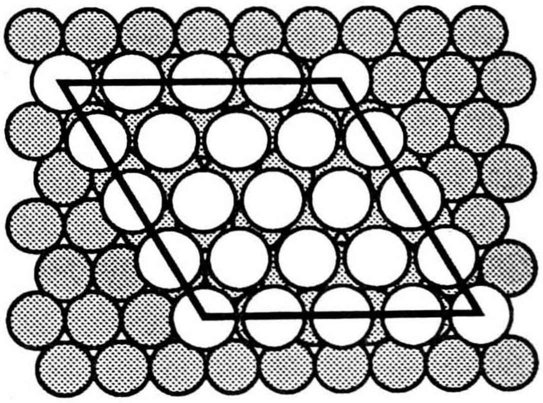

Fig. 5.21 Structure of Sm(0001)-(5 X 5)

The most interesting of these four reports concerns the results of Stenborg *et al.* for Sm(0001) [159], epitaxially grown on a Mo(110) substrate. The structural properties of Sm are unique. It has the complex structure shown in fig. 2.3 and in addition has a trivalent bulk with a divalent surface. These divalent surface atoms would be expected to be somewhat larger then their bulk counterparts and for many years it was not at all clear what surface structures Sm would exhibit. Growth of single crystals of Sm is close to impossible [94] as stacking faults easily occur in the 13 layer unit cell. Epitaxial growth is a more tractable route, but Stenborg *et* *al.* did not determine the stacking sequence so it is far from clear exactly what the bulk structure of their Sm crystal was. What they did find was that the divalent surface atoms formed a (5 × 5) overlayer relative to the bulk: the structure is shown in fig. 5.21, with the interatomic distance of the bigger divalent atoms being 25 % bigger than those of the bulk. Soft XPS spectra from this surface (fig. 5.22) clearly show the two sets of $4f$ multiplets from the $4f^4$ (surface) and $4f^5$ (bulk) ground state configurations.

Fig. 5.22 Soft XPS spectrum of Sm(0001) (after Stenborg *et al.* [159])

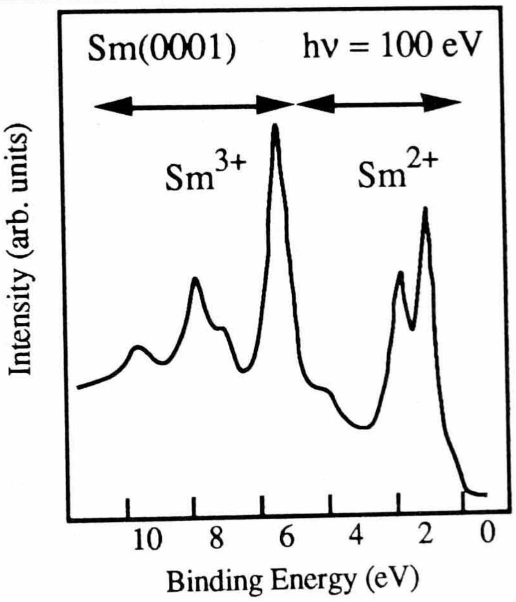

This is fascinating result, being both a unique example of a reconstruction and a dramatic example of mixed valence behaviour.

CHAPTER 6

KRIPES and ARUPS studies

The first ARUPS study of a rare earth metal was reported in 1983, by Himpsel and

Fig. 6.1 Normnal emission ARUPS spectra of Gd(0001) (after Himpsel and Reihl [20])

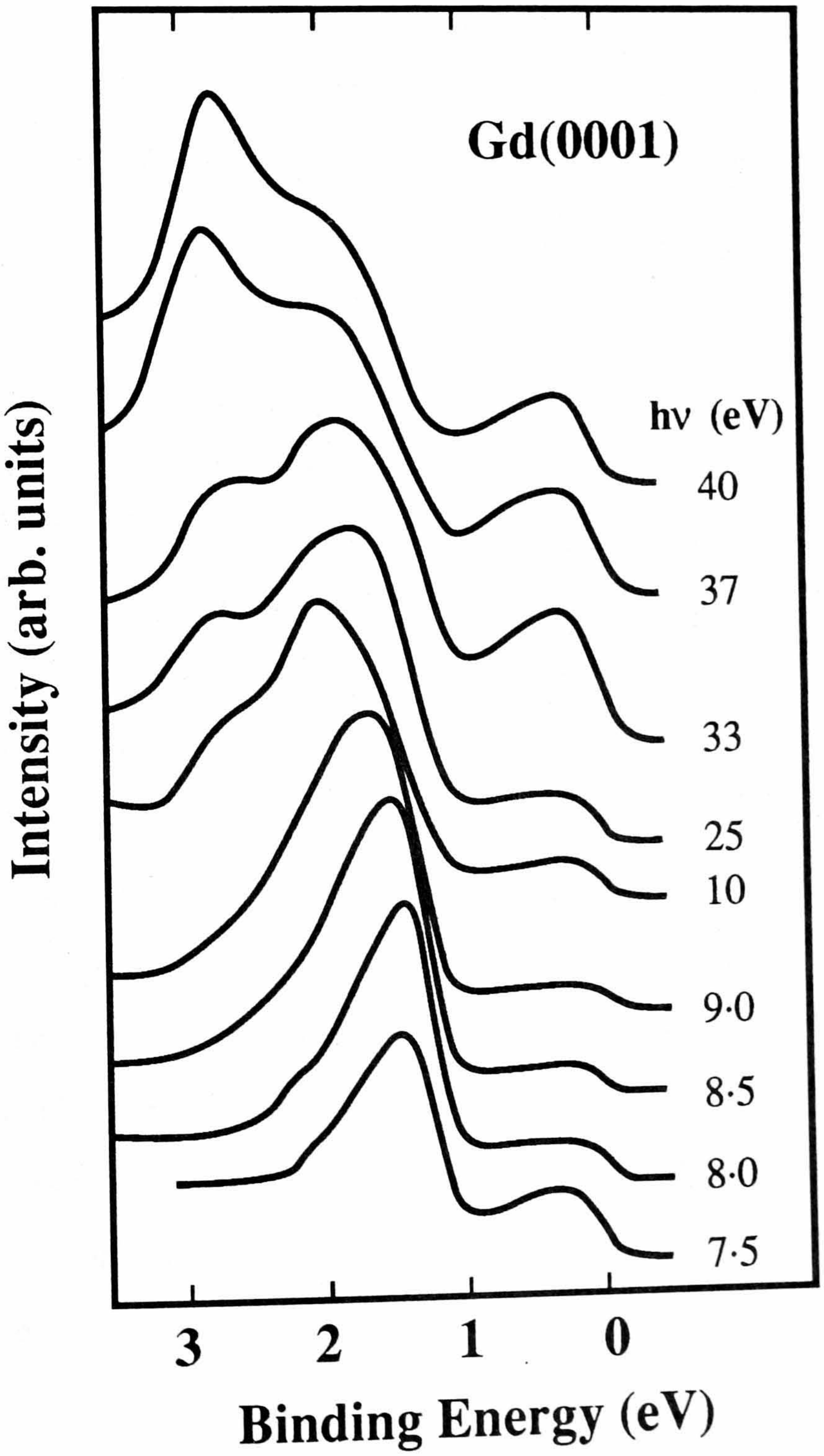

Reihl[20]. Their results, for Gd(0001) are shown in fig. 6.1. The amount of dispersion exhibited by the peaks in fig. 6.1 is rather small, and almost negligible for photon energies greater than 20 eV. Himpsel and Reihl attributed this to momentum broadening, a result of the short mfp of low energy electrons in rare earth metals. By comparison with the very early (non-relativistic) bandstructure of Dimmock and Freeman [68] they identified the peaks labelled *b* and *c* in fig. 6.1 as the Gd Γ_{4-} and Γ_{1+} critical points. The experimental results of Himpsel and Reihl were later confirmed by those of Jordan [138], although Jordan assumed that the valence band was exchange split and that peaks *b* and *c* corresponded to the spin-down and spin-up Γ_{4-} points respectively. Jensen and Wielickza [21] and Rosina *et al.* [22] have reported ARUPS studies of γ-Ce(001). The normal emission results, using different gases in a discharge lamp rather than a synchrotron, of Rosina *et al.* are shown in fig. 6.2. The peaks at ~ 0.2 and 2.0 eV correspond to emission from 4*f* derived states, the two peaks being due to differently screened final states. Rosina *et al.* also measured off-normal emission spectra at several different photon energies (their results for hν = 40.8 eV i.e. He II radiation are shown in fig. 6.3). In contrast to normal emission spectra from rare earths, off-normal spectra show pronounced dispersion and thus enable detailed band-mapping, although as the component of momentum normal to the surface is not conserved direct comparison with the calculated bands is not possible. Rosina *et al.* calculated the final states explicitly and showed that (i) for low photon energies the free-electron final state approximation produced very poor agreement with the calculated bands (fig. 3.18), and (ii) with calculated final states good agreement was found with the bands of fig. 3.18. This suggests two things. Firstly, as discussed in chapter 3, that the band model for the electronic structure of Ce may be valid. Secondly, and more important with respect to other rare earth ARUPS studies, the common free-electron final state approximation appears to be invalid for these heavy metals. This implies that photocurrent calculations will have a major role in interpreting ARUPS results from lanthanides, and in fact this has been the case.

Fig. 6.2 Normal emission ARUPS spectra from Ce(001) (after Rosina *et al.* [22])

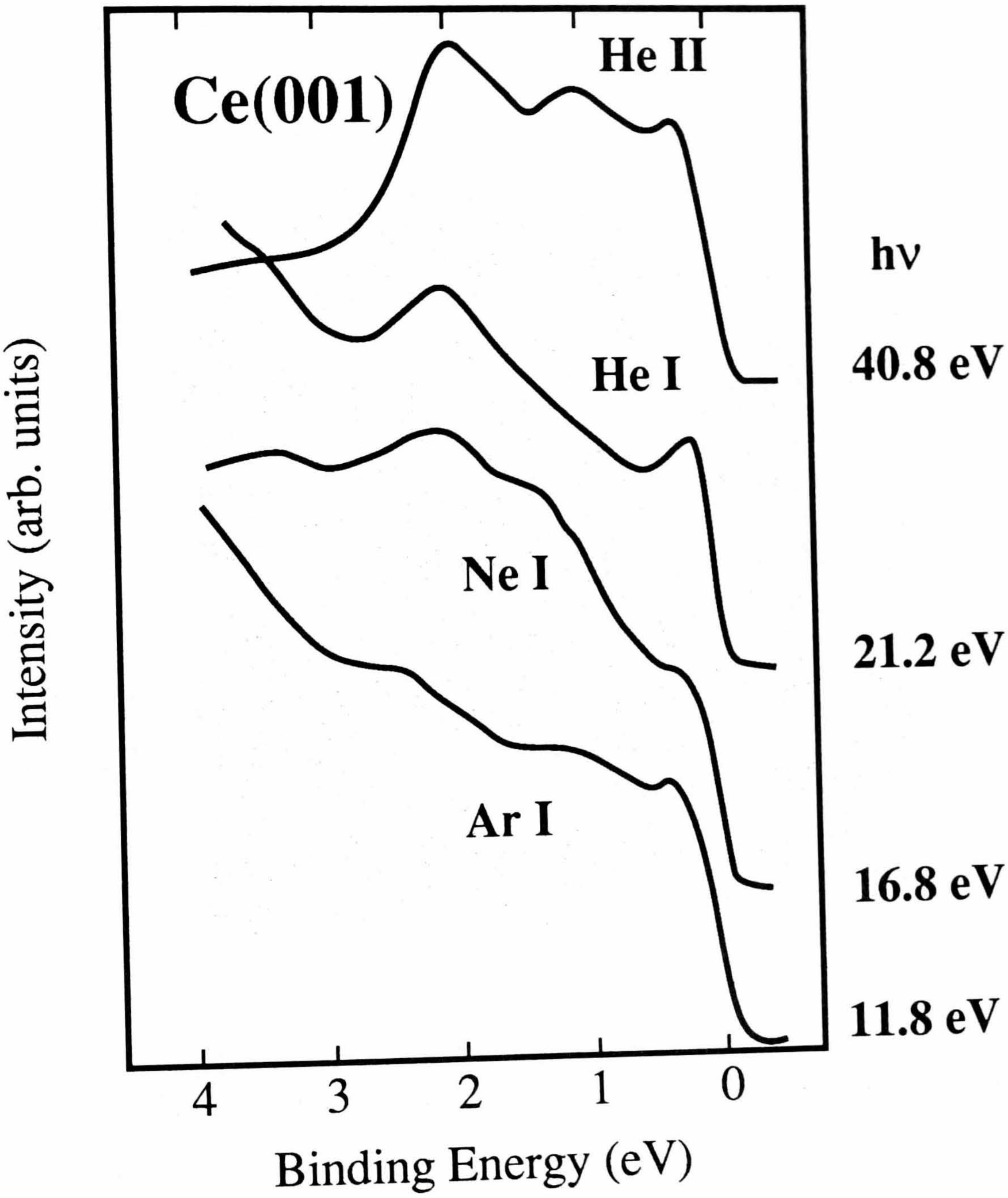

Fig. 6.3 Off-normal emission ARUPS spectra from Ce(001) (after Rosina *et al.* [22])

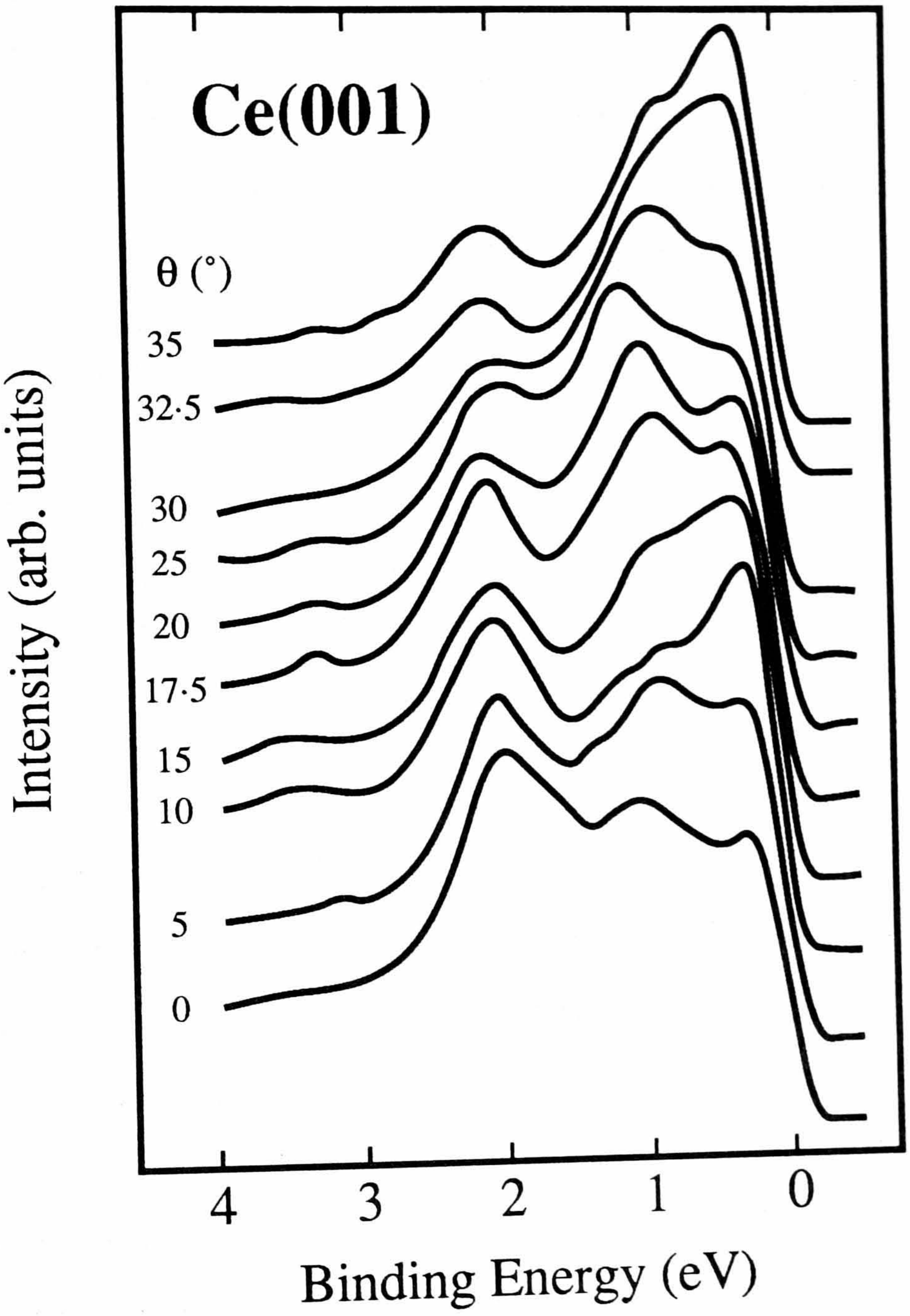

The first ARUPS study of a non-lanthanide rare earth - Y(0001) - was reported by Barrett and Jordan [23]: their results are shown in fig. 5.4. They were only able to fully account for peak *b*, which they identified as the Γ_{4-} critical point of the bulk bandstructure using photocurrent calculations employing a *bulk* yttrium potential. Fig. 6.4 shows their calculations for the photon energy dependence of peak *b*, compared to the experimental results. Given that the calculations are non-relativistic, and take no account of $4p$ - $4d$ resonance or self-energy effects, the agreement is extremely good.

Fig. 6.4 Experimental and theoretical intensities of peak *b* on Y(0001) (after Barrett and Jordan [23])

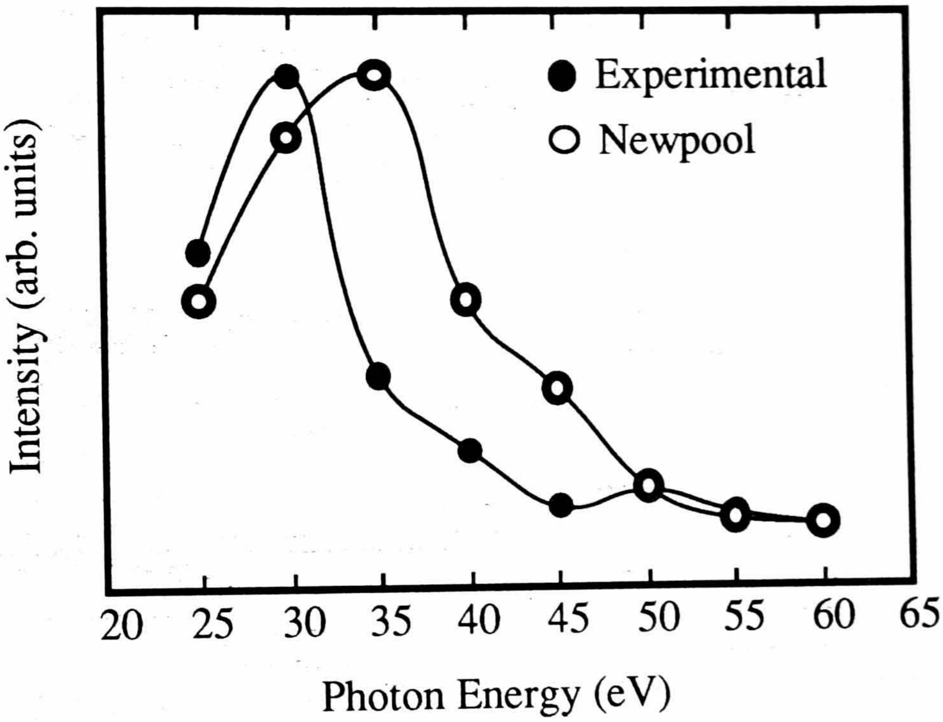

This is in agreement with the Gd results of Himpsel and Reihl [20] regarding the origin of peak *b*, but they did not agree with Himpsel and Reihl's assignment for peak *c* as the Γ_{1+} point. Barrett and Jordan did not find any peak that could be identified with peak *c* in the calculations and concluded that peak *c* was a many body effect, possibly a satellite of the SODS. A peak at E_F was produced in the calculations by the truncation and convolution used to simulate the experimental resolution, but this did not appear to be the same peak as peak *a*, which they suggested might be due to a surface state.

In order to determine whether many body effects would be present in KRIPES spectra of rare earths, to learn about the validity of the bandstructure calculations for unoccupied states and to search for possible surface states implicated in the origin of the SODS , a KRIPES study of Y(0001) was performed.

6.1 KRIPES of Y(0001)

Normal incidence KRIPES spectra in the photon energy ranges 12-19 eV and 24-32 eV, corresponding to direct transitions along the ΓA direction of the Brillouin zone, are shown in figs 6.5 and 6.6 respectively. The spectrometer efficiency deteriorates rapidly below hv = 15 eV, hence the rather poor signal to noise ratio in that photon energy range. The spectra in the photon energy range 18-23 eV were all obscured to some degree by fluorescence from the decay of a $4p$ core hole (see chapter 7).

There are four features in the spectra of figs. 6.5 and 6.6, at energies (± 0.2 eV) of 0.5 eV, 2.0 eV, 4.8 eV and 7.0 eV above E_F, labelled a^*, b^*, c^* and d^* respectively. We choose this notation to avoid confusion with that of the ARUPS peaks of fig. 5.4. None of these features displays significant dispersion with photon energy. As with the ARUPS spectra of Gd(0001) [20] (fig. 6.1) and Y(0001) [21] (fig. 5.4) momentum broadening prevents the observation of peak dispersions with photon energy. The apparent shift of a^* towards higher energy in fig. 6.6 is attributed to the worsening energy resolution in the higher photon energy range (see fig. 4.8). Peaks b^* and c^* are most likely due to transitions to high density of states points along ΓA, since such points occur at 1.8 eV (A_3) and 4.9 eV (Γ_{5-}) in the calculated bandstructures (fig 3.5). The calculated total density of states (fig. 3.4 (b)) also shows peaks at these energies and, as shown in fig. 6.7, these have been observed in inverse photoemission [160] and bremsstrahlung isochromat spectra [161] of polycrystalline Y films. The LMTO bands become steadily less reliable for energies higher then 5 eV above E_F and so it is unwise to compare the energy of peak d^* with any features in fig. 3.4 (b). Neither the published LAPW or KKR results show energies greater than 6 eV so it was not possible to determine the origin of peak d^* from these bandstructures. However the calculation of Papaconstantopoulos [162] shows the unoccupied Γ_{4-} point at 6.9 eV and this may well be the origin of this peak. The feature labelled a^* lies in the gap between the Γ_{4-} and Γ_{3+} critical points thus it is tempting to associate it with a surface state — it is possible that peak a in the

Fig. 6.5 Normal incidence KRIPES spectra of Y(0001) in the photon energy range 12 - 19 eV normalised to the intensity of peak *b**

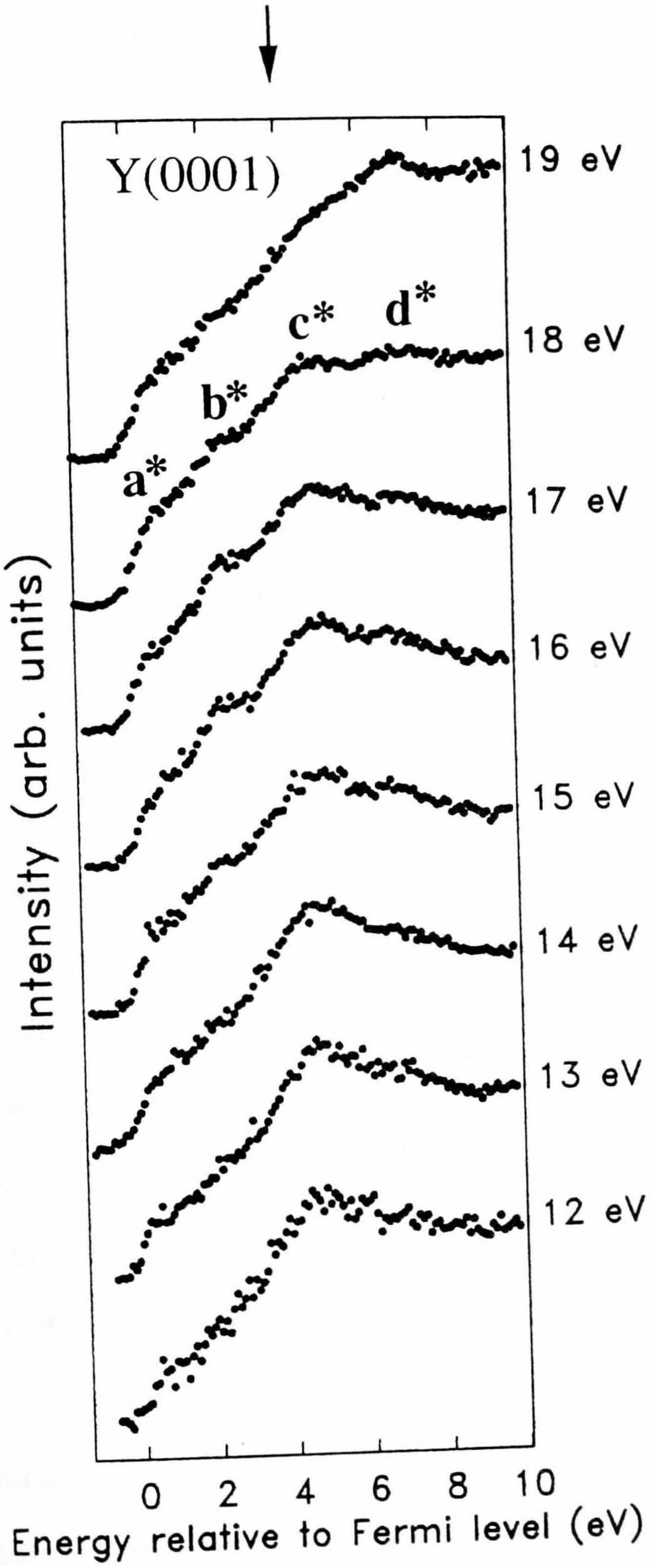

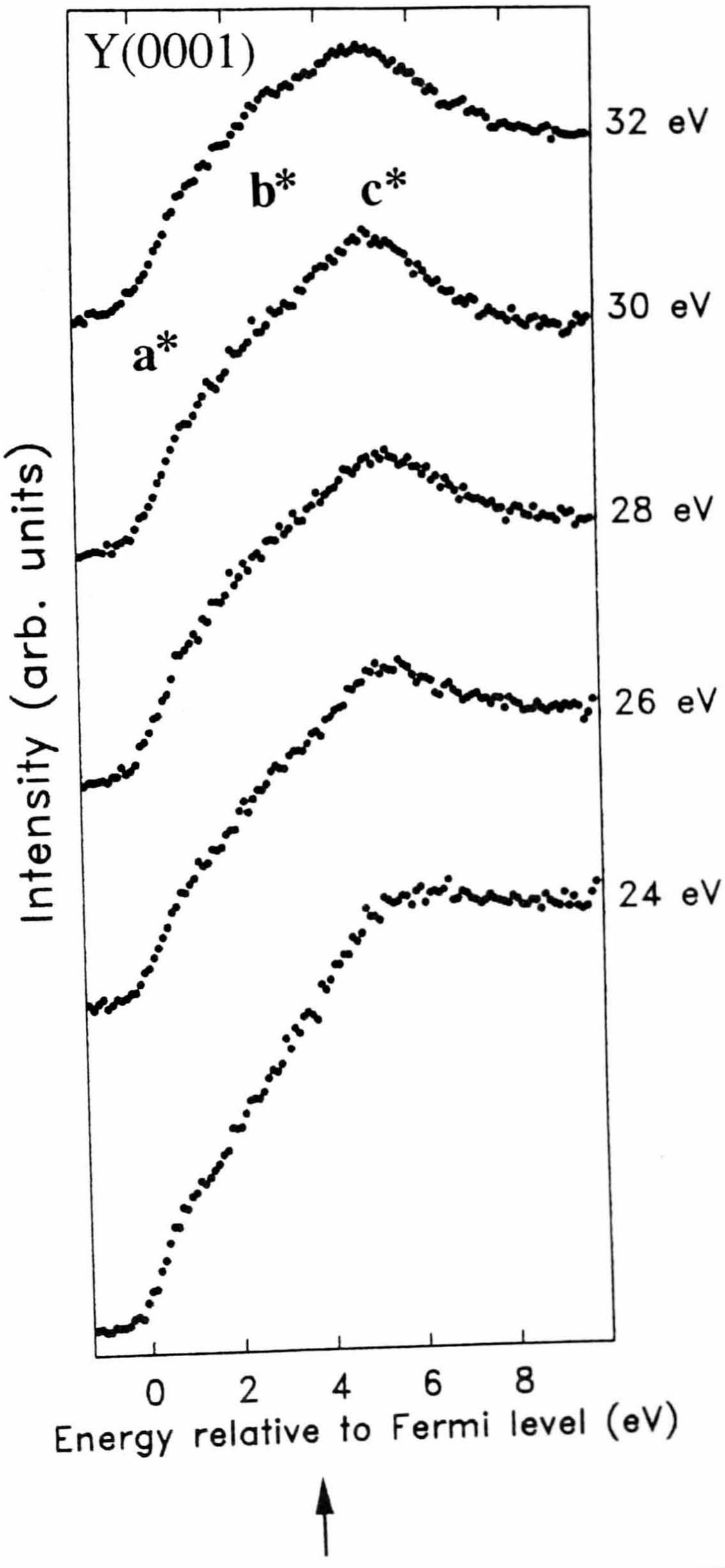

Fig. 6.6 Normal incidence KRIPES spectra of Y(0001) in the photon energy range 24 - 32 eV normalised to the incident electron flux

Fig. 6.7 Inverse photoemission spectra of Y

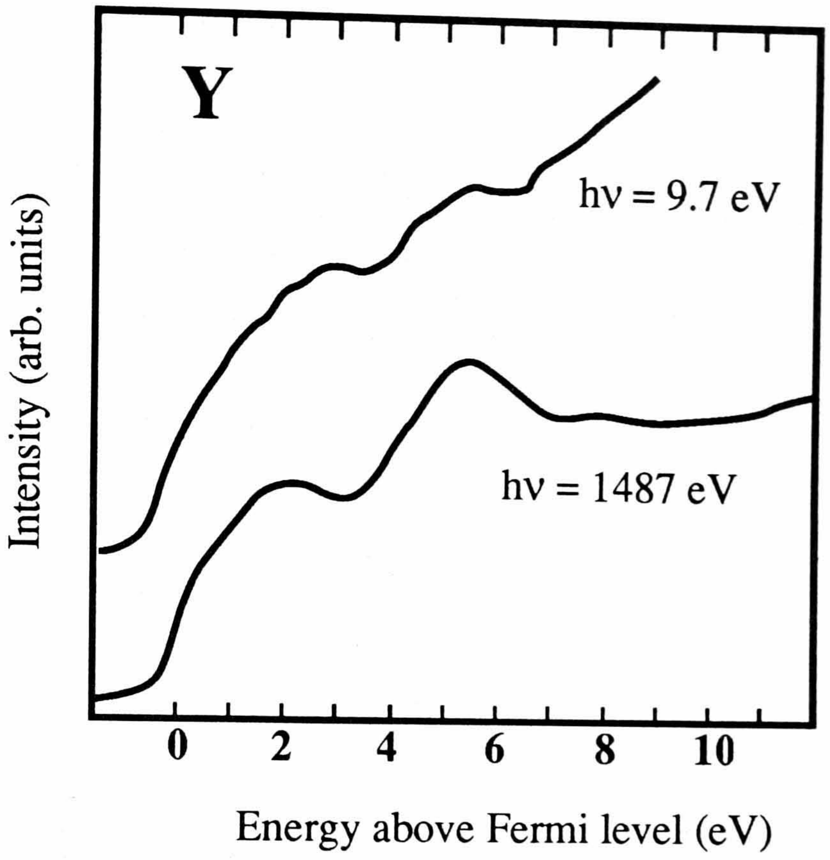

ARUPS spectra of Y(0001) [23] (fig. 5.4) is the occupied tail of this state. It was not possible to determine whether the intensities of the two features have the same photon energy dependence, as the design of the KRIPES instrument does not permit us to take measurements in the same photon energy range as the ARUPS spectra (25-60 eV) (see chapter 4). It is also possible that a^* is due to a failure of momentum conservation. Although fig 3.4 (b) implies that the density of states along ΓA is very low at this point the total density of states is peaked at E_F, due to the flat bands along the LM and KH directions

It appears that the features seen in the KRIPES spectra of Y(0001) are entirely explicable in terms of one-electron bands, in marked contrast to the conclusions of Barrett and Jordan [23] regarding their ARUPS spectra. The feature labelled a^* cannot be unambiguously assigned to a surface state, and it is difficult to see how such a weak feature could be responsible for an ARUPS peak as intense as the SODS. As shown in section 6.x the results of

Barrett and Jordan [23] have been reproduced using the same crystal as was used in this KRIPES study, so it appears that the KRIPES results are characteristic of the same surface as the ARUPS results. Thus the absence of intense surface related features in the KRIPES spectra which might be related to the SODS cannot be attributed to differences in the surfaces studied by the different techniques.

6.2 ARUPS of Ho(0001)

With the apparent absence of serious many body effects in the Y(0001) KRIPES data it appeared more likely that the valence band features seen in the Y(0001) ARUPS data of fig. 5.4 might be due to one electron states. At the same time observation of dispersing features on Ho(11$\bar{2}$0)-(7 × 1) (see fig. 5.18) suggested that a study of Ho(0001) would be useful, in order to compare the electronic structure of the two surfaces. A comprehensive ARUPS study of Ho(0001) was therefore performed, and compared to NEWPOOL photocurrent calculations using slab potentials as described in chapter 3. This represents a further level of sophistication over the NEWPOOL calculations of Barrett and Jordan [23], which employed bulk potentials.

Normal emission valence band ARUPS spectra of Ho(0001), for a range of photon energies, corresponding to emission from states along the ΓA direction of the Brillouin zone, are shown in Fig. 6.8. There are four features, none of which show any significant dispersion with photon energy : three peaks labelled *a, b* and *c*, at binding energies of 0.3, 1.7 and 2.9 eV respectively, and a shoulder at ~ 4 eV. These appear to be the same features as were seen in the ARUPS spectra of Gd(0001) and Y(0001). The Gd(0001) spectra [20] were taken over a different photon energy range and so the dependence of peak intensity upon photon energy cannot be directly compared. For Y(0001) [23] the photon energy dependence is extremely similar to Ho; peaks *a, b* and *c* resonate at hν=38, 32 and 38 eV respectively, compared to 40, 28 and 40 eV for Ho(0001). This represents strong experimental evidence that the bandstructures of Ho and Y are indeed very similar, as was suggested in chapter 3. In both cases peaks *a* and *c* resonate at very similar energies, which suggests that they may share a

Fig. 6.8 Flux-normalised normal emission ARUPS spectra of Ho(0001), incidence angle 30°, p-polarised radiation

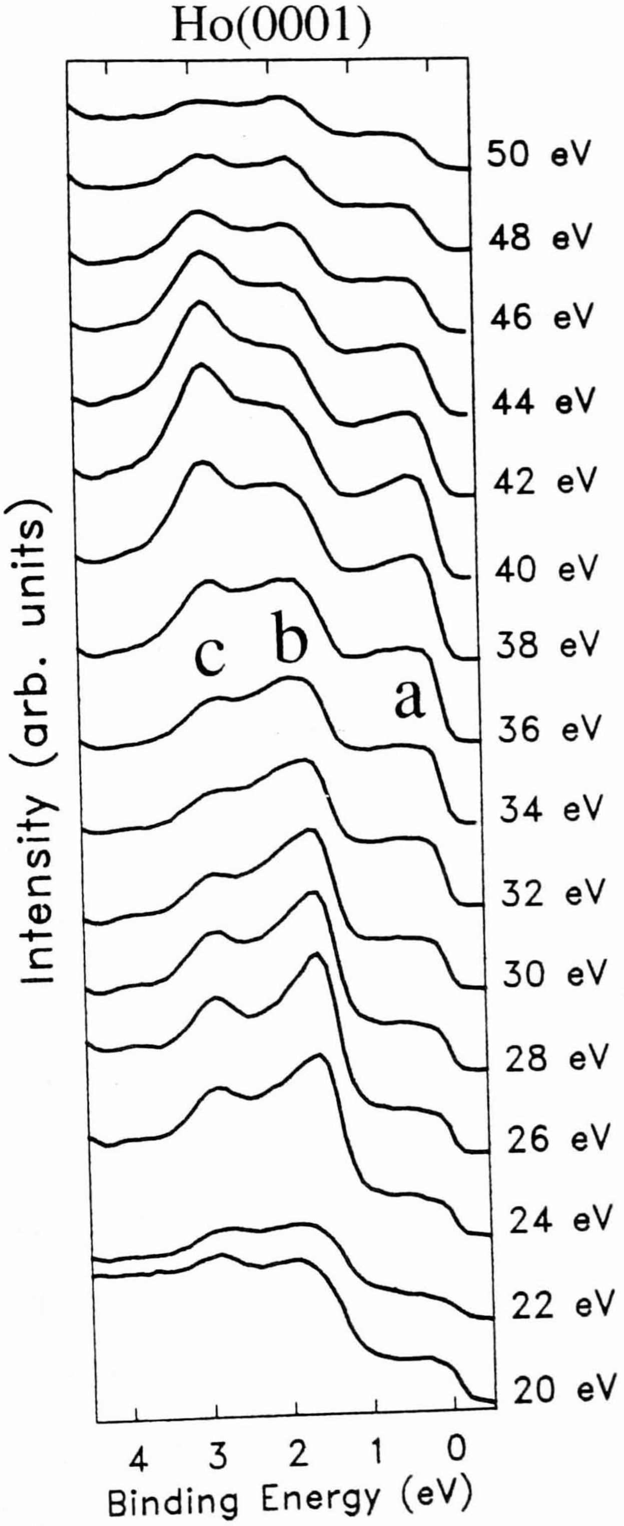

common origin, whilst the significantly different photon energy dependence of peak *b* suggests a different origin for this peak. Given the close similarity between the behaviour of peak *b* on Y(0001) [23] and Ho(0001), and between the calculated bandstructures of Y and Ho it seems reasonable to conclude that peak *b* on Ho(0001) is due to emission from the Γ_{4-} point of the Ho bandstructure. Himpsel and Reihl [20] suggested that peaks *b* and *c* in their Gd(0001) spectra were due to emission from, respectively, the and Γ_{4-} and Γ_{1+} points of the same Δ_1 band in the Gd bandstructure. However, these peaks on Ho(0001) exhibit different polarisation dependence (Fig. 6.9), and must therefore originate from initial state bands of different symmetry. Thus, if we assume peaks *b* and *c* share the same origins on Gd(0001) as on Ho(0001), and that peak *b* on Gd(0001) is due to emission from the Gd Γ_{4-} point, it follows that Himpsel and Reihl [20] were incorrect in assigning peak *c* to emission from the Gd Γ_{1+} point.

A normal emission photocurrent calculation for the valence band of Ho(0001) is shown in Fig. 6.10. Note that, in contrast to the Y(0001) calculations of Barrett and Jordan [23], the existence of peak *a* is reproduced, as is that of the 4 eV shoulder. The calculated peak *a* probably arises from the truncation of the tail of an unoccupied surface state. It does not show the same photon energy dependence as the experimental peak *a*, but the polarisation dependence is reproduced correctly. The intensity of the experimental peak *a* was gradually attenuated with time as the sample contamination level increased, and could be greatly reduced by a very light Ar^+ bombardment (500 eV for ~15s) as has also been reported for peak *a* on Y(0001) [23]. This suggests the involvement of a surface state and there is evidence for such an (unoccupied) state from the Y(0001) KRIPES results (section 6.1).

It appears from Fig. 6.10 that peak *b* is reproduced, at 2.05 eV binding energy, but not peak *c*. However this calculated peak was found to have the wrong polarisation dependence to be the experimental peak *b*, instead showing the same dependence as peak *c*. Further, the photon energy dependence of the calculated peak is very similar to that of peak *c* (fig. 6.11) suggesting that the calculated peak at 2.05 eV binding energy in fact corresponds to

Fig. 6.9 Polarisation dependent ARUPS spectra of Ho(0001) hv = 40 eV, emission angle 30°, p-polarised radiation

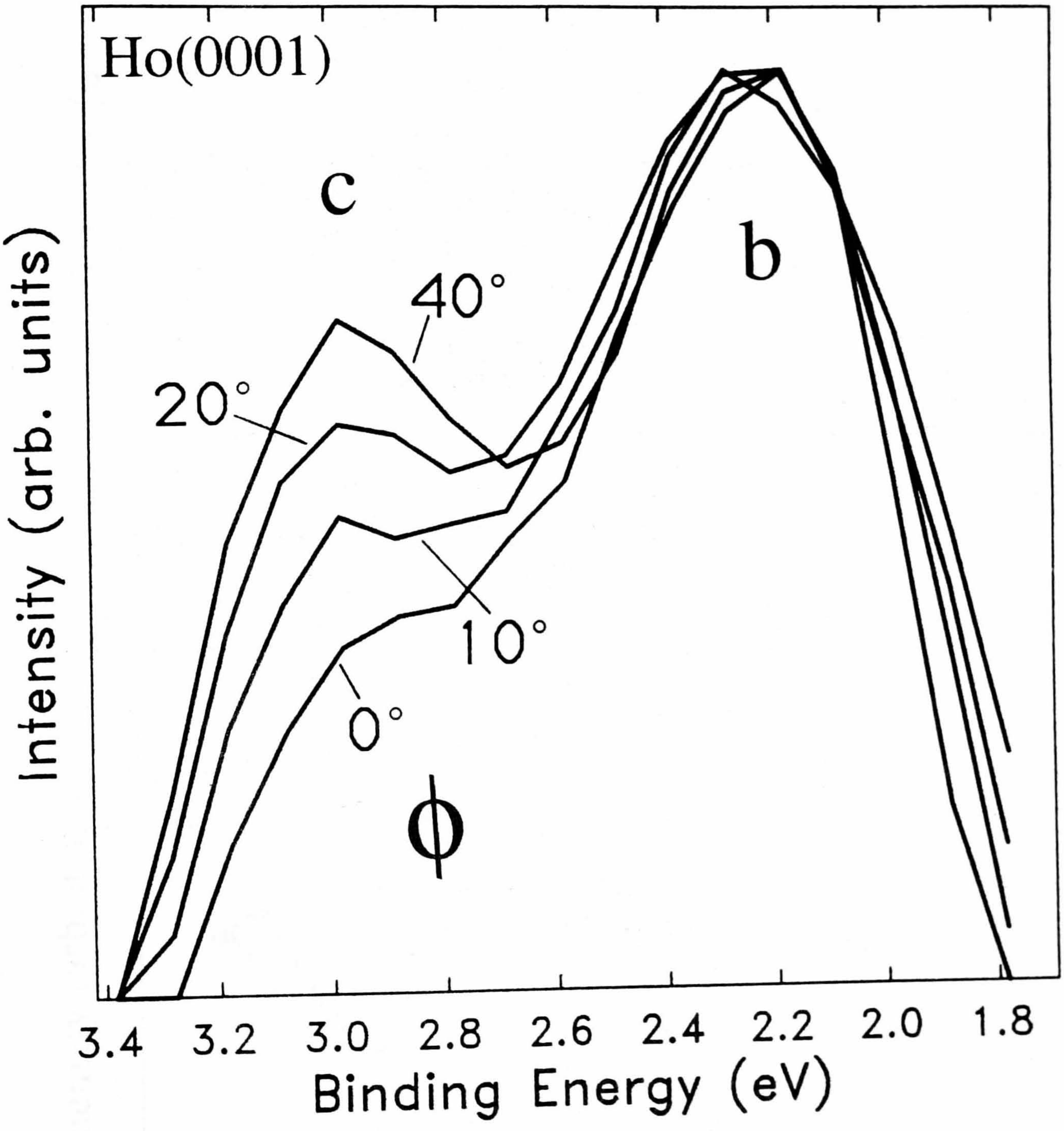

Fig. 6.10 NEWPOOL normal emission photocurrent calculation for Ho(0001), hν = 40 eV

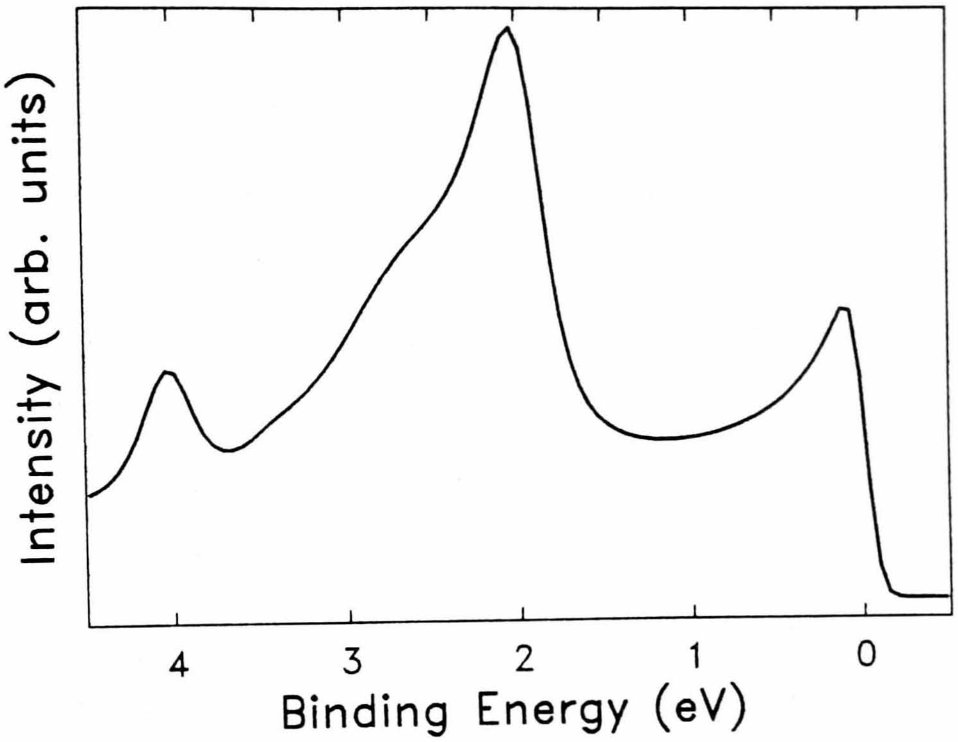

Fig. 6.11 Experimental and theoertical intensities of peak *c*

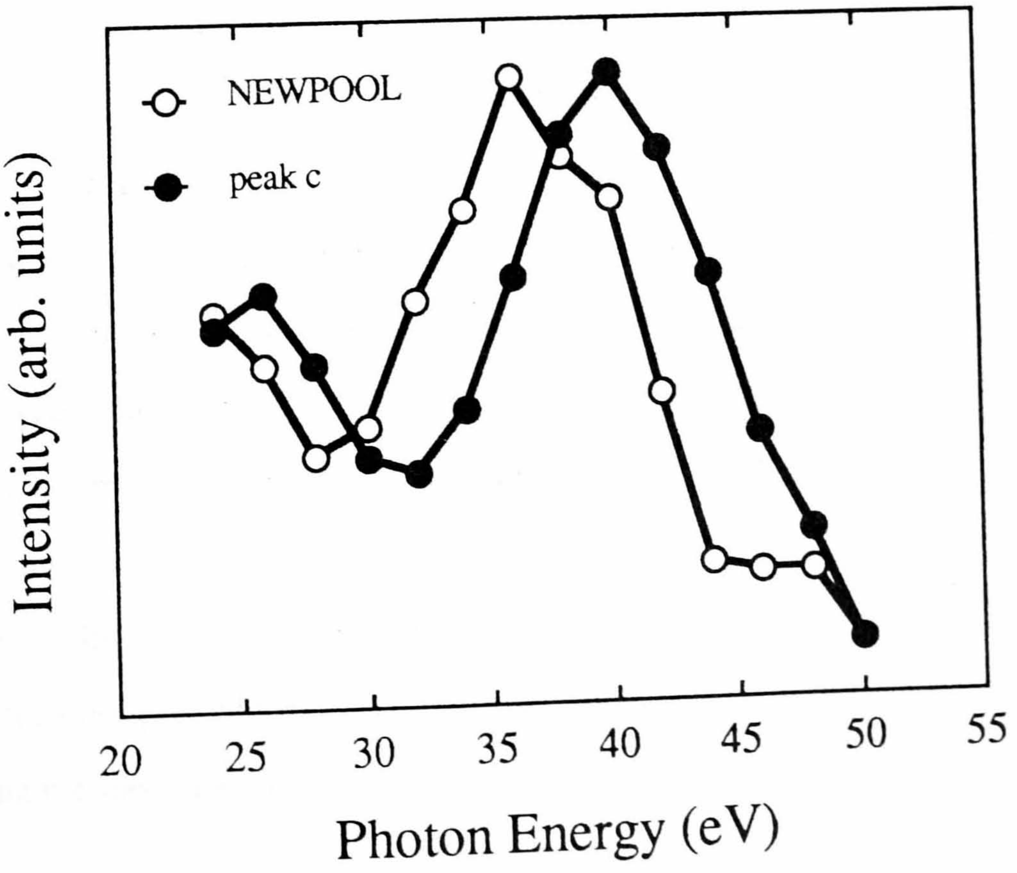

peak *c*, with the binding energy underestimated by the calculations. Since peaks *a* and *c* were not reproduced in the Y calculations [23], and given the similarity in the calculated bandstructures of the two elements, this suggests that both these features are due to surface effects.

Off-normal emission spectra of Ho(0001), with the emission angles chosen such that $\mathbf{k}_{\|}$, the component of electron momentum parallel to the surface, varies along the two high symmetry directions of the surface Brillouin zone, $\overline{\Gamma \mathrm{KM}}$ and $\overline{\Gamma \mathrm{M}}$ (see Fig. 2.5), are shown in Fig. 6.12. Plots of binding energy against $\mathbf{k}_{\|}$ are shown in Fig. 6.13, with $\mathbf{k}_{\|}$ determined using equation 1.2. There is obviously considerable dispersion evident in these spectra, in marked contrast to the normal emission data. There are several other points of note: (i) the intensity at E_F is considerably enhanced at the first $\overline{\mathrm{M}}$ points, [corresponding approximately to $\theta = \pm 20°$ in Fig. 6.12], yet not at the $\overline{\mathrm{K}}$ points, in agreement with the data of Himpsel and Reihl [20] on Gd(0001). This is the opposite to what would be expected from the bandstructure [Fig. 3.9 (d)] as there is a close grouping of four bands along KH close to E_F, and only two along LM, (ii) There is a gap between ~0.5 eV and ~1.5 eV binding energy which is not present in the bandstructure [Fig. 3.9 (d)]. Momentum broadening may well be responsible for this apparent discrepancy; off-normal emission photocurrent calculations for Y(0001) [163] show that peak *b*, which is due to emission from the bulk bandstructure, exhibits negligible dispersion with emission angle. Thus instead of observing the dispersion of the bulk band we see emission from the Γ_{4-} point, where the DOS is high, and the dispersion of peak *c*, which is *not* due to emission from bulk one-electron bands, (iii) A band appears to cross E_F between $\overline{\Gamma}$ and $\overline{\mathrm{K}}$, and possibly also between $\overline{\Gamma}$ and $\overline{\mathrm{M}}$, although in the latter case this is difficult to determine owing to the enhanced emission at E_F close to $\overline{\mathrm{M}}$. These may well correspond to the crossings seen along ΓK and ΓM in the bandstructure, but *direct* comparison of the crossing points and dispersions seen in Fig. 6.13 with the calculated bandstructure is not possible, as $\mathbf{k}_{\perp}$ is unknown. However, indirect comparison may be made by comparing the spectra with *ab initio* photocurrent calculations.

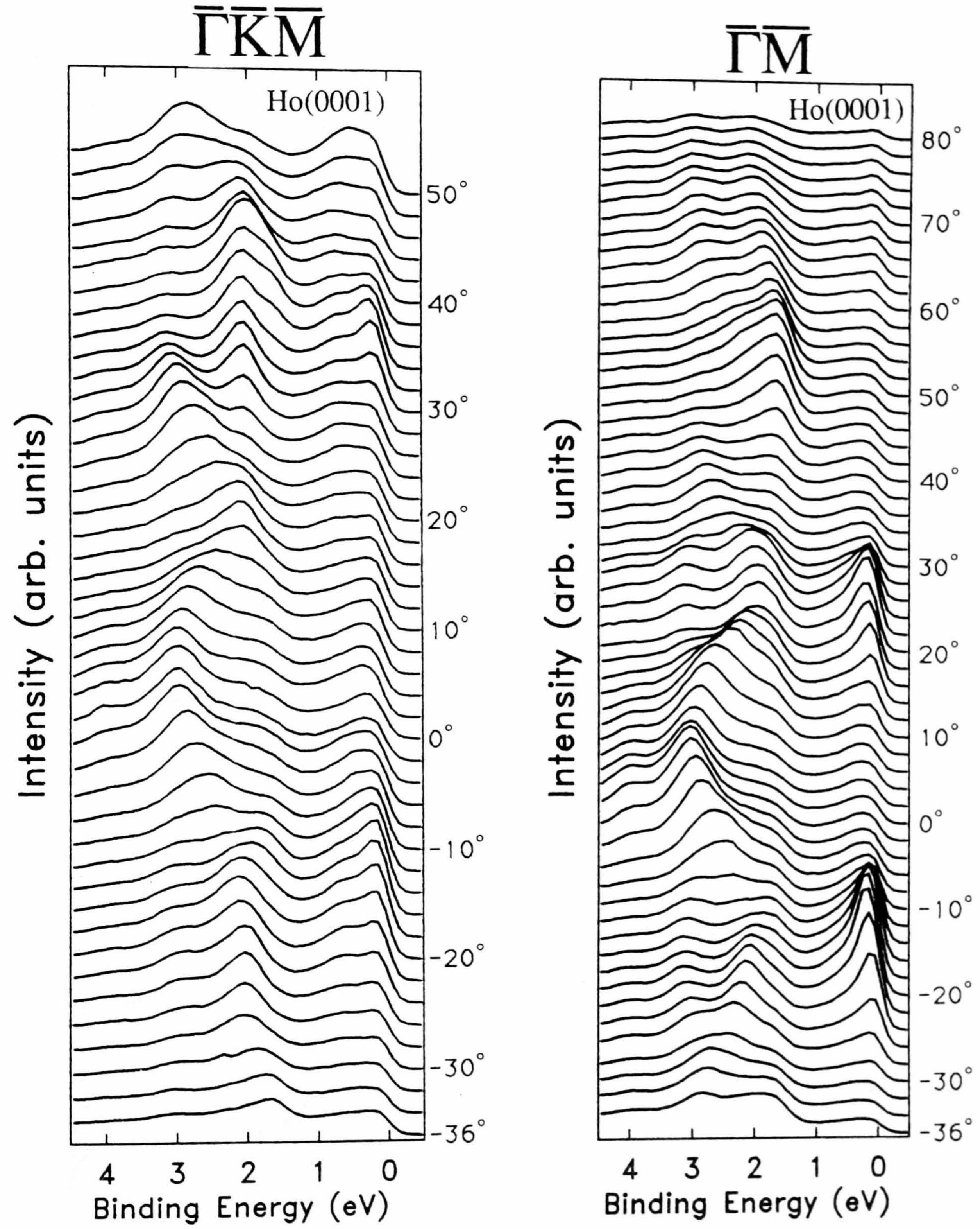

Fig. 6.12 Off-normal emission ARUPS spectra of Ho(0001)
$h\nu = 40$ eV, incidence angle 55°, p-polarised radiation

Fig. 6.13 E(**k**) curves for Ho(0001), derived from the data of Fig. 6.12

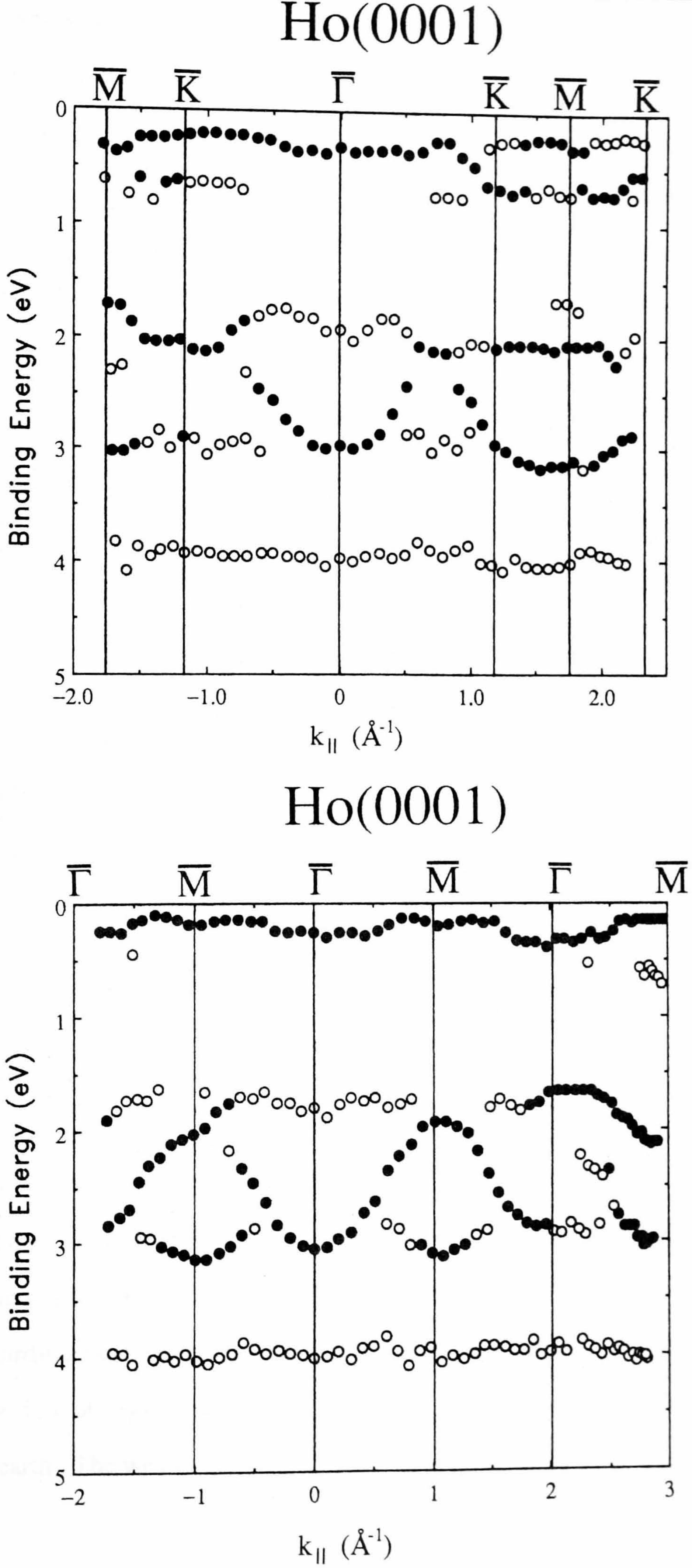

Fig. 6.14 shows calculated off-normal photoemission spectra, using the same photon energy and incidence angle as were used in the experiment, with emission angles varied along $\overline{\Gamma \mathrm{KM}}$ and $\overline{\Gamma \mathrm{M}}$. In both cases the angles covered correspond to values of $\mathbf{k}_{\|}$ from zero to the boundary of the first Brillouin zone. Note that although the binding energy of peak *c* is underestimated the extent of its dispersion is correctly calculated. This causes the calculated peak to overlap with the features close to E_F, which obscures the possible Fermi level crossings seen in the experimental data. In order to clarify the detail we repeated the calculations for the regions of interest in smaller angular increments, with the initial state inverse lifetime decreased. This will reduce the width of the photocurrent peaks without shifting their position. The results are shown in Fig. 6.15. For the $\overline{\Gamma \mathrm{M}}$ direction a band does seem to cross E_F at about $\theta = 8^\circ$, remaining close to E_F as far as the zone boundary. This seems to be in agreement with Fig. 6.12, although the high intensity of peak *a* close to the M point, which is not reproduced by the calculations, makes the experimental data unclear. If the band crossing E_F is a bulk band, which is likely given that a such a crossing exists in the bands of Fig. 3.9 (d) along ΓM, it is entirely feasible that its intensity relative to peak *a*, which appears to be a surface feature, would be overestimated by the calculation. For the $\overline{\Gamma \mathrm{K}}$ direction there is no obvious crossing, but a feature emerges at $\theta = 16^\circ$ at ~1 eV below E_F. Comparison with Fig. 6.12 suggests that this feature may in fact be responsible for the apparent crossing

All the features seen in the ARUPS spectra appear to be explicable in terms of emission from one-electron bands; by analogy with the Y(0001) results of Barrett and Jordan [23] peak *b* is due to emission from the Γ_4- point of the bulk bandstructure, and peaks *a* and *c*, and the 4 eV shoulder are reproduced in the photocurrent calculations, which suggests that they are due to surface effects. Since these features are very similar to those seen on Y(0001) [23] it follows that the same may also apply to that surface. This supports the suggestions of Barrett and Jordan [23] regarding peak *a*, but contradicts their suggestion that peak *c* is due to a many-body effect. The data of Figs. 6.12 and 6.13 represent the first detailed surface band mapping of any hcp rare earth . The wealth of detail present in these data suggests that even subtle trends

Fig. 6.14 NEWPOOL off-normal emission photocurrent calculations for Ho(0001) using the same experimental geometry as the data of Fig. 6.12

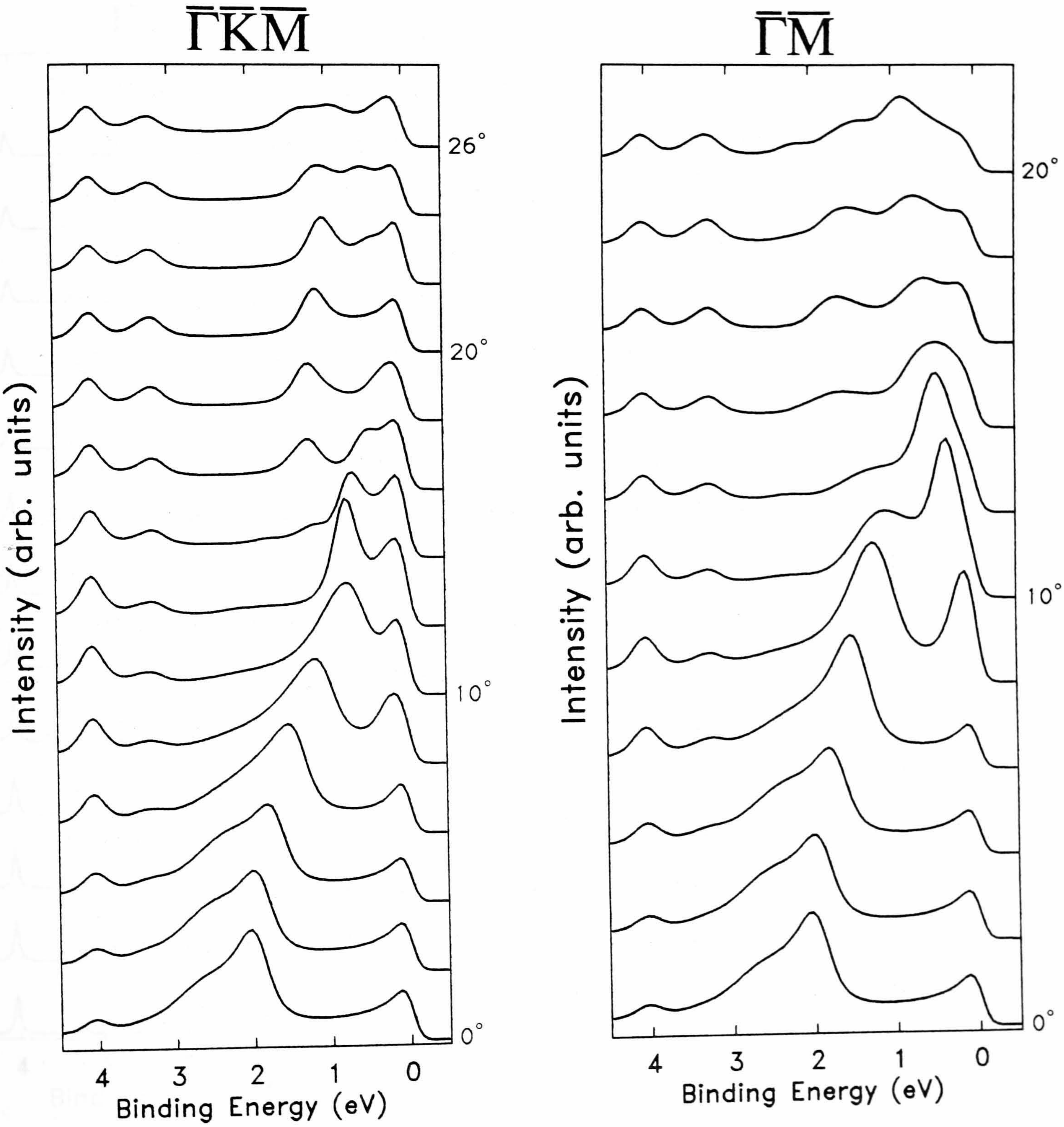

Fig. 6.15 NEWPOOL off-normal emission photocurrent calculations for Ho(0001) with the initial and final state inverse lifetimes artificially reduced

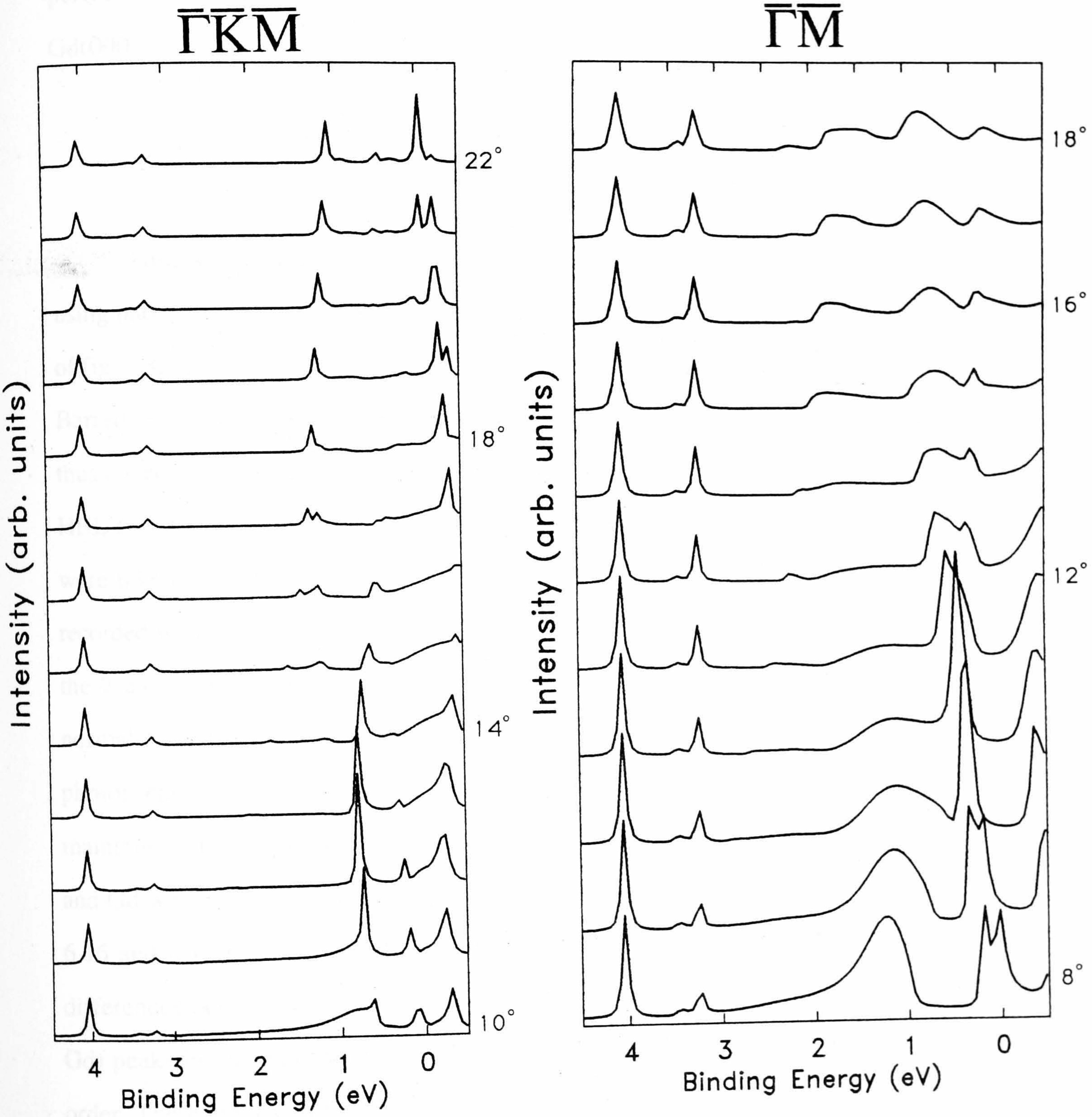

in electronic structure across the series may well be observable if these experiments are repeated on other hcp rare earths. In order to begin such an investigation, and to provide a more rigourous comparison with the ARUPS data from Ho(0001), detailed ARUPS were performed on the two hcp (0001) surfaces previously investigated i.e., Y(0001) and Gd(0001).

6.3 ARUPS of Y(0001) and Gd(0001)

Himpsel and Reihl's normal emission spectra of Gd(0001) [20] were largely recorded using photon energies below 20 eV i.e., a different range to that used for the Ho(0001) spectra of fig. 6.8, this being largely dictated by their monochromator design. The Y(0001) spectra of Barrett and Jordan [23] were taken using the same monochromator as those of fig. 6.8 and thus cover the same photon energy range, but were recorded before the SRS was fitted with the HBL (see chapter 4). This meant that the photon flux available at the time the Y(0001) data were taken was considerably less than at present, and as a result the Y(0001) spectra were recorded with a coarser energy resolution, and in photon energy increments of 5 eV rather than the 2 eV steps of fig. 5.4. To enable more direct comparisons with the Ho(0001) spectra normal emission measurements of Y(0001) and Gd(0001) were performed using the same photon energy range, increment and resolution as those of fig. 6.8. The Gd sample was maintained at 373 K in order to be above the Curie temperature, thus the spectra from Ho, Y and Gd were all taken from paramagnetic surfaces. The Gd and Y results are shown in figs. 6.16 and 6.17 respectively. The similarity between fig. 6.8, 6.16 and 6.17 is striking, the differences being largely for photon energies less than 24 eV, where the 4*p* (Y) or 5*p* (Ho, Gd) peaks in second order lie in the same kinetic energy region as the valence band in first order. There are also a few subtle differences in lineshape - peak *b* on Gd is more rounded than on Y or Ho, and peak *a* is more pronounced on Y - and the binding energies of peaks *b* and *c* differ slightly on the different surfaces. The binding energies of the peaks, and photon

Fig. 6.16 Flux-normalised normal emission ARUPS spectra of Gd(0001), incidence angle 30°, p-polarised radiation

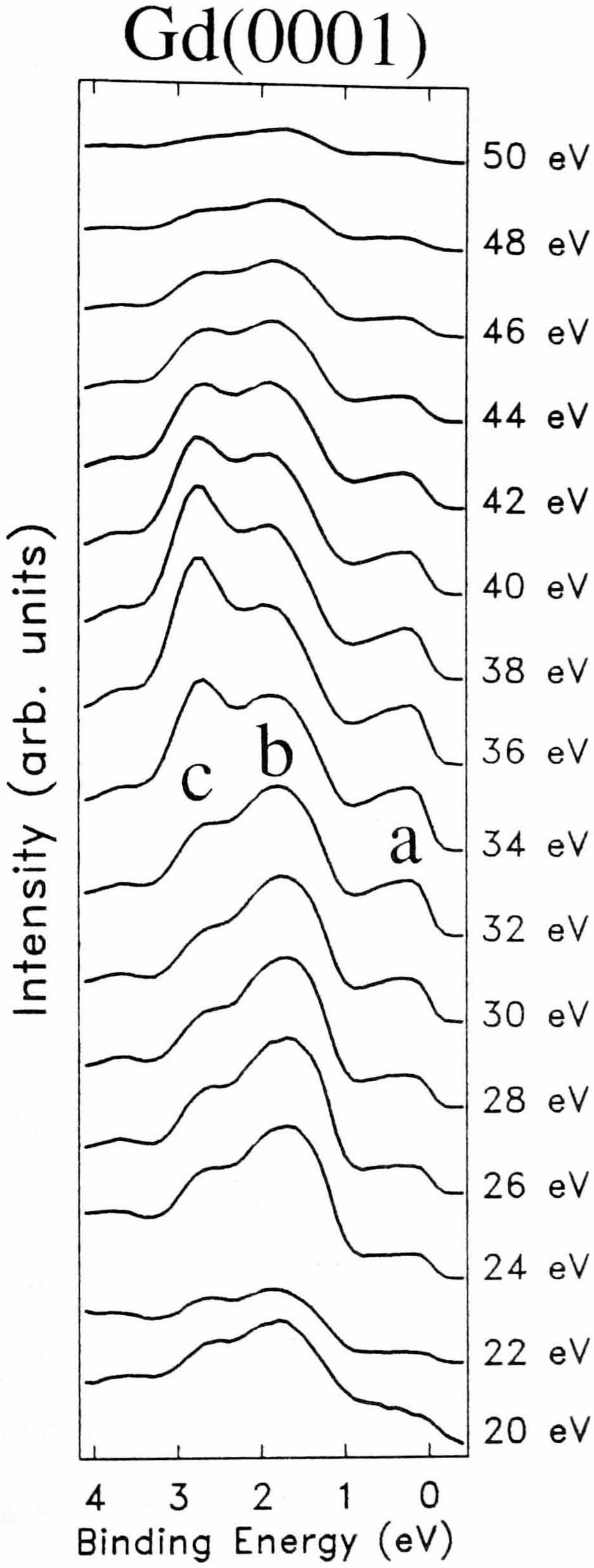

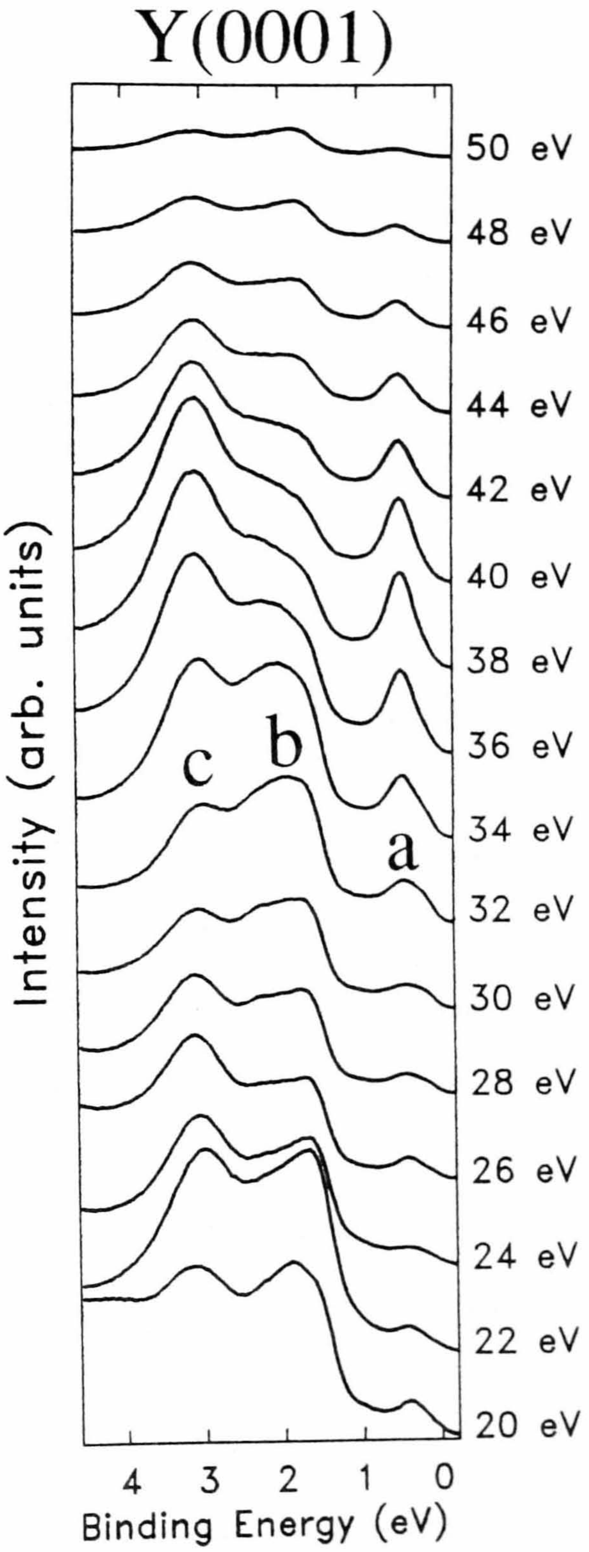

Fig. 6.17 Flux-normalised normal emission ARUPS spectra of Y(0001), incidence angle 30°, p-polarised radiation

energies at which each has its maximum intensity, are shown in table 6.1.

Table 6.1 Resonant and binding energies of valence band photoemission peaks

Surface	Resonant energy (eV)			Binding energy (eV)		
	a	*b*	*c*	*a*	*b*	*c*
Y(0001)	38	32	38	0.4	1.7	3.2
Gd(0001)	36	30	36	0.2	1.6	2.8
Ho(0001)	40	28	40	0.3	1.7	2.9

For each individual element the resonant energy of peak *a* is the same as that for peak *c*, but different to that of peak *b*. The resonant energies differ slightly between elements which perhaps indicates some differences in the final state bands. In the previous section it was shown that peaks *b* and *c* on Ho(0001) have different polarisation dependence, and in fig. 6.18 it can be seen that the same result is also found for Gd(0001). This is direct confirmation that these peaks on Gd originate from states of different symmetry, and thus cannot be due to different critical points of the same Δ_1 band, as was suggested by Himpsel and Reihl [20]. The same result was also found for Y(0001). Given the very close similarity between the results from all three elements it seems most unlikely that peaks *b* and *c* on Gd are spin-split states, as was suggested by Jordan [138]. Normal emission spectra of Gd(0001) taken both well above and well below the Curie temperature are shown in fig. 6.19. There is essentially little difference between these spectra, other than an increase in the intensity of peak *c* at low temperature which may well indicate nothing more than a decrease in thermal surface disorder. This implies that the ferromagnetic exchange splitting of the Gd Γ_{4-} point i.e., peak *b*, persists

Fig. 6.18 Polarisation dependent ARUPS spectra of Gd(0001)
hν = 40 eV, emission angle 30°, p-polarised radiation

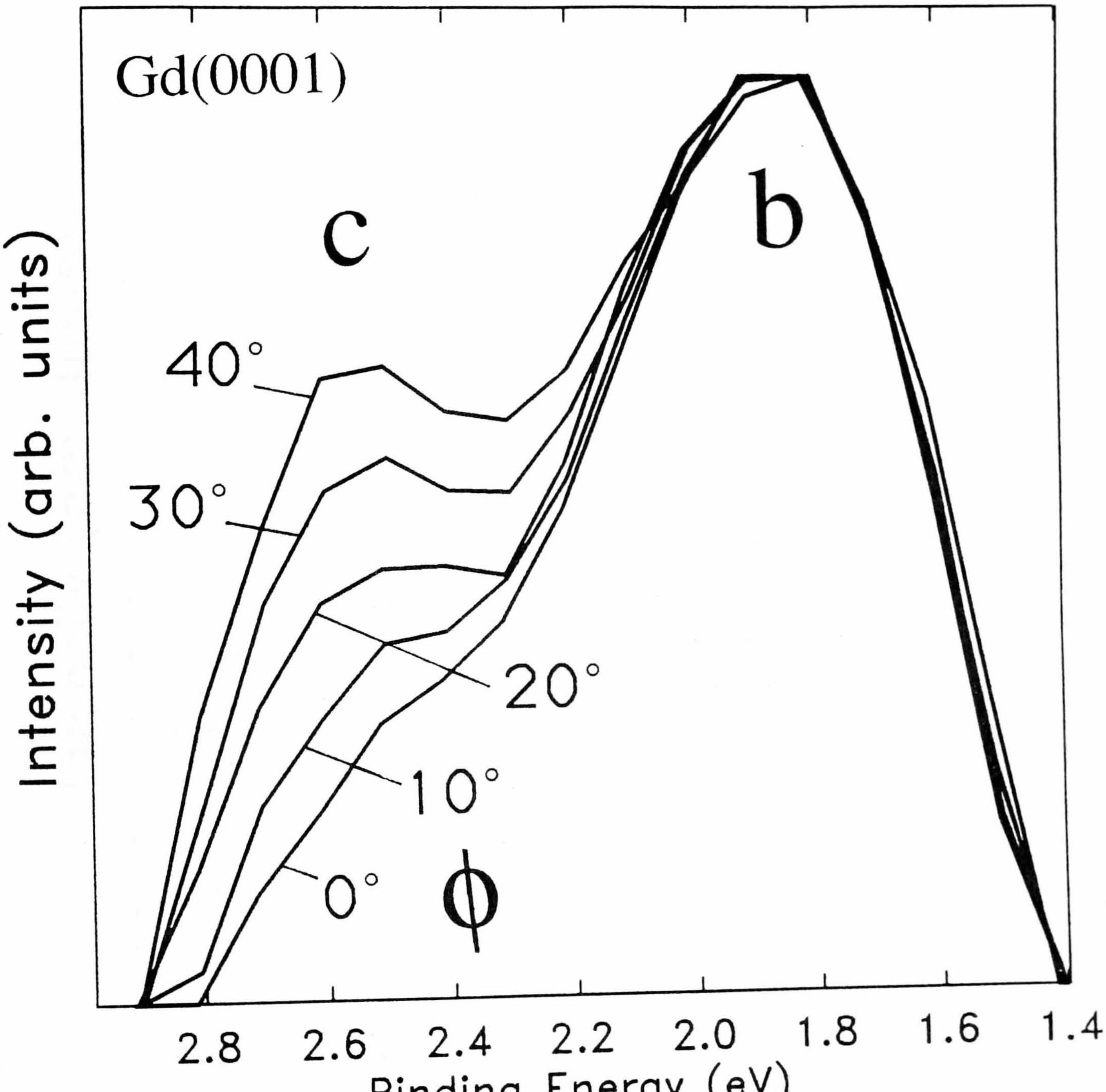

Fig. 6.19 Temperature dependent normal emission ARUPS spectra of Gd(0001)
hν = 40 eV, incidence angle 30°, p-polarised radiation

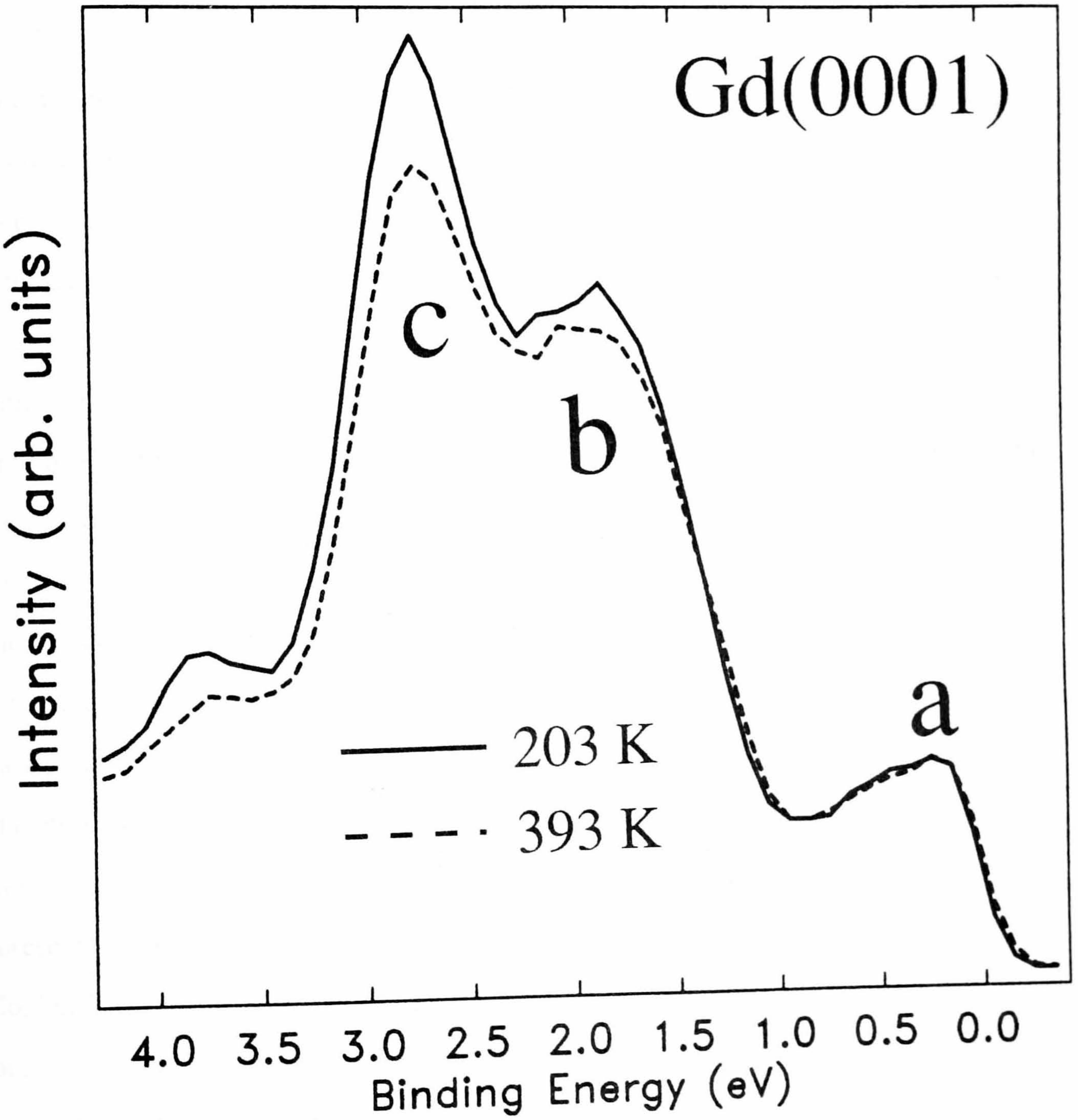

above the Curie temperature, which could explain why peak *b* on Gd is rather broader than on either Ho or Y. Gd has the highest 4*f* moment of the rare earths, and thus magnetic effects on the ARUPS spectra should be strongest on Gd. The magnetic effects on the Gd spectra are thus rather small, and it seems likely that spin-resolved photoemission will be required to resolve the exchange splitting, if any, of peak *b*.

The normal emission and polarisation dependent spectra all suggest that the peak assignments for Ho(0001) also apply to Y(0001) and Gd(0001). If this is the case then the dispersions seen in the off-normal emission spectra of Ho(0001) should also occur on Y and Gd. In order to test this, off-normal measurements were performed for Gd(0001) and Y(0001) using the same photon energy (40 eV) and incidence angle (55°) as were used for Ho and, as far as possible, the same emission angles. The maximum emission angle attainable for a particular sample was dictated by the exact arrangement of the sample holder and so it was not possible to exactly duplicate the full range of angles measured for Ho. As for the normal emission data the Gd sample was maintained at 373 K. The spectra for Gd and Y are shown in figs. 6.20 and 6.21, and the E(**k**) curves derived from them are shown in figs. 6.22 and 6.23. In general the Gd features are broader, with the dispersion less well resolved than for Ho, while the Y features are very sharp. This is reflected in the E(**k**) curves by the relative scatter of the data points, with the smoothest curves found for Y, and the roughest for Gd. For Gd the broad features and relatively narrow bandwidth combine to make it difficult to determine all but the most pronounced dispersions. The gap between the peaks *a* and *b* seen on Ho is clearly also present on both Y and Gd, while Gd shows the non-dispersing 4 eV feature already noted for Ho, but Y does not. This was reproduced in the Ho photocurrent calculations so it seems reasonable to assume it is an intrinsic feature, but it is far from obvious why it should not appear on Y. It does not appear to be 4*f* related as (i) the photocurrent calculations did not include the 4*f* levels, yet reproduced this peak, and (ii) the 4*f* multiplets of Gd and Ho are very dissimilar (see fig. 3.2) and further, do not have any components at binding energies as low as 4 eV. As far as it is possible to determine, being limited by the different angular ranges

Fig. 6.20 Off-normal emission ARUPS spectra of Gd(0001)
hν = 40 eV, incidence angle 55°, p-polarised radiation

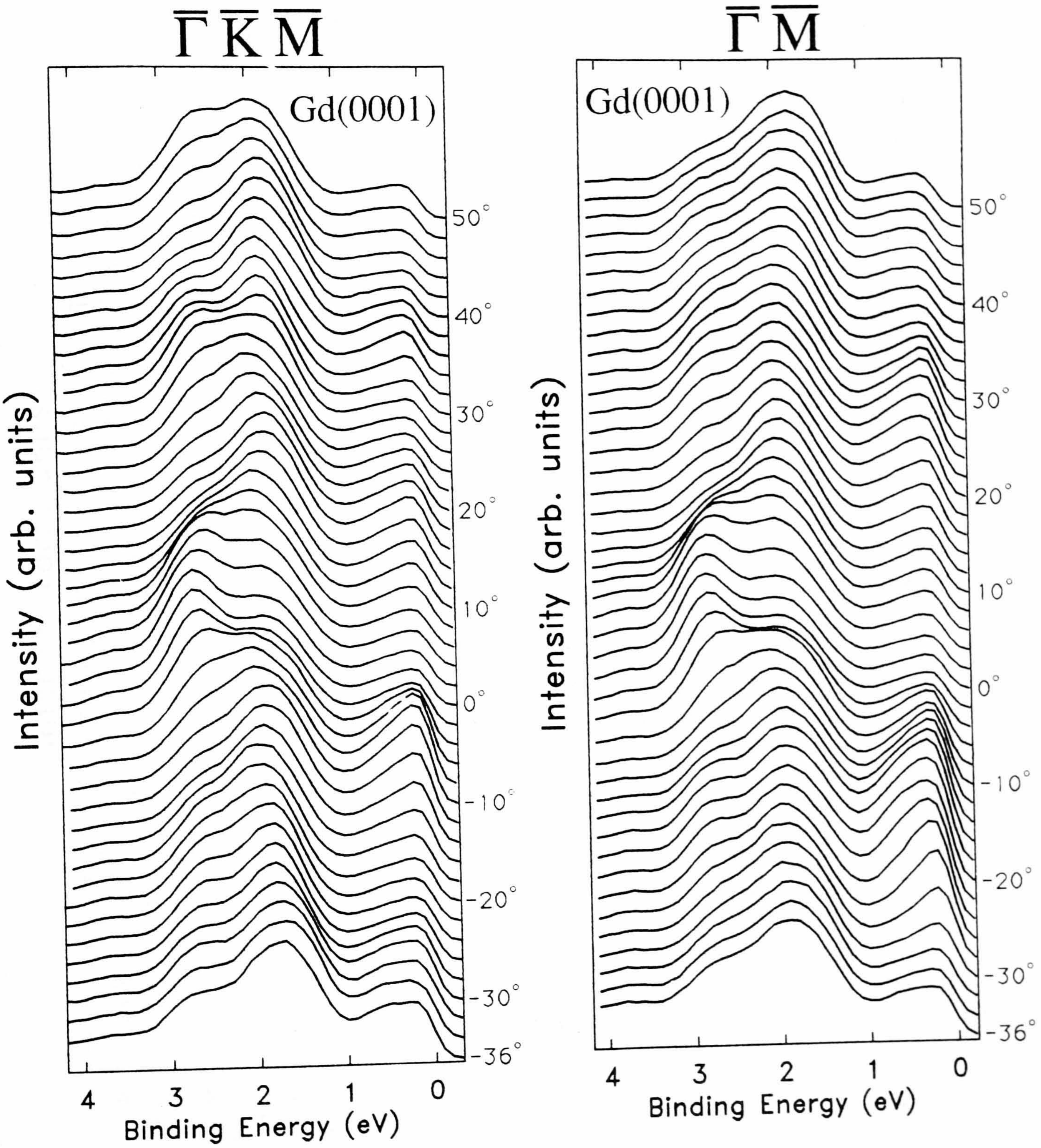

Fig. 6.21 Off-normal emission ARUPS spectra of Y(0001)
hν = 40 eV, incidence angle 55°, p-polarised radiation

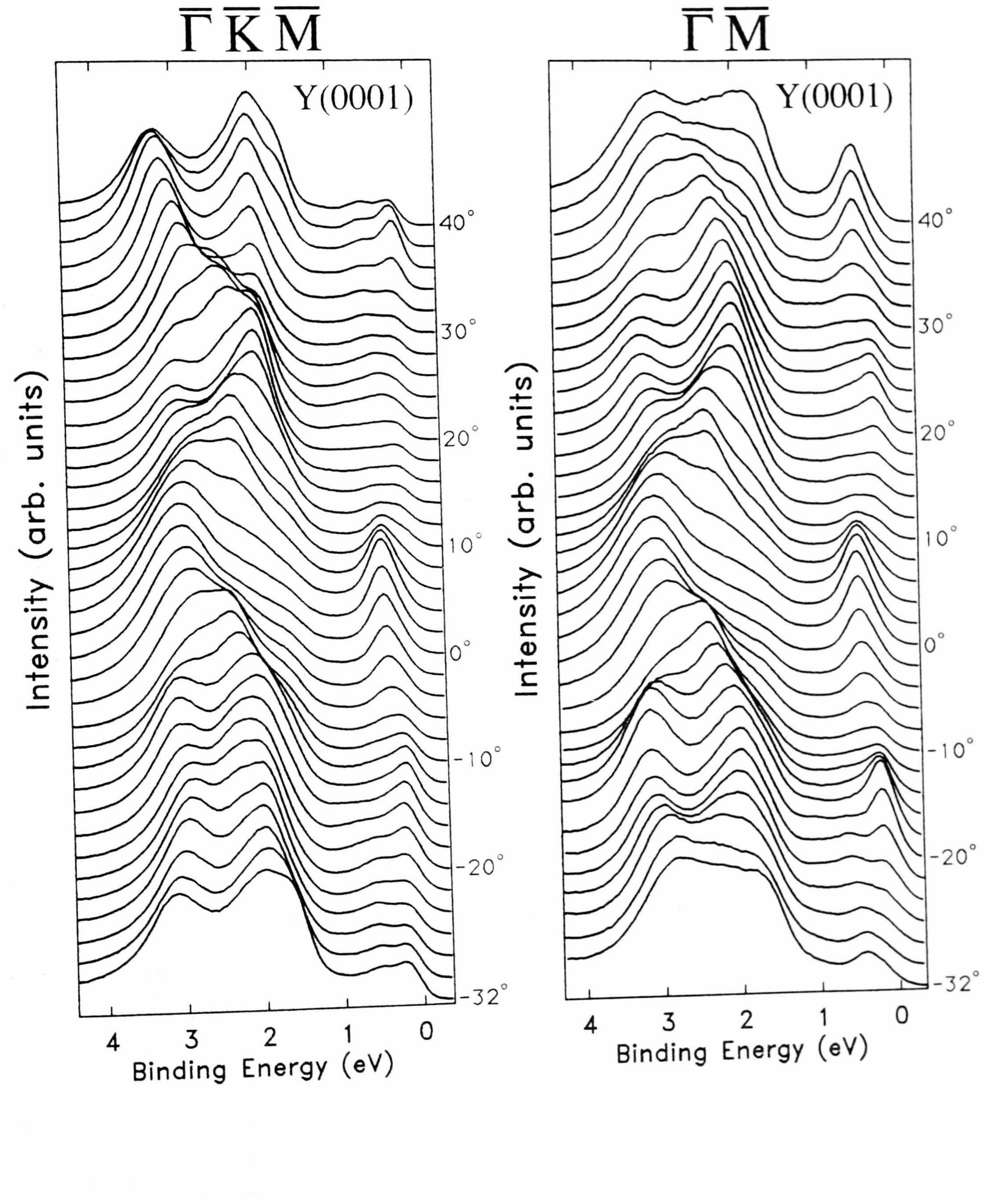

Fig. 6.22 E(k) curves for Gd(0001), derived from the data of Fig. 6.20

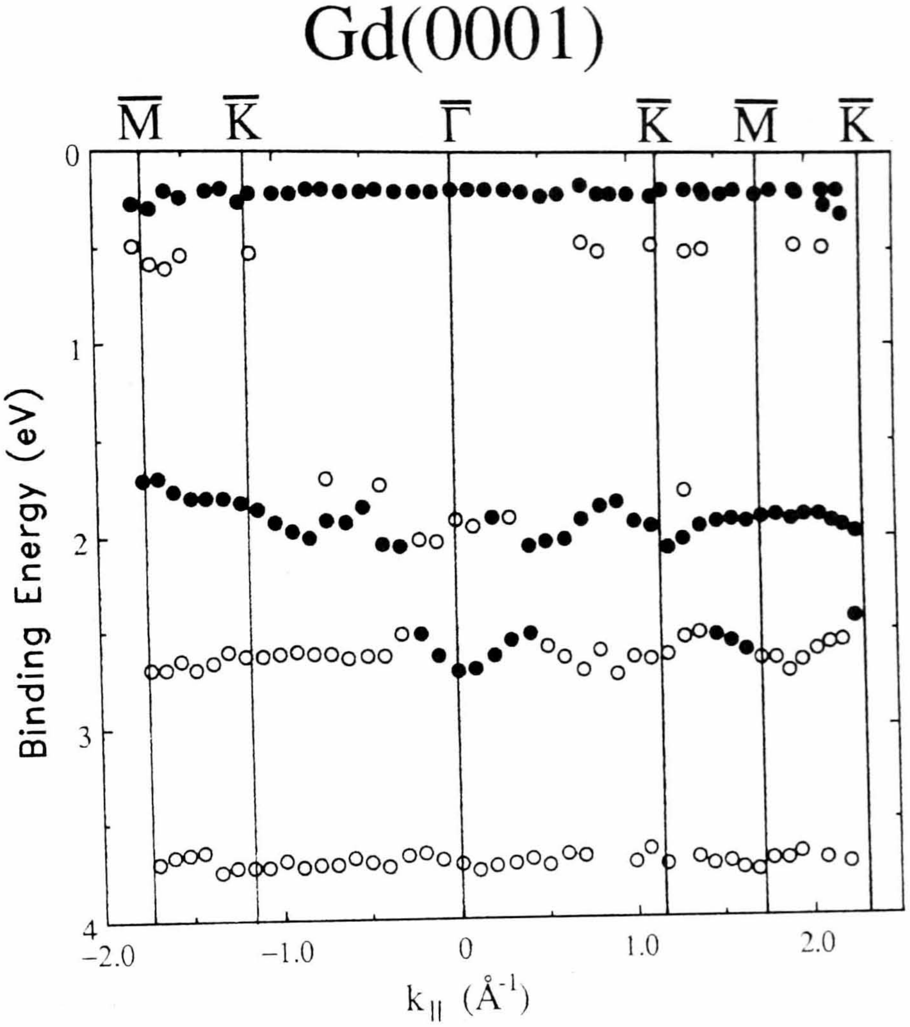

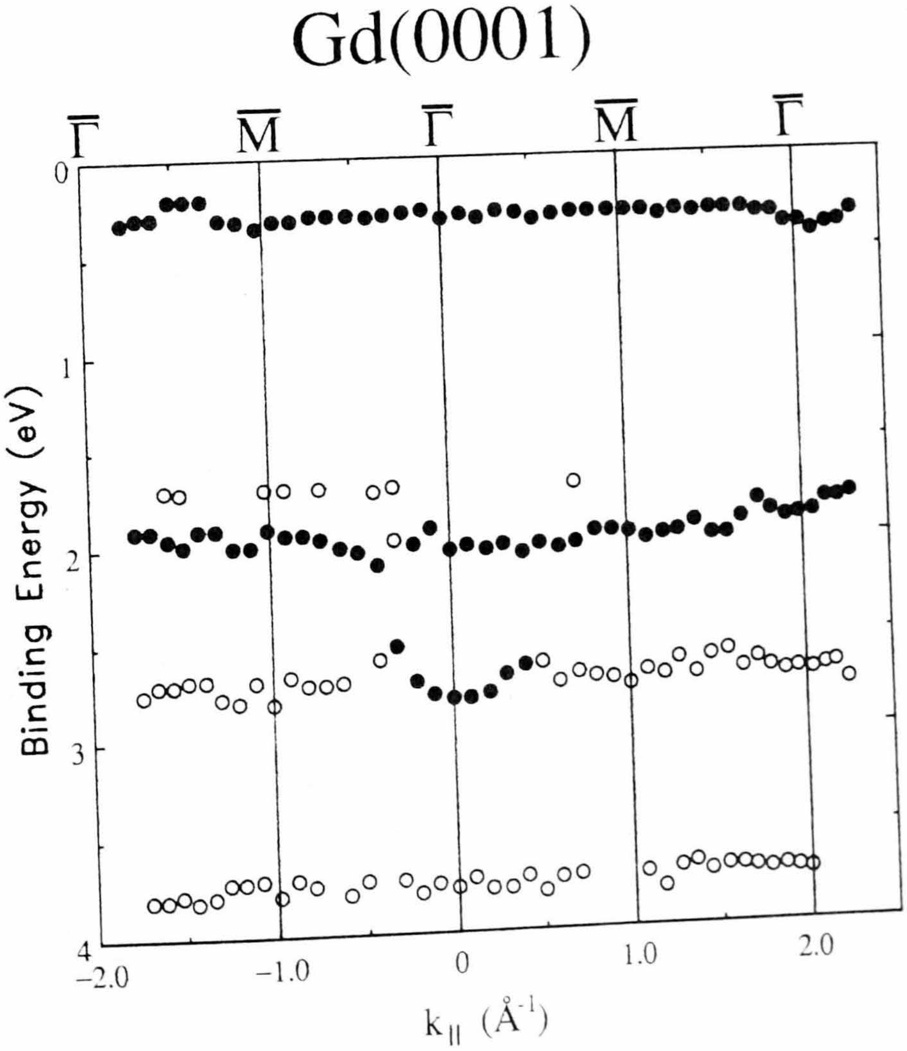

Fig. 6.23 E(k) curves for Y(0001), derived from the data of Fig. 6.21

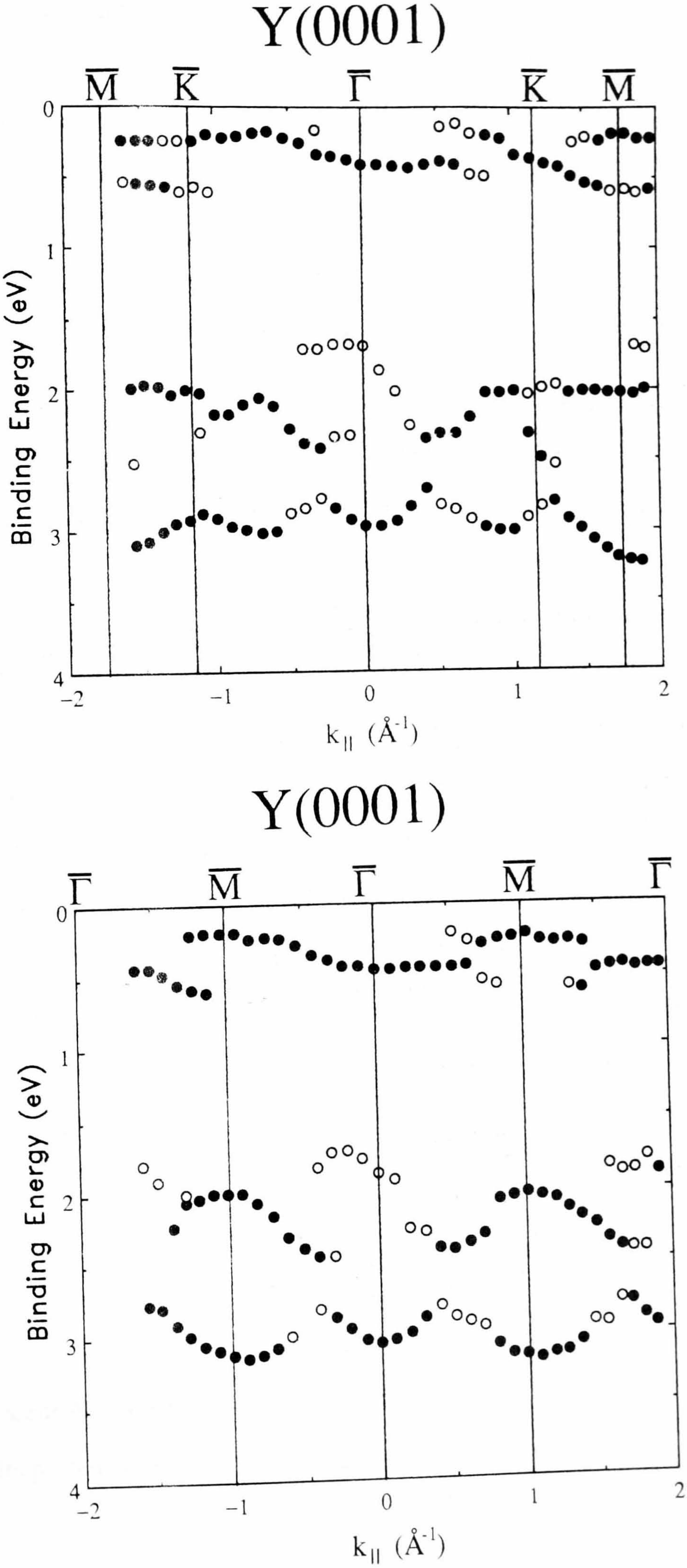

and the different peak widths, the behaviour of all the other valence band features is the same on all three surfaces. With increasing emission angle, along both azimuths, peak *c* disperses towards E_F, reaching a minimum binding energy of ~1.8 eV, before dispersing back to lower binding energies. The Fermi level emission is enhanced at the $\overline{M}$ points rather more than at the K points. Along $\overline{\Gamma K M}$ peak *b* has an intensity maximum at $\theta \approx +40°$, and shows very gentle dispersion to lower binding energy for negative emission angles. There is also some indication that a peak at ~ 3 ev binding energy is dispersing gently to higher binding energy for negative emission angles. The E(**k**) curves for Y show the band crossing E_F between $\overline{\Gamma}$ and $\overline{K}$ that was seen on Ho, but the crossing between $\overline{\Gamma}$ and $\overline{M}$ which was only possibly seen on Ho is quite clearly occurring on Y. With Gd these crossings are difficult to identify and it cannot be unambiguously determined whether or not they occur. The Gd data were recorded using the same spectrometer resolutions as the other data, and higher resolution spectroscopy is unlikely to provide further evidence as the broader peak widths thus appear to be intrinsic. So, to the extent it is possible to determine, the off-normal emission results from Gd and Y support the conclusions drawn from the normal emission and polarisation dependent results, namely that the features seen on Y(0001) and G(0001) are indeed the same as those seen on Ho(0001). Since these three metals represent a reasonable cross section of the hcp rare earths it does not seem unreasonable to suggest that the same features will also be seen on the (0001) surfaces of the rest of the series. Further, given the similarity already noted (see chapter 5) between the spectra from Ho(0001), Ho(11$\bar{2}$0)-(7 × 1) and (reconstructed) Ho(10$\bar{1}$0) surfaces, it is far from impossible that the ARUPS spectra from *all* surfaces of *all* hcp rare earths will show the same features.

6.4 ARUPS of Tb(0001)

The recent ARUPS results from Tb(0001) reported by Wu *et al.* [73] are inconsistent with the results presented in the previous two sections. Their spectra, taken at normal

Fig. 6.24 Normal emission ARUPS spectra of Tb(0001) (after Wu *et al.* [73])

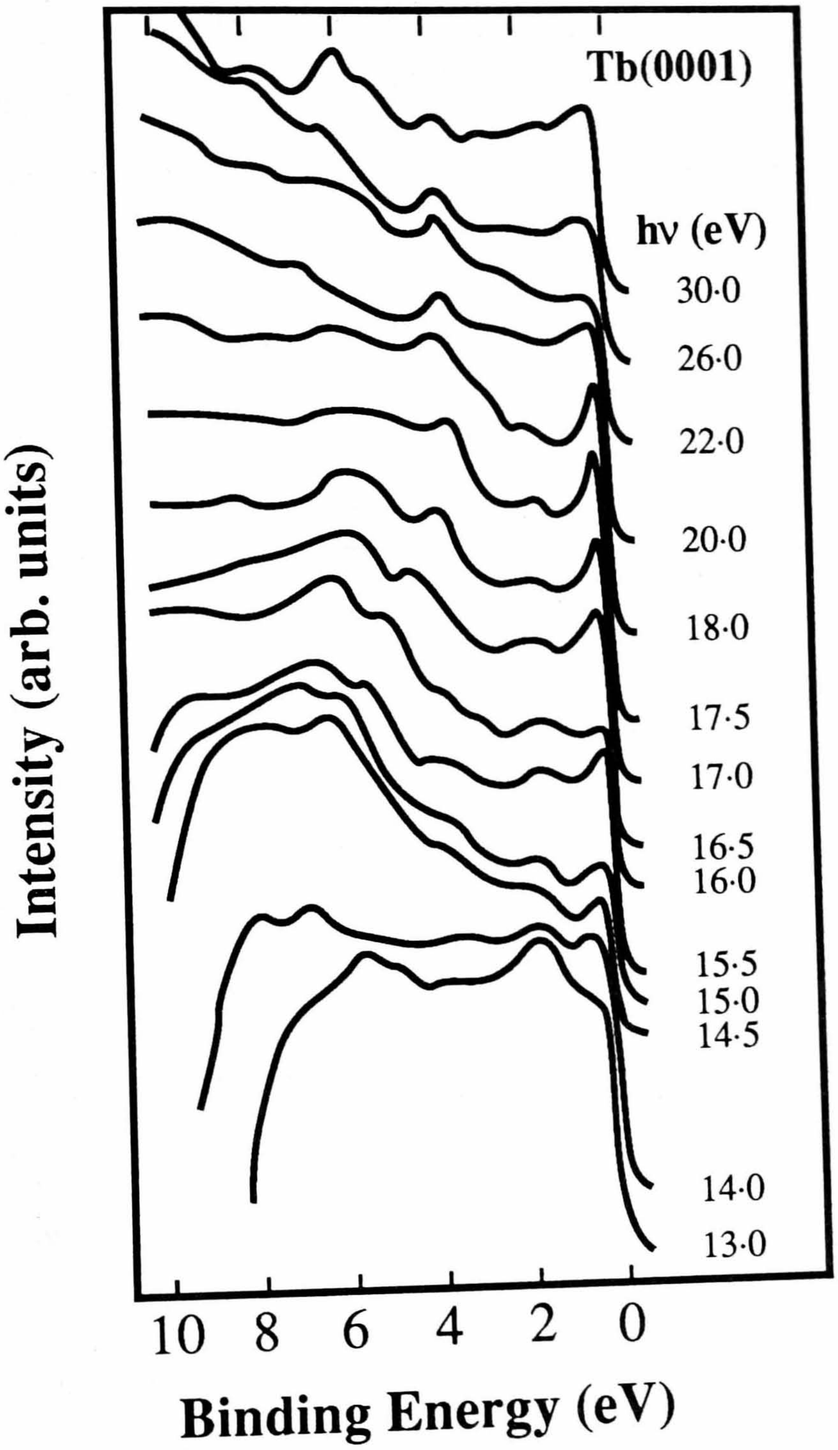

emission, are shown in fig. 6.24. Their analysis of these results showed a shift of the Δ_1 band to a binding energy 1.5 eV deeper than that predicted by their own LMTO bandstructure calculation, with the experimental Γ_{4-} critical point determined to be at a binding energy of 3.6 (±0.15) eV. As mentioned in chapter 3, this result is inconsistent with all the other ARUPS studies of hcp rare earth metals, in which the Γ_{4-} point has been observed at binding energies (± 0.1 eV) of 1.4 eV (Gd) [20, 138], 1.7 eV (Y) [23] and 1.7 eV (Ho). Given the close similarity between the bandstructures of the hcp rare earths (see chapter 3), the value of 3.6 eV for Tb [73] is rather high. Wu *et al* [73] have assumed that their results were characteristic of a clean surface, despite the fact that they observed 10-15% Fe contamination on their Tb sample. This Fe presence is responsible for the weight at E_F seen in fig. 6.24, completely obscuring any intrinsic Tb features which might occur in this region. In order to determine whether the their measurement of the Γ_{4-} point was influenced by the presence of Fe, normal emission ARUPS measurements were performed on Tb(0001) to re-determine the Tb Γ_{4-} critical point binding energy.

The Tb sample, grown using the SSE technique described in chapter 2, proved to be one of the best samples studied for this work. The cleaning procedure described in chapter 4 produced a surface displaying an excellent (1 × 1) LEED pattern (fig. 6.25) and the photoemission spectra showed an intense SODS with a very low contamination level (fig. 6.26). Spectra were also measured around the Fe 3*p* binding energy, and as shown in fig. 6.27 no Fe 3*p* signal could be detected, placing an upper limit of 1% on possible Fe contamination.

To compare more directly with the spectra of Wu *et al.* [73], and with the Gd spectra of Himpsel and Reihl [20], ARUPS spectra were recorded using photon energies down to 12 eV . Although at such low photon energies the second order content from the TGM on beamline 6.2 is rather high (see chapter 4) only the 20 eV spectrum contained *peaks* from second order photoemission. Thus for the low photon energy spectra the background intensity will be rather high but the peak *binding energies* will be unaffected. Normal emission ARUPS spectra of the valence band region (0-5 eV binding energy) are shown in figure 6.28. The spectra show the same three main features as Y, Gd and Ho (labelled *a*, *b* and *c*), at binding energies (± 0.1 eV) of 0.3, 1.5 and 2.7 eV respectively. The $4f\,^8S_{7/2}$ multiplet peak, at a binding energy of 2.3 (± 0.1) eV, can also be seen at photon energies above 40 eV. Note that these spectra bear no resemblance to those of Wu *et al.* shown in fig. 6.24, but are very

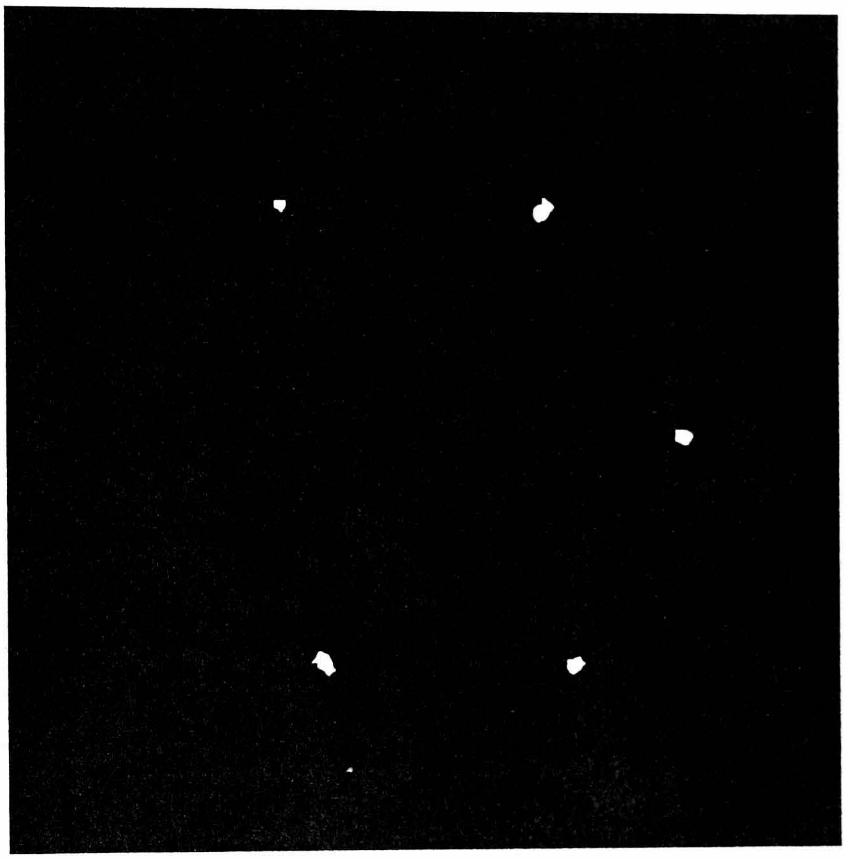

Fig. 6.25 LEED pattern from Tb(0001), beam energy 50 eV

Fig. 6.26 Normal emission ARUPS spectrum of Tb(0001), hν = 40 eV

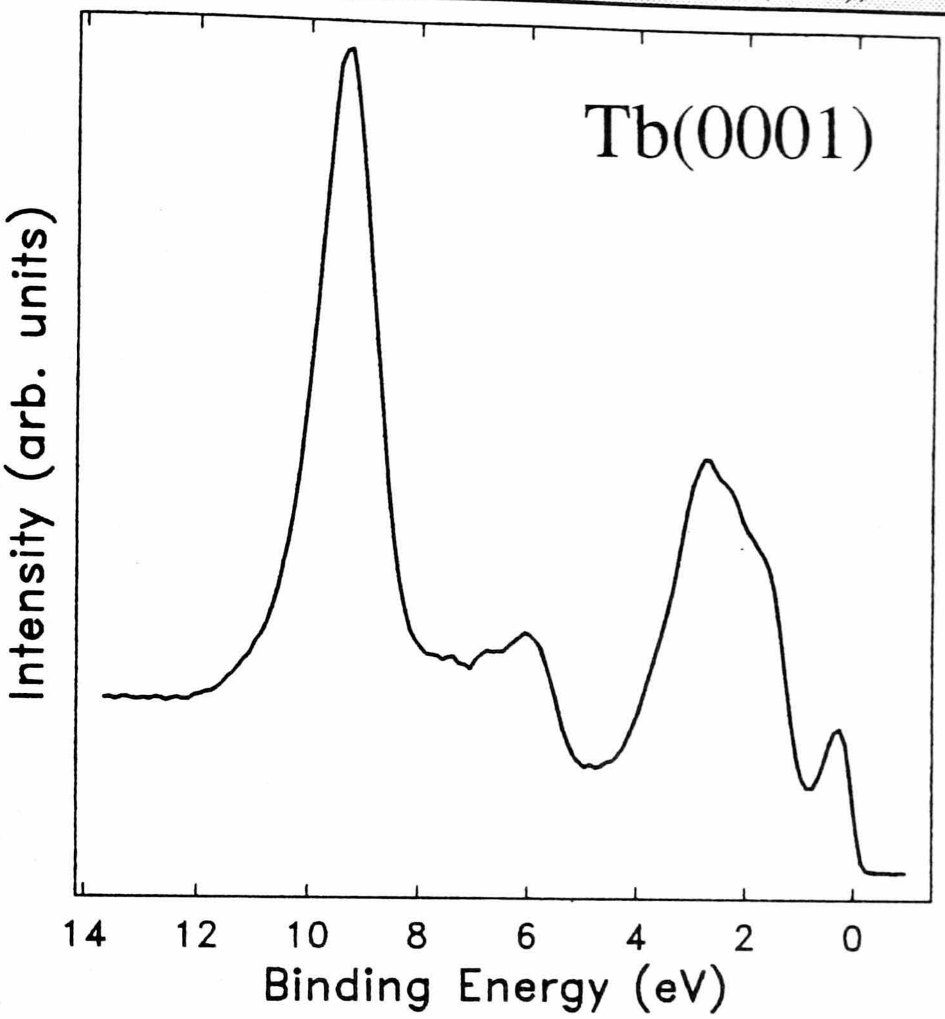

Fig. 6.27 ARUPS spectrum of Tb(0001), hν = 100 eV

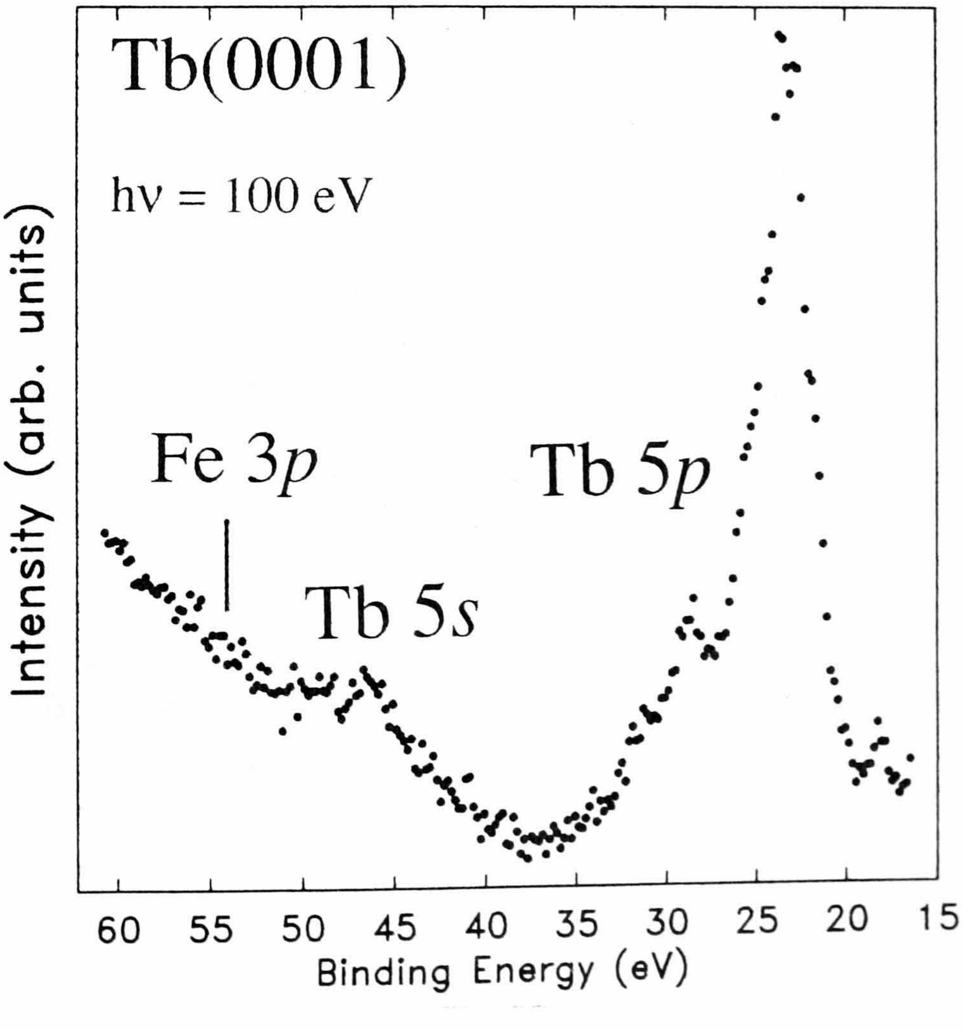

Fig. 6.28 Flux-normalised normal emission ARUPS spectra of Tb(0001), incidence angle 30°, p-polarised radiation

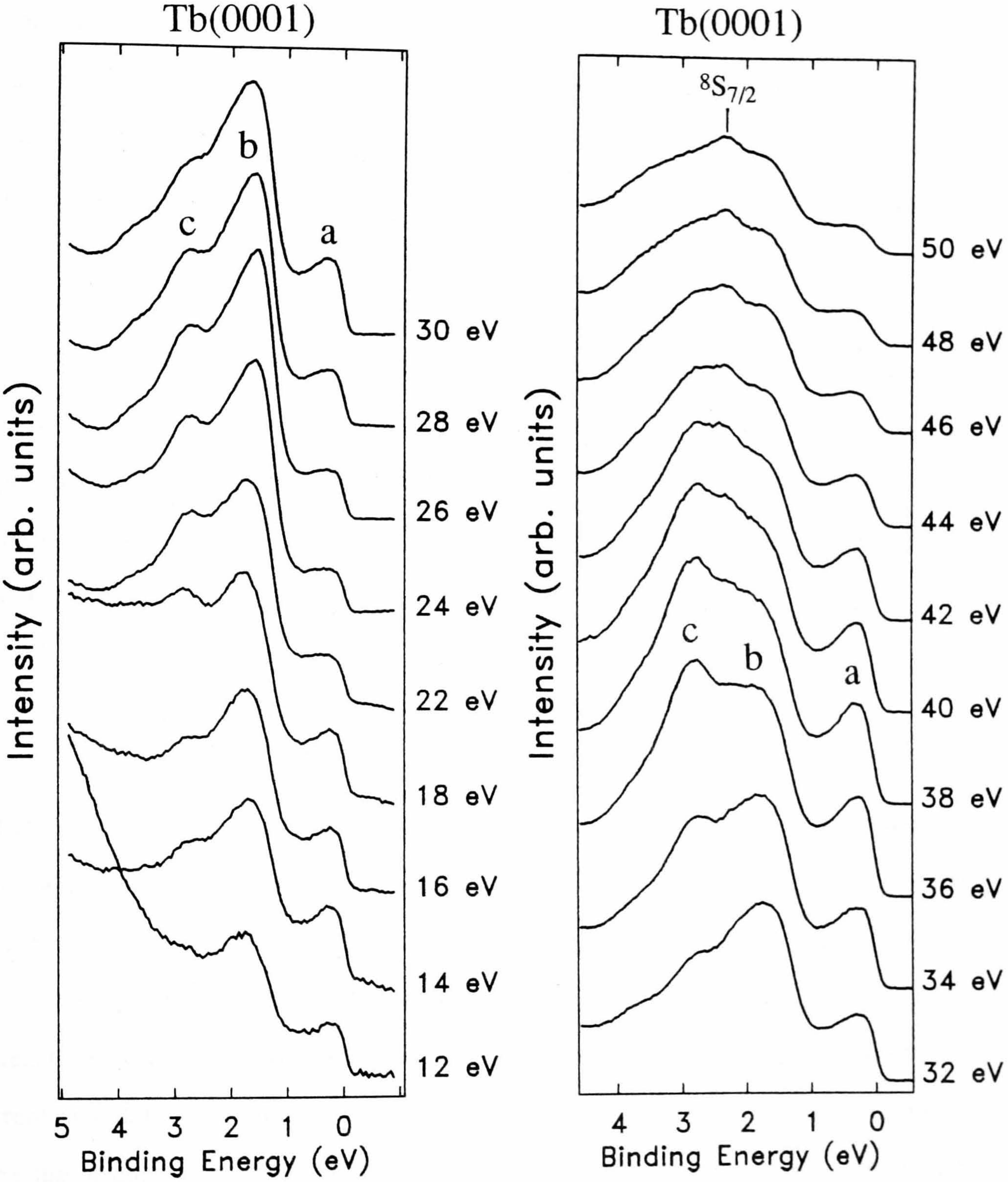

similar to the Gd(0001) results of Himpsel and Reihl shown in fig. 6.1. As Gd and Tb are neighbouring elements in the lanthanide series this is hardly surprising. For the Gd(0001) spectra, as for Y(0001) and Ho(0001), peak *b* was determined to be due to emission from the Γ_{4-} critical point and, by analogy, it is suggested the same assignment applies to Tb(0001). Thus, the binding energy of the Tb Γ_{4-} critical point is found to be 1.5 (± 0.1) eV. In common with Y , Gd and Ho this value is somewhat lower than that predicted theoretically (see table 3.1). This is in marked contrast to the value of 3.6 eV determined experimentally for Tb by Wu *et al* [73], *i.e.*, a shift of 1.5 eV to ***higher*** binding energy. This suggests that the results of Wu *et al* were influenced by the significant level of Fe contamination on their sample.

The value for the binding energy of the Tb Γ_{4-} critical point found from this work is consistent with those of other hcp rare earth metals. The decrease in metallic radii across the lanthanide series (the lanthanide contraction, see fig. 2.2) leads to a corresponding increase in the occupied bandwidth (see chapter 3). It follows that the critical point binding energies for Tb (Z=65) would be expected to lie between those of Gd (Z=64) and Ho (Z=67). Clearly, this is seen to be the case.

6.5 ARUPS from rare earths: general conclusions

It appears, at least for the photon energy range used in this work, that momentum broadening will limit the bulk bandstructure information obtainable from ARUPS of hcp rare earths to the binding energy of the Γ_{4-} critical point. In contrast, it would seem that the surface electronic structure can be comprehensively mapped, with many body effects, in the valence band at least, considerably less troublesome than was at one time thought. The role of photocurrent calculations, combined with improved surface potentials, has proven vital in identifying the origins of the ARUPS features, and as more surfaces are investigated and the calculations improved this looks set to continue. NEWPOOL does not include any relativistic effects, but comparison of the relativistic bands [Fig. 3.9(d)] with the non-relativistic bands

(Fig. 3.10) shows that the relativistic effects on the electronic structure are insufficient to account for the discrepancy between the observed and calculated binding energies of peak *c*. It is possible that the difference in electron-photon matrix elements between non-relativistic and relativistic photocurrent calculations could account for the discrepancy but until relativistic photocurrent calculations are performed for Ho(0001) this will remain an unknown. The differences in binding energies obtained when comparing the theoretical spectra with those of experiment may well be due to the inadequacies of the model. Whilst the use of the supercell slab potentials represents a significant improvement over the rather crude NEWPOOL surface model (Fig. 3.22), the surface potential remains somewhat inaccurate; it is not possible to calculate the work function or the surface energetics for example. As noted in chapter 3, it unlikely that meaningful calculations of the self-energy for the lanthanides can be performed, which effectively precludes the inclusion of many-body effects in the calculations, so the extent of such effects on the lanthanide spectra may remain an unknown. However, given the close similarity between the spectra from Y(0001) with those from the hcp lanthanides, a potentially informative route could be to calculate the self-energy for Y, where of course the DOS is well known (see chapter 3). Since relativistic effects are less important in Y it would even be a useful exercise to include self-energy corrections in NEWPOOL, rather than the comparatively untested relativistic codes.

CHAPTER 7

Core levels

It is far from clear, particularly for the lanthanides, exactly what constitutes a core level. The 4*f* shell is often only partly occupied and usually energetically degenerate with the 5*s*6*d* levels and might therefore be thought part of the valence band. As explained in chapter 3 however, the 4*f*s have many of the properties of core levels, being highly localised and playing a negligible role in the bonding. In contrast the 5*p* levels, although fully occupied and some 20 eV below E_F, have a significant effect on the lattice constants. Such levels are often referred to as "semi-core". As with the definition of a rare earth, the term "core-level" is applied as much by convention as by physics, and for convenience in this work is taken to include both the 4*f*s and the shallow n*p* levels, where n = 3 (Sc), 4 (Y) or 5 (La and the lanthanides), plus any deeper levels.

As already explained the lanthanide 4*f*s and 5*p*s are not without interest from the point of view of bulk electronic structure, but there are other core level phenomena which deserve attention. The measurement of surface core level shifts (SCLS) provides valuable information on surface electronic structure, and comprehensive theoretical [30] and experimental [29] studies of lanthanide 4*f* SCLSs have been reported (see chapter 3). The 4*f* photoemission peaks consist of narrow atomic multiplets (see fig. 3.2) and are thus particularly suited to SCLS measurements. Other core levels, such as the 5*p*s or 4*d*s (at binding energies between 100 and 200 eV) suffer from broad linewidths, finite bandstructure or complex magnetic structure [164], and it is thus much more difficult to extract values for the SCLS. The lanthanide 5*s* levels, at binding energies of around 50 eV, also display multiplets due to magnetic interaction with the 4*f*s, but here the structure is very simple. The 5*s* photoemission peak is a doublet, and the splitting has been correlated [165] to the magnetic moment of the 4*f* shell. It has recently been demonstrated [166] that the analogous Fe 3*s* peak is split into spin-up and spin-down components, and it does not seem unreasonable to assume that the same applies to the lanthanide 5*s* peak. In a series of XPS measurements on Fe-V alloys Jordan *et al.* [167] showed that the Fe 3*s* splitting was correlated to the *local* moment on the Fe site. There seems no reason why this could not also be applied to lanthanide compounds, and it may well prove a useful probe of rare earth alloy and interface magnetism. Much information is thus available from direct photoemission studies of rare earth core levels, but there are also a number of indirect phenomena which are not without interest. The photoionisation cross section of a core level, for photon energies a few eV above the absorption edge, is modulated by the unoccupied DOS, as these are the final states for the ionised electrons. Near-edge X-ray absorption fine structure (NEXAFS) spectroscopy using synchrotron radiation is developing into a powerful probe of the local unoccupied DOS around a core hole, and has found particular application for surface adsorbate studies. This spectroscopy is complementary to BIS, since it does not give momentum resolved information, but since it is a local probe it is potentially useful in the study of rare earth alloys and compounds. Another potentially useful local probe is resonant photoemission at the lanthanide 4*d* edge. The large overlap of the 4*d* and 4*f* wavefunctions gives a very high probability of the promotion of a 4*d* electron into the unoccupied 4*f* levels, a so-called "giant" resonance. The resulting decay of this excited state ejects a 4*f* electron with energy hν - BE, where BE is the 4*f* binding energy. This of course gives an emitted electron with energy identical to that of the 4*f*s emitted by the normal photoemission process. Hence at the 4*d* edge the 4*f* photoemission signal is greatly enhanced. Similar, though less probable, decay routes give enhancement of the rare earth valence band emission, which in an alloy or compound can be used to identify the rare earth contribution to the DOS [168]. The decay of a lanthanide 4*d* core hole can also proceed via the more familiar Auger process. The lineshapes of CCV and CVV Auger features are well known to carry information on local DOS and core hole screening [169], but in the lanthanides these are usually energetically degenerate with the super-Koster-Kronig $N_{4,5}N_{6,7}N_{6,7}$ and $N_{4,5}N_{2,3}N_{6,7}$ features: a comprehensive study of electron excited 4*d* Auger and Koster-Kronig spectra [170] of polycrystalline lanthanides shows that the spectra are exceedingly complex, with a multitude of features superimposed. It thus seems unlikely that Auger spectroscopy will be of much use for lanthanide alloys and compounds.

To date there have been only reports of core level photoemission from two single crystal rare earth surfaces: the *4f*s of Tb(0001) [73] and the *4p*s of Y(0001) [23, 101, 106]. The Tb(0001) *4f* results of Wu *et al.* [73] were obtained from the same surface as their ARUPS valence band data. As shown in chapter 6, the significant degree of Fe contamination on this sample causes significant changes in the valence band emission compared to that from a clean surface, and suggests that their *4f* results cannot be regarded as characteristic of the clean Tb(0001) surface. For this work the Y(0001) measurements were extended to cover the *4s* levels, and measurements made of the *4f* and *5p* levels of Ho(0001) and Gd(0001)

7.1 Y(0001)

In their ARUPS study of Y(0001) Barrett and Jordan [23] showed a wide scan which included the *4p* emission (fig. 7.1), with the apparent binding energy of the *4p* levels slightly

Fig. 7.1 Wide scan ARUPS spectrum of Y(0001) (after Barrett and Jordan [23])

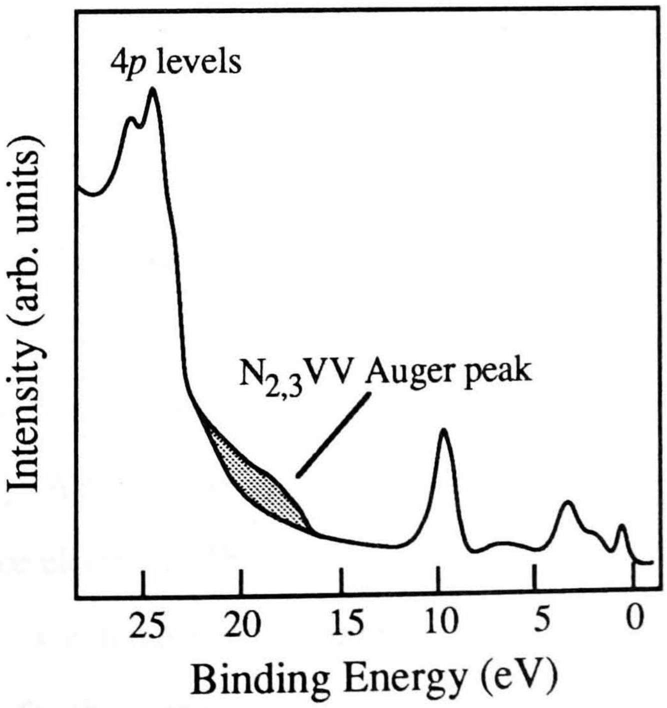

higher than the values obtained by XPS [171] for polycrystalline Y. They suggested that the increased surface sensitivity of ARUPS compared to XPS resulted in emission primarily from surface-shifted 4*p* levels, and noted a shoulder on the low binding energy side of the $4p_{3/2}$ peak which they tentatively attributed to the bulk $4p_{3/2}$ level. In a more detailed study [101] Barrett *et al.* showed that there was a surface core level shift of 0.7 - 0.9 eV to higher binding energy. A supercell slab calculation for Y(0001) [100] showed an SCLS of 0.74 eV to higher binding energy between the top two layers, which is consistent with the photoemission result. The calculation [100] also showed a small, but finite, 4*p* bandwidth. It is therefore to be expected that the experimental lineshape of the various 4*p* peaks will *not* be of a standard form [e.g., Doniach-Sunjic], and thus a more accurate experimental value for the SCLS cannot be obtained by the common practice of curve fitting. To provide a closer comparison between the experimental and calculated shifts, Jordan *et al.* [106] used photocurrent calculations to model the 4*p* lineshape. They used the NEWPOOL code, employing potentials from the slab calculation as described in chapter 3. Their results are compared to the spectra of Barrett *et al.* [101] in fig. 7.2. The absence of relaxation or correlation effects in the calculations leads them to underestimate the binding energy, but otherwise the agreement is impressive. This highlights the effectiveness of slab potentials with the NEWPOOL code, and suggests that the calculated Y(0001) SCLS is reliable. The success of these calculations prompted both the use of the supercell slab geometry to calculate the SCLSs for the lanthanides (see chapter 3), and the use of the slab potential / NEWPOOL combination for the Ho(0001) valence band (see chapter 6).

7.1.1 4*p* core hole Auger and fluorescence decay

The decay of a 4*p* core-hole can proceed along two major routes, i.e., Auger or fluorescence decay. With no core levels at shallower binding energies both these decay routes involve the valence electrons. The corresponding Auger transition is designated $N_{2,3}VV$ and the resulting peak, which has constant kinetic energy, is shown shaded on fig. 7.1. This peak is also responsible for the rising background on the 35 eV spectrum of fig. 5.4, and as it

Fig. 7.2 Experimental and theoretical ARUPS spectra from the 4 *p* levels of Y(0001) (after Jordan *at al.* [106])

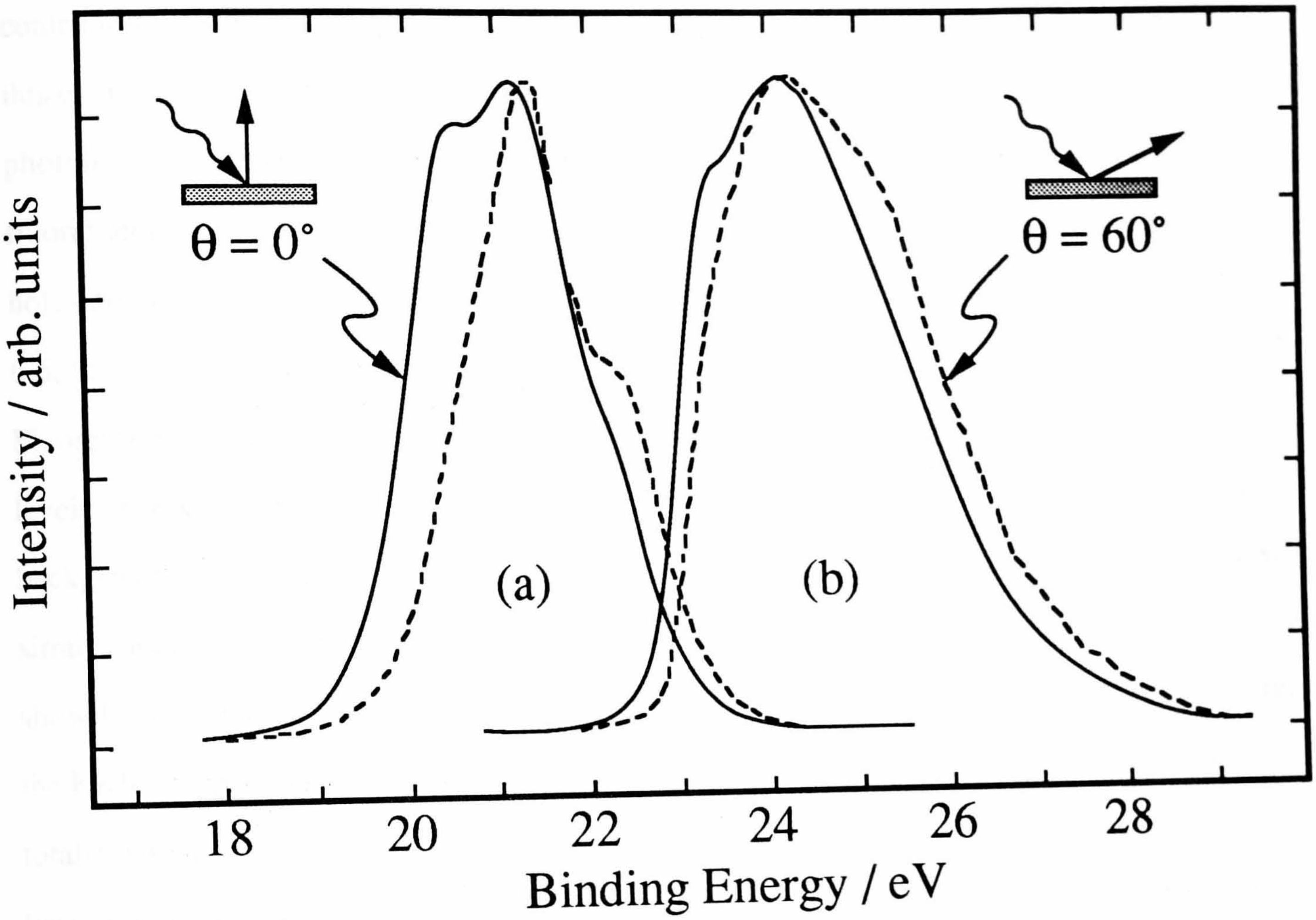

crosses the binding energy region of the SODS it effectively prevents the accurate measurement of the SODS photon energy dependence (see chapter 5). The lineshape of the Auger peak carries information regarding the local electronic structure around the core-hole [169], but the current Cini-Sawatzky [172 -175] model for Auger lineshape analysis is unable to deal with partially occupied *d*-bands, and so at present this information remains inaccessible. A close analogy to the Auger feature is seen in the KRIPES spectra from Y(0001). When the incident electron energy is sufficient to create a 4*p* hole it is possible that the resulting fluorescent photons will be detected by the photon counter. This occurs if the photon energy being detected lies in the range of photon energies produced by the $N_{2,3}V$ radiative transition. This range is determined by the binding energy of the 4*p* hole (E_{4p}), and the valence band width (W), with

$h\nu_{max} = E_{4p}$ and $h\nu_{min} = E_{4p} - W$. The cross section for this transition is somewhat higher than that for direct KRIPES transitions, and so fluorescent photons tend to swamp the KRIPES signal. Fig. 7.3 shows KRIPES spectra from Y(0001) which have a significant contribution from fluorescence. The tick marks indicate the onset of 4*p* ionisation, and since this occurs at a constant electron energy the marks move closer to E_F as $h\nu$ is increased. As the photon energy being detected increases so eventually it will be greater than $h\nu_{max}$ of the fluorescent decay, and as a result fluorescent photons will not be detected even though 4*p* core holes are still being created by the incident electron beam. Thus the KRIPES spectra of fig. 6.6, at photon energies higher than those of fig. 7.3, show only direct KRIPES transitions. Fluorescence features have been seen in KRIPES studies of several metals with shallow core levels. The CIS KRIPES spectra of Nb(110) [176] show an $N_{4,5}V$ peak rather than a rising background, since all the photon energies produced by the fluorescent decay are detected simultaneously (see chapter 4). The isochromat spectra of Na(110) [125] and Ta(110) [122] show fluorescence from the Na 2*p* levels and the Ta 4*f* levels respectively, but their effect on the KRIPES spectra are rather different. For Na the KRIPES transitions are very weak, and are totally swamped, whereas for Ta the fluorescence photons cause only a somewhat higher background. As for Auger features the fluorescence lineshape, in CIS KRIPES at least, carries local DOS information. Unlike CVV Auger the final state is a single hole, analogous to the photoemission final state, and so the relationship between the lineshape and the local DOS might be thought simpler than in CVV Auger. However, as relatively low energy electrons are used in KRIPES the distribution of the unoccupied DOS will play a role in determining the lineshape. The ionisation probability for electrons with energy close to the binding energy of the 4*p*s is modulated by the unoccupied DOS, in a similar manner to the structure seen in NEXAFS. Thus, the dependence of the fluorescence lineshape on the local DOS is in fact rather complex.

Fig. 7.3 KRIPES spectra from Y(0001), showing 4*p* fluorescence, onset shown by tick marks

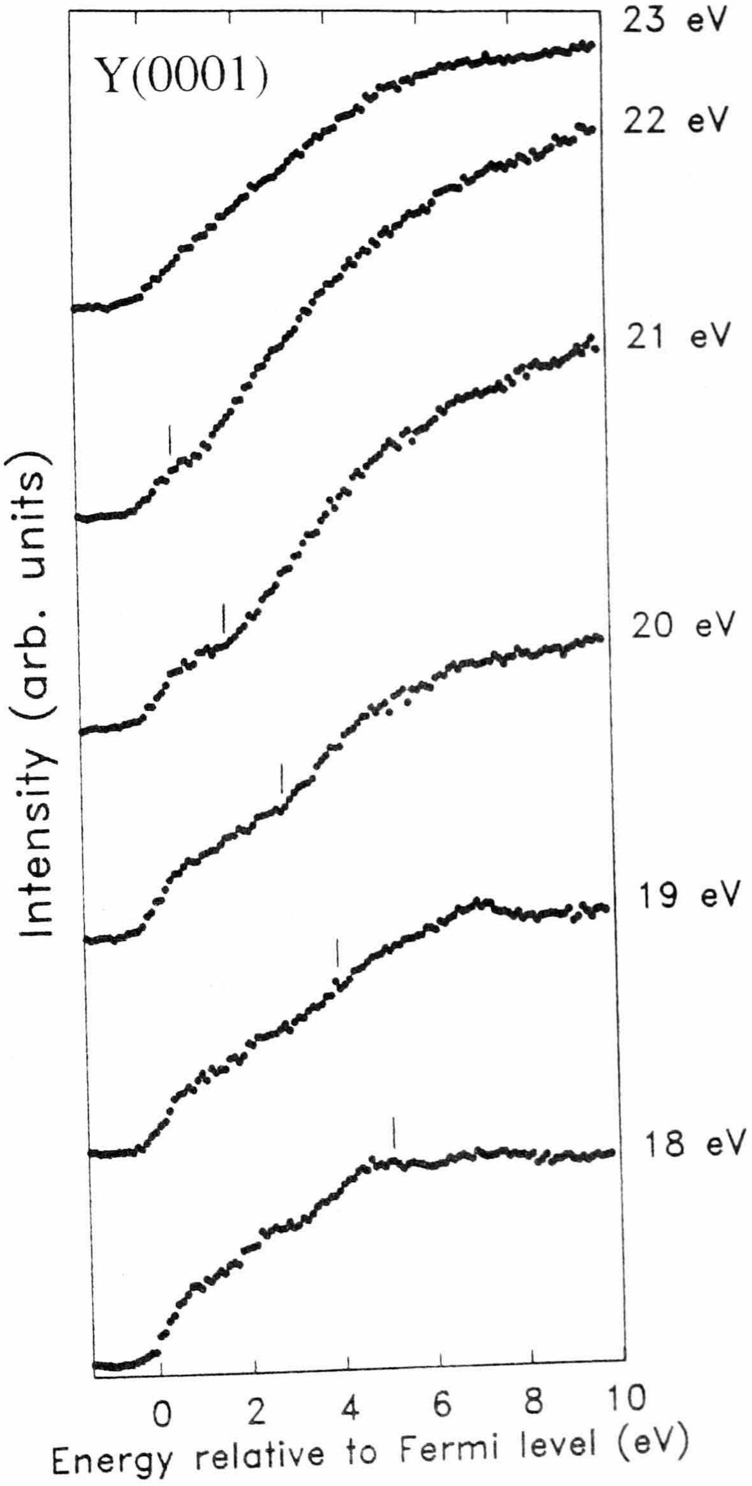

7.1.2 4*s* ARUPS spectra

Measurements of the Y(0001) 4*s* levels were made using the same crystal as used in the KRIPES and (valence band) ARUPS measurements described in chapter 6. The 4*s* levels , with significantly greater binding energy, are much more localised than the 4*p*s. This means that the rather large lifetime broadening of a 4*s* core hole, which has the Koster-Kronig decay routes denied to a 4*f* hole, need not be a problem, since it is most unlikely that the 4*s* levels will have a significant bandwidth. As it follows that curve fitting is probably a valid exercise, it might be then possible to extract a more accurate experimental value for the Y(0001) SCLS from measurements of the 4*s* peaks than from the 4*p*s. However, the practical details of such a measurement on the equipment available, i.e., beamlines 6.1 and 6.2 at Daresbury make this rather difficult. The photoionisation cross-section of the Y 4*s* levels has a maximum for hν = 80 eV [143]. In this energy region the flux from the TGM on beamline 6.2 is very poor (see fig. 4.4). On beamline 6.1 the flux is rather better, but the photon energy resolution is ~ 0.7 eV, i.e. of the same order as the SCLS. In addition the chamber on 6.1 is not at present fitted with an angle-resolving analyser, thus the experiment had to be performed on 6.2. The 4*s* peaks lie on a large inelastic background produced by the valence band, SODS and 4*p* emission. The low cross section of the 4*s* levels compared to the 4*p*, 4*d* and 5*s* subshells [143] results in a very poor signal-to-noise ratio in the 4*s* region. Background subtracted 4*s* spectra, each recorded over a 12 hour period, are shown in fig. 7.4. Note that the absence of a magnetic moment results in a single 4*s* peak as the degeneracy of the spin-up and spin-down components is not lifted. It is possible that the off-normal spectrum, which is more surface sensitive, indicates the presence of an SCLS, but it is far from clear. Given the large degree of data point scatter, and the probable effects of contamination built up during the long count times, it does not seem reasonable to extract an SCLS value from curve fitting to these spectra. However, if the analyser on 6.2 is replaced by a multi-channel analyser, as has been mooted, it may well be possible to repeat these measurements with sufficient signal to noise ratio, and in

Fig. 7.4 ARUPS spectra from the 4*s* levels of Y(0001), hν = 80 eV

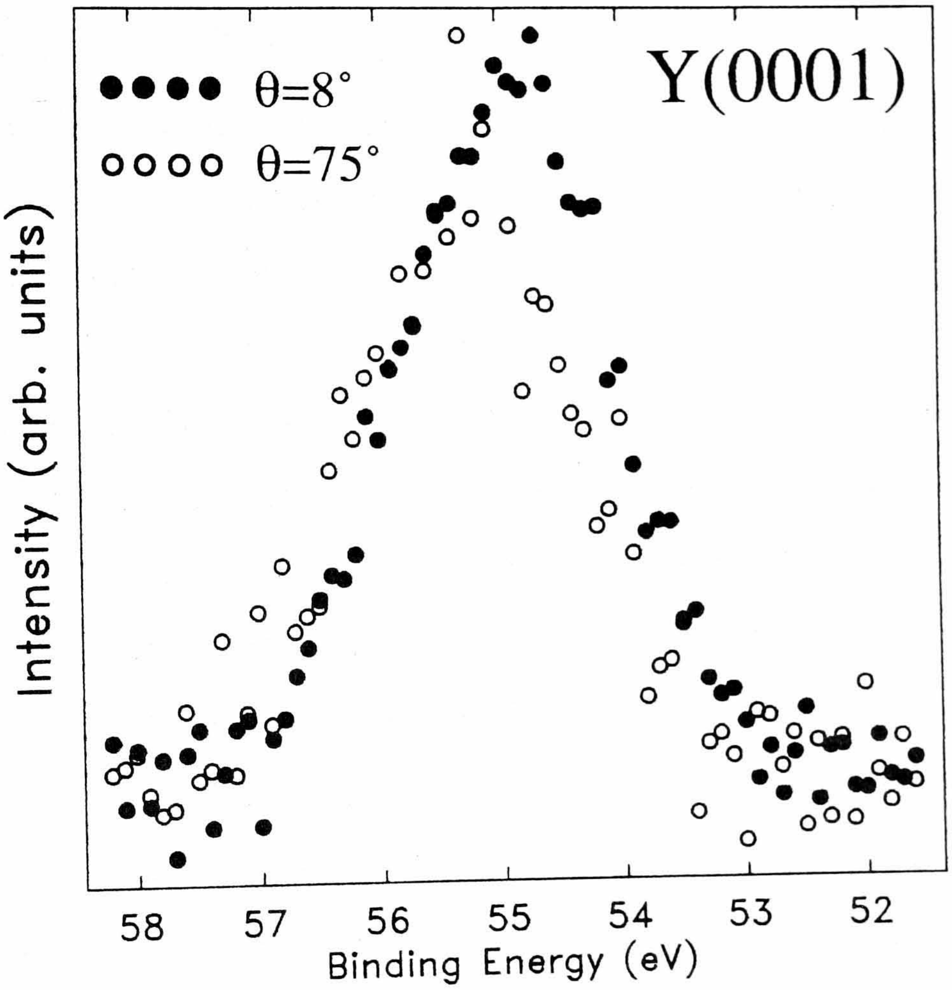

short enough time, for an accurate value of the SCLS to be determined. This is also likely to apply to the 3*s* levels of Sc, which may be the most accurate route to determining SCLSs for Sc since it is possible that the Sc 3*p*s will have a finite bandwidth similar to that of the Y 4*p*s.

7.2 Ho(0001) and Gd(0001)

Measurements of the Ho(0001) and Gd(0001) 4*f* and 5*p* levels were performed on the same samples as were used for the valence band ARUPS measurements described in chapter 6. Both types of core level were investigated using photons from the 1800 mm^{-1} grating on the TGM, but the reasons for this were rather different. For 4*f* measurements it is preferable to use photon energies of ~ 100 eV, since the lanthanide 4*f* photoionisation cross sections show maxima in this region [143] and the cross-section of the 5*d* levels is declining towards their Cooper minima [143]. This gives the largest 4*f* / 5*d* ratio of photoemission spectra in the VUV range. However, as already noted in section 7.1.2 the flux from the TGM is very low in this photon energy range, and so it is necessary to use rather a low resolution (0.25 eV) to obtain a reasonable count rate. For the 5*p* levels the photoionisation cross section has a maximum at $h\nu \approx 40$ eV, and declines with increasing photon energy [143]. But in order to separate the 5*p* peaks from the $N_{4,5}VV$ Auger peak, and from the secondary electron tail such that the 5*p* peaks lie on a smooth background (for convenience in background subtraction), high photon energies are required. As shown in fig. 4.4 the TGM flux tails off rapidly with increasing photon energy, and as a compromise 60 eV photons were used. The flux was again rather poor and so, as for the 4*f* measurements, a resolution of 0.25 eV was used.

7.2.1 4*f* SCLS

The motivation for measuring the SCLS of the lanthanide metals stems from the slab calculations of Begley *et al.* [30]. Measurements of the SCLS of the (0001) surfaces would provide a critical test of these calculations, which are also used to provide potentials for photocurrent calculations such as those described in chapter 6. Further, comparisons of the SCLS of the (0001)-(1 × 1), $(11\bar{2}0)$-(7 × 1) and $(11\bar{2}0)$-(1 × 1) surfaces might give some insight into the energetics of the $(11\bar{2}0)$ reconstruction mechanism. The obvious core levels to use in lanthanide SCLS measurements are the 4*f*s, and a comprehensive study of the 4*f* SCLSs for polycrystalline lanthanides has been published [29]. On clean (0001) surfaces however, the presence of the SODS causes serious problems in measuring the SCLS. Spectra of Gd(0001), taken using 90 eV photons, are shown in fig. 5.7. The SODS appears as a shoulder on the high binding energy side of the 4*f* peak, and effectively prevents the determination of an SCLS from these data. For Ho(0001) similar problems are encountered. Fig. 7.5 shows spectra from Ho(0001) taken using 100 eV photons. As with Gd(0001) the SODS obscures part of the 4*f* multiplet, but the low binding energy region, which can be seen in fig. 3.2, is clear of SODS interference. However the low resolution means that the individual components are not resolved, and curve fitting would be required to extract a value for the SCLS from these data. Unfortunately there is some contribution from residual contamination to this region of the spectrum (see figs. 4.9 and 5.8 for examples of contamination related features), and, given that the lineshape of these features is both unknown and will probably vary with emission angle, curve fitting is not a viable option. It seems likely that the same problems will be encountered for all the (0001) surfaces. In all cases the 4*f* multiplet lineshape will be modified by the SODS, residual contamination, or valence band features. A possible solution to this might be high resolution XPS, using deeper core-levels such as the 3*d*s. The 5*p* levels almost certainly have a significant bandwidth (see chapter 3 and section 7.2.2), which precludes their use, the 5*s* peak is very weak, broad and split by magnetic effects, and the 4*d*s display multiplets due to interaction with the partially occupied 4*f*s. An alternative might be to perform measurements at the 4*d*-4*f* giant resonance, where the intensity of the 4*f* emission is greatly enhanced over the other components of the spectrum including, presumably, the SODS. As yet there have been no 4*d*-4*f* resonant photoemission studies of any clean rare earth single crystal surfaces.

Fig. 7.5 ARUPS spectra from the 4*f* levels of Ho(0001), hν = 100 eV

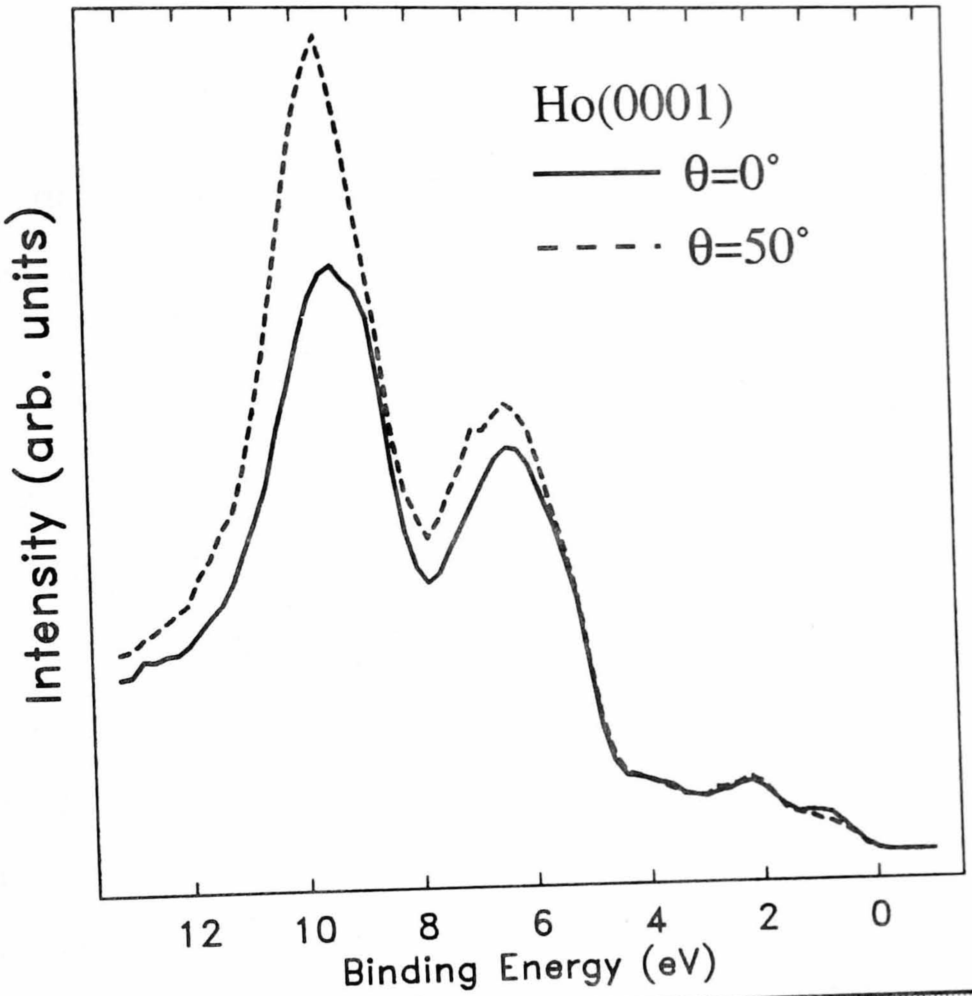

Fig. 7.6 ARUPS spectra from the 5*p* levels of Gd(0001), hν = 60 eV

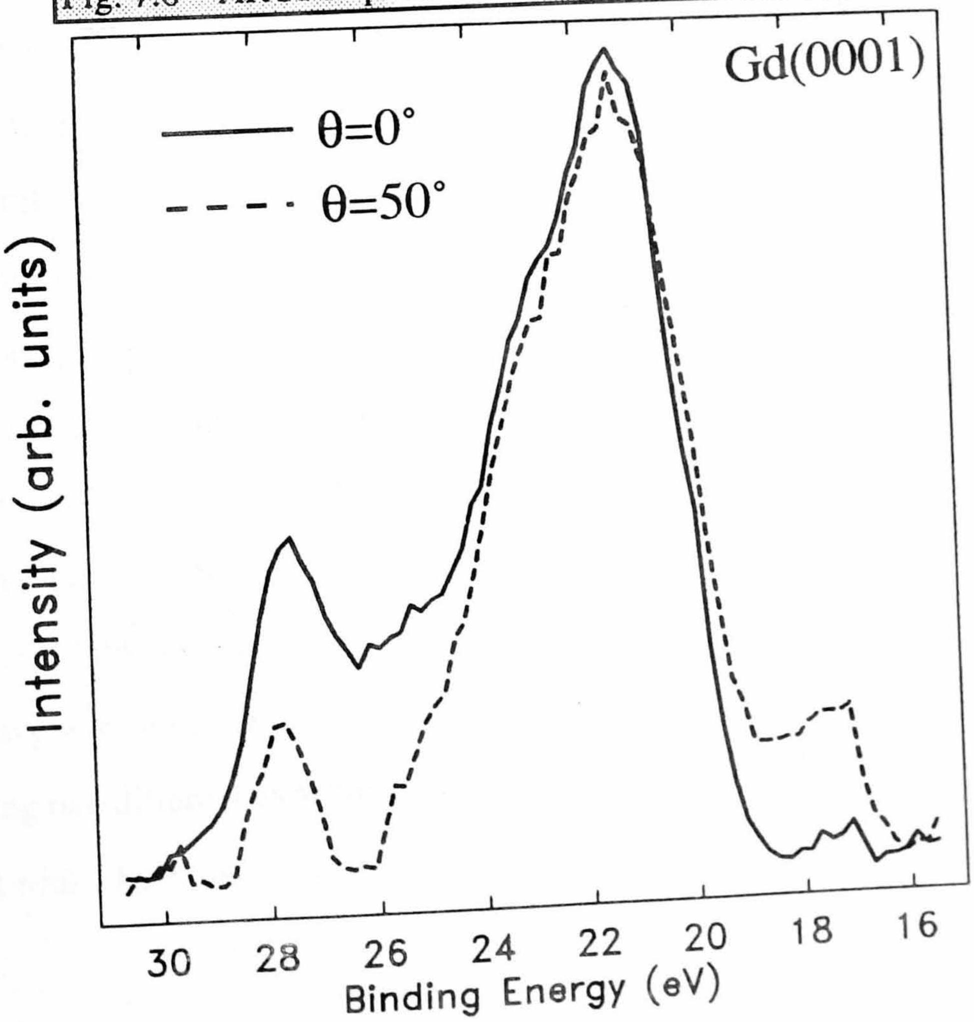

7.2.2 5*p* band effects

The bandstructure calculations of Temmerman and Sterne [81] indicated that the Gd 5*p* levels possessed a significant bandwidth (see chapter 3), probably sufficient to be identified by ARUPS measurements. However, as shown in fig. 7.6, ARUPS results from Gd(0001) do not give the expected spin-orbit split 5*p* peak. Instead a complicated multiplet structure is observed, as has also been seen for polycrystalline Gd films [164], due to magnetic interactions with the 4*f* shell. It seems reasonable to assume that the results of Temmerman and Sterne [81] also apply to the other heavy rare earths, since their electronic and geometric structures are so similar. Thus 5*p* bandstructure investigations by ARUPS need not be limited to Gd. The 5*p* levels of Ho(11$\bar{2}$0)-(7 × 1) were measured during the course of the ARUPS study of its valence band presented in chapter 5. These were seen to have the nominal $5p_{1/2}$ and $5p_{3/2}$ peaks and thus it seemed that Ho might be a better subject for 5*p* ARUPS investigation than Gd. To avoid complications arising from the (11$\bar{2}$0)-(7 × 1) reconstruction ARUPS measurements were performed on Ho(0001). Fig. 7.7 shows ARUPS spectra from Ho(0001) taken at normal ($\theta = 0°$) and off-normal ($\theta = 50°$) emission. At normal emission the intensity ratio of the $5p_{1/2}$ and $5p_{3/2}$ peaks is, to a reasonable approximation, that expected from the relative occupancies of these levels, i.e., 1:2. At off-normal emission this no longer holds - the $5p_{1/2}$ peak is more intense than the $5p_{3/2}$ peak. Although at $\theta = 50°$ the surface sensitivity is greatly enhanced this intensity changeover cannot be attributed to either a surface core level shift (~ 0.6 eV for Ho [29, 101]) or a chemical shift due to residual surface contamination, since these would affect both peaks equally. However, if the 5*p* levels possess significant bandwidth it is entirely feasible that the intensities of the spin-orbit split components might vary with emission angle. Further evidence is provided by an additional experiment employing two different experimental geometries (fig. 7.8). The photon incidence angle is kept constant while the emission angle is set to the same value either side of the surface normal. The

Fig. 7.7 ARUPS spectra from the $5p$ levels of Ho(0001), hν = 60 eV

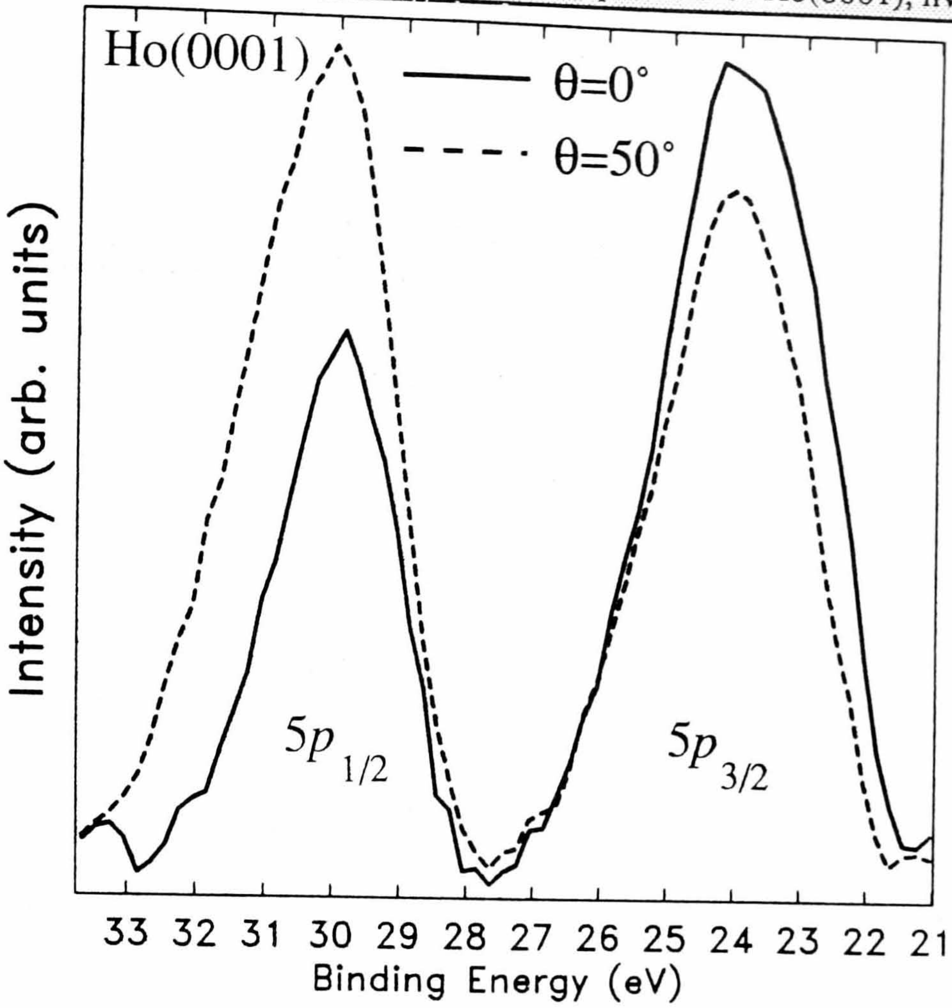

Fig. 7.9 ARUPS spectra from the $5p$ levels of Ho(0001), using the geometry of Fig. 7.8

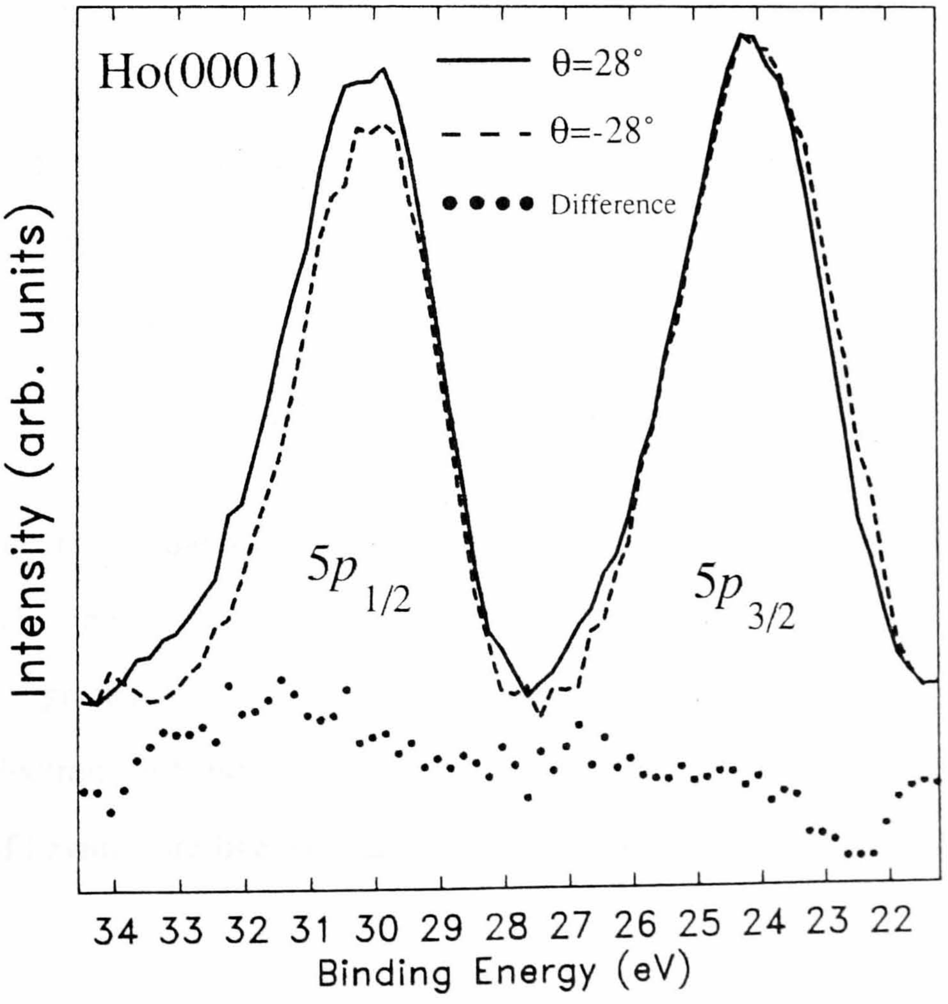

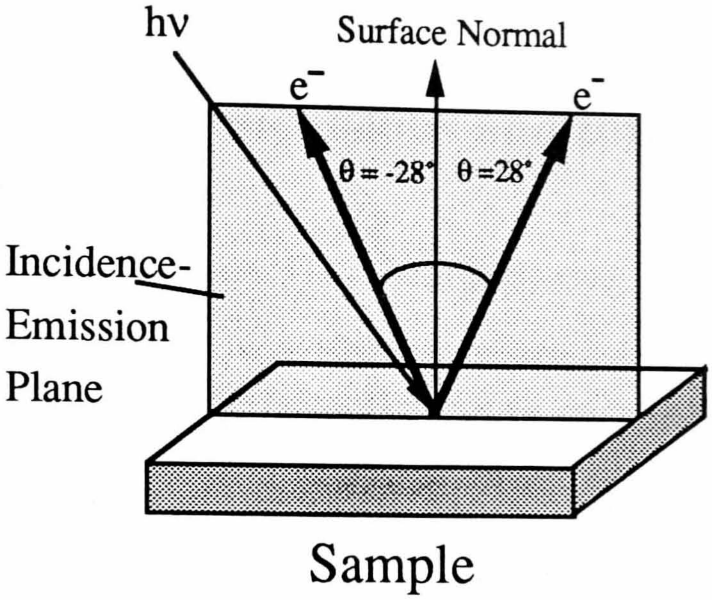

Fig. 7.8 Geometry used to test for momentum dependence

only difference between these geometries is the polarisation of the light relative to the momentum of the emitted electron. In comparing the results from these two geometries the existence, or otherwise, of an SCLS or chemical shifts due to contamination are essentially irrelevant since the surface sensitivity remains constant. If the 5*p* levels were 'true' core levels, i.e., with no momentum dependence, then spectra recorded in these two geometries should be identical. Fig. 7.9, which shows the results of this experiment, demonstrates that the two different geometries produce different spectra.

There are several conclusions to be drawn from these results. As this phenomenon seems unlikely to be limited to the heavy rare earths it follows that caution should be applied when attempting to use the combination of shallow *p* levels and ARUPS to measure SCLSs. It also appears that the results of Temmerman and Sterne [81] have been vindicated. The 5*p* levels of Ho, and by analogy those of the other heavy lanthanides (including Gd) probably do possess a significant bandwidth, and should therefore be treated on an equal footing to the valence electrons in bandstructure calculations. This puts the heavy rare earths in the unusual position of having core-like valence electrons (the 4*f*s) and band-like core levels (the 5*p*s).

CHAPTER 8

Overall conclusions and future prospects

Bandstructure calculations have been performed for all the hcp and dhcp rare earths, and the results compared with the available theoretical and experimental data, much of the latter coming from the KRIPES and ARUPS studies of chapter 6. With regard to the bulk energy bands of these metals there are several general conclusions that can be drawn:

The bulk energy bands of Y can be regarded as well understood. Three different calculation methods (KKR, LAPW and LMTO) have been shown to produce essentially the same results for this metal, and the KRIPES measurements of Y(0001) have shown that the unoccupied critical point energies observed experimentally are in good agreement with the calculations. The agreement between the occupied Γ_{4-} point energy observed in ARUPS and that given by the calculations is not as good, but the discrepancy is not serious. It does not seem unreasonable to suggest that the calculations for Sc can also be regarded as reliable since Sc, like Y, has no localised levels close to E_F.

The situation for the hcp lanthanides is much less clear. It would appear that treating the 4*f*s as bands within the LDA produces erroneous results, and that with current bandstructure methods the preferred alternative is to treat them as core levels. The early non-self-consistent calculations for these metals have been shown to be reasonably correct when compared to self-consistent LMTO calculations. The Fermi surfaces produced using these early calculations may therefore be regarded as accurate, an argument supported by such dHvA measurements as exist. There is clearly a requirement for more such measurements, as there are almost no results for the rare earths where the Fermi surface is of most interest i.e., the magnetic lanthanides Tb - Tm. Such experiments will however, be extremely difficult. It would also be useful to have dHvA results for Eu, as the Fermi surface calculation of fig. 3.14 remains entirely untested. The Eu bandstructure (fig. 3.15) remains similarly untested, and ARUPS or KRIPES measurements for this metal would be very instructive.

It is not possible to completely rule out the effects of hybridisation of the 4*f*s with the *sd* levels, although the evidence for this is circumstantial to say the least. A comparison of the ARUPS results for Y(0001) with those from the (0001) surfaces of Gd, Tb and Ho suggests that the influence of the 4*f* levels on the *sd* bands is minimal, but there may be subtle effects too small for these measurements to resolve. A very promising theoretical development is the inclusion of the self-interaction correction (SIC) within the LDA. This goes part way to simulating correlation effects in localised *bands*, and in a recent calculation Szotek *et al.* [177] showed that the inclusion of the SIC in a calculation for Pr split the 4*f* bands around E_F. It would be interesting to see if the results of this calculation produce better agreement with the ARUPS data of Dhesi *et al.* [87] than the calculation of fig. 13(b). Perhaps of equal concern is the treatment of the lanthanide 5*p* core levels. The ARUPS results for the Ho(0001) 5*p*s are strongly suggestive of a significant bandwidth for these levels, and they should therefore be included as bands in bandstructure calculations. However, they are still very localised and in order to treat them correctly the resulting correlation effects must be included i.e., the SIC is required for the 5*ps* as well as the 4*f*s. It also appears that spin-polarisation must be included to give good agreement with the ARUPS results from the lanthanides. It would be useful to have ARUPS data from further along the series than Ho, to see if the agreement with the non-spin-polarised LMTO calculations of fig. 3.9 improves as the 4*f* moment decreases. The temperature dependent ARUPS data from Gd(0001) suggests that the exchange splitting of the *sd* bands persists above the Curie temperature, and it is likely that the same will also be true of the other magnetic rare earths. Spin-polarised ARUPS measurements are required to unambiguously identify the exchange split components of the Gd(0001) valence band.

The situation for bulk energy bands of the rare earth metals can be summarised as follows. Spin-polarised calculations including the SIC for both the 4*f* and 5*p* levels represent a potentially tractable route to determining their electronic structure with some accuracy. However, such calculations will consume large amounts of computer time, and non-spin polarised calculations without the SIC, treating the 4*f* and 5*p* levels as part of the atomic core may well be a more cost-effective exercise when sub-eV accuracy is not required. The same is likely to apply to lanthanide alloys and compounds.

In addition to the bulk electronic structure information provided by the ARUPS studies, there is also a wealth of detail concerning the electronic structure of the (0001) surfaces of hcp rare earths. The detail seen in the off-normal ARUPS spectra presented in this thesis offer several opportunities. Firstly the investigation of subtle trends in surface electronic structure throughout the rare earth series, which may shed further light onto the bulk electronic structure problem. Secondly, with the calculation of suitable surface bands to compare with experiment it may lead to a detailed *ab-initio* understanding of the (0001) surface electronic structure of rare earths. This is of not only of intrinsic interest, but may in turn lead to insights into the mechanism of the (7 × 1) reconstruction, and to the growth mode of rare earth superlattices. Since it is the electronic structure of the rare earth – rare earth interfaces which ultimately govern the magnetic structure of these superlattices, knowledge of the rare earth surface electronic structure is a useful starting point in understanding their unique magnetic behaviour. Other interfaces of interest are those between rare earths and semiconductors, and it may be possible to grow semiconductor films on single crystal rare earth substrates. The usual mode of studying such interfaces consists of a rare earth film grown on a semiconductor substrate, and this leads to the interesting possibility of studying these interfaces from underneath. Finally, since an understanding of the electronic structure of the clean surface would appear to be a pre-requisite to understanding the chemical properties of adsorbate systems, this opens up the prospect of the kind of surface chemistry which has been studied for many years on transition metal surfaces. To date there have been exactly zero studies of adsorbates on hcp or dhcp rare earth single crystals. It would be surprising if this were to remain so for much longer.

References

[1] K.Arrhenius *Svenska Akad. Handl.* 217 (1788)

[2] *1787 - 1987 Two Hundred Years of Rare Earths* ed. K.A.Gschneidner Jr. and J.Capellen, RIC, Ames and North-Holland, Amsterdam (1987)

[3] *Handbook on the Physics and Chemistry of Rare Earths* eds. K.A.Gschneidner Jr. and L.Eyring, vol. 11, North-Holland, Amsterdam (1988)

[4] K.A.Gschneidner Jr. *J. Less-common Metals* **100** 1 (1984)

[5] R.C.Young *J. Physique* **40** *colloque* **C5** 71 (1979)

[6] S.Tanuma, Y.Ishizawa, H.Nagasawa and T.Suguwara *Phys. Lett.* **25A** 669 (1967)

[7] S.Tunuma, W.R.Datar, H.Doi and A.Dunsworth *Solid State Comms.* **8** 1107 (1970)

[8] J.A.Hoekstra and R.A.Phillips *Phys. Rev.* **4A** 4184 (1971)

[9] R.C.Young, R.G.Jordan and D.W.Jones *Phys. Rev. Lett.***31** 1473 (1973)

[10] P.G.Mattocks and R.C.Young *J. Phys. F: Metal Phys.* **7** L19 (1977)

[11] P.G.Mattocks and R.C.Young *J. Phys. F: Metal Phys.* **7** 1219 (1977)

[12] S.J.C.Irvine, R.C.Young, D.Fort and D.W.Jones *J. Phys. F: Metal Phys.* **8** L269 (1978)

[13] P.G.Mattocks and R.C.Young *J. Phys. F: Metal Phys.* **8** 1417 (1978)

[14] W.R.Johanson, G.W.Crabtree and F.A.Schmidt *J. Appl. Phys.* **53** 2041 (1983)

[15] F.P.Netzer and J.A.D.Matthew *Rep. Prog. Phys.* **49** 621 (1986)

[16] F.Gerken, J.Barth, R.Kammerer, L.I.Johansson and A.Flodstrom *Surf. Sci.* **117** 468 (1982)

[17] N.V.Smith in *Photoemission from Solids I: General Principles* ed. M.Cardona and L.Ley , Springer-Verlag, Berlin (1978)

[18] N.V.Smith *Rep. Prog. Phys.* **51** 1227 (1988)

[19] J.B.Pendry *J. Phys. C: Solid State Phys.* **14** 1381 (1981)

[20] F.J.Himpsel and B.Reihl *Phys. Rev.* **28B** 574 (1983)

[21] E.Jensen and D.M.Wieliczka *Phys. Rev.* **30B** 7340 (1984)

[22] G.Rosina, E.Bertel, F.P.Netzer and J.Redinger *Phys. Rev.* **33B** 2364 (1986)

[23] S.D.Barrett and R.G.Jordan *Z. Phys. B- Cond. Matter* **66** 375 (1987)

[24] S.D.Barrett, R.G.Jordan and A.M.Begley *J. Phys. F: Metal Phys.* **17** L145 (1987)

[25] W.Alexander and A.Street *Metals in the Service of Man* (9th. edition), Penguin, London (1989). Since this edition was published the term 'pandemonium' has gained colloquial use as the name for (hypothetical) hcp praseodymium.

[26] F.Szabadvary in *Handbook on the Physics and Chemistry of Rare Earths* eds. K.A.Gschneidner Jr. and L.Eyring, vol. 11, North-Holland, Amsterdam (1988)

[27] H.L.Skriver in *Systematics and Properties of the Lanthanides* ed. S.P.Sinha, Reidel, Dordrecht (1982)

[28] W.A.Grosshans, Y.K.Vohra and W.B.Holzapfel *J. Mag. Mag. Mat.* **29** 282 (1982)

[29] F.Gerken, A.S.Flodstrom, J.Barth, L.I.Johansson and C.Kunz *Physica Scripta* **32** 43 (1985)

[30] A.M.Begley, R.G.Jordan, W.M.Temmerman and P.J.Durham *Phys. Rev.* **41B** 11780 (1990)

[31] K.A.Gschneidner Jr. *J. Less-common Metals* **110** 1 (1985)

[32] D.C.Koskenmaki and K.A.Gschneidner Jr. in *Handbook on the Physics and Chemistry of Rare Earths* eds. K.A.Gschneidner Jr. and L.Eyring, vol. 1, North-Holland, Amsterdam (1978)

[33] W.C.Koehler in *Magnetic Properties of Rare Earth Metals* ed. R.J.Elliott, Plenum, London (1972)

[34] W.C.Koehler and R.M.Moon *Phys. Rev. Lett.* **29** 1468 (1972)

[35] S.K.Sinha in *Handbook on the Physics and Chemistry of Rare Earths* eds. K.A.Gschneidner Jr. and L.Eyring, vol. 1, North-Holland, Amsterdam (1978)

[36] H.Bjerrem-Moller, J.Z.Jensen, M.Wulff, A.R.Mackintosh, O.D.McMasters and K.A.Gschneidner Jr. *Phys. Rev. Lett.* **49** 482 (1982)

[37] T.Kasuya *Prog. Theoret. Phys. (Japan)* **16** 45 (1956)

[38] K.Yosida *Phys. Rev.* **106** 893 (1957)

[39] M.A.Ruderman and C.Kittel *Phys. Rev.* **96** 99 (1954)

[40] R.W.Erwin, J.J.Rhyne, M.B.Salamon, J.Borchers, S.Sinha, R.Du, J.E.Cunningham and C.P.Flynn *Phys. Rev.* **35B** 6808 (1987)

[41] S.H.Liu in *Handbook on the Physics and Chemistry of Rare Earths* ed. K.A.Gschneidner Jr. and L.R. Eyring, North-Holland, Amsterdam (1978)

[42] D.Weller, S.F.Alvarado, W.Gudat, K.Schroder and M.Campagna *Phys. Rev. Lett.* **54** 1555 (1985)

[43] D.Weller and S.F.Alverado *Phys. Rev.* **37B** 9911 (1988)

[44] B.J.Beaudry and K.A.Gschneidner Jr. in *Handbook on the Physics and Chemistry of Rare Earths* eds. K.A.Gschneidner Jr. and L.Eyring, vol. 1, North-Holland, Amsterdam (1978)

[45] D.Fort *J. Crystal Growth* **94** 85 (1989)

[46] D.Fort *J. Less-common Metals* **134** 45 (1987)

[47] J.S.Abell in *Handbook on the Physics and Chemistry of Rare Earths* eds. K.A.Gschneidner Jr. and L.Eyring, vol. 12, North-Holland, Amsterdam (1989)

[48] F.H.Spedding, D.Cress and B.J.Beaudry *J. Less-common Metals* **23** 263 (1971)

[49] T.G.Carnahan and T.E.Scott *Metall. Trans.* **4** 27 (1973)

[50] H.E.Nigh *J. Appl. Phys.* **34** 3323 (1963)

[51] L.R.Edwards and S.Legvold *Phys. Rev.* **176** 753 (1968)

[52] M.Schieber in *Crystal Growth* ed. H.S.Perser, Pergamon, New York (1967)

[53] F.J.Cadieu and D.H.Douglas *J. Appl. Phys.* **40** 2376 (1969)

[54] D.A.Hukin *Clarendon Lab. report* 24/71 (1971) unpublished

[55] K.A.McEwen and P.Touborg *J. Phys. F: Metal Phys.* **3** 1903 (1973)

[56] O.N.Carlson, F.A.Schmidt and D.T.Peterson *J. Less-common Metals* **19** 1 (1966)

[57] R.G.Jordan, D.W.Jones and P.G.Mattocks *J. Less-common Metals* **34** 25 (1974)

[58] R.G.Jordan *Contemp. Phys.* **15** 375 (1974)

[59] J.Kolaczkiewicz and E.Bauer *Surf. Sci.* **175** 487 (1986)

[60] A.Stenborg and E.Bauer *Surf.Sci.* **189/190** 570 (1987)

[61] A.Stenborg and E.Bauer *Phys. Rev.* **36B** 5840 (1987)

[62] A.Stenborg and E.Bauer *Surf. Sci.* **185** 394 (1987)

[63] N.Martensson, A.Stenborg, O.Bjorneholm, A.Nilsson and J.N.Anderson *Phys. Rev. Lett.* **60** 1731 (1988)

[65] C.F.Majkrzak, J.Kwo, M.Hong, Y.Yafet, D.Gibbs, C.L.Chien and J.Bohr *Adv. in Phys.* **40** 99 (1991)

[66] G.A.Sawatzky in *Auger Spectroscopy and Electronic Structure* eds. G.Cubiotti, G.Mondio and K.Wandelt, Springer-Verlag, Berlin (1988)

[67] J.K.Lang, Y.Baer and P.A.Cox *J. Phys. F: Metal Phys.* **11** 121 (1981)

[68] J.O.Dimmock and A.J.Freeman *Phys. Rev. Lett.* **13** 750 (1964)

[69] H.L.Skriver *The LMTO Method* Springer-Verlag, Berlin (1983)

[70] O.K.Anderson *Phys. Rev.* **12B** 3060 (1975)

[71] U.von Barth and L.Hedin *J. Phys. C: Solid State Phys.* **5**, 1629 (1972)

[72] D.D.Koelling and B.N.Harmon *J. Phys. C: Solid State Phys.* **10** 3107 (1977)

[73] S.C.Wu, H.Li, D.Tian, J.Quinn, Y.S.Li, F.Jona, J.Sokolov and N.E.Christensen *Phys. Rev.***41B** 11912 (1990), and *Phys. Rev.* **43B** 12060 (1991)

[74] M.Matsumoto, J.B.Staunton and P.Strange *J. Phys.: Condens. Matter* **3** 1453 (1991)

[75] P.Blaha, K.Schwarz and P.H.Dederichs *Phys. Rev.* **38B** 9368 (1988)

[76] C.Jackson *Phys. Rev.* **178** 949 (1969)

[77] S.C.Keeton and T.L.Loucks *Phys. Rev.* **168** 672 (1968)

[78] T.L.Loucks *Phys. Rev.* **144** 504 (1966)

[79] J.Sticht and J.Kubler *Solid State Commun.* **53** 529 (1985)

[80] B.C.H.Krutzer and F.Springelkamp *J. Phys.: Condens. Matter* **1** 8369 (1989)

[81] W.M.Temmerman and P.A.Sterne *J. Phys.: Condens. Matter* **2** 5529 (1990)

[82] A.R.Mackintosh *Phys .Lett.* **28A** 217 (1968)

[83] S.C.Keeton and T.L.Loucks *Phys. Rev.* **146** 429 (1966)

[84] G.S.Fleming, S.H.Liu and T.L.Loucks *Phys. Rev. Lett.* **21** 1524 (1968)

[85] G.S.Fleming, S.H.Liu and T.L.Loucks *J.Appl.Phys.* **40** 1285 (1969)

[86] D.Glotzel *J. Phys. F: Metal Phys.* **8** L163 (1978)

[87] S.S.Dhesi, R.I.R.Blyth, P.A.Gravil, R.J.Cole and S.D.Barrett *Surf. Sci.* (submitted)

[88] A.J.Freeman and J.O.Dimmock *Bull. Am. Phys. Soc.* **11** 216 (1966)

[89] O.K.Anderson and T.L.Loucks *Phys. Rev.* **167** 551 (1968)

[90] A.M.Begley (private communication)

[91] G.Johannson and A.R.Mackintosh *Solid State Commun.* **8** 121 (1970)

[92] B.N.Harmon *J.Physique* **40**, *Colloque* **C5**, 5 (1979)

[93] O.Jepson and O.K.Anderson *Solid State Commun.* **9** 1763 (1971)

[94] D.Fort and S.D.Barrett (private communication)

[95] D.R.Gustafson, J.D.McNutt and L.O.Roellig *Phys. Rev.* **183** 435 (1969)

[96] B.Johansson *Phil. Mag.* **30** 469 (1974)

[97] W.E.Pickett, A.J.Freeman and D.D.Koelling *Phys. Rev.* **23B** 1266 (1981)

[98] P.J.Feibelmann and D.R.Hamann *Solid State Commun.* **31** 413 (1979)

[99] M.Erbaduk, P.Kalt, L.Schlapbach and K.Bennemann *Surf. Sci.* **126** 101 (1982)

[100] S.D.Barrett, A.M.Begley, P.J.Durham, R.G.Jordan and W.M.Temmerman *J.Phys.: Condens. Matter* **1** SB243 (1989)

[101] S.D.Barrett, A.M.Begley, P.J.Durham and R.G.Jordan *Solid State Commun.* **71** 111 (1988)

[102] N.T.Barrett, C.Guillot, B.Villette, G.Treglia and B.Legrand, *Surf. Sci.* **251/252** 717 (1991)

[103] C.G.Larsson *Surf. Sci.* **152/153** 213 (1985)

[104] J.B.Pendry *Surf. Sci.* **57** 679 (1976)

[105] J.F.L.Hopkinson, J.B.Pendry and D.J.Titterington *Comp. Phys. Comm.* **19** 69 (1980)

[106] R.G.Jordan, A.M.Begley, S.D.Barrett, P.J.Durham and W.M.Temmerman *Solid State Commun.* **76** 579 (1990)

[107] B.Ginatempo, P.J.Durham and B.L.Gyorffy *J. Phys.: Condens. Matter* **1** 6483 (1989)

[108] I.R.Collins, A.D.Laine, P.T.Andrews and P.J.Durham *J. Phys.: Condens. Matter* **3** 5307 (1991)

[109] L.C.Davis *J. Appl. Phys.* **59** R25 (1986) and references therein

[110] R.G.Jordan *J. Phys.: Condens. Matter* **1** 9795 (1989)

[111] G.Treglia, F.Ducastelle and D.Spanjaard *J. Physique* **43** 341 (1982)

[112] R.H.Williams *Surf. Sci.* **251/252** 12 (1991)

[113] W.F.Egelhoff *Surf. Sci. Rep.* **6** 253 (1987)

[114] K.Wille *Rep. Prog. Phys.* **54** 1005 (1991)

[115] E.-E. Koch *Handbook on synchrotron radiation* North-Holland, Amsterdam (1983)

[116] P.D.Johnson and S.L.Hulbert *Rev. Sci. Inst.* **61** 2277 (1990)

[117] A.D.Laine, PhD Thesis, University of Liverpool, U.K. (1986)

[118] I.R.Collins, PhD Thesis, University of Liverpool, U.K. (1988)

[119] G.Denninger, V.Dose and M.Scheidt *Appl. Phys.* **81** 375 (1979)

[120] S.L.Hulbert, P.D.Johnson, N.G.Stoffel, W.A.Royer and N.V.Smith *Phys. Rev.* **31B** 6815 (1985)

[121] G.Chauvet and R.Baptist *J. Electron Spectrosc. Relat. Phenom.* **24** 255 (1981)

[122] P.T.Andrews and I.R.Collins *Physica Scripta* **T29** 116 (1989)

[123] M.K.Debe and D.A.King *Phys. Rev. Lett.* **39** 708 (1977)

[124] I.R.Collins, A.D.Laine and P.T.Andrews (unpublished)

[125] I.R.Collins, A.R.Law and P.T.Andrews *J. Phys. C: Solid State Phys.* **21** L655 (1988)

[126] E.Jensen and E.W.Plummer *Phys. Rev. Lett.* **55** 1912 (1985)

[127] N.Heritage and P.T.Andrews (unpublished)

[128] E.T.Jensen, R.E.Palmer, R.F.Willis, I.R.Collins and P.T.Andrews *Vacuum* **38** 353 (1988)

[129] P.D.Johnson, D.A.Wesner, J.W.Davenport and N.V.Smith *Phys. Rev.* **30B** 4860

(1984)

[130] I.R.Collins, P.T.Andrews and A.R.Law *Phys. Rev.* **38B** 13348 (1988)

[131] A.R.Law, P.T.Andrews and H.P.Hughes *Vacuum* **41** 553 (1990)

[132] A.R.Law, P.T.Andrews and H.P.Hughes *J. Phys.: Condens. Matter* **3** 813 (1991)

[133] A.R.Law, H.P.Hughes, P.T.Andrews and F.A.Levy *Solid State Commun.* **78** 599 (1991)

[134] A.R.Law, P.T.Andrews and H.P.Hughes (unpublished)

[135] M.A.Hoyland and R.G.Jordan *J. Phys.: Condens. Matter* **3** 1337 (1991) and (many) references therein

[136] S.Tougaard and A.Ignatiev *Surf. Sci.* **115** 270 (1982)

[137] J.Sokolov, J.Quinn, F.Jona and P.M.Marcus *Bull. Am. Phys. Soc.* **34** 579 (1989)

[138] R.G.Jordan *Physica Scripta* **T13** 22 (1986)

[139] J.Onsgaard, S.Tougaard, P.Morgen and F.Ryborg in *Proceedings of the 4th international conference on solid surfaces, and the 3rd European conference on surface science, Surf. Sci. Suppl.* **201** 1361 (1980)

[140] J.Onsgaard, S.Tougaard, P.Morgen and F.Ryborg *J. Electron Spectrosc. Relat. Phenom.* **18** 29 (1980)

[141] E.Zanazzi and F.Jona *Surf. Sci.* **62** 61 (1977)

[142] R.Kammerer, J.Barth, F.Gerken, A.Flodstrom and L.I.Johansson *Solid State Commun.* **41** 435 (1982)

[143] J.J.Yeh and I.Lindau *At. Data Nuc. Data Tables* **32** 1 (1985)

[144] F.P.Netzer, R.A.Wille and M.Grunze *Surf. Sci.* **102** 75 (1981)

[145] F.P.Netzer and E.Bertel in *Handbook on the Physics and Chemistry of Rare Earths* eds. K.A.Gschneidner Jr. and L.Eyring, vol. 5, North-Holland, Amsterdam (1982)

[146] G.G.Libowitz and A.J.Maeland in *Handbook on the Physics and Chemistry of Rare Earths* eds. K.A.Gschneidner Jr. and L.Eyring, vol. 3, North-Holland, Amsterdam (1979)

[147] J.H.Weaver, R.Rosei and D.T.Peterson *Solid State Commun.* **25** 201 (1979)

[148] J.H.Weaver, R.Rosei and D.T.Peterson *Phys. Rev.* **19B** 4855 (1979)

[149] D.J.Peterman, B.N.Harmon, J.Marchiando and J.H.Weaver *Phys. Rev.* **19B** 4867 (1979)

[150] J.H.Weaver, D.T.Peterson and R.L.Benbow *Phys. Rev.* **20B** 5301 (1979)

[151] D.J.Peterman and B.N.Harmon *Phys. Rev.* **20B** 5313 (1979)

[152] D.J.Peterman, B.N.Harmon, D.L.Johnson and J.Marchiando *Z. Phys. Chem. NF* **116** 47 (1979)

[153] J.H.Weaver and D.T.Peterson *Z. Phys. Chem. NF* **116** 57 (1979)

[154] D.J.Peterman, D.T.Peterson and J.H.Weaver *J. Less-common Metals* **74** 167 (1980)

[155] J.H.Weaver and D.T.Peterson *J. Less-common Metals* **74** 207 (1980)

[156] R.Baptiste, A.Pellisier and G.Chauvet *Z. Phys. B - Cond. Matter* **73** 107 (1988)

[157] R.Du, F.Tsui and C.P.Flynn *Phys. Rev.* **38B** 2941 (1988)

[158] J.E.Inglesfield *Prog. Surf. Sci.* **20** 105 (1985)

[159] A.Stenborg, J.N.Anderson, O.Bjorneholm, A.Nilsson and N.Martensson *Phys. Rev. Lett.* **63** 187 (1989)

[160] J.Osterwalder *Z. Phys. B - Cond. Matter* **61** 113 (1985)

[161] W.Speier, J.C.Fuggle, R.Zeller, B.Ackerman, K.Szot, F.U.Hillebricht and M.Campagna *Phys. Rev.* **30B** 6921 (1984)

[162] D.A.Papaconstantopoulos *Handbook of the Band Structures of Elemental Solids* Plenum, New York (1986)

[163] A.M.Begley PhD Thesis, University of Birmingham, U.K. (1990)

[164] D.Li, P.A.Dowden and M.Onellion *Bull. Am. Phys. Soc.* **36** 905 (1991)

[165] F.R.McFeely, S.P.Kowalcyk, L.Ley and D.A.Shirley *Phys. Lett.* **49A** 301 (1974)

[166] C.Carbone, T.Kachel, R.Rochow and W.Gudat *Z. Phys. B - Cond. Matter* **79** 325 (1990)

[167] R.G.Jordan, X.Wang, A.M.Begley, S.L.Qiu and Y.Liu *Solid State Commun.* **78** 1045 (1991)

[168] W.Lenth, F.Lutz, J.Barth, G.Kalkoffen and C.Kunz *Phys. Rev. Lett.* **41** 1185 (1978)

[169] P.Weightman.*Physica Scripta* **T25** 165 (1989)

[170] J.C.Riviere, G.Strasser, G.Rosina, F.P.Netzer and J.A.D.Matthew *J.Electron Spectrosc.Relat.Phenom.* **36** 331 (1985)

[171] M.Cardona and L.Ley *Photoemission in Solids I: General Principles* Appendix 1 Springer, Berlin (1978)

[172] M.Cini *Solid State Commun.* **20** 605 (1976)

[173] M.Cini *Solid State Commun.* **24** 681 (1977)

[174] M.Cini *Phys. Rev.* **17B** 2788 (1978)

[175] G.A.Sawatzky *Phys. Rev. Lett.* **39** 504 (1977)

[176] P.D.Johnson and X.Pan *Phys. Rev.* **38B** 9447 (1988)

[177] Z.Szotek, W.M.Temmerman and H.Winter *Daresbury Preprint* DI/SCI/P726T (1991)

List of abbreviations and acronyms used

ADES	Angle dispersed electron spectroscopy
AES	Auger electron spectroscopy
APW	Augmented plane wave
ARUPS	Angle-resolved ultraviolet photoemission spectroscopy
ASA	Atomic sphere approximation
ASW	Augmented spherical wave
bcc	Body centred cubic
BIS	Bremsstrahlung isochromat spectroscopy
CCV	Core-core-valence
CIS	Constant initial state
CFS	Constant final state
CMA	Cylindrical mirror analyser
CVV	Core-valence-valence
dhcp	Double c-axis hexagonal close packed
dHvA	de Haas - van Alphen
DOS	Density of states
EDC	Energy distribution curve
EELS	Electron energy loss spectroscopy
E_F	Fermi level
fcc	Face centred cubic
GIM	Grazing incidence monochromator
HBL	High brightness lattice
HREELS	High resolution electron energy loss spectroscopy
I-V	Intensity (voltage)
IPE	Inverse photoemission

hcp	Hexagonal close packed
KKR	Korringer-Kohn-Rostoker
KRIPES	Momentum (**k**) resolved inverse photoemission spectroscopy
LAPW	Linear augmented plane wave
LDA	Local density approximation
LEED	Low energy electron diffraction
LINAC	Linear accelerator
LMTO	Linear muffin tin orbital
MBE	Molecular beam epitaxy
mfp	Mean free path
NEXAFS	Near edge extended X-ray absorption fine structure
RAPW	Relativistic augmented plane wave
RKKY	Ruderman-Kittel-Kasuya-Yosida
RLMTO	Relativistic linear muffin tin orbital
RRR	Residual resistance ratio
SCF	Self-consistent field
SCLS	Surface core-level shift
SEXAFS	Surface extended X-ray absorption fine structure
SIC	Self-interaction correction
SODS	Surface-order-dependent state
SPRASW	Spin-polarised relativistic augmented spherical wave
SRS	Synchrotron radiation source
SSE	Solid state electrotransport
TGM	Toroidal grating monochromator
$\mathbf{T_R}$	Reconstruction temperature
U	Correlation energy
UHV	Ultra high vacuum
UPS	Ultraviolet photoemission spectroscopy

VUV	Vacuum ultraviolet
W	Bandwidth
XPS	X-ray photoemission spectroscopy

Periodic Table of the Elements